Thermal and dielectric behavior of porous media

DISSERTATION

in fulfillment of the requirements for the degree

"Doktor-Ingenieur (Dr.-Ing.)"

of the Faculty of Mathematics and Natural Sciences

at Kiel University

submitted by

Henok Hailemariam

Kiel, 2019

Schriftenreihe des Lehrstuhls Geomechanik und Geotechnik
Christian-Albrechts-Universität zu Kiel
Heft 3

ISSN 2365-7162

Herausgeber:

Lehrstuhl für Geomechanik und Geotechnik

Christian-Albrechts-Universität zu Kiel

Prof. Dr.-Ing. habil. Frank Wuttke

Ludewig-Meyn-Straße 10

24118 Kiel

Telefon: ++49 – (0)431 – 880 2857

Telefax: ++49 – (0)431 – 880 7606

Internet: www.geotechnics.ifg.uni-kiel.de

Bezugsadresse:

Christian-Albrechts-Universität zu Kiel
Lehrstuhl für Geomechanik und Geotechnik

First referee: Prof. Dr.-Ing. habil. Frank Wuttke
Kiel University

Second referee: Prof. Dr. Dante Fratta
University of Wisconsin-Madison

Date of the oral examination: 03.07.2019.
Approved for publication: 05.09.2019.

The Dean

Declaration of Authorship

I, Henok Hailemariam, declare that apart from my supervisor's guidance, the content and design of this thesis titled "Thermal and dielectric behavior of porous media" is all my own work and only using the sources listed. I confirm that:

- The thesis has not been submitted either partially or wholly as part of a doctoral degree to any other examining body, and it has not been published or submitted for publication.
- The thesis has been prepared in accordance to the Rules of Good Scientific Practice of the German Research Foundation.
- An academic degree of mine has never been withdrawn.

Kiel, 02.04.2019

Henok Hailemariam

Vorwort des Herausgebers

Die vorliegende Promotionsschrift von Herrn Dr.-Ing. Henok Hailemariam ist dem Forschungs- und Arbeitsgebiet „Bodenmechanik“ und dem „Struktur- und Parametermonitoring“ zuzuordnen. Die in der Arbeit zugrundeliegende Problemstellung hatte sich in der Bearbeitung von offenen Fragen auf dem Gebiet der Energie-Geotechnik ergeben, ist allerdings für die Analyse weiterer poröser Medien auf dem Gebiet der Geotechnik nutzbar. Die Zielstellung der Promotionsarbeit liegt in der Entwicklung einer Methodik zur Detektion von thermischen Bodenparametern, wie der thermischen Leitfähigkeit, durch indirekte geophysikalische, elektromagnetische Methoden. Ausgehend von unterschiedlichen Mischmodellen in Abhängigkeit von den Materialparametern, wie Porosität, Wassergehalt und dielektrische Leitfähigkeit, wird die effektive thermische Leitfähigkeit abhängig von der effektiven dielektrischen Leitfähigkeit und von Bodenmikroparametern in Mehrphasenmedien modelliert. Neben der analytischen Methodenentwicklung erfolgte eine ausführliche Validierung anhand unterschiedlicher Geomaterialien und Randbedingungen. Zusätzlich zu den entwickelten semi-analytischen Ansätzen wurde eine numerische Simulationssoftware, die Lattice-Elemente-Methode (LEM), auf der Mikro- und Mesoskala für gekoppelte thermo-dielektrische Problemstellungen weiterentwickelt. Mit Hilfe der LEM konnten die entwickelten semi-analytischen Modelle der effektiven Wärmeleitfähigkeit basierend auf mikrostrukturellen Parametern und der dielektrischen Leitfähigkeit zusätzlich validiert werden.

Die Dissertationsschrift beinhaltet die konsequente Weiterentwicklung und Kopplung von bisherigen Ansätzen und Modellen zur Bestimmung der effektiven Wärmeleitfähigkeit und von mikrobasierten Mischmodellen der effektiven dielektrischen Leitfähigkeit in Böden. In zahlreichen Validierungsstudien wurde durch verschiedene experimentelle Analysen die Leistungsfähigkeit und hohe Prognosefähigkeit der entwickelten Methode in der Dissertationsschrift dokumentiert. Mit der Entwicklung der neuen Methodik zur Bestimmung effektiver thermischer Leitfähigkeiten basierend auf elektromagnetischen Meßmethoden ist ein sehr kraftvolles Werkzeug entstanden, um zukünftige Erkundungsvorhaben für Bauvorhaben in der Energie-Geotechnik effektiv durchführen zu können.

Kiel, im Juli 2019 Frank Wuttke

Acknowledgements

I would like to take this opportunity to first and foremost thank God Almighty for granting me the opportunity, health and strength to complete this thesis.

I am very grateful to all the people who contributed in this work, for their unreserved support, guidance and encouragement played a vital role in the completion of this thesis.

Firstly, I would like to express my deep gratitude and sincere appreciation to my supervisor, Prof. Dr.-Ing. Frank Wuttke, for his meticulous guidance and patience throughout my period of candidature. This doctoral research would undoubtedly not have been possible without his support and encouragement. Besides my supervisor, I would like to thank Prof. Dr. Dante Fratta for his agreement to be reviewer and member of the committee of this dissertation, and for his valuable remarks and comments. I would also like to cordially thank the other three members of the committee, Prof. Dr. Romain Bousquet, Prof. Dr. Wolfgang Rabbel and Prof. Dr. Ludger Klinkenbusch.

I would also like to express my deep and sincere appreciation to Dr. Norman Wagner (Institute of Material Research and Testing - MFPA, Bauhaus-University Weimar) for his useful discussions and for helping me to develop my background in electromagnetics. His technical advice and contribution to the present work was substantial.

Completing this work would have been all the more difficult were it not for the enlightening scientific discussions, support and friendship provided by all my past and present colleagues and members of the Department of Geomechanics and Geotechnics of Kiel University. I am indebted to them for their help. Special thanks go to Dr. Ahmed Al-Janabi, Mr. Dinesh Shrestha and Mr. Binod Kafle for their valuable assistance in the experiments and the ever fruitful discussions.

Last, but not least, I would like to thank all my family members and friends from the bottom of my heart for their endless love and support. They have made me what I am today, and I would like to dedicate this thesis to them.

Henok Hailemariam

Abstract

Understanding the heat transfer and electromagnetic (EM) porous media behavior is vital in conducting analysis and modeling operations in various fields of geomechanics and geotechnics, engineering, geology, hydrology, agriculture etc. These processes (mainly controlled by the thermal conductivity and complex dielectric permittivity or complex electrical conductivity) also play a vital role in solving problems in energy geotechnics with transient temperature, moisture content, stress and other hydro-mechanical parameter changes in unsaturated porous media conditions.

Furthermore, the thermal and dielectric processes of porous media are highly correlated and are both affected by changes in chemical composition, grain structure and hydro-mechanical conditions. In this thesis, relationships between the effective thermal conductivity and effective complex dielectric permittivity of soils and oil sands, with known hydro-mechanical properties, are experimentally studied using transient/steady state and high frequency electromagnetic (HF-EM) measurement techniques, respectively. As expected, a strong correlation between the two parameters is obtained for a wide range of porous media hydro-mechanical conditions such as water content, porosity, matric suction, effective stress and temperature. Additionally, semi-theoretical models for the prediction of the effective thermal conductivity of soils and oil sands as a function of effective complex dielectric permittivity are proposed. The new models can be used to estimate the effective thermal conductivity of large scale subsurface porous media deposits using dielectric data collected from non-destructive HF-EM measurement techniques such as the ground penetrating radar or at laboratory scale measurements using devices such as a time domain reflectometry or a vector network analyzer, without the need to extract samples for moisture and bitumen content measurement.

The experimental and theoretical findings of the inter-relationship between the effective thermal conductivity and effective complex dielectric permittivity are further complemented with the development of a new numerical model based on the lattice element method (LEM). As a discrete element based approach, the LEM provides a good basis for simulating the thermal and dielectric behavior of porous media, as the different constituent phases of the porous medium can be modeled as discrete nodal elements which conduct applied thermal and electromagnetic energy according to their rates of thermal and electrical conductance, which would otherwise be difficult to model with continuum based models such as the finite element method (FEM). The experimental measurements are finally compared with the predictions of the new semi-theoretical and numerical models with satisfactory results.

Zusammenfassung

Das Verständnis von Wärmeübertragung und dem elektromagnetischen Verhaltens poröser Medien ist für die Durchführung von Analyse- und Modellierungsvorgängen in viele Bereichen der Geomechanik, Geotechnik, der Ingenieurwissenschaft, der Geologie, Hydrologie, der Landwirtschaft und vielen weiteren von grundlegender Bedeutung. Diese Prozesse (vor allem kontrolliert durch die Wärmeleitfähigkeit und durch komplexe dielektrische Permitivität) spielen außerdem eine entscheidende Rolle bei der Lösung von Problemen in der Energie-Geotechnik mit variabler Temperatur, Feuchtigkeitsgehalt, Belastung und weiteren Änderungen hydromechanischer Parameter unter den Bedingungen ungesättigter poröser Medien.

Darüber hinaus korrelieren die thermischen und die dielektrischen Prozesse poröser Medien, stark miteinander und werden beide durch Änderungen der chemischen Zusammensetzung, der Kornstruktur und der hydromechanischen Eigenschaften beeinflusst. In dieser Arbeit wird die Beziehung zwischen der effektiven Wärmeleitfähigkeit und der effektiven komplexen dielektrischen Permittivität von Böden und Ölsanden mit bekannten hydromechanischen Eigenschaften experimentell untersucht, indem transient/stationär und Hochfrequenz elektromagnetische (HF-EM) Messverfahren verwendet werden. Wie erwartet wird eine starke Korrelation zwischen den beiden Parametern über eine Vielzahl hydromechanischer Eigenschaften für poröse Medien. Des Weiteren werden halbtheoretische Modelle zur Vorhersage der effektiven Wärmeleifähigkeit von Böden und Ölsanden als Funktion der effektiven Dielektrizitätskonstante geplant. Die neuen Modelle können verwendet werden, um die effektive Wärmeleitfähigkeit von unterirdischen Ablagerungen poröser Medien unter Verwendung von dielektrischen Daten abzuschätzen. Diese Daten können aus zerstörungsfreien HF-EM-Messtechniken gewonnen werden ohne, dass Proben für die Messung von Feuchtigkeit und Bitumenanteil genommen werden müssen, indem Messtechniken wie das Bodenradar oder Messungen im Labor mit z.B. einer Zeitbereichsreflektometrie oder einem Vektornetzwerkanalysator vorgenommen werden.

Die experimentellen und theoretischen Ergebnisse der Wechselbeziehung zwischen der effektiven Wärmeleitfähigkeit und der effektive komplexe dielektrische Permittivität werden durch die Entwicklung eines neuen numerischen Modells auf der Grundlage der Lattice-Element-Methode (LEM) ergänzt. Als Modellansatz bietet die LEM eine gute Grundlage für die Simulation des Mesoskala thermischen und dielektrischen Verhaltens poröser Medien, da die verschiedenen konstituierenden Phasen des porösen Mediums als einzelne Knotenelemente modelliert werden können, was mit kontinuumsbasierten Modellen wie der Finite-Element-Methode (FEM) schwierig zu simulieren ist. Der abschließende Vergleich der experimentellen Messungen mit den Vorhersagen der semitheoretischen und numerischen Modelle führt zu zufriedenstellenden Ergebnissen.

Contents

List of Figures

List of Tables

List of Abbreviations

AEV	**A**ir **E**ntry **V**alue
ALRM	**A**dvanced **L**ichtenecker (and) **R**other **M**odel
API	**A**merican **P**etroleum **I**nstitute
ASTM	**A**merican **S**ociety (for) **T**esting (and) **M**aterials
ATT	**A**xis **T**ranslation **T**echnique
BEM	**B**oundary **E**lement **M**ethod
CA	**C**ellulose **A**cetate
CHNS	**C**arbon **H**ydrogen **N**itrogen (and) **S**ulfur
CL	**C**lays (with) **L**ow (plasticity)
CPU	**C**entral **P**rocessing **U**nit
CRIM	**C**omplex **R**efractive **I**ndex **M**odel
CSS	**C**yclic **S**team **S**imulation
DEM	**D**iscrete **E**lement **M**ethod
DTS	**D**istributed **T**emperature **S**ensing
EM	**E**lectro**M**agnetic
ERI	**E**lectrical **R**esistivity **I**maging
ERT	**E**lectrical **R**esistivity **T**omography
FDM	**F**inite **D**ifference **M**ethod
FDR	**F**requency **D**omain **R**eflectometry
FEM	**F**inite **E**lement **M**ethod
FFT	**F**ast **F**ourier **T**ransform
GM	**G**eometric **M**ean
GPR	**G**round **P**enetrating **R**adar
HF-EM	**H**igh **F**requency **E**lectro**M**agnetic
HG	**H**igh **G**rade (oil sand)
HS-L	**H**ashin (and) **S**htrikman **L**ower (bound)
HS-U	**H**ashin (and) **S**htrikman **U**pper (bound)
IEEE	**I**nstitute (of) **E**lectrical (and) **E**lectronics **E**ngineers
L	**L**oess (soil)
LEM	**L**attice **E**lement **M**ethod
LG	**L**ow **G**rade (oil sand)

LLLM	**L**ooyenga **L**andau **L**ifshitz **M**odel
LRM	**L**ichtenecker (and) **R**other **M**odel
MG	**M**edium **G**rade (oil sand)
MPM	**M**aterial **P**oint **M**ethod
OPEC	**O**rganization (of the) **P**etroleum **E**xporting **C**ountries
OWL	**O**pen **W**ater **L**iquid (calibration)
OWS	**O**pen **W**ater **S**hort (calibration)
PIC	**P**article **I**n **C**ell (method)
PONA	**P**araffins **O**lefins **N**aphthenes (and) **A**romatics
PRL	**P**oisson **R**andom **L**attice
SAGD	**S**team **A**ssisted **G**ravity **D**rainage
SARA	**S**aturates **A**romatics **R**esins (and) **A**sphaltenes
SC	**S**ilty **C**lay (soil)
SP	**S**elf **P**otential (method)
SS	**S**teady **S**tate
SWCC	**S**oil **W**ater **C**haracteristic **C**urve
TDR	**T**ime **D**omain **R**eflectometry
T-DE	**T**hermo **D**i**E**lectric
TR	**TR**ansient
USCS	**U**nified **S**oil **C**lassification **S**ystem
VET	**V**apor **E**quilibrium **T**echnique
VF	**V**olume(tric) **F**raction
VNA	**V**ector **N**etwork **A**nalyzer
VRL	**V**ectorized **R**andom **L**attice

Physical Constants

Speed of light	$c_0 = 2.997\,924\,58 \times 10^{8}\,\mathrm{m\,s^{-1}}$
Planck constant	$h = 6.626\,070\,04 \times 10^{-34}\,\mathrm{m^2\,kg\,s^{-1}}$
Boltzmann constant	$k_B = 1.380\,648\,52 \times 10^{-23}\,\mathrm{m^2\,kg\,s^{-2}\,K^{-1}}$
Gas constant	$R = 8.314\,462\,\mathrm{J\,mol^{-1}\,K^{-1}}$
Dielectric permittivity of free space	$\varepsilon_0 = 8.854\,187\,817 \times 10^{-12}\,\mathrm{F\,m^{-1}}$
Magnetic permeability of free space	$\mu_0 = 1.256\,637\,061\,4 \times 10^{-6}\,\mathrm{H\,m^{-1}}$

List of Symbols

a	structure factor or exponent	–
a_k & b_k	incident and reflected waves of a two-port network	–
a_l & b_l	empirical parameters of Lu et al. (2007) model	–
a_{sw} & b_{sw}	saline pore-water static permittivity and relaxation time modification factors of Blanch and Aguasca (2004) model	–
a_w	empirical parameter for permittivity limits of water of the Kaatze (2007b) model	–
A	size of the sub-cell in VRL technique	m
A_c	cross sectional area of element/medium	m^2
A_h	area through which heat flows	m^2
b_0, b_1 & b_2	fitted constants for SH-1 probe	–
b_v	viscosity characterization parameter of the Miadonye et al. (1994) model	–
$\mathbf{B}$	magnetic flux density	T
c	specific heat capacity of medium	$\mathrm{J\,kg^{-1}\,K^{-1}}$
c_1, c_2 & c_3	complex bilinear calibration parameters	–
c_b	specific heat capacity of bitumen	$\mathrm{J\,kg^{-1}\,K^{-1}}$
c_s	specific heat capacity of solids of porous media	$\mathrm{J\,kg^{-1}\,K^{-1}}$
c_{sw}	specific heat capacity of saline or seawater	$\mathrm{J\,kg^{-1}\,K^{-1}}$
c_w	specific heat capacity of water	$\mathrm{J\,kg^{-1}\,K^{-1}}$
C	constant of the Johansen (1975) model	–
C_c & C_u	coefficients of curvature and uniformity of medium	–
C_c & C_v	primary compressibility index and coefficient of consolidation of medium	– / $\mathrm{cm^2\,s^{-1}}$
C_f	capacitance determined by fringing-field effects inside a probe	F
C_o	capacitance determined by fringing-field effects outside a probe that couples to a specimen	F
C_T	thermal conductance	$\mathrm{W\,K^{-1}}$
C_v	constant of the Miadonye et al. (1994) model	–

d & h	diameter and length of specimen	m
$\mathbf{D}$	electric flux density	$\mathrm{C\,m^{-2}}$
D_{10}	grain diameter at 10% passing	mm
D_{50}	grain diameter at 50% passing	mm
e	void ratio of medium	–
e_o	initial void ratio of medium	–
$\mathbf{E}$	electric field intensity	$\mathrm{V\,m^{-1}}$
$\mathbf{E_0}$	amplitude of applied electric field intensity	$\mathrm{V\,m^{-1}}$
Ei	exponent integral	–
f	frequency	Hz
G_E	electrical conductance	S
G_s	specific gravity of solid grain particles	–
h_0	initial height of porous medium	m
$\mathbf{H}$	magnetic field intensity	$\mathrm{A\,m^{-1}}$
I	electric current	A
j	imaginary unit	–
$\mathbf{J}$	electric current density	$\mathrm{A\,m^{-2}}$
$\mathbf{J_D}$	displacement current density	$\mathrm{A\,m^{-2}}$
$\mathbf{J_{eff}}$	effective total current density	$\mathrm{A\,m^{-2}}$
k	transmission coefficient	–
k^*	complex wave number or propagation factor of an EM wave in a medium	$\mathrm{m^{-1}}$
k'	real part of complex wave number or the phase constant of an EM wave in a medium	$\mathrm{m^{-1}}$
k''	imaginary part of complex wave number or the attenuation factor of an EM wave in a medium	$\mathrm{m^{-1}}$
k_0	wave number of an electromagnetic wave in free space	$\mathrm{m^{-1}}$
K	soil texture dependent constant of the Minkov et al. (1977) model	–
K_e	Kersten's number	–
l	length of element/medium	m
L_L	liquid limit	%
n	porosity of medium	–
n^*	complex index of refraction of an electromagnetic wave in a medium	–
n'	real part of complex index of refraction of an EM wave in a medium	–

n''	imaginary part of complex index of refraction of an EM wave in a medium	–
n_i	LEM model step or iteration number	–
n_o	initial porosity of medium	–
p_1	AEV parameter of the Fredlund and Xing (1994) model	kPa
p_2 & p_3	slope parameters of the Fredlund and Xing (1994) model	–
P_I	plasticity index	%
q	heat flux	$\mathrm{W\,m^{-2}}$
q_E	electric charge	C
q_f	volumetric quartz fraction	–
qq	phonon scattering coefficient of the Hailemariam and Wuttke (2018b) model	–
Q	rate of heat transfer	$\mathrm{W\ (J\,s^{-1})}$
Q_s	constant rate of heat application of the TR-1 probe	$\mathrm{W\,m^{-1}}$
Q_T	heat quantity	J
r	distance between the heater and the sensor of the TR-1 probe	m
r_h	distance between the two needles of SH-1 probe	m
R	randomness factor	–
R_E	electrical resistance	Ω
R_T	thermal resistance	$\mathrm{K\,W^{-1}}$
R_λ	thermal resistivity	$\mathrm{m\,K\,W^{-1}}$
s_m	size of the main-cell or generated mesh in VRL technique	m
S	pore-water salinity	psu $(\mathrm{g\,kg^{-1}})$
S^*	complex scattering parameter	–
S_{12}	distance between top and reference disc thermocouples of SS device	m
S_{23}	distance between bottom and reference disc thermocouples of SS device	m
S^*_{kl}	elements of complex scattering matrix	–
S^*_m	measured complex reflection coefficient	–
$S^*_{m,eff}$	measured effective complex reflection coefficient of porous media	–
$S^*_{m,m}$	measured complex reflection coefficient of methanol	–
$S^*_{m,o}$	measured complex reflection coefficient of open/air	–
$S^*_{m,s}$	measured complex reflection coefficient of short circuit	–
$S^*_{m,w}$	measured complex reflection coefficient of water	–

S_p & S_v	heights of specimen and reference disc of SS device	m
S_r	degree of saturation of medium	–
S_v	measure of the variation of viscosity with temperature in the Miadonye et al. (1994) model	–
t	time	s
t_h	duration of heating for SH-1 probe	s
T	temperature of medium	K / °C
T_0	temperature at the start of the measurement for SH-1 probe	K
T_1	temperature of the top heating plate of SS device	°C
T_2	temperature of the reference plate of SS device	°C
T_3	temperature of the bottom cooling plate of SS device	°C
T_{av}	average specimen temperature in SS device	°C
T_o	reference temperature of the Hailemariam and Wuttke (2018b) model	°C
u_a	pore-air pressure in ATT	kPa
u_w	pore-water pressure in ATT	kPa
v	propagation velocity of an electromagnetic wave in a medium	$\mathrm{m\,s^{-1}}$ ($\mathrm{cm\,ns^{-1}}$)
V	volume fraction	–
V_E	voltage	V
V_b	volumetric fraction of bitumen	–
V_s	volumetric fraction of solids of porous media	–
V_w	volumetric fraction of water	–
w	gravimetric water content of medium	–
w_o	initial gravimetric water content of medium	–
w_n	natural gravimetric water content of medium	–
W	weight fraction / volume	– / $\mathrm{m^3}$
W_b	weight fraction of bitumen	–
W_s	weight fraction of solids of porous media	–
W_w	weight fraction of water	–
x	thickness of medium	m
Y^*	complex admittance	S
$\mathbf{z}$	attenuation distance vector of an EM wave in a medium	m
Z^*	complex impedance	Ω
Z_o	real characteristic impedance of probe	Ω
α	thermal diffusivity of medium	$\mathrm{m^2\,s^{-1}}$

α_s	soil texture dependent parameter of Lu et al. (2007) model	–
β	Power-law exponent	–
β_{CC}	stretching exponent or Cole-Cole parameter	–
Γ^*	true complex reflection coefficient	–
δ	loss tangent of medium	$^\circ$
δ_b	loss tangent of bitumen	$^\circ$
δ_{eff}	effective loss tangent of medium	$^\circ$
δ_g	loss tangent of solid grains of porous medium	$^\circ$
$\delta_{np,3}$	water-driven settlement potential of medium	–
δ_{sd}	skin depth of medium	m
δ_{sw}	loss tangent of saline or seawater	$^\circ$
δ_w	loss tangent of water	$^\circ$
Δe	change in void ratio of medium	–
$\Delta G_w^\#$	free enthalpy of activation or Gibbs free energy of water	$\mathrm{J\,mol^{-1}}$
Δh	change in height of porous medium	m
$\Delta H_w^\#$	activation enthalpy of water	$\mathrm{J\,mol^{-1}}$
ΔS_i	distance between respective temperature gradient points across the central axis of SS device	m
$\Delta S_w^\#$	activation entropy of water	$\mathrm{J\,mol^{-1}\,K^{-1}}$
ΔT	change in temperature of medium	K / °C
$\Delta\varepsilon$	relaxation magnitude	–
$\Delta\sigma'$	applied effective stress increment	kPa
ϵ	LEM model convergence error	–
ε^*	complex absolute permittivity of medium	$\mathrm{F\,m^{-1}}$
ε^*_{eff}	effective complex absolute permittivity of medium	$\mathrm{F\,m^{-1}}$
ε'_{eff}	real part of effective complex absolute permittivity of medium	$\mathrm{F\,m^{-1}}$
ε''_{eff}	imaginary part of effective complex absolute permittivity of medium	$\mathrm{F\,m^{-1}}$
$\varepsilon_{m,w}$	empirical parameter for permittivity limits of water of the Kaatze (2007b) model	–
$\varepsilon_{r,a}$	real apparent relative permittivity of medium according to Topp et al. (1980)	–
$\varepsilon^*_{r,a}$	relative complex dielectric permittivity of air	–
$\varepsilon^*_{r,b}$	relative complex dielectric permittivity of bitumen	–
$\varepsilon'_{r,b}$	real part of relative complex permittivity of bitumen	–
$\varepsilon''_{r,d}$	dielectric loss of medium	–

ε_r^*	relative complex dielectric permittivity of medium	–
ε_r'	real part of relative complex permittivity of medium	–
ε_r''	imaginary part of relative complex permittivity of medium	–
$\varepsilon_{r,eff}^*$	relative effective complex permittivity of medium	–
$\varepsilon_{r,eff}'$	real part of relative effective complex permittivity of medium	–
$\varepsilon_{r,eff}''$	imaginary part of relative effective complex permittivity of medium	–
$\varepsilon_{r,f}^*$	relative complex dielectric permittivity of fluids	–
$\varepsilon_{r,g}^*$	relative complex dielectric permittivity of solids of porous media	–
$\varepsilon_{r,g}'$	real part of relative complex permittivity of solid grain particles of porous media	–
$\varepsilon_{r,m}^*$	relative complex dielectric permittivity of methanol	–
$\varepsilon_{r,sw}^*$	relative complex dielectric permittivity of saline or seawater	–
$\varepsilon_{r,sw}'$	real part of relative complex permittivity of seawater	–
$\varepsilon_{r,sw}''$	imaginary part of relative complex permittivity of seawater	–
$\varepsilon_{r,w}^*$	relative complex dielectric permittivity of water	–
$\varepsilon_{r,w}'$	real part of relative complex permittivity of water	–
$\varepsilon_{r,w}''$	imaginary part of relative complex permittivity of water	–
ε_s	static permittivity	–
ε_∞	high frequency limit of permittivity	–
η	parameter of the Côté and Konrad (2005) model	–
θ	volumetric water content of medium	–
θ_o	initial volumetric water content of medium	–
κ	soil texture dependent parameter of the Côté and Konrad (2005) model	–
λ	thermal conductivity of medium	$\mathrm{W\,m^{-1}\,K^{-1}}$
λ_a	thermal conductivity of air	$\mathrm{W\,m^{-1}\,K^{-1}}$
λ_b	thermal conductivity of bitumen	$\mathrm{W\,m^{-1}\,K^{-1}}$
λ_d	effective thermal conductivity of medium in dry condition	$\mathrm{W\,m^{-1}\,K^{-1}}$
λ_{dom}	thermal conductivity of the dominant mineral of the Hailemariam and Wuttke (2018b) model	$\mathrm{W\,m^{-1}\,K^{-1}}$
λ_f	thermal conductivity of fluids	$\mathrm{W\,m^{-1}\,K^{-1}}$

λ_l	lower bound of thermal conductivity	$\mathrm{W\,m^{-1}\,K^{-1}}$
λ_{meas}	measured thermal conductivity	$\mathrm{W\,m^{-1}\,K^{-1}}$
λ_o	thermal conductivity of minerals other than quartz	$\mathrm{W\,m^{-1}\,K^{-1}}$
λ_p	thermal conductivity of specimen in SS device	$\mathrm{W\,m^{-1}\,K^{-1}}$
$\lambda_{parallel}$	thermal conductivity in parallel condition	$\mathrm{W\,m^{-1}\,K^{-1}}$
λ_{pre}	predicted thermal conductivity	$\mathrm{W\,m^{-1}\,K^{-1}}$
λ_q	thermal conductivity of quartz mineral	$\mathrm{W\,m^{-1}\,K^{-1}}$
λ_s	thermal conductivity of solids of porous media	$\mathrm{W\,m^{-1}\,K^{-1}}$
λ_{sw}	thermal conductivity of saline or seawater	$\mathrm{W\,m^{-1}\,K^{-1}}$
$\lambda_{s\parallel}$	thermal conductivity of solids parallel to the *c*-axis	$\mathrm{W\,m^{-1}\,K^{-1}}$
$\lambda_{s\perp}$	thermal conductivity of solids perpendicular to the *c*-axis	$\mathrm{W\,m^{-1}\,K^{-1}}$
λ_{sat}	effective thermal conductivity of medium in saturated condition	$\mathrm{W\,m^{-1}\,K^{-1}}$
λ_{series}	thermal conductivity in series condition	$\mathrm{W\,m^{-1}\,K^{-1}}$
λ_{T_o}	thermal conductivity at reference temperature of the Hailemariam and Wuttke (2018b) model	$\mathrm{W\,m^{-1}\,K^{-1}}$
λ_u	upper bound of thermal conductivity	$\mathrm{W\,m^{-1}\,K^{-1}}$
λ_v	thermal conductivity of reference disc in SS device	$\mathrm{W\,m^{-1}\,K^{-1}}$
λ_w	thermal conductivity of water	$\mathrm{W\,m^{-1}\,K^{-1}}$
λ_{wl}	wavelength of an electromagnetic wave in a medium	m
$\lambda_{wl,0}$	wavelength of an electromagnetic wave in free space	m
μ^*	complex absolute magnetic permeability of medium	$\mathrm{H\,m^{-1}}$
μ^*_{eff}	effective complex absolute magnetic permeability of medium	$\mathrm{H\,m^{-1}}$
$\mu^*_{r,eff}$	relative effective complex magnetic permeability of medium	–
μ_v	dynamic viscosity of bitumen	$\mathrm{Pa\,s}$
$\mu_{v,30}$	dynamic viscosity of bitumen at 30°C	$\mathrm{Pa\,s}$
ρ	bulk density of medium	$\mathrm{kg\,m^{-3}}$
ρ_d	bulk density of medium in dry condition	$\mathrm{kg\,m^{-3}}$
ρ_{do}	initial bulk density of medium in dry condition	$\mathrm{kg\,m^{-3}}$
ρ_E	electrical resistivity	$\Omega\,\mathrm{m}$
ρ_s	density of solids of porous media	$\mathrm{kg\,m^{-3}}$
ρ_v	density of free electric charges	$\mathrm{C\,m^{-3}}$
σ^*	complex absolute electrical conductivity of medium	$\mathrm{S\,m^{-1}}$
σ'	effective stress	kPa
σ_{DC}	direct current conductivity of medium	$\mathrm{S\,m^{-1}}$

σ_E	electrical conductivity	$\mathrm{S\,m^{-1}}$
σ^*_{eff}	effective complex absolute electrical conductivity of medium	$\mathrm{S\,m^{-1}}$
σ'_o	initial effective stress of medium	kPa
τ	relaxation time	s
τ_{sw}	relaxation time of saline or seawater	s
τ_w	relaxation time of water	s
ϕ	saline pore-water direct current conductivity modification factor of Blanch and Aguasca (2004) model	–
ϕ_L	LEM model preset error limit	–
χ	parameter of the Côté and Konrad (2005) model	$\mathrm{W\,m^{-1}\,K^{-1}}$
ψ_m	matric suction	kPa
ω	angular frequency	rad

Δ	change / variation of
∂	partial derivative
∇	gradient
$\nabla\cdot$	divergence operator
$\nabla\times$	curl operator

Chapter 1

Introduction

1.1 Background and motivation

Heat transfer and electromagnetic (EM) processes in porous media play a key role in the understanding and modeling operations in various fields of energy geotechnics and engineering in general. Understanding of the interrelation and coupling of these two processes provides key tools and solutions for several problems in energy geotechnics. In this regard, knowledge of EM processes and geophysical approaches have recently gained much interest in solving major problems facing the fields of energy geotechnics and geotechnical engineering in monitoring the spatial and temporal variations of temperature and moisture content as well as the recovery of bituminous or heavy oils from oil sands and shales by EM heating among others.

With regards to the first application (temperature monitoring), several geophysical approaches such as electrical resistivity tomography (ERT) or electrical resistivity imaging (ERI), in-situ fiber optic distributed temperature sensing (DTS) and self-potential method (SP) are widely used to study/monitor geothermal systems (Hermans et al., 2014) and to monitor temperature distribution of heat tracing experiments (Hermans et al., 2015). When compared to other alternative methodologies such as thermal tracing experiments (solute tracer experiments) (Vandenbohede et al., 2011; Giambastiani et al., 2013), which could not fully capture the heterogeneity and complexity of geothermal and hydrogeological systems (Brouyère, 2001; Jardani et al., 2013), the geophysical approaches have found to be more useful in monitoring the temporal and spatial and temperature distributions of shallow geothermal systems.

Considering the second application (moisture monitoring), geophysical methods such as high-frequency electromagnetic (HF-EM) measurement techniques (remote sensing, TDR, GPR, FDR and capacitance methods) are typically used to obtain temporal and spatial variations of soil moisture within several scientific and practical fields of geotechniques, hydrology and soil physics (Rowe et al., 2001; Huisman et al.,

2003; Robinson et al., 2003). Furthermore, HF-EM techniques exhibit high accuracy and precision, are comparatively non-invasive, are relatively insensitive to extreme physical and chemical conditions, and are flexible to automation and multiplexing needs (Wraith and Or, 1999; Heimovaara et al., 2004; Wagner et al., 2014).

The third application (EM heating of porous media) contributes in several fields of geotechnics and engineering such as the clearing of porous media from viscous hydrocarbons and other contaminants by selective heating, indirect (without contact) charging/loading operations of saturated porous media based sensible heat energy storage systems, thermal desorption of pollutants from porous media (vapor extraction and stripping), biodegradation or bioremediation of porous media, thawing of frozen porous media deposits etc. Furthermore, EM heating of porous media plays a key role in solving one of the main challenges of the 21st century, which is closing the gap between energy demand and supply by using alternatives or providing additional options to the increasingly unreliable and cost fluctuating light oil resources with the widely available and mostly undiscovered unconventional fossil fuels such as heavy oil deposits around the world (OPEC, 2011; Banerjee, 2012; Robinson et al., 2014), until we have the technologies and resources capable to fulfill the global energy demand with clean and reliable sources of energy. The shift from the use of conventional oil resources to renewable energies can be generally expected to happen gradually over the coming decades, considering the fact that the current world oil demand (which contributes to around 86% of the overall worldwide energy demand) is expected to increase from 85 million barrels/day to 110 million barrels/day by 2030 (Robinson et al., 2014).

Furthermore, the recovery of bituminous materials from oil sands contributes in enriching the supply of bitumen for civil engineering and construction purposes all around the world. Bitumen is a comparatively cheaper (cost usually around 30 - 40% lower than concrete), non-spalling, flexible (little cracking as compared to concrete), durable and high performance construction binding material, and requires lower maintenance costs when compared to the other main construction materials. The demand for bitumen in the construction industry is expected to rise rapidly over the coming decades, and world oil reserves containing massive quantities of bitumen (Alboudwarej et al., 2006) are expected to play a big role in satisfying this demand.

Studying the variations of effective thermal conductivity and effective complex dielectric permittivity of oil sands with moisture or bitumen content is essential for use in the recovery of highly viscous bituminous or heavy oils from oil sands and shales using both conventional (such as ex-situ hot water separation techniques and in-situ thermal and non-thermal techniques) and unconventional (such as electromagnetic

heating) techniques. Accurate determination of the two parameters of oil sands is essential for the simulation / operation of both methods of recovery of heavy oils and bitumen from oil sands.

The accurate estimation of thermal conductivity of soils is also essential in the simulation of the operation of seasonal thermal energy storage systems (Doughty et al., 1983; Hart and Whiddon, 1984), embedding of underground high-voltage cables in suitable geomaterials, assessing the effects of berms on the heat loss from thermal energy storage tanks (Rosen and Hooper, 1990), ensuring the safe design and location of underground storage facilities for nuclear and other hazardous waste materials etc (Doughty et al., 1983; Hart and Whiddon, 1984; Rosen and Hooper, 1989).

Furthermore, the effective thermal conductivity and effective complex dielectric permittivity or complex electrical conductivity of soils and oil sands are highly correlated and are both affected by the changes in chemical composition, grain structure, percolation and hydro-mechanical conditions. The findings of several studies on the behavior of effective thermal conductivity and dielectric permittivity or electrical conductivity of porous media (independently and/or in combination), which have been carried out in the past (Archie, 1942; De Vries, 1963; Fragkogiannis et al., 2010; Logsdon et al., 2010; Hailemariam et al., 2017), confirm the strong correlation between the two parameters. The strong correlation between the two parameters is essential in order to employ geophysical approaches such as high frequency electromagnetic (HF-EM) measurement techniques (in the form of the effective complex dielectric permittivity) to monitor porous media thermal properties such as the effective thermal conductivity via theoretical modeling (Hailemariam et al., 2017).

In this research, new semi-theoretical models for the prediction of the effective thermal conductivity of unsaturated soils and bitumen-water saturated oil sands from effective complex dielectric permittivity are developed and experimentally validated to provide a direct correlation between the two parameters. Unlike most of the existing effective thermal conductivity prediction models of porous media, the new models presented in this study do not require moisture or bitumen content as an input parameter, thus providing the opportunity to obtain accurate estimation of the effective thermal conductivity of soils and oil sands both in-situ and in the laboratory using dielectric measurements only, avoiding medium disturbance or the need to extract samples for moisture/bitumen content determination. For large scale sub-surface thermal exploration purposes, spatial sub-surface dielectric data over high depths and wide areas of soil and oil sand deposits can be obtained using non-destructive HF-EM measurement techniques such as ground penetrating radar (GPR), to be used as an input for the effective thermal conductivity models presented in this research.

For laboratory and small scale in-situ measurements, complex dielectric permittivity measurement techniques such as an open-ended coaxial line with time domain reflectometry (TDR) or vector network analyzers (VNAs) are typically employed.

Considering the various applications of thermal conductivity and complex dielectric permittivity in energy geotechnics and engineering, it is vital to develop models which can accurately predict their local spatial distributions considering the heterogeneity of naturally occurring porous media formations. Majority of the available continuum based models fail to include information on the heterogeneous nature of porous media fabric at the micro- and meso-scale levels (i.e. actual thermal and electric conduction paths). To overcome these shortcomings, a new lattice element method (LEM) based numerical model, which replicates the actual heat and electric conduction paths of the constituent phases of the porous media thus providing accurate simulations for the magnitude of the two parameters and their local spatial variations within the porous medium, is presented in this study. The model is also able to provide estimates of the two parameters and their local spatial distributions at various medium temperatures, pore-water salinities, frequencies (in case of complex dielectric permittivity) and moisture or bitumen contents.

The predictions of the new semi-theoretical and numerical models are validated via experimental measurements of the effective thermal conductivity and effective complex dielectric permittivity of an oil sand and soils at different hydro-mechanical conditions such as water content, porosity, stress, matric suction, temperature etc. with good results.

1.2 Scope

The main objectives of this thesis are to:

- Study the heat transfer and electromagnetic porous media processes and the parameters affecting them.
- Analyze the variations of key thermal and electromagnetic parameters, such as thermal conductivity, specific heat capacity and dielectric properties of soils and oil sands for different hydro-mechanical conditions.
- Propose new semi-theoretical prediction models for the thermal conductivity of soil deposits and oil sand reservoirs from dielectric measurements carried out using small and large scale exploration techniques such as GPR.

- Propose a new LEM based numerical model for predicting the effective thermal and dielectric porous media parameters as well as their spatial distributions.

To achieve these objectives, the thesis is structured accordingly as shown next.

1.3 Organization of the thesis

The thesis consists of nine chapters, of which the content can be summarized as follows:

- Chapter 1: Introduces the background, scope and objectives of the thesis.
- Chapter 2: Presents a literature review on heat transfer and electromagnetic phenomenon.
- Chapter 3: Discussion on the structure and thermo-dielectric behavior of unsaturated soils and bitumen-water saturated oil sands as part of the developments for the new semi-theoretical and numerical models is presented.
- Chapter 4: Presents a detailed study on the theoretical modeling of the thermo-dielectric porous media parameters, and the new theoretical models for the prediction of the thermal conductivity of porous media based on dielectric measurements are developed. The model results are further compared to experimental results and prediction of existing models in chapter 7. Furthermore, the influence of applied vertical stress and the associated settlement as well as matric suction and temperature on the thermal and dielectric properties of porous media is studied, and prediction models are presented.
- Chapter 5: The new LEM model for predicting the effective thermal and dielectric porous media parameters is presented. The model results are further compared to the experimental results in chapter 8 for verification.
- Chapter 6: The different materials analyzed in this thesis, the equipments used and the experimental procedure followed for obtaining the thermo-dielectric parameters are discussed.
- Chapter 7: Presents the results and key findings of the research with focus on the semi-theoretical models. The new findings are discussed in detail in view of the existing body of knowledge on the topics of heat transfer and electromagnetic theory. The model prediction results are further verified by comparing with the experimental results.

- Chapter 8: Presents the results and key findings of the research in view of the newly developed LEM model. The model prediction results are further verified by comparing with the experimental results.
- Chapter 9: Concludes the thesis by providing a summary of the study's outcomes, and presents an outlook for future studies.

Chapter 2

Heat transfer and electromagnetic phenomenon

2.1 Introduction

In this chapter, a literature review of the basics of heat transfer and electromagnetic wave propagation in porous media is provided. Furthermore, the most commonly used theoretical and empirical thermal and dielctric parameter prediction models are discussed.

2.2 Heat transfer in porous media

2.2.1 Background

Heat transfer in porous media occurs via three main processes, namely conduction, convection and radiation. Out of the three, conduction is the dominant form of heat transfer, while convection and radiation generally have relatively small contribution but they may have a significant influence in certain conditions (Farouki, 1981; Clauser and Huenges, 1995).

Heat conduction occurs in all the constituent phases of porous media (i.e. solids, liquid and gaseous phases). Although a considerable contact resistance exists, the predominant form of conduction occurs via the soil grains (such as quartz) and paths through contacting solid grains.The heat flow in the crystalline solids is mainly attributed to increased atomic vibrations (also known as phonons) and their corresponding collisions upon the application of heat (Farouki, 1981; Hofmeister, 1999; McKenzie et al., 2005). Other paths include portions of solid grains and fluid-filled pore fractions or solely of fluid-filled spaces. Conduction in the liquid and gaseous

phases is facilitated due to the collisions between the molecules and a consequent increase in their mean kinetic energy as heat energy passes from warmer to colder regions (Sengers and Watson, 1986; Ramires et al., 1995). In the case of liquid water, energy transfer due to the breaking or forming of hydrogen bonds also contributes to conduction.

The convective mode of heat transfer involves fluid flow accompanied with conduction, or diffusion, and is essentially divided in to two processes. When the motion of the fluid arises from an external cause, the process is termed as forced convection. Whereas, if no such externally caused flow exists and the flow arises naturally from the effect of a density difference, resulting from a difference in the concentration or temperature in body forces such as gravity, the process is known as natural or buoyancy driven convection (Farouki, 1981; Hailemariam and Wuttke, 2016). Natural convection is typically seen for porous media with high hydraulic permeabilities (Clauser and Huenges, 1995; Hailemariam and Wuttke, 2016). In this thesis, heat transfer due to conduction only is considered, and the effects of convection on the heat transfer mechanism of a porous medium was studied in Hailemariam and Wuttke (2016).

Radiative heat transfer occurs across air spaces (or within transparent media) by heat energy propagation in the form of electromagnetic waves. The temperature of the radiating body plays the most crucial factor, and heat transfer by radiation in solids is usually neglected for temperatures below 727°C (Farouki, 1981; Hofmeister, 1999; Jokinen, 2000; McKenzie et al., 2005), and hence has not been considered in our study.

2.2.2 Conductive heat transfer

According to the theory of heat conduction, heat flows from regions of higher temperature to regions with a lower temperature. The heat flux density (commonly known as heat flux) is defined as the rate of heat energy transfer per unit area (amount of heat transferred per unit area per unit time). The heat flux is expressed as $q = Q/A_h$ (Q, $\mathrm{J\,s^{-1}}$ or W, is the rate of heat transfer and A_h, $\mathrm{m^2}$, is the total area through which the heat flows). The heat flux is proportional to the gradient of the temperature in the direction of heat flow, and for an infinite and isotropic medium, the one-dimensional conductive heat flux is given by:

$$q = -\lambda \nabla T = -\lambda \frac{\Delta T}{\Delta x} \tag{2.1}$$

where, q ($\mathrm{W\,m^{-2}}$) is the heat flux, T (K) is the temperature, x (m) is the medium

thickness (distance along which the heat flows) and λ ($\mathrm{W\,m^{-1}\,K^{-1}}$) is the proportionality constant or the thermal conductivity of the medium. The negative sign indicates that heat flows in the direction of the lower temperature. ∇T is the temperature gradient. Equation 2.1 is typically known as the Fourier's law of heat conduction. For a three-dimensional heat flow case:

$$q = -\lambda\left(\frac{\Delta T}{\Delta x} + \frac{\Delta T}{\Delta y} + \frac{\Delta T}{\Delta z}\right) \tag{2.2}$$

Except in the special case of steady state condition, the conductive heat flow is always associated with a change in temperature, which for an infinite and isotropic medium is given by:

$$\frac{\partial T}{\partial t} = \frac{\lambda}{\rho c}\left(\frac{\partial^2 T}{\partial x^2}\right) \tag{2.3}$$

And the thermal diffusivity of the medium is given by:

$$\alpha = \frac{\lambda}{\rho c} \tag{2.4}$$

where, α ($\mathrm{m^2\,s^{-1}}$) is the thermal diffusivity of the medium, ρ ($\mathrm{kg\,m^{-3}}$) is the density of the medium and c ($\mathrm{J\,kg^{-1}\,K^{-1}}$) is the specific heat of the medium. Combining Equations 2.3 and 2.4 we get:

$$\left(\frac{1}{\alpha}\right)\frac{\partial T}{\partial t} = \left(\frac{\partial^2 T}{\partial x^2}\right) \tag{2.5}$$

And for a three-dimensional conductive heat flow, we obtain the general form (Equation 2.6) which was first derived by Fourier in 1822.

$$\left(\frac{1}{\alpha}\right)\frac{\partial T}{\partial t} = \frac{\partial^2 T}{\partial x^2} + \frac{\partial^2 T}{\partial y^2} + \frac{\partial^2 T}{\partial z^2} \tag{2.6}$$

Generally, the medium temperature changes with time for the non-steady state (transient) solution of Equation 2.6. However, for a steady state heat flow condition, the temperature does not change with time and the term $\partial T/\partial t$ is zero.

2.2.3 Thermal conductivity

Thermal conductivity plays a vital role in the conductive heat transfer analysis of engineering applications, such as the operation of small and large scale seasonal thermal energy storage, embedding of underground power cables in porous media, nuclear waste disposal facilities, heat exchanger piles of structures, assessing the effect of berms on the heat loss from thermal energy storage tanks etc. (Doughty et al., 1983; Hart and Whiddon, 1984; Rosen and Hooper, 1989). The thermal conductivity of porous media is highly dependent on the number and quality of contacts in the solid matrix, moisture content and to a slightly lower extent on the medium density (degree of packing). Other factors which play a significant role on the thermal conductivity of a medium are: grain size arrangement, particle size, solute concentration, mineralogy and temperature (De Vries, 1963; Tarnawski et al., 2000; Smits et al., 2013).

Several methods exist for measuring the soil thermal conductivity (Mitchell and Kao, 1978). These methods generally fall into one of two categories: steady state or non-steady state (transient) methods (Farouki, 1981; Mitchell and Kao, 1978).

Steady state methods involve the application of one-directional heat flow through a specimen and the observation of power or temperature difference across the specimen when a steady state condition is reached (Mitchell and Kao, 1978; Farouki, 1981; Low et al., 2013; Hailemariam et al., 2016). The thermal conductivity of the specimen is calculated using the Fourier's law. Generally, steady state methods are employed when the temperature of the specimen does not vary with time, and are deemed to be more accurate than transient methods (McGuinness et al., 2014; Hailemariam et al., 2016). However, the main limitation of these methods is that a well-engineered experimental setup and ample time is needed for establishing a steady state condition. Steady state techniques are further classified as absolute and comparative methods (Alrtimi, 2008). The former includes the guarded hot plate method, unguarded hot plate method and the heat flow meter technique, where the determination of power and temperature distribution across the specimen is directly obtained from the input power and temperature parameters. The latter includes methods, such as the divided bar apparatus and the guarded comparative longitudinal heat flow technique, which uses a series of reference materials of known thermal conductivity aligned in series with the specimen (Momose et al., 2008; McGuinness et al., 2014; Hailemariam et al., 2016).

Transient methods on the other hand involve the application of heat to the specimen and monitoring the temperature changes over time, and then after using the

transient data to determine the thermal conductivity of the specimen, usually by applying analytical solutions to the heat diffusion equation (Mitchell and Kao, 1978; Farouki, 1981; Low et al., 2013; Alessandro, 2007). The method by which the transient data is analyzed can affect the obtained thermal conductivity considerably. Transient methods of measuring thermal conductivity provide better versatility when compared with steady state methods because of their ease of application and the required short measurement time. Some of the most commonly used transient methods include the hot wire method, transient plane source method and the thermal needle probe (single or dual probes) method. The probe methods have been widely in use for the past century (Farouki, 1981).

Due to the difficult and time consuming nature of experimental techniques of thermal conductivity determination, several researchers have proposed models relating thermal conductivity of porous media to readily obtainable parameters, such as porosity, mineral content, particle size, water content etc. (Kersten, 1949; Johansen, 1975; Farouki, 1981; Gavriliev, 2004; Gori and Corasaniti, 2004; Côté and Konrad, 2005; Lu et al., 2007; Yun and Santamarina, 2007; Abuel-Naga et al., 2008). Some of the common theoretical and semi-empirical thermal conductivity prediction models are discussed next.

2.2.4 Theoretical models of thermal conductivity

Numerous theoretical approaches have been developed in the past to model the thermal conductivity of soils based on the volumetric fractions of their constituent phases as well as the texture/fabric of the medium (Farouki, 1981; Yun and Santamarina, 2007; Abuel-Naga et al., 2008). Unlike most empirical models, the validity of theoretical models is not usually limited to specific soil types, and hence they can be used to predict the thermal conductivity for a wide variety of soil types (Abuel-Naga et al., 2008). Figure 2.1 shows a plot of the thermal conductivity prediction for a dry soil with a specific gravity G_s of 2.65 and a volumetric quartz fraction q_f of 0.70 using some theoretical models.

The parallel and series heat flow models can be considered as the upper and lower bounds of theoretical models, respectively (Figure 2.1) (Farouki, 1981; Abuel-Naga et al., 2008). The two-phase parallel $\lambda_{parallel}$ and series λ_{series} thermal conductivities are given by Equations 2.7 and 2.8, respectively.

$$\lambda_{parallel} = n\lambda_f + (1-n)\lambda_s \tag{2.7}$$

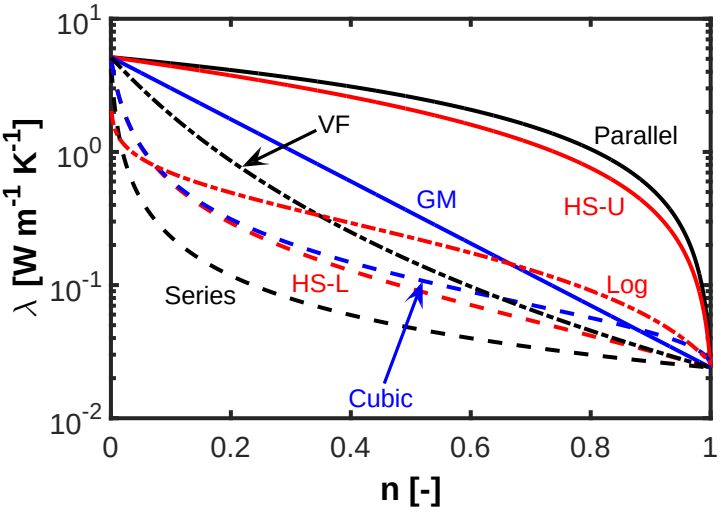

Figure 2.1: Thermal conductivity λ vs porosity n of a soil in dry state obtained using theoretical models (VF is the volume fraction model, GM is the geometric mean model and HS-U & HS-L are the upper and lower bounds of the Hashin and Shtrikman model, respectively).

$$\frac{1}{\lambda_{series}} = \frac{n}{\lambda_f} + \frac{(1-n)}{\lambda_s} \tag{2.8}$$

where, n is the soil porosity, λ_f ($\mathrm{W\,m^{-1}\,K^{-1}}$) is the fluid thermal conductivity (for water λ_w = $0.594\,\mathrm{W\,m^{-1}\,K^{-1}}$ or air λ_a = $0.024\,\mathrm{W\,m^{-1}\,K^{-1}}$ at 20°C, for saturated or dry soil states, respectively), λ_s ($\mathrm{W\,m^{-1}\,K^{-1}}$) is the thermal conductivity of the solid soil particles. At low λ_s/λ_f ratios, parallel flow dominates, while, at high λ_s/λ_f ratios, series heat flow is dominant (Farouki, 1981).

A very useful 'average' of the parallel and series heat flow models is obtained by taking the geometric mean as shown by Equation 2.9 (Farouki, 1981). The geometric mean (GM) equation has been widely used for predicting the thermal conductivity λ ($\mathrm{W\,m^{-1}\,K^{-1}}$) of various types of porous media (McGaw, 1969; Farouki, 1981). Several researchers (Johansen, 1975; Côté and Konrad, 2005; Lu et al., 2007) have also adopted the GM method for developing semi-empirical models with good accuracy.

$$\lambda = \lambda_s^{(1-n)} \lambda_f^n \tag{2.9}$$

Hashin and Shtrikman (1962) proposed Equations 2.10 and 2.11 for the upper (HS-U) λ_u ($\mathrm{W\,m^{-1}\,K^{-1}}$) and lower (HS-L) λ_l ($\mathrm{W\,m^{-1}\,K^{-1}}$) bounds of thermal conductivity, respectively.

$$\lambda_u = \lambda_s + \frac{n}{\frac{1}{(\lambda_f - \lambda_s)} + \frac{(1-n)}{3\lambda_s}} \tag{2.10}$$

$$\lambda_l = \lambda_f + \frac{(1-n)}{\frac{1}{(\lambda_s - \lambda_f)} + \frac{n}{3\lambda_f}} \tag{2.11}$$

According to the cubic cell model (Gori and Corasaniti, 2004), the effective dry soil thermal conductivity λ_d ($\mathrm{W\,m^{-1}\,K^{-1}}$) can be obtained as:

$$\lambda_d = \left[\frac{(\beta_d - 1)}{\lambda_a \beta_d} + \frac{\beta_d}{\lambda_a[(\beta_d)^2 - 1] + \lambda_s}\right]^{-1}; \beta_d = \left[\frac{1}{(1-n)}\right]^{1/3} \tag{2.12}$$

Yun and Santamarina (2007) fitted the volume fraction (VF) model and the log-model for obtaining the effective dry thermal conductivity of soils λ_d ($\mathrm{W\,m^{-1}\,K^{-1}}$) as shown by Equations 2.13 and 2.14, respectively.

$$\lambda_d = \left[n\lambda_a^s + (1-n)\lambda_s^s\right]^{1/s}; s = -0.25 \tag{2.13}$$

$$\lambda_d = -a\ln(n) + p; a = 0.291\,\mathrm{W\,m^{-1}\,K^{-1}} \& p = 0.026\,\mathrm{W\,m^{-1}\,K^{-1}} \tag{2.14}$$

2.2.5 Semi-empirical models of thermal conductivity

Semi-empirical models predict the thermal conductivity of porous media based on water content, porosity and other hydro-mechanical parameters (Kersten, 1949; Van Rooyen and Winterkorn, 1959; Farouki, 1981; Johansen, 1975; Côté and Konrad, 2005; Lu et al., 2007). Most semi-empirical models provide a better accuracy of thermal conductivity prediction when compared to theoretical models (due to provisions for soil fabric, which is not the case with theoretical models), but are usually applicable for limited porous media types under a given set of conditions. Figure 2.2 shows results of the thermal conductivity prediction for a dry soil with a specific gravity G_s of 2.65 and a volumetric quartz fraction q_f of 0.70 using some semi-empirical models.

Johansen (1975) proposed a semi-empirical equation to predict the thermal conductivity of dry natural soils based on the bulk dry density and density of solids of the soil as:

$$\lambda_d = \frac{0.135\rho_d + 64.7}{\rho_s - 0.947\rho_d} \tag{2.15}$$

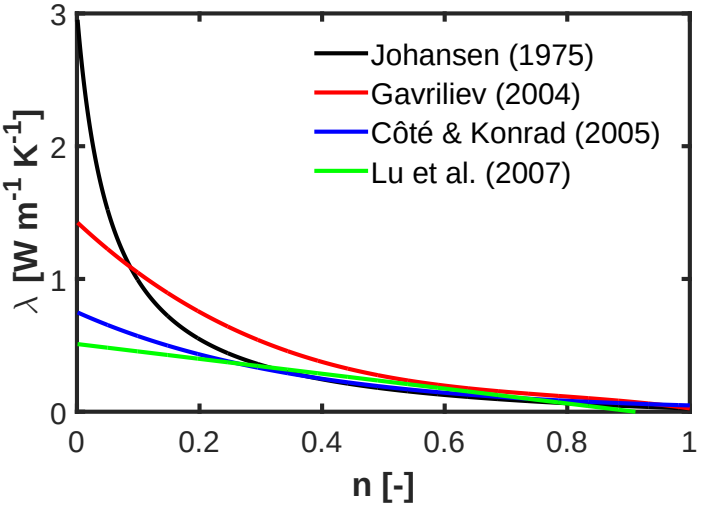

Figure 2.2: Thermal conductivity λ vs porosity n of a soil in dry state obtained using semi-empirical models (Lu et al. model is valid for porosities within the range $0.2 < n < 0.6$).

where, λ_d ($\mathrm{W\,m^{-1}\,K^{-1}}$) is the dry soil thermal conductivity, ρ_d ($\mathrm{kg\,m^{-3}}$) is the soil dry density and ρ_s ($\mathrm{kg\,m^{-3}}$) is the density of soil solids. Johansen proposed a thermal conductivity prediction model for un-saturated soil conditions based on the concept of normalized thermal conductivity (Equation 2.16) by using the thermal conductivity data at dry and saturated states as well as a dimensionless function of soil saturation (commonly known as Kersten's number), for soils and crushed rock minerals, at frozen and unfrozen conditions. Johansen derived Equation 2.17 as the Kersten number for unfrozen natural soils based on the findings of Kersten (1949). However, the equation for Kersten's number suggested by Johansen is limited for soils with a degree of saturation higher than 20%.

$$\lambda = (\lambda_{sat} - \lambda_d)K_e + \lambda_d \tag{2.16}$$

$$K_e = C\log(S_r) + 1.0 \tag{2.17}$$

where, λ ($\mathrm{W\,m^{-1}\,K^{-1}}$) is the un-saturated soil thermal conductivity, λ_{sat} ($\mathrm{W\,m^{-1}\,K^{-1}}$) is the saturated soil thermal conductivity, λ_d ($\mathrm{W\,m^{-1}\,K^{-1}}$) is the dry soil thermal conductivity, K_e is the Kersten's number, C is a constant (with typical values of 0.7 and 1.0 for coarse and fine-grained soils, respectively) S_r is the degree of soil saturation (in fraction).

Johansen also suggested that the solid grain thermal conductivity can be obtained by using the GM function, based on the volumetric quartz fraction of the total soil

grains and the thermal conductivities of the constituent minerals (Equation 2.18).

$$\lambda_s = \lambda_q^{q_f} \lambda_o^{(1-q_f)} \tag{2.18}$$

where, λ_s ($\mathrm{W\,m^{-1}\,K^{-1}}$) is the thermal conductivity of the soil solids, λ_q = $7.7\,\mathrm{W\,m^{-1}\,K^{-1}}$ is the thermal conductivity of quartz mineral, q_f is the volumetric quartz fraction of the solids and λ_o = $2.0\,\mathrm{W\,m^{-1}\,K^{-1}}$ or $3.0\,\mathrm{W\,m^{-1}\,K^{-1}}$, for soils with q_f > 0.2 or $q_f \leq 0.2$, respectively (Johansen, 1975; Clauser and Huenges, 1995; Lu et al., 2007).

Gavriliev (2004) proposed an empirical relationship for estimating the dry thermal conductivity of mineral soils using the bulk dry density only. The relationship (Equation 2.19) is valid only for mineral soils with a dry density lower than $2\,\mathrm{g\,cm^{-3}}$.

$$\lambda_d = 0.025 + 0.238\rho_d - 0.193\rho_d^2 + 0.114\rho_d^3 \tag{2.19}$$

where, λ_d ($\mathrm{W\,m^{-1}\,K^{-1}}$) is the dry soil thermal conductivity, ρ_d ($\mathrm{g\,cm^{-3}}$) is the soil dry density.

Côté and Konrad (2005) developed a new empirical formula for obtaining the thermal conductivity of dry soils and construction materials as:

$$\lambda_d = \chi 10^{-\eta n} \tag{2.20}$$

where, λ_d ($\mathrm{W\,m^{-1}\,K^{-1}}$) is the dry soil thermal conductivity, χ ($\mathrm{W\,m^{-1}\,K^{-1}}$) and η are particle shape effect parameters, with values of $1.70\,\mathrm{W\,m^{-1}\,K^{-1}}$ and 1.80 for crushed rock materials, $0.75\,\mathrm{W\,m^{-1}\,K^{-1}}$ and 1.20 for naturally occuring mineral soils and $0.30\,\mathrm{W\,m^{-1}\,K^{-1}}$ and 0.87 for organic fibrous soils.

For the prediction of the un-saturated thermal conductivity of soils and construction materials, Côté and Konrad further suggested a new empirical function for the Kersten's number of Johansen's model (Equation 2.21), thus eliminating the logarithmic function of soil saturation and enabling the model to be used for the whole soil saturation range.

$$K_e = \frac{\kappa(\theta/n)}{1 + (\kappa - 1)(\theta/n)} \tag{2.21}$$

where, K_e is the Kersten's number, κ is a soil texture dependent parameter (with values of 4.60, 3.55, 1.90 and 0.60 for gravel and coarse sands, medium and fine sands, silty & clayey soils and for organic soils in unfrozen state, respectively), n is the porosity of the material and θ is the volumetric water content fraction of the material.

Lu et al. (2007) proposed a linear function (Equation 2.22) that describes the relationship between the dry soil thermal conductivity and porosity for naturally occurring mineral soils based on two empirical parameters, whose values were calculated as the best fit of heat pulse measured data.

$$\lambda_d = -a_l(n) + b_l \tag{2.22}$$

where, λ_d ($\mathrm{W\,m^{-1}\,K^{-1}}$) is the dry soil thermal conductivity, n (0.2 < n < 0.6) is the soil porosity and a_l & b_l are empirical parameters with values of 0.56 and 0.51, respectively.

For predicting the thermal conductivity of soils at un-saturated states, Lu et al. proposed another Kersten's number to replace the equation suggested by Johansen's model (Equation 2.23). Lu et al. also compared their new model prediction results with the Côté and Konrad model, and concluded that their new model provides better prediction especially for fine-textured soils and at lower values of degree of soil saturation (Lu et al., 2007).

$$K_e = \exp\left\{\alpha_s\left[1 - \left(\frac{\theta}{n}\right)^{(\alpha_s - 1.33)}\right]\right\} \tag{2.23}$$

where, K_e is the Kersten's number, α_s is a soil texture dependent parameter (with values of 0.96 and 0.27 for coarse-textured and fine-textured soils, respectively), 1.33 is a shape parameter, θ is the volumetric water content fraction of the soil and n is the soil porosity.

Johansen, Côté and Konrad and Lu et al. all used the GM function (Equation 2.9) to obtain the thermal conductivity of the soils at saturated condition with $\lambda_f = \lambda_w$.

2.3 Electromagnetic phenomena in porous media

2.3.1 Background

During the past century, geotechnical engineering, soil science, agriculture, hydrology, geophysical prospecting etc. have greatly benefited from developments in radio and microwave technology. The dielectric permittivities of porous media are function of the water content, soil fabric, solute concentration, mineralogy, temperature and bulk density (Archie, 1942; Olhoeft, 1981; Shen et al., 1985; Wraith and Or, 1999; Rowe et al., 2001; Huisman et al., 2003; Robinson et al., 2003; Kelleners et al., 2005;

Wagner et al., 2007b), consequently, high frequency electromagnetic (HF-EM) measurement techniques are frequently used to obtain estimates of soil and rock physical characteristics, such as moisture content, and to a lesser extent density or porosity via both invasive methods (such as time domain reflectometry, TDR and cross borehole radar) and non-invasive methods (such as capacitance methods and ground penetrating radar, GPR).

HF-EM measurement techniques such as capacitance methods (Evett et al., 2009), GPR (Jol, 2009), or TDR (Robinson et al., 2003; Robinson et al., 2009a) work on the basis of detecting changes in the spatial and temporal variations of the electromagnetic properties of porous media at or near the earth's subsurface (Lauer et al., 2012). At low frequency ranges (1 MHz - 200 MHz), capacitance methods (Evett et al., 2009), such as the parallel-plate configuration are generally used. At higher frequency ranges (1 MHz - 10 GHz), time or frequency domain reflectometry (TDR/FDR) techniques are typically employed (Behari, 2005; Wagner et al., 2011a). Using non-destructive geophysical approaches, such as GPR (Jol, 2009), large scale sub-surface exploration projects by transmitting HF-EM pulses (12.5 MHz - 1 GHz) from an irradiating antenna to the ground, and consequently measuring the travel time of the emitted pulses via a receiving antenna, the dielectric permittivities of the porous media can be obtained and then used to estimate a wide variety of geophysical and geotechnical parameters of the deposits (Lowry et al., 2009).

2.3.2 EM wave propagation and Maxwell's equations

The propagation of a planar electromagnetic wave can be described as a space and time harmonic field, where the electric **E** and magnetic **H** waves oscillate transversely. The electric and magnetic waves oscillate in time and space with a certain period time (time distance between two repeating waves) and a wavelength. The relationship of the electromagnetic fields are expressed by four basic equations governing electromagnetism, commonly known as Maxwell's equations (Maxwell Garnett, 1904). These four equations were formulated originally via numerous experiments of several researchers and were then combined in to their final form of harmonic vector fields by James Clerk Maxwell in 1873.

Maxwell's equations (Equations 2.24 - 2.27) and the constitutive relations (Equations 2.28 - 2.30), which are needed to describe the coupled behavior of electric and magnetic fields, are given as follows:

$$\nabla \times \mathbf{E} = -\frac{\partial \mathbf{B}}{\partial t} \tag{2.24}$$

$$\nabla \times \mathbf{H} = \mathbf{J} + \frac{\partial \mathbf{D}}{\partial t} \tag{2.25}$$

$$\nabla \cdot \mathbf{D} = \rho_v \tag{2.26}$$

$$\nabla \cdot \mathbf{B} = 0 \tag{2.27}$$

$$\mathbf{D}(\omega) = \varepsilon^* \mathbf{E}(\omega) \tag{2.28}$$

$$\mathbf{B}(\omega) = \mu^* \mathbf{H}(\omega) \tag{2.29}$$

$$\mathbf{J}(\omega) = \sigma^* \mathbf{E}(\omega) \tag{2.30}$$

where, **E** ($\mathrm{V\,m^{-1}}$) is the electric field, **B** (T) is the magnetic flux density, **H** ($\mathrm{A\,m^{-1}}$) is the magnetic field intensity, **J** ($\mathrm{A\,m^{-2}}$) is the electric current density, **D** ($\mathrm{C\,m^{-2}}$) is the electric flux density, ρ_v ($\mathrm{C\,m^{-3}}$) is the density of 'free' electric charges, i.e. electric charges that are not initially part of a medium, $\nabla\times$ is the curl operator, $\nabla\cdot$ is the divergence operator, ε^* ($\mathrm{F\,m^{-1}}$) is the complex absolute permittivity of a medium, μ^* ($\mathrm{H\,m^{-1}}$) is the complex absolute magnetic permeability of a medium and σ^* ($\mathrm{S\,m^{-1}}$) is the electrical conductivity of a medium. All boldface symbols are vectors.

Equation 2.24 is commonly known as Faraday-Lenz's law, which states that a time-varying magnetic field creates a circulating electric field. Equation 2.25 is called the Maxwell-Ampere law and indicates that a circulating magnetic field (Equation 2.29) is produced by both a current of electric charges (Equation 2.30) and by a time-varying electric field (Equation 2.28). Gauss's law declares that for a static electric field, the electric flux through any closed surface is proportional to the total electric charge enclosed by the surface (Equation 2.26), whereas for a static magnetic field, no magnetic monopole exists and that the total flux through a closed surface is zero (Equation 2.27).

The parameters ε^*, μ^* and σ^* are second order tensors with nine independent material parameters (Wagner et al., 2013), however, with the assumption of a quasi-isotropic state (which is typically applied for porous media such as soils) at the sample scale (Robinson, 2004), they are taken as material type dependent scalar quantities.

These material-specific constitutive parameters are frequency f or $\omega = 2\pi f$, temperature T and pressure p dependent. The electrical conductivity σ^* characterizes the movement of free electric charges within a material when an external electric field is applied (Ulaby, 2007). For a 'perfect' conductor, the value of σ^* approaches infinity, as the charges are able to move freely without resistance in the medium. Whereas, for a 'perfect' dielectric, σ^* is zero, indicating that the bonding forces between the atoms and electrons are too tight, preventing the free movement of electric charges (Ulaby, 2007). Hence, the electrical conductivity is typically used to describe high conductive materials (such as metals) using Equation 2.30.

Low conductive materials (such as dielectrics and insulators) also exhibit conductivity due to the displacement of electric charges when an external alternating electric field is applied (Von Hippel, 1954; Wagner et al., 2011a). While another type of electrical conductivity (electrolyte conductivity) is observed when an external electric field is applied to a material with a high concentration of free ions. The electrical conductivity in this case is caused due to the movement of the ions in the material towards the opposite charge (Von Hippel, 1954).

When an alternating (time varying) electric field $\mathbf{E}(t) = \mathbf{E_0}e^{j\omega t}$ is applied to a medium, the electric current density of Equation 2.30, is replaced by the effective total current density, to account for the additional displacement current density as (Wagner et al., 2011a):

$$\mathbf{J_{eff}} = \mathbf{J} + \mathbf{J_D} = \sigma^*\mathbf{E} + j\omega\varepsilon^*\mathbf{E} = \sigma^*\mathbf{E} + \varepsilon^*\frac{\partial \mathbf{E}}{\partial t} \tag{2.31}$$

$$\tan\delta = \frac{|\mathbf{J}|}{|\mathbf{J_D}|} \tag{2.32}$$

where, $\mathbf{J_{eff}}$ ($\mathrm{A\,m^{-2}}$) is the effective total current density, $\mathbf{J}$ ($\mathrm{A\,m^{-2}}$) is the conduction (electric) current density, $\mathbf{J_D}$ ($\mathrm{A\,m^{-2}}$) is the displacement current density (which is a function of ε^*, $\mathrm{F\,m^{-1}}$, and $\mathbf{E}$, $\mathrm{V\,m^{-1}}$), σ^* ($\mathrm{S\,m^{-1}}$) is the complex absolute electrical conductivity, $j^2 = -1$ is the imaginary unit, $\omega = 2\pi f$ (rad) is the angular frequency, ε^* ($\mathrm{F\,m^{-1}}$) is the complex absolute permittivity of the medium and $\tan\delta$ is the loss tangent.

For very low frequencies, the ratio $\tan\delta$ becomes $\gg 1$, as the displacement current density is negligible when compared to the conduction current density. This condition represents the boundary between steady and quasi-steady state in wave phenomena and the material behaves as a conductor. For the case $\tan\delta \ll 1$ at which point the conduction current density can be neglected when compared to the displacement current

density, the material behaves as a dielectric (Wagner et al., 2011a).

Under the latter condition ($\tan\delta \ll 1$), the broadband effective electromagnetic transfer functions ε^*_{eff} or σ^*_{eff} of a porous medium can be introduced by assuming the dependence of complex electrical conductivity σ^* and complex dielectric permittivity ε^* on frequency $w = 2\pi f$. In addition to the frequency, these transfer functions are also dependent on the thermodynamic state parameters such as temperature, pressure, moisture content etc. (Jonscher, 1977; Wagner et al., 2011a). Hence, using Equation 2.31 the effective current density for a porous medium will be given as:

$$\mathbf{J_{eff}} = \mathbf{J_D} = j\omega\varepsilon^*_{eff}\mathbf{E} = \varepsilon^*_{eff}\frac{\partial \mathbf{E}}{\partial t} \tag{2.33}$$

with the effective complex absolute permittivity ε^*_{eff} ($\mathrm{F\,m^{-1}}$) as:

$$\varepsilon^*_{eff} = \varepsilon'_{eff} - j\varepsilon''_{eff} = \varepsilon_0(\varepsilon'_{r,eff} - j\varepsilon''_{r,eff}) \tag{2.34}$$

or the effective complex absolute electrical conductivity σ^*_{eff} ($\mathrm{S\,m^{-1}}$) as:

$$\sigma^*_{eff} = j\omega\varepsilon^*_{eff} \tag{2.35}$$

and the relative effective complex magnetic permeability $\mu^*_{r,eff}$ as:

$$\mu^*_{r,eff} = \frac{\mu^*_{eff}}{\mu_0} \tag{2.36}$$

where, $\varepsilon_0 = 8.854\,187\,817 \times 10^{-12}\,\mathrm{F\,m^{-1}}$ is the dielectric permittivity of free space and $\mu_0 = 4\pi \times 10^{-7}$ or $1.256\,637\,061\,4 \times 10^{-6}\,\mathrm{H\,m^{-1}}$ is the magnetic permeability of free space. For a typical porous media, such as those considered in this thesis (soils and oil sands), the presence of iron content is negligible and the materials are considered non magnetizable, consequently, the relative magnetic permeability is set to 1 (i.e. magnetic effects are neglected).

The relative effective complex permittivity $\varepsilon^*_{r,eff} = \varepsilon'_{r,eff} - j\varepsilon''_{r,eff}$ has two components, where the real part $\varepsilon'_{r,eff}$ represents the amount of energy stored in the material when it is exposed to an electromagnetic field (Lauer et al., 2012). Whereas, the imaginary part $\varepsilon''_{r,eff} = \varepsilon''_{r,d} + \sigma_{DC}/(\omega\varepsilon_0)$ (σ_{DC}, $\mathrm{S\,m^{-1}}$, is the direct current conductivity) represents the polarization and Ohmic losses (the displacement of the randomly orientated and non-polarized electrical charges in a dielectric relative to each other in order to compensate for an applied electric field leading to a polarized medium) (Hasted, 1973; Topp et al., 1980; Robinson et al., 2003). The important parameter for

the measure of the strength of the losses in a porous medium, i.e. effective loss tangent $\tan\delta_{eff}$, can also be obtained as (Saarenketo, 1998; Zajicek et al., 2006):

$$\tan\delta_{eff} = \frac{\varepsilon''_{eff}}{\varepsilon'_{eff}} = \frac{\varepsilon''_{r,eff}}{\varepsilon'_{r,eff}} \tag{2.37}$$

The polarization of a material (represented in terms of its complex dielectric permittivity) generally increases monotonically from high frequencies to very low frequencies. This phenomenon is called dielectric dispersion or relaxation, and is discussed further in the study of the structure and thermo-dielectric behavior of porous media presented in section 3.4.1.

An adequate approach for solving Maxwell's equations is the plane wave approach (Ulaby, 2007; Takahashi et al., 2012). The plane wave approach is typically used to solve for the magnitude of electric field of an EM field in a medium (Ma et al., 1995; Dinčov et al., 2004; Kopyt and Celuch-Marcysiak, 2006).

For a time-harmonic electromagnetic plane wave traveling in **z**-direction of a lossy medium, the electric field vector **E** is mathematically described as:

$$\mathbf{E}(\mathbf{z},t) = \mathbf{E_0}e^{j(\omega t - k^*\mathbf{z})} \tag{2.38}$$

where, $\mathbf{E_0}$ is the amplitude factor and k^* is the wave number or propagation factor of the medium. Lossy mediums have wave numbers k^* that are complex: $k^* = k' - jk''$. The real part k' acts as the phase constant and determines the wavelength and propagation velocity of the electromagnetic wave as it propagates in the medium. Whereas, the imaginary part k'' of the wavenumber attenuates the wave. Wave attenuation in a medium always appears when $\varepsilon''_r \neq 0$. The relationship between the wave number, relative complex permittivity, wavelength and propagation velocity is given by the following equations (Ulaby, 2007; Minet et al., 2010; Takahashi et al., 2012):

$$k' = k_0 n' \tag{2.39}$$

$$k'' = k_0 n'' \tag{2.40}$$

$$n' = \left[\frac{\sqrt{(\varepsilon'_r)^2 + (\varepsilon''_r)^2} + \varepsilon'_r}{2}\right]^{\frac{1}{2}} \tag{2.41}$$

$$n'' = \left[\frac{\sqrt{(\varepsilon_r')^2 + (\varepsilon_r'')^2} - \varepsilon_r'}{2}\right]^{\frac{1}{2}} \tag{2.42}$$

$$\varepsilon_r' = (n')^2 - (n'')^2; \varepsilon_r'' = 2n'n'' \tag{2.43}$$

$$\lambda_{wl} = \frac{\lambda_{wl,0}}{n'} \tag{2.44}$$

$$v = \frac{c_0}{n'} \tag{2.45}$$

$$k_0 = \frac{2\pi f}{c_0}; \lambda_{wl,0} = \frac{c_0}{f} \tag{2.46}$$

where, k_0 (m^{-1}), $\lambda_{wl,0}$ (m) and $c_0 = 2.997\,924\,58 \times 10^8\,\mathrm{m\,s}^{-1}$ are the wave number, wavelength and propagation velocity of an electromagnetic wave in free space, $k^* = k' - jk''$ (m^{-1}), λ_{wl} (m), v ($\mathrm{m\,s}^{-1}$), $n^* = n' - jn''$ and $\varepsilon_r^* = \varepsilon_r' - j\varepsilon_r''$ are the wave number, wavelength, propagation velocity, index of refraction and relative complex permittivity of the medium.

The amplitude of the attenuated electric field of a lossy medium can be found using (Kopyt and Celuch-Marcysiak, 2006; Ulaby, 2007; Takahashi et al., 2012):

$$|\mathbf{E}(\mathbf{z})| = |\mathbf{E_0}|e^{-k''\mathbf{z}} \tag{2.47}$$

where, $|\mathbf{E}(\mathbf{z})|$ and $|\mathbf{E_0}|$ ($\mathrm{V\,m}^{-1}$) are the attenuated magnitude and the original magnitude of the electric field in the lossy medium. Generally, when $|\mathbf{E}|$ is e^{-1} = 37% of its original amplitude $|\mathbf{E_0}|$, then $\mathbf{z} = 1/k'' = \delta_{sd}$, m, is called the *skin depth* of the material. The skin depth is an indicator of how far an electromagnetic wave penetrates into a medium. When the medium is lossless (i.e. $k'' = 0$) then the skin depth is infinite and the electromagnetic wave propagates indefinitely. Metallic materials have high electrical conductivities (i.e. high k'' or ε_r'') and hence have very small skin depths.

2.3.3 Broadband dielectric mixture models

Porous media such as soils typically consist of four phases, namely: solid (mineral) phases, pore-fluid (mostly water), pore-air and a solid-phase - pore-fluid interface. Generally, the quantitative fractions of these phases in a porous medium vary in both

time and space. Generally, the electromagnetic behavior of the solid particles is assumed to be frequency independent, with the relative dielectric permittivity of inorganic mineral particles ranging from 3 - 15 (Robinson and Friedman, 2003; Shön, 2015). Whereas, the pore-water is an aqueous solution, and its temperature and frequency dependent relative complex dielectric permittivity is obtained according to the modified Cole-Cole model (Kaatze and Feldman, 2006; Ellison, 2007; Kaatze, 2007b). The modified Cole-Cole model is discussed further in section 3.4.1 of this thesis.

Due to its simple structure, the theoretical mixing rule (volumetric fraction model) suggested by Lichtenecker and Rother (1931) (which is typically called the Lichtenecker and Rother model, LRM) (Equation 2.48), is widely used in soil physics, geophysics, remote sensing and geotechnical applications (Dobson et al., 1985; Malicki et al., 1992; Mironov et al., 2004; Schwartz et al., 2009; Wagner and Scheuermann, 2009; Hailemariam et al., 2017).

$$\varepsilon_{r,eff}^{*a} = \sum_{k=1}^{N} V_k \varepsilon_{r,k}^{*a} \tag{2.48}$$

where, $\varepsilon_{r,eff}^{*}$ is the relative effective complex permittivity of the porous medium, V_k is the volume fraction, with $\sum_{k=1}^{N} V_k = 1$ and $\varepsilon_{r,k}^{*}$ is the corresponding relative complex permittivity of the k^{th} constituent phase and a is the so-called structure factor or exponent. The LRM is commonly known as a three-phase (solid grains, free water and air) or a four-phase (solid grains, free water, bound water and air) mixing rule.

The exponent a contains structural information of the bound and free pore-water in porous media. However, the electrical behavior of the bound water phase in porous media is poorly understood and difficult to quantify, and is consequently neglected in practical applications (Blonquist Jr. et al., 2006; Wagner and Scheuermann, 2009). An extensive study on the theoretical justification of the LRM based on the effective medium theory by considering the distribution of depolarization factors which are linked to the structure parameter a was carried out by Zakri et al. (1998). The LRM is commonly used with an exponent $a = 1/2$, and is then called the complex refractive index model (CRIM) (Birchak et al., 1974) or the generalized refractive mixing dielectric model (Mironov et al., 2004). For an exponent $a = 1/3$, the LRM transforms to the Looyenga-Landau-Lifshitz model (LLLM) (Landau and Lifschitz, 1985; Campbell, 1990).

Based on the LRM, Wagner et al. (2011a) suggested a model for a broadband generalization (Equation 2.49), which is known as the advanced Lichtenecker and Rother

model (ALRM).

$$\varepsilon_{r,eff}^{*a(\theta,n)} = \theta\varepsilon_{r,w}^{*a(\theta,n)} + (1-n)\varepsilon_{r,g}^{\prime a(\theta,n)} + (n-\theta) \tag{2.49}$$

where, $\varepsilon_{r,eff}^{*}$ is the relative effective complex permittivity of the porous medium, $\varepsilon_{r,w}^{*}$ is the relative complex permittivity of water, structural exponent $0 < a \leq 1$, n is the soil porosity, θ is the volumetric water content fraction and $\varepsilon_{r,g}^{\prime}$ is the relative real permittivity of the solid grain particles.

Topp et al. (1980) proposed Equation 2.50 for obtaining the real apparent relative permittivity $\varepsilon_{r,a}$ of a soil based on the volumetric water content fraction θ as:

$$\varepsilon_{r,a} = 3.03 + 9.3\theta + 146.0\theta^2 - 76.7\theta^3 \tag{2.50}$$

2.4 Summary of chapter 2

The chapter reviewed the fundamentals of heat transfer and the propagation of electromagnetic waves in porous media. A discussion on the more frequently used prediction models for assessing the thermal and dielectric parameters of porous media was also presented.

Chapter 3

Structure and thermo-dielectric behavior of analyzed porous media

3.1 Introduction

In this chapter, a comprehensive study on the behavior and structure of unsaturated soils and oil sands is presented. The thermo-dielectric (T-DE) behavior of the constituent phases of both porous media types is discussed as part of the development of the semi-theoretical and numerical models in chapters 4 & 5 of this thesis, respectively.

3.2 Behavior of unsaturated soils

Naturally occurring unsaturated soils typically contain four phases, namely solid grains, free and bound water, air and contractile skin (or air-water interface) (Figure 3.1) (Fredlund and Morgenstern, 1977; Fredlund, 1979). Soils which commonly exhibit these phases in unsaturated state are the natural, desiccated soils and compacted soils. These soils generally have a negative pore-water pressure, and their most evident problems are related to their shrinkage and expansion behavior. The thermo-dielectric properties of the bound water phase of porous media are poorly understood and difficult to quantify, and hence are generally neglected for practical purposes (Wagner and Scheuermann, 2009; Hailemariam et al., 2017).

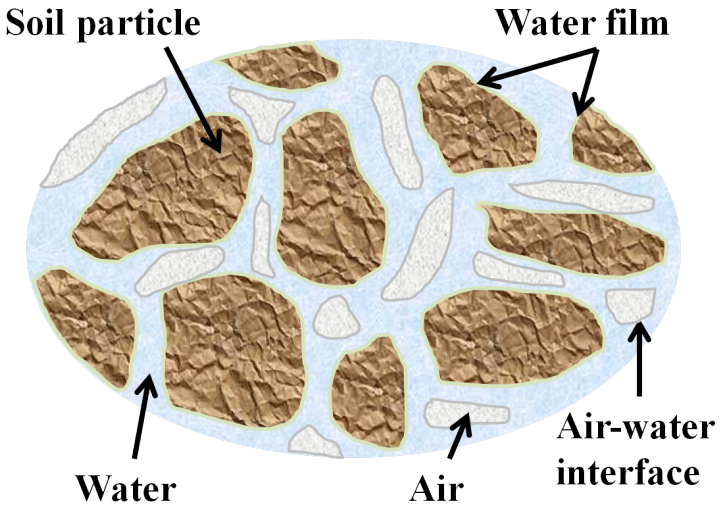

Figure 3.1: Classical model of the structure of unsaturated soils, after Fredlund and Morgenstern (1977).

3.3 Behavior of oil sands

3.3.1 Background

Wide varieties and sizes of heavy oil deposits, estimated to around 8 trillion barrels according to OPEC (OPEC, 2011; Robinson et al., 2014), are found around different parts of the world. The heavy oil deposits make up about 70% of the world's total oil resources (Figure 3.2) (Alboudwarej et al., 2006). Among them, those found in Alberta (Canada) ~$50\,000\,\mathrm{km}^2$ with estimated 1.8 trillion barrels (Figure 3.3), the Orinoco belt (Venezuala) ~1.2 trillion barrels and Alaska (United States) ~20 - 25 billion barrels are the biggest and mostly explored reserves (Canadian Energy Research Institute, 2011; OPEC, 2011; Banerjee, 2012; Robinson et al., 2014). The deposits in Alaska and the Orinoco belt primarily consist of extraheavy oil reserves, while Alberta's deposits (with a current daiy production of around 1.5 million barrels (Canadian Energy Research Institute, 2011; Robinson et al., 2014)) contain oil sands with highly viscous hydrocarbons that fall in the various groups of bitumen. Heavy oil energy resources also promise a bright near future solution for the ever increasing energy demand of my native land, Eritrea, with the recent discovery of the oil impregnated sands of the Defnein islands on the Red Sea coastline and the long known oil seeps on the coastal areas near Massawa and offshores close to the islands of the Dahlak Archipelago (Eritrean Ministry of Energy and Mines, 2006).

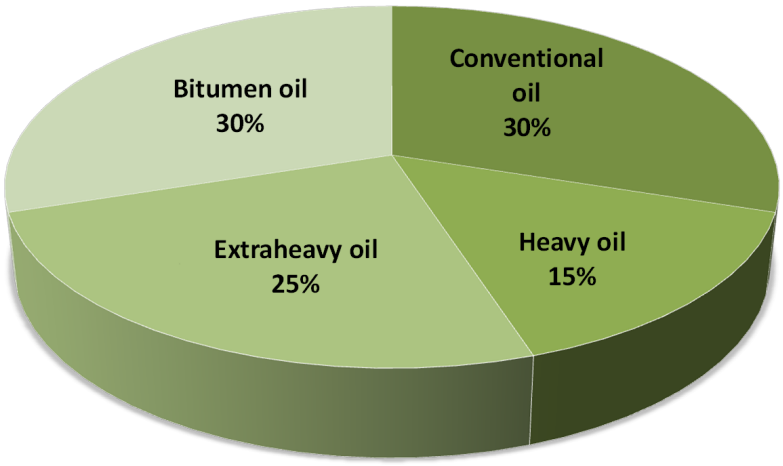

Figure 3.2: Total world oil reserves, after Alboudwarej et al. (2006).

Figure 3.3: Alberta's oil sands, Canada[1].

Petroleum and crude oil are mainly characterized by their very low viscosity and can be recovered from the subsurface by conventional means (Banerjee, 2012). On the other hand, heavy oils are usually highly viscous and much heavier than water at reservoir conditions, and hence more difficult to recover from the subsurface by conventional means (Moore et al., 1995; Ali, 2003; Liu et al., 2006; Upreti et al., 2007;

[1]Source: Getty Images iStock, credit: Dan Prat

Canadian Energy Research Institute, 2008; Shah et al., 2010; Pan and Xiao, 2011). Although, there is no fixed classification rule and the existing ones change from time to time, heavy oils are broadly classified in to conventional heavy oils and unconventional heavy oils. Conventional heavy oils have an API gravity from 10° to 21°, and in spite of their name behave like light oils and float on water (Banerjee, 2012). API gravity is a measure of how dense a liquid is compared to water, which has an API gravity of 10° at room temperature. Whereas, unconventional heavy oils have an API gravity < 10° and do not float on water. Using only the API gravity to characterize oil sands in generally not sufficient, hence it is more accurate to categorize heavy oils in terms of their viscosity, rather than API gravity.

Conventional heavy oils have a low viscosity (< 1 $\mathrm{Pa\,s}$ or $1000\,\mathrm{cP}$, centipoise) as compared to unconventional heavy oils which have a high viscosity (> 1 $\mathrm{Pa\,s}$). Unconventional heavy oils are further classified in to extraheavy oils (viscosity < 10 $\mathrm{Pa\,s}$) and bitumen (viscosity > 10 $\mathrm{Pa\,s}$) (Speight, 2007; Banerjee, 2012). It is a normal practice to upgrade bitumen (with API gravity < 10°) to API gravity of around 20° and viscosity below 1 $\mathrm{Pa\,s}$ to make it transportable in pipelines.

3.3.2 Structure of oil sands

In contrast to the structure of unsaturated soils, oil sands typically consist of a mixture of quartz/sands, clay fines, pore-water (which also includes a thin water film or bound water phase) and a dense and viscous form of petroleum or bitumen (Figure 3.4) (Takamura, 1982; Czarnecki et al., 2005; Masliyah et al., 2010; Banerjee, 2012). Oil sand reservoirs are generally highly heterogeneous in nature owing to the variation in the environmental deposition of the constituent sand and bitumen phases, as well as the bitumen chemistry (Banerjee, 2012). Understanding the behavior and heterogeneity of oil sand reservoirs is vital for the prediction of their thermal and dielectric behavior. The bitumen content of oil sands generally varies with the type and location of deposit and may range between 0 to 15 wt.%. Oil sands are usually divided into one of the three main categories given below, based on the fraction of bitumen present (Banerjee, 2012):

- Low grade oil sands, bitumen content 6 - 8 wt.%.
- Medium grade oil sands, bitumen content 8 - 10 wt.%.
- High grade (rich) oil sands, bitumen content > 10 wt.%.

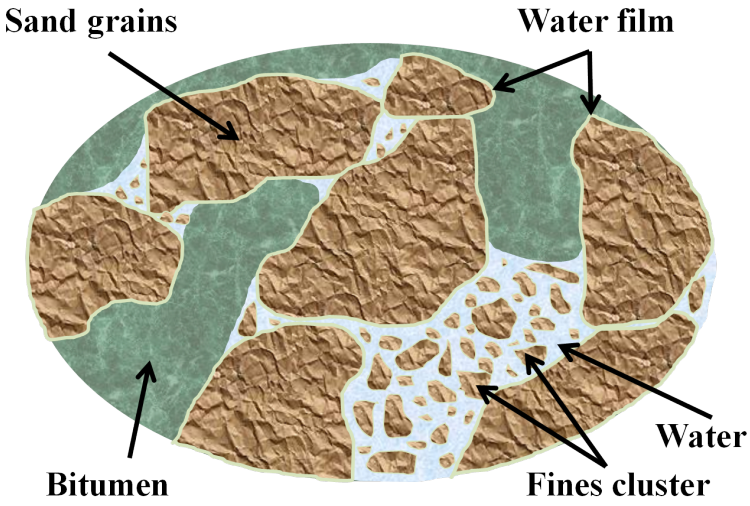

Figure 3.4: Classical model of the structure of oil sands, after Takamura (1982).

The solid grains in oil sands generally have hydrophilic character and are in most cases covered with a thin water film of around $10\,\mathrm{nm}$ - $10\,\mu\mathrm{m}$ thick (Takamura, 1982; Czarnecki et al., 2005; Banerjee, 2012). The oil sands are then typically called *water-wet*, and this plays a vital role in the separation of bitumen when the hot-water extraction technique is used (Banerjee, 2012). Czarnecki et al. (2005) performed a theoretical analysis on the nature, stability and thickness of the bound water phase of oil sands. However, due to the lack of direct experimental research, the behavior of the bound water phase of oil sands is not yet fully understood, and needs further investigation (Czarnecki et al., 2005). Shale oils, acidic ores and oil sands with organic coatings on the other hand, are known as *oil-wet* (Czarnecki et al., 2005; Banerjee, 2012), since they do not have a thin water layer between the solid and oil phases, and as a result cannot undergo hot-water extraction (Banerjee, 2012). In those instances, the formation of water film is intrinsically unstable and does not exist as a bound water. The presence of organic coatings with humic matter/asphaltenic molecules, which make the solids of oil sands hydrophobic, are also likely to make them oil-wet (Czarnecki et al., 2005).

3.3.3 Formation of bitumen

One of the most widely accepted hypothesis for the formation of bituminous materials is *biodegradation* of conventional oil resources (Speight, 2007; Banerjee, 2012). The degree of biodegradation varies significantly across the length and depth of oil sand deposits, and is directly related to the quantity of hydrocarbons with molecular range lower than C_{20} *n*-alkanes and mono-aromatic hydrocarbons in the oil (Banerjee, 2012). Generally, undegraded oils have a higher percentage of *n*-alkanes when compared to

degraded oil. The degree of biodegradation is usually measured by the concentration of below C_{20} *n*-alkanes (such as C_{17}-C_{18} *n*-alkanes), as cyclic saturated hydrocarbons are not affected by biodegradation (Strausz and Lown, 1978; Strausz and Lown, 2003; Banerjee, 2012).

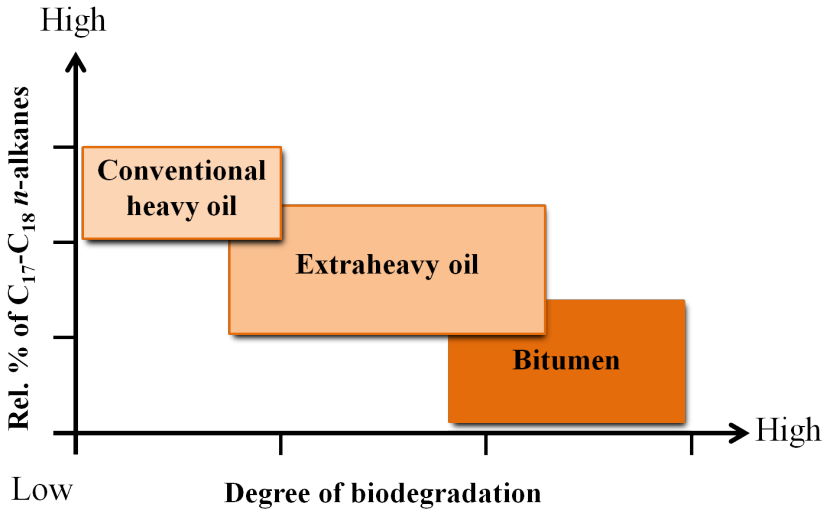

Figure 3.5: Biodegradation of heavy oil and bitumen, after Banerjee (2012).

The concentrations of C_{17}-C_{18} *n*-alkanes are the highest in conventional heavy oils when compared to extraheavy oils, and are the lowest in bitumen (Figure 3.5) (Banerjee, 2012). Biodegradation of oils is highly dependent on the environmental or reservoir conditions, and hence, results in the variations of the distribution of bitumen and the heterogeneous nature of oil sand reservoirs.

3.3.4 Composition of bitumen

Bitumen is typically characterized to various classes based on two most widely used solvent extraction or analysis techniques known as SARA (saturates, aromatics, resins and asphaltenes) and PONA (paraffins, olefins, naphthenes and aromatics) (Speight, 2007; Banerjee, 2012). Out of the two, SARA is predominantly used, and its four groups are defined as:

- Saturates: Contain straight or branched hydrocarbon chains which are known as paraffins and isoparaffins as well as cyclic hydrocarbons or naphthenes. Generally, the amount of saturates in bitumen is relatively low due to biodegradation.
- Aromatics: Contain hydrocarbons with aromatic rings, such as benzene, toluene, naphthalene etc.

- Resins: Contain polar aromatic rings with nitrogen, oxygen and sulfur. Along with aromatics, resins are the primary constituents of bitumen.
- Asphaltenes: Include complex organic compounds of high molecular weight. They are soluble in light aromatics, such as benzene and toluene but insoluble in lighter paraffins.

The elemental analysis of oil sands bitumen has also been widely studied (Camp, 1976; Bunger et al., 1979; Speight, 2007; Banerjee, 2012), but the data generally lacks site specific identification and is too general (Speight, 2007). Wallace et al. (1988) conducted programs which were focused on producing sound and reproducible data from samples for which the source was carefully identified, and provided a valuable database for the characterization of oil sands bitumen. In terms of its elemental composition, bitumen is a complex hydrocarbon containing carbon, hydrogen, nitrogen and sulfur (CHNS), with the carbon and hydrogen contributing higher than 80 wt.% and 10 wt.%, respectively (Speight, 2007; Banerjee, 2012). The elemental composition of oil sand bitumen is generally constant and falls in to a narrow range (Table 3.1) (Speight, 2007).

Table 3.1: Elemental composition of bitumen (Speight, 2007).

Element	**Range**
Carbon	83.4 ± 0.5 wt.%
Hydrogen	10.4 ± 0.2 wt.%
Nitrogen	0.4 ± 0.2 wt.%
Oxygen	1.0 ± 0.2 wt.%
Sulfur	5.0 ± 0.5 wt.%
Metals (Ni and V)	> 1000 ppm

3.3.5 Viscosity of bitumen

The viscosity of oil sand bitumen is an important parameter which plays a major role in the production of bitumen from oil sand reservoirs and its subsequent transportation via pipelines to refineries (Speight, 2007; Banerjee, 2012). Unlike conventional crude oils, which flow at room temperature, bitumen is highly viscous and resists motion at room temperature, and hence its viscosity measurement is difficult. At high temperatures, where the bitumen is able to flow by itself, standard tests, such as the capillary viscometer method (also used for measuring the viscosity of conventional crude at normal conditions) (ASTM D 445 - 97, 1997) are used. For measuring the viscosity of bitumen or other highly viscous fluids at room temperature, special

viscosity measurement techniques which work on the basis of shear effects, such as the bob-and-cup and the cone-and-plate viscometers are used (Seyer and Gyte, 1989).

The viscosity of bitumen is acutely sensitive to temperature changes, commonly decreasing exponentially from values higher than 100 $\mathrm{Pa\,s}$ or $100\,000\,\mathrm{cP}$ at room temperature to below 0.1 $\mathrm{Pa\,s}$ or $100\,\mathrm{cP}$ at 100°C (Speight, 2007; Banerjee, 2012; Cerutti et al., 2013). At temperatures above 100°C (viscosity values below 0.1 $\mathrm{Pa\,s}$), bitumen is considered mobile enough to be extracted from the pores of oil sands (Cerutti et al., 2013).

3.3.6 Recovery of oil sands

The methods of recovery of oil sands are broadly classified in to two categories: conventional and unconventional techniques.

Conventional methods of processing oil sands include the ex-situ hot water separation or surface mining technique (Canadian Energy Research Institute, 2008; Shah et al., 2010; Robinson et al., 2014) and several types of in-situ thermal and non-thermal techniques (Moore et al., 1995; Ali, 2003; Liu et al., 2006; Upreti et al., 2007; Shah et al., 2010; Pan and Xiao, 2011; Robinson et al., 2014). Surface mining methods are usually employed for shallow depth oil sand reservoirs, while in-situ methods are used for mining deep oil sand reservoirs ($> 80\,\mathrm{m}$) where the use of surface mining techniques is not economically feasible. In surface mining technique, the oil sand is dug and transported to the extraction plant where the bitumen is separated from the sand using the hot water separation method. In-situ extraction methods are used to extract bitumen from oil sand reservoirs by lowering its viscosity by heating while the solid phase remains intact. The two commonly used commercial in-situ bitumen recovery techniques are the steam assisted gravity drainage (SAGD) and cyclic steam simulation (CSS).

Conventional methods of processing oil sands have limitations, such as restrictions of depth, formation type and medium permeability, high energy requirements, long processing times, difficulty processing clay fines, need for the addition of hot water, solvents and/or gases, inability to further process heavy oils and the need for further upgrading (Robinson et al., 2014). Hence, a small portion of existing oil sand reservoirs can be effectively processed, and therefore alternative technologies are required to exploit the full potential of the oil sand deposits.

An unconventional technique that has gained much interest in recent years as having a potential application to oil sands is EM heating of reservoirs (Mutyala et al.,

2010; Robinson et al., 2014). EM heating of oil sand deposits provides the best option of harnessing heavy oils and is a greener and environmentally friendlier technique of harnessing energy when compared with the traditional methods. Electromagnetic waves have the unique ability to heat phase-selectively and volumetrically, which leads to the possibility of significant energy savings with much smaller process equipments and without the addition of huge amounts of water or causatic solutions. With electromagnetic heating, the water phase is targeted and heated selectively and converted to steam, which then acts as an in-situ media of mass transfer stripping or desorbing the hydrocarbons from the solid phase (Robinson et al., 2009b; Robinson et al., 2014). Hence, energy is only required to primarily heat the water phase, rather than the entire volume of the material, resulting in processes that use only one-fifth of the energy requirement of their conventional heating counterparts (Robinson et al., 2009b; Robinson et al., 2014). Previous studies have shown the recovery of up to in excess of 95% of oil yields from oil sand reservoirs with continuous EM heating at an industrial scale (Robinson et al., 2010; Robinson et al., 2014).

Electromagnetic waves are characterized according to their frequency spectrum. Microwaves are electromagnetic waves whose frequencies lie in the range between 300 MHz (wavelength of 100 cm) and 30 GHz (wavelength of 1 cm) (Porch et al., 2012). Above 30 GHz frequencies, the microwave spectrum gives way to the millimeter wave spectrum, and below 300 MHz to the radio frequency spectrum. In the microwave part of the electromagnetic spectrum, dielectric heating phenomena dominates (Porch et al., 2012). When the oil sand deposit is irradiated with an electric field, the polar molecules in the oil sand align themselves with the changing electric field, a phenomena which is called polarization or dipolar rotation, which in turn leads to dielectric losses. The dielectric medium properties, in particular the dielectric loss or loss tangent, determines the efficiency of the amount of polarization or dielectric losses of a medium and is directly proportional to the quantity of the entrapped porewater, salinity and the presence of other chemicals in the liquid phase. Conversely, in the radio frequency part of the spectrum, heat is generated by electromagnetic induction, which is driven by the eddy currents induced in electrically conducting or magnetic objects. Hence, small conducting or magnetic particles are added to the dielectric material to initiate the heating process, which is then transfered to the dielectric material via conduction (Porch et al., 2012). Generally, EM heating at low frequencies is preferred in the case of irradiating large areas (depths) of oil sand reservoirs, as the electromagnetic waves can penetrate further than higher frequencies (Mutyala et al., 2010).

3.4 Thermo-dielectric properties of the constituent phases of porous media

The thermo-dielectric properties of porous media vary significantly with frequency (in the case of dielectric parameters) and temperature (Smith-Magowan et al., 1982; Skauge et al., 1983; Scott, 1989; Ramires et al., 1995; Buchner et al., 1999; Gong et al., 2003; Kaatze, 2007b; Wagner et al., 2007b; Wagner and Scheuermann, 2009; Hirono and Hamada, 2010; Chen et al., 2015; Irani and Cokar, 2016). Hence, in order to effectively model the effective thermal and dielectric behavior of porous media, the frequency and temperature dependence of the different constituent phases should be defined.

3.4.1 Dielectric properties

3.4.1.1 Dielectric properties of solid particles and bitumen

The electromagnetic behavior of the solid phases (grains) of most porous media show minor variations with changes in frequency and temperature (Robinson and Friedman, 2003; Shön, 2015). Similarly, the bituminous phase of oil sands exhibits comparatively small changes in its dielectric behavior with changes in frequency and temperature (especially at higher frequencies) (Chen et al., 2015). Hence, the dielectric permittivity and loss tangent of these constituent phases are frequency and temperature independent. Typical values of the real part of the relative complex dielectric permittivity of the solid grains can be obtained using Equation 3.1 (Dobson et al., 1985), and for bitumen $\varepsilon'_{r,b} = 2.5$ can be taken (Rambabu et al., 2011; Oloumi and Rambabu, 2016).

$$\varepsilon'_{r,g} = (1.01 + 0.44G_s)^2 - 0.062 \tag{3.1}$$

where, $\varepsilon'_{r,g}$ and G_s are the real part of the relative complex dielectric permittivity and the specific gravity of the solid grain particles.

3.4.1.2 Dielectric properties of pore-water

Unlike the solid grains and the bituminous phase, the pore-water is an aqueous solution which is highly sensitive to both frequency and temperature changes. The

complex permittivity of water as a function of frequency is determined by their polarizability and dielectric losses. The polarization in turn describes the ability of the water molecules to store energy due to charge displacements under the applied electromagnetic field. Once the applied electric field is removed, the energy stored in the water molecules starts to dissipate with time (Hilhorst, 2000). The restoration of the charges to equilibrium due to the removal of the electromagnetic field is known as *dielectric relaxation* (Von Hippel, 1954; Santamarina et al., 2001; Wagner et al., 2007a).

A typical single type dielectric relaxation behavior of a porous medium is described by the Debye model (Equation 3.2) (Debye, 1929; Debye, 1934; Hilhorst et al., 2001).

$$\varepsilon^*_{r,eff}(\omega, T) = \varepsilon_\infty(T) + \frac{\Delta\varepsilon(T)}{1 + j\omega\tau(T)} \tag{3.2}$$

where, $\varepsilon^*_{r,eff}$ is the relative effective complex permittivity of the porous medium, ε_∞ is the high frequency limit of permittivity, $\Delta\varepsilon = \varepsilon_s - \varepsilon_\infty$ is the relaxation magnitude, ε_s is the static permittivity, $j^2 = -1$ is the imaginary unit, $\omega = 2\pi f$ (rad) is the angular frequency and τ (s) is the relaxation time.

As discussed in chapter 2, the imaginary part of complex permittivity is affected by the electrical conductivity, and hence, in order to take the contribution from the electrical conductivity in to account, the Debye model (Equation 3.2) is modified by an additional term for the direct current conductivity σ_{DC} $(\mathrm{S\,m^{-1}})$ and the dielectric permittivity of free space $\varepsilon_0 = 8.854\,187\,817 \times 10^{-12}\,\mathrm{F\,m^{-1}}$ as (Kaatze, 2000; Wagner et al., 2011a):

$$\varepsilon^*_{r,eff}(\omega, T) = \varepsilon_\infty(T) + \frac{\Delta\varepsilon(T)}{1 + j\omega\tau(T)} - j\frac{\sigma_{DC}(T)}{\omega\varepsilon_0} \tag{3.3}$$

Equations 3.2 (Debye model) and 3.3 (modified Debye model) are the simplest forms of the dielectric spectrum and typically represents the behavior of single-phased homogeneous materials, such as pure water as follows (Asami, 2002; Zajicek et al., 2006; Wagner and Scheuermann, 2009):

$$\varepsilon^*_{r,w}(\omega, T) = \varepsilon_\infty(T) + \frac{\Delta\varepsilon(T)}{1 + j\omega\tau_w(T)} - j\frac{\sigma_{DC}(T)}{\omega\varepsilon_0} \tag{3.4}$$

where, $\varepsilon^*_{r,w}$ is the relative complex dielectric permittivity of water, and τ_w (s) is the relaxation time of water. Equation 3.4 is used to describe the frequency and temperature dependence of the dielectric properties (mainly the dielectric constant) of pore-water of porous media in the new models presented in this thesis (Figure 3.6).

The equation can also be used to estimate the loss tangent or the imaginary part of the relative effective complex permittivity of porous media when the pore-water solution contains low amounts of dissolved solutes, which typically occurs in oil sands and soils where the dominant solid fraction is of a sandy texture. However, the equation may face limitations for predicting the loss tangent of porous media with considerable clay content, where a high concentration of dissolved solutes may be expected in the pore-water solution, exhibiting large degrees of polarization or loss tangent especially at frequencies lower than 1 GHz. Other studies (Wagner et al., 2011a; Hailemariam et al., 2017) have also pointed out the difficulty of modeling the loss tangent of porous media with empirical equations, particularly due to the presence of solutes in the pore-water solution.

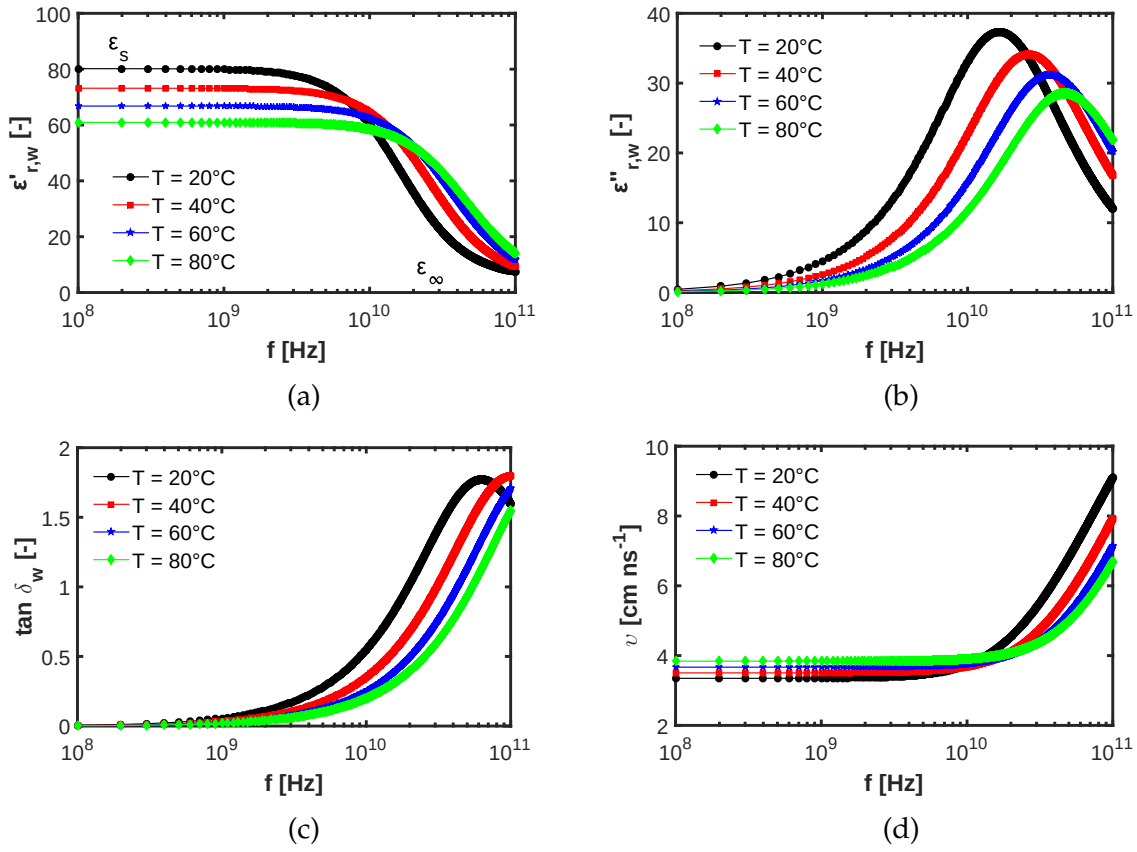

Figure 3.6: Dielectric spectrum of water under the effect of a relaxation process according to the modified Debye model (Equation 3.4) with the real $\varepsilon'_{r,w}$ a) and imaginary $\varepsilon''_{r,w}$ b) parts of the relative complex dielectric permittivity, loss tangent $\tan\delta_w$ c) and propagation velocity v d) of water.

The temperature dependence of ε_∞ and ε_s is expressed in terms of empirical relations of the form (Kaatze, 2007b; Wagner et al., 2014):

$$\varepsilon_{k,w} = \varepsilon_{m,k,w} \exp(a_{k,w} T) \tag{3.5}$$

where, $\varepsilon_{m,k,w}$ and $a_{k,w}$ are two empirical parameters for $k = \{s, \infty\}$. The temperature dependence of the relaxation time of water can be characterized according to the Eyring equation as (Buchner et al., 1999; Kaatze, 2007a):

$$\tau_w(T) = \frac{h}{k_B T} k \exp\left[\frac{\Delta G_w^{\#}(T)}{RT}\right] \tag{3.6}$$

where, τ_w (s) is the relaxation time of water, $h = 6.626\,070\,04 \times 10^{-34}\,\mathrm{m^2\,kg\,s^{-1}}$ is the Planck constant, $k_B = 1.380\,648\,52 \times 10^{-23}\,\mathrm{m^2\,kg\,s^{-2}\,K^{-1}}$ is the Boltzmann constant, $k \approx 1$ is the transmission coefficient, $R = 8.3145\,\mathrm{J\,mol^{-1}\,K^{-1}}$ is the gas constant and $\Delta G_w^{\#} = \Delta H_w^{\#} - T\Delta S_w^{\#}$ ($\mathrm{J\,mol^{-1}}$) is the free enthalpy of activation or Gibbs free energy, with activation enthalpy $\Delta H_w^{\#}$ ($\mathrm{J\,mol^{-1}}$) and activation entropy $\Delta S_w^{\#}$ ($\mathrm{J\,mol^{-1}\,K^{-1}}$) (Ishida et al., 2000; Ishida et al., 2003).

To model the temperature dependence of the dielectric relaxation time of the free water of a porous media under atmospheric conditions based on the Eyring's model (Equation 3.6), the approach suggested by Buchner et al. (1999) is applied:

$$\Delta G_w^{\#}(T) = \Delta H_{w,298}^{\#} + \Delta c_{p,298}^{\#}(T - T^*) - T[\Delta S_{w,298}^{\#} + \Delta c_{p,298}^{\#} \ln(T/T^*)] \tag{3.7}$$

where, $\Delta G_w^{\#}$ ($\mathrm{J\,mol^{-1}}$) is the free enthalpy of activation, $\Delta H_{w,298}^{\#} = 15\,900\,\mathrm{J\,mol^{-1}}$ is the activation enthalpy, $\Delta S_{w,298}^{\#} = 20.4\,\mathrm{J\,mol^{-1}\,K^{-1}}$ is the activation entropy and $\Delta c_{p,298}^{\#} = (\partial \Delta H_{w,298}^{\#}/\partial T)_p = T(\partial \Delta S_{w,298}^{\#}/\partial T)_p = -160\,\mathrm{J\,mol^{-1}\,K^{-1}}$ is the heat capacity of activation at a reference temperature $T^* = 298.15\,\mathrm{K}$ (Buchner et al., 1999).

According to the Debye model, the real part of the complex permittivity shows two asymptotes, namely a static permittivity ε_s, which is found at low frequency ($f \longrightarrow 0$), and the high frequency limit of permittivity ε_∞, which is found at ($f \longrightarrow \infty$) (Figure 3.6a). And the characteristic difference between the two gives the relaxation magnitude $\Delta\varepsilon$. The imaginary part of complex permittivity exhibits a log-normal distribution of the dielectric spectrum, where the peak value is found at the inflection point of the relaxation magnitude (Figure 3.6b).

Heterogeneous and complex porous materials, which are comprised of multiple constituent phases with different electromagnetic behavior, may exhibit not only a single type relaxation pattern, but also a distribution of relaxation times (Santamarina et al., 2001; Zajicek et al., 2006; Wagner et al., 2007b). In this regard, the Cole-Cole model (Equation 3.8) is introduced to describe the range of a distribution of relaxation times (Cole and Cole, 1941; Asami, 2002; Kaatze and Feldman, 2006; Ellison, 2007; Kaatze, 2007b; Wagner and Scheuermann, 2009).

$$\varepsilon^*_{r,eff}(\omega,T) = \varepsilon_\infty(T) + \frac{\Delta\varepsilon(T)}{1+[j\omega\tau(T)]^{\beta_{CC}(T)}} - j\frac{\sigma_{DC}(T)}{\omega\varepsilon_0} \tag{3.8}$$

where, β_{CC} ($0 \leq \beta_{CC} \leq 1$) is the stretching exponent or Cole-Cole parameter which refers to the relaxation time distribution. For the special case of $\beta_{CC} = 1$ the Cole-Cole model reduces to the Debye model.

In terms of the intrinsic dielectric behavior, the bound water effects can not be ignored for porous media with high clay fraction. The free water, which is also called bulk water, has a dielectric constant $\varepsilon'_{r,w} = 80$ at 1 GHz and 20°C, hence it shows a high degree of polarization as it is able to rotate freely when an external electrical field is applied (Gong et al., 2003). Whereas, the bound water phase consists primarily of water molecules which are bound to the solid grains by cohesive, adhesive and osmotic forces (Hilhorst et al., 2001; Gong et al., 2003). The rotation of the bound water phase when an electrical field is applied is restricted, resulting in less polarization (less dielectric constant) compared with that of free water (Gong et al., 2003). Or and Wraith (1999) obtained values of dielectric constant of bound water of $\varepsilon'_{r,w} = 6$, 10 and 14 by harmonic averaging for bound water regions made up of one, two and three molecular thicknesses, respectively. Sun and Young (2001) found a value of $\varepsilon'_{r,w} = 30.2$ as the distance-weighted average for a bound water made up of four water-molecule layers in Rideau clay.

3.4.1.3 Dielectric properties of saline pore-water

For porous media (soils and oil sands) with considerable salinity (such as those obtained at or near seashores or in saline soils), the dielectric properties of saline pore-water rather than pure pore-water should be used.

The dielectric properties of saline water differ from those of pure water (Klein and Swift, 1977; Ellison et al., 1998; Blanch and Aguasca, 2004; Meissner and Wentz, 2004; Zhou et al., 2012). At low GHz frequency ranges (< 10 GHz), saline water exhibits much higher loss tangent as compared to pure water, and hence shows a higher rate of heat dissipation when irradiated with an electric field (Mukhametshina and Martynova, 2013).

Unlike pure or distilled water, where the dielectric properties are only influenced by changes in frequency and temperature, the complex dielectric permittivty of saline or seawater is also dependent on salinity in addition to frequency and temperature (Meissner and Wentz, 2004). In this thesis, the complex dielectric permittivity model

for seawater suggested by Blanch and Aguasca (2004) is discussed due to its simplicity and accuracy of prediction. Blanch and Aguasca used a modified version of the modified Debye model for distilled water (Equations 3.4) as:

$$\varepsilon^*_{r,sw}(\omega, T, S) = \varepsilon_\infty + \frac{\varepsilon_s(T,S) - \varepsilon_\infty}{1 + j\omega\tau_{sw}(T,S)} - j\frac{\sigma_{DC}(T,S)}{\omega\varepsilon_0} \tag{3.9}$$

where, $\varepsilon^*_{r,sw}$ is the frequency f, temperature T and salinity S dependent relative complex dielectric permittivity of seawater, ε_∞ is the high frequency limit of permittivity, ε_s is the static permittivity, τ_{sw} (s) is the relaxation time of seawater, σ_{DC} ($\mathrm{S\,m^{-1}}$) is the direct current conductivity and $\varepsilon_0 = 8.854\,187\,817 \times 10^{-12}\,\mathrm{F\,m^{-1}}$ is the dielectric permittivity of free space.

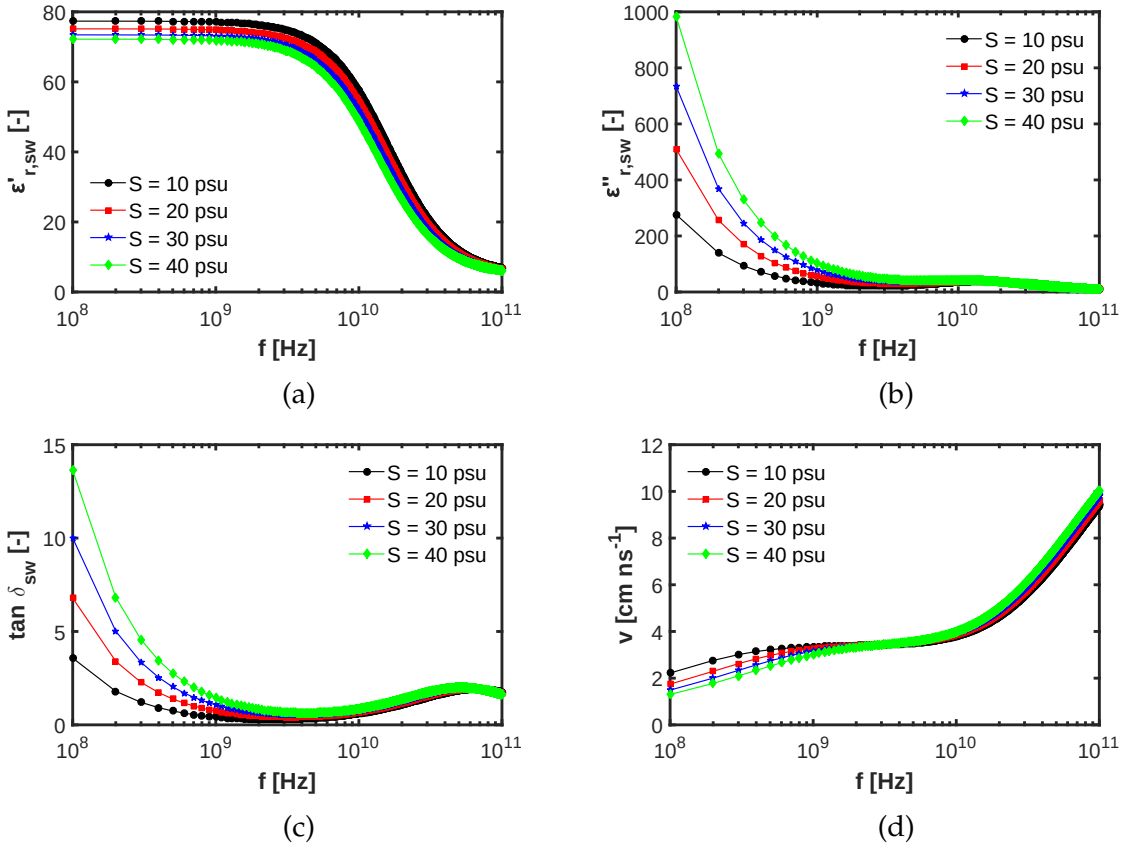

Figure 3.7: Dielectric spectrum of seawater at temperature $T = 20°\mathrm{C}$ under the effect of a relaxation process according to the modified Debye model of Blanch and Aguasca (2004) (Equation 3.9) with the real $\varepsilon'_{r,sw}$ a) and imaginary $\varepsilon''_{r,sw}$ b) parts of the relative complex dielectric permittivity, loss tangent $\tan\delta_{sw}$ c) and propagation velocity v d) of seawater at salinities $S = 10$, 20, 30 and 40 psu.

Blanch and Aguasca suggested that the high frequency limit of permittivity ε_∞ be assumed to be independent of frequency, temperature and salinity with a value of 4.9. However, the static permittivity ε_s, relaxation time τ_{sw} and direct current conductivity

σ_{DC} of seawater are all temperature and salinity dependent, and hence they suggested Equations 3.10 - 3.12 to obtain these parameters based on permittivity measurements on 23 seawater samples with salinities in the range between 0 to 40 psu (practical salinity unit) and frequency range between 0.5 to 2.5 GHz.

$$\varepsilon_s(T,S) = \varepsilon_s(T,0)a_{sw}(T,S) \tag{3.10}$$

$$\tau_{sw}(T,S) = \tau_{sw}(T,0)b_{sw}(T,S) \tag{3.11}$$

$$\sigma_{DC}(T,S) = \sigma_{DC}(25,S)\exp[-\phi(T,S)] \tag{3.12}$$

with the following additional modification equations for obtaining the parameters in Equations 3.10 - 3.12 [salinity S (psu) & temperature T (°C)]:

$$\varepsilon_s(T,0) = 87.38 - 3.436\times10^{-1}T - 1.912\times10^{-3}T^2 + 3.812\times10^{-5}T^3 \tag{3.13}$$

$$a_{sw}(T,S) = 1 + 1.1552\times10^{-5}TS - 3.9073\times10^{-3}S + 3.0596\times10^{-5}S^2 \tag{3.14}$$

$$\tau_{sw}(T,0) = 17.385 - 5.78\times10^{-1}T + 1.084\times10^{-2}T^2 - 9.098\times10^{-5}T^3(\mathrm{ps}) \tag{3.15}$$

$$b_{sw}(T,S) = 1 + 2.9832\times10^{-4}TS - 2.3871\times10^{-3}S + 5.625\times10^{-5}S^2 \tag{3.16}$$

$$\sigma_{DC}(25,S) = 1.90\times10^{-1}S - 2.35\times10^{-3}S^2 + 3.46\times10^{-5}S^3 \tag{3.17}$$

$$\phi(T,S) = \Delta[1.9479\times10^{-2}+1.6532\times10^{-4}\Delta - S(-1.0024\times10^{-6}+6.9946\times10^{-7}\Delta)];\ \Delta = 25-T \tag{3.18}$$

Prediction results of the model from Blanch and Aguasca at a room temperature of $T = 20$°C is shown in Figure 3.7, and at temperatures of $T = 30$ and 40°C are shown in appendix A.

3.4.2 Thermal properties

3.4.2.1 Previous studies

Thermal conductivity is one of the important thermal properties of soils known to be highly influenced by the changes in water/saturating fluid content. In a typical three-phase unsaturated soil system of solid particles, water and dry air, the effective thermal conductivity of the resulting wet soil is a function of water and air contents (Johansen, 1975; Clauser and Huenges, 1995; Lu et al., 2007).

The effective thermal conductivity of saturated oil sands is also highly affected by the quantity of the saturating fluid (bitumen and water). Somerton et al. (1974) studied the effects of temperature changes on the thermal conductivity of oil-water saturated unconsolidated oil sands, and concluded that the degree of saturation of the wetting fluid has a dominant effect on the thermal conductivity of the oil sands.

This is in agreement with the findings of Cervanan et al. (1981), where a high degree of increase in the thermal conductivity of some reconstituted Athabasca oil sand samples at room temperature and pressure was observed with an increase in water content of the samples. Somerton et al. further suggested that the temperature effects could be deemed to be essentially linear and proposed an empirical equation for predicting the variation of thermal conductivity of oil sands with temperature based on data from Scott and Seto (1986). Irani and Cokar (2016) later proposed a modified model by reducing the number of empirical terms of the original model presented by Somerton et al. (1974).

Karim and Hanafi (1981) studied the thermal conductivities of various natural and reconstituted oil sand samples from Athabasca at temperatures ranging from 20°C to 120°C using a coaxial type steady state device. They adjusted the bitumen contents during the preparation of the remolded samples, and noted a significant decrease in the thermal conductivities with an increase in temperature.

Seki et al. (1981) devised a transient state thermal testing apparatus for the determination of thermal conductivity and specific heat values of specimens from a disturbed medium grade Alberta oil sand samples. The results showed a sudden drop in the measured thermal properties at around 100°C due to vaporization of fluids in

the specimen, as a provision of a back-fluid pore-pressure system to prevent fluids from vaporizing at elevated temperatures was not provided.

With regards to the heat capacity, several researchers have provided detailed models for the specific heat capacity of porous media and their corresponding constituent phases (Smith-Magowan et al., 1982; Skauge et al., 1983; Mains et al., 1984).

3.4.2.2 Thermal properties of solids, bitumen and pore-water

The thermal properties of porous media are influenced by temperature changes, due to the temperature sensitivity of the different constituent phases (Smith-Magowan et al., 1982; Skauge et al., 1983; Scott, 1989; Ramires et al., 1995; Hirono and Hamada, 2010; Irani and Cokar, 2016).

Tables 3.2 and 3.3 show the thermal conductivity and specific heat capacity models of the different components of porous media as a function of temperature, respectively. The corresponding results are plotted in Figures 3.8a and 3.8b, respectively.

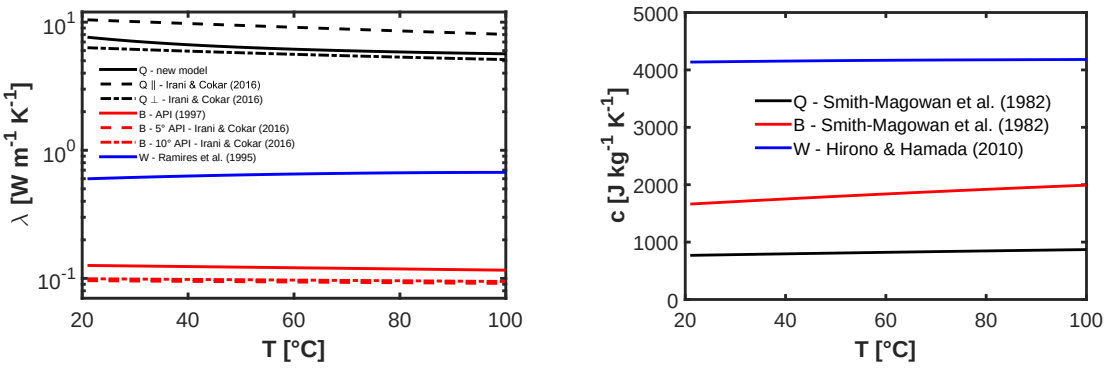

(a) (b)

Figure 3.8: Thermal conductivity a) and specific heat capacity b) of the different components of porous media as a function of temperature (Q - quartz, B - bitumen and W - water).

Table 3.2: Thermal conductivity vs temperature models of the different constituents of porous media.

Constituent	**Model**	**Suggested by**
Quartz, average crystal[a]	$\lambda_s(T) = \lambda_{T_o} - qq(1/2)^{(\frac{T_o}{T})}\lambda_{dom}(\frac{T-T_o}{T})$	Hailemariam and Wuttke (2018b)
Quartz $\parallel$ to the *c*-axis[b]	$\lambda_{s\parallel}(T) = -8.52 \times 10^{-14}T^5 + 3.02 \times 10^{-10}T^4 - 4.47 \times 10^{-7}T^3 + 3.56 \times 10^{-4}T^2 - 0.158T + 35.40$	Irani and Cokar (2016)
Quartz $\perp$ to the *c*-axis[b]	$\lambda_{s\perp}(T) = -3.19 \times 10^{-13}T^5 + 9.54 \times 10^{-10}T^4 - 1.13 \times 10^{-6}T^3 + 6.81 \times 10^{-4}T^2 - 0.214T + 32.66$	Irani and Cokar (2016)
Bitumen[c]	$\lambda_b(T) = 0.1289 - 1.3 \times 10^{-4}T$	American Petroleum Institute (1997)
Bitumen with 5° API[d]	$\lambda_b(T) = 0.113 - 5.8 \times 10^{-5}T$	Irani and Cokar (2016)
Bitumen with 10° API[d]	$\lambda_b(T) = 0.117 - 6.0 \times 10^{-5}T$	Irani and Cokar (2016)
Water[e]	$\lambda_w(T) = \lambda_{w,298.15}\big[-1.48445 + 4.12292(\frac{T}{298.15}) - 1.63866(\frac{T}{298.15})^2\big]$	Ramires et al. (1995)

[a]: λ_s ($\mathrm{W\,m^{-1}\,K^{-1}}$), T (°C), for quartz grains: $\lambda_{T_o} = \lambda_{dom} = \lambda_q = 7.7\,\mathrm{W\,m^{-1}\,K^{-1}}$ at $T_o = 20$°C, $qq = 0.38$; for porous medium solids which are composed of quartz and other minerals: $\lambda_{T_o} = \lambda_q^{q_f}\lambda_o^{(1-q_f)}(\mathrm{W\,m^{-1}\,K^{-1}})$, $\lambda_o = 2.0$ or $3.0\,\mathrm{W\,m^{-1}\,K^{-1}}$ depending on q_f (see section 2.2.5 or Hailemariam and Wuttke (2018b))

[b]: Suggested based on data from Powell et al. (1966), $\lambda_{s\parallel}$ or $\lambda_{s\perp}$ ($\mathrm{W\,m^{-1}\,K^{-1}}$) and T (K)

[c]: λ_b ($\mathrm{W\,m^{-1}\,K^{-1}}$) and T (°C)

[d]: Suggested based on data from Bland and Davidson (1967), λ_b ($\mathrm{W\,m^{-1}\,K^{-1}}$) and T (K)

[e]: λ_w ($\mathrm{W\,m^{-1}\,K^{-1}}$), $\lambda_{w,298.15} = 0.6065\,\mathrm{W\,m^{-1}\,K^{-1}}$ and T (K)

Table 3.3: Specific heat capacity vs temperature models of the different constituents of porous media.

Constituent	**Model**	**Suggested by**
Quartz[a]	$c_s(T) = [0.738 + 1.518 \times 10^{-3}T - 2.026 \times 10^{-6}T^2]10^3$	Smith-Magowan et al. (1982)
Bitumen[a]	$c_b(T) = [1.557 + 5.219 \times 10^{-3}T - 8.686 \times 10^{-6}T^2]10^3$	Smith-Magowan et al. (1982)
Water[b]	$c_w(T) = 95909 - 184.43T + 1.3833 \times 10^{-1}T^2 - 2.0119 \times 10^7T^{-1} + 1.6358 \times 10^9T^{-2}$	Hirono and Hamada (2010)

[a]: c_s or c_b ($\mathrm{J\,kg^{-1}\,K^{-1}}$) and T (°C)

[b]: Suggested based on data from Japan Society of Mechanical Engineers (1983), c_w ($\mathrm{J\,kg^{-1}\,K^{-1}}$) and T (K)

3.4.2.3 Thermal properties of saline pore-water

As in the dielectric properties, the thermophysical properties of saline water are also affected by temperature and salinity (Jamieson et al., 1969; Jamieson and Tudhope, 1970; Sharqawy et al., 2010).

The thermal conductivity of liquids is a difficult property to measure, and hence available data on seawater thermal conductivity is scarce. Generally, for aqueous solutions with an electrolyte, such as saline water, the thermal conductivity decreases with an increase in the concentration of the dissolved salts (Poling et al., 2001; Sharqawy et al., 2010). The prediction equation given by Jamieson and Tudhope (1970) (Equation 3.19) based on measurements of synthetic saline water for temperatures between $T = 0$ and 180°C and salinities between $S = 0$ and 160 psu is presented in this thesis. The accuracy of the prediction equation is ±3% (Jamieson and Tudhope, 1970; Sharqawy et al., 2010). Figure 3.9a shows the results of the prediction of (Equation 3.19) for four seawater salinities.

$$\log[\lambda_{sw}(T,S)] = \log(240+0.0002S)+0.434\left(2.3-\frac{343.5+0.037S}{T+273.15}\right)\left(1-\frac{T+273.15}{647+0.03S}\right)^{0.333} \tag{3.19}$$

where, λ_{sw} ($\mathrm{mW\,m^{-1}\,K^{-1}}$) is the thermal conductivity of seawater, and the model is valid for temperature (0 < T < 180°C) and salinity (0 < S < 160 psu).

As with the thermal conductivity, the specific heat of saline water decreases with

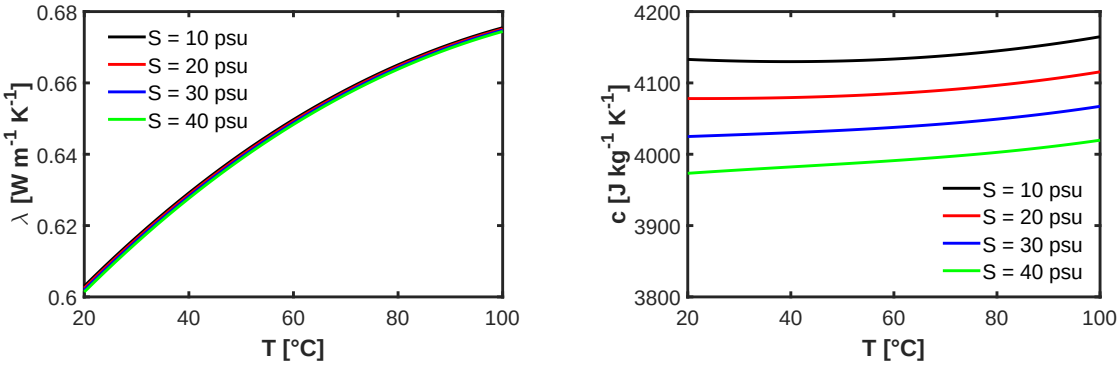

Figure 3.9: Thermal conductivity λ_{sw} a) and specific heat capacity c_{sw} b) of seawater at salinities $S = 10$, 20, 30 and 40 psu as a function of temperature.

an increase in the concentration of the dissolved salts (Jamieson et al., 1969; Sharqawy et al., 2010). The prediction equation given by Jamieson et al. (1969) (Equation 3.20) based on measurements of synthetic saline water for temperatures between $T = 0$ and 180°C and salinities between $S = 0$ and 180 psu is discussed in this thesis. The maximum deviation of the prediction equation is ±0.28% (Jamieson et al., 1969; Sharqawy et al., 2010). Figure 3.9b shows the results of the prediction of (Equation 3.20) for four seawater salinities.

$$c_{sw}(T,S) = A(S) + B(S)T + C(S)T^2 + D(S)T^3 \tag{3.20}$$

$$A(S) = 5.328 - 9.76 \times 10^{-2}S + 4.04 \times 10^{-4}S^2 \tag{3.21}$$

$$B(S) = -6.913 \times 10^{-3} + 7.351 \times 10^{-4}S - 3.15 \times 10^{-6}S^2 \tag{3.22}$$

$$C(S) = 9.6 \times 10^{-6} - 1.927 \times 10^{-6}S + 8.23 \times 10^{-9}S^2 \tag{3.23}$$

$$D(S) = 2.5 \times 10^{-9} + 1.666 \times 10^{-9}S - 7.125 \times 10^{-12}S^2 \tag{3.24}$$

where, c_{sw} ($\mathrm{kJ\,kg^{-1}\,K^{-1}}$) is the specific heat of seawater, and the model is valid for temperature (273.15 < T < 453.15 K) and salinity (0 < S < 180 psu).

3.4.3 Bitumen viscosity

Over the past decades, several models have been proposed to predict the viscosities of bitumen at different temperatures (Briggs et al., 1984; Puttagunta et al., 1993; Miadonye et al., 1994; Singh et al., 1994). A simplified and effective model for predicting the variation of bitumen viscosity with temperature was presented by Miadonye et al. (1994). Miadonye et al.'s model (Equation 3.25) is similar to the viscosity model of heavy oils and bitumens proposed by Briggs et al. (1984), and was formulated based on the principle of a curvilinear relationship between viscosity and temperature for unrefined oils.

$$\log(\mu_v) = \frac{b_v}{\left(1 + \frac{T-30}{303.15}\right)^{S_v}} + C_v \tag{3.25}$$

$$b_v = \log(\mu_{v,30}) - C_v \tag{3.26}$$

$$C_v = -3.0020 \tag{3.27}$$

$$S_v = 0.0066940 b_v + 3.5364 \tag{3.28}$$

where, μ_v ($\mathrm{Pa\,s}$) is the dynamic viscosity of the bitumen at temperature T (°C), b_v is the viscosity characterization parameter obtained from a single viscosity data of the particular bitumen or heavy oil at 30°C and one atmospheric pressure, $\mu_{v,30}$ ($\mathrm{Pa\,s}$) is the dynamic viscosity of the bitumen at 30°C, C_v is a constant and S_v is a measure of the variation of viscosity with temperature.

3.5 Summary of chapter 3

A detailed study on the behavior and structure of unsaturated soils and oil sands was presented. Moreover, the thermal and dielectric behavior of the constituent phases of both porous media types was discussed as part of the development of the semi-theoretical and numerical models which are discussed in the next chapters.

Chapter 4

Semi-theoretical thermo-dielectric modeling of porous media

4.1 Introduction

This chapter presents the theoretical study of the relationship between the thermal conductivity and complex dielectric permittivity of porous media. These two parameters govern the thermal and dielectric processes of porous media. On this basis, new theoretical models for the prediction of thermal conductivity of porous media (primarily naturally occurring unsaturated soils and bitumen-water saturated oil sands) deposits based on dielectric measurements are presented. Moreover, the variations of the thermo-dielectric (T-DE) parameters of porous media with matric suction, applied vertical stress and temperature are studied (as these factors play a key role in the thermo-dielectric behavior of porous media), and models predicting the water-driven settlement potential of unsaturated weak or loessy porous media based on thermo-dielectric measurements are presented.

4.2 Thermal conductivity prediction using dielectric measurements

The thermal conductivity and complex dielectric permittivity of soils and oil sands are highly correlated and are both affected by the changes in chemical composition, grain structure and hydro-mechanical conditions. The findings of several studies on the behavior of thermal conductivity and dielectric permittivity or electrical conductivity of porous media (independently and/or in combination), which have been carried out in the past (Archie, 1942; De Vries, 1963; Fragkogiannis et al., 2010; Logsdon et al., 2010), confirm the correlation between the two parameters. Although none of the

studies provide a direct theoretical correlation of the two parameters, the strong correlation between the parameters is vital in order to employ geophysical approaches such as HF-EM techniques (in the form of the complex dielectric permittivity) to monitor porous media thermal properties such as the thermal conductivity via theoretical modeling (Hailemariam et al., 2017). In this research, new theoretical models are developed and experimentally verified to provide a direct theoretical correlation between the two parameters.

The thermal conductivity and complex dielectric permittivity of porous media are key parameters for assessing porous media physical states, subsurface water and energy balances, unsaturated porous media mechanics and land-atmosphere interactions. Thermal conductivity occurs through both solid and liquid phases and to a lower extent through the gaseous phase of porous media. Moisture content has a most prominent effect on the thermal conductivity of porous media (Salomone and Kovacs, 1984; Salomone et al., 1984; Salomone and Marlowe, 1989). The thermal conductivity of porous media is also highly affected by changes in dry density (Salomone and Kovacs, 1984; Salomone et al., 1984; Salomone and Marlowe, 1989), mineral composition (Kersten, 1949; Salomone and Marlowe, 1989), freezing and thawing (Kersten, 1949; Penner et al., 1975; Salomone and Marlowe, 1989), solid matrix texture (Kersten, 1949; Salomone and Marlowe, 1989) and temperature (Mottaghy et al., 2008). Similarly, the complex dielectric permittivity of porous media is influenced by factors such as solid matrix texture and moisture content (Topp et al., 1980; Hilhorst, 2000; Wagner et al., 2011a), level of porous medium solution concentration (Shainberg et al., 1980), temperature (Wraith and Or, 1999) etc.

Experimental techniques for the precise determination of the effective thermal conductivity of porous media are difficult and usually time-consuming to conduct. Hence, several researchers have suggested empirical and semi-empirical porous media thermal conductivity prediction models relating the thermal conductivity to readily obtainable parameters such as moisture content, porosity, temperature, mineral content, pressure etc. (Farouki, 1981). However, the majority of these models are applicable only to selected types of soils/geo-materials, and moisture content is a primary input parameter. This approach has its limitations both in-situ and in laboratory applications, as the user is required to use methods of moisture measurement, which disturb the structure of the porous medium or to extract samples for moisture content measurement. This procedure is usually a time-consuming practice, and there are instances where it is not possible to extract samples for moisture measurement. A typical example would be a laboratory test that involves the application of stress on a porous medium, where the moisture content has a temporal variation. It is difficult

to predict or monitor the thermal conductivity of the porous medium throughout the test, as it would not be possible to extract samples or to insert a thermal conductivity measurement device inside the medium due to the application of stress. However, using a non-destructive dielectric measurement device, such as an open-ended coaxial line, where only the tip of the needle (with 2.2 mm dia) needs to be in contact with the porous medium, one can easily monitor the changes in the complex dielectric permittivity of the medium throughout the duration of the test. The obtained porous media complex dielectric permittivity data can then be used to predict the thermal conductivity of the porous medium using the correlation models presented in this study.

Unlike most of these thermal conductivity prediction models, the new theoretical models presented in this study do not require moisture content as an input parameter, thus providing the opportunity to obtain accurate estimation of thermal conductivity both in-situ and in the laboratory using dielectric measurement techniques only, avoiding soil disturbance or the need to extract samples for moisture content measurement. For large scale sub-surface thermal exploration purposes, spatial subsurface complex dielectric data over high depths and wide areas of oil sands or soil deposits can be obtained using non-destructive HF-EM measurement techniques such as GPR, to be used as an input for the thermal conductivity prediction models presented in this research. The GPR technique works by emitting HF-EM pulses (50 MHz - 1 GHz) from a transmitting antenna in to the ground. The dielectric permittivity of the sub-surface is then estimated by recording the time of travel of the emitted pulses via a receiving antenna. For laboratory and small scale in-situ measurements, complex dielectric permittivity measurement techniques such as an open-ended coaxial line with TDR or VNAs are typically employed.

4.2.1 Thermal conductivity prediction for naturally occurring soils

The model for predicting the thermal conductivity of two-phase/three-phase soils from complex dielectric permittivity measurement is obtained by combining a modified form of the Johansen's semi-empirical model of thermal conductivity (Equation 2.16) (Johansen, 1975) and the volume fraction (VF) model of complex dielectric permittivity (Equation 2.48) (Lichtenecker and Rother, 1931), which for naturally occurring soils can be rewritten as Equation 4.1 and Equations 4.2/ 4.3, respectively.

$$\lambda = (\lambda_{sat} - \lambda_d)\frac{\kappa(\theta/n)}{1 + (\kappa - 1)(\theta/n)} + \lambda_d \tag{4.1}$$

$$\varepsilon_{r,eff}^{*a} = V_s \varepsilon_{r,g}^{*a} + V_a \varepsilon_{r,a}^{*a} + V_w \varepsilon_{r,w}^{*a} \tag{4.2}$$

$$\varepsilon_{r,eff}^{\prime a} = (1-n)\varepsilon_{r,g}^{\prime a} + (n-\theta) + \theta \varepsilon_{r,w}^{\prime a} \tag{4.3}$$

where, λ ($\mathrm{W\,m^{-1}\,K^{-1}}$) is the effective thermal conductivity of the soil, λ_{sat} and λ_d ($\mathrm{W\,m^{-1}\,K^{-1}}$) are the thermal conductivities of the soil in saturated and dry states, respectively, κ is the soil texture dependent parameter of Côté and Konrad (2005) model (with values of 4.60, 3.55, 1.90 and 0.60 for gravel and coarse sands, medium and fine sands, silty & clayey soils and for organic soils in unfrozen state, respectively), n is the soil porosity, θ is the soil volumetric water content, V_s, V_a and V_w are the volumetric fractions of the solids, air and water constituent phases of the soil, respectively, $\varepsilon_{r,eff}^{*}$ is the relative effective complex permittivity of the soil, $\varepsilon_{r,g}^{*}$, $\varepsilon_{r,a}^{*}$ and $\varepsilon_{r,w}^{*}$ are the relative complex permittivities of the solid grains, air and water constituent phases of the soil, respectively, structural exponent $a = 1/2$ (CRIM) (Birchak et al., 1974), $\varepsilon_{r,eff}^{\prime}$ is the real part of the relative effective complex permittivity of the soil and $\varepsilon_{r,g}^{\prime}$, $\varepsilon_{r,a}^{\prime} = 1$ and $\varepsilon_{r,w}^{\prime}$ are the real parts of the relative complex permittivities of the solid grains, air and water constituent phases of the soil, respectively. In Equation 4.1, the Kersten's number of Johansen's model (Equation 2.17) has been replaced by the Kersten's function suggested by Côté and Konrad (Equation 2.21), in order to rectify its limitations for predicting thermal conductivities of soils with a degree of saturation lower than 20% (Hailemariam et al., 2017).

Equation 4.3 can be rewritten in terms of the volumetric water content θ as:

$$\theta = \frac{\varepsilon_{r,eff}^{\prime a} - (1-n)\varepsilon_{r,g}^{\prime a} - n}{\varepsilon_{r,w}^{\prime a} - 1} \tag{4.4}$$

The effective thermal conductivity model (at room temperature of 20°C), which is independent of moisture content, is thus obtained by substituting the value of θ from Equation 4.4 in to Equation 4.1 as:

$$\lambda = (\lambda_{sat} - \lambda_d) \frac{\kappa \left[\frac{\varepsilon_{r,eff}^{\prime a} - (1-n)\varepsilon_{r,g}^{\prime a} - n}{n(\varepsilon_{r,w}^{\prime a} - 1)} \right]}{1 + (\kappa - 1) \left[\frac{\varepsilon_{r,eff}^{\prime a} - (1-n)\varepsilon_{r,g}^{\prime a} - n}{n(\varepsilon_{r,w}^{\prime a} - 1)} \right]} + \lambda_d \tag{4.5}$$

Moreover, the thermal conductivities of the soil in dry and saturated states as well as of the solid particles are obtained as $\lambda_d = (0.135\rho_d + 64.7)/(\rho_s - 0.947\rho_d)$, $\lambda_{sat} = \lambda_s^{(1-n)}\lambda_w^n$ and $\lambda_s = \lambda_q^{q_f}\lambda_o^{(1-q_f)}$ ($\mathrm{W\,m^{-1}\,K^{-1}}$), respectively (Johansen, 1975). ρ_d ($\mathrm{kg\,m^{-3}}$)

is the soil bulk dry density and ρ_s ($\mathrm{kg\,m^{-3}}$) is the density of soil solid particles. And the real part of the relative complex permittivity of the solid grains can be calculated based on the specific gravity of the solid grain particles using Equation 3.1 (Dobson et al., 1985) as $\varepsilon'_{r,g} = (1.01 + 0.44G_s)^2 - 0.062$.

The model is valid for the full range of soil saturation and takes in to account the mineral composition, soil structure and the three-phase form. The model is also sensitive to frequency changes in the complex dielectric permittivity analysis in the form of $\varepsilon'_{r,eff}$, $\varepsilon'_{r,g}$ and $\varepsilon'_{r,w}$ of Equations 4.4 and 4.5. In this study, the values at 1 GHz frequency only are considered. At this frequency range, information on the free water in the porous medium can be obtained, and the dispersion and absorption processes can be compared directly (Blonquist Jr. et al., 2006; Wagner and Scheuermann, 2009; Wagner et al., 2014).

For a typical silty-clay soil with specific gravity of solid particles $G_s = 2.655$ (taken as the average of the silty-clay soils used in this study, section 6.2.1.1), $\varepsilon'_{r,g} = 4.683$ (Equation 3.1), $\varepsilon'_{r,w} = 80$ (at 1 GHz) (Hailemariam et al., 2017), structural exponent $a = 1/2$, Equations 4.4 and 4.5 can be simplified as:

$$\theta = 0.126\varepsilon'^{0.5}_{r,eff} + 0.147n - 0.272 \tag{4.6}$$

$$\lambda = (\lambda_{sat} - \lambda_d)\frac{\kappa\left(\frac{0.126\varepsilon'^{0.5}_{r,eff}+0.147n-0.272}{n}\right)}{1+(\kappa-1)\left(\frac{0.126\varepsilon'^{0.5}_{r,eff}+0.147n-0.272}{n}\right)} + \lambda_d \tag{4.7}$$

4.2.2 Thermal conductivity prediction for bitumen-water saturated oil sands

The new model for predicting the thermal conductivity of bitumen-water saturated oil sands from complex dielectric permittivity measurement is obtained by combining the volume fraction (VF) models for thermal conductivity (Equation 2.13) (Lichtenecker and Rother, 1931; Yun and Santamarina, 2007) and complex dielectric permittivity (Equation 2.48) (Lichtenecker and Rother, 1931), which for bitumen-water saturated oil sands can be rewritten as Equations 4.8/ 4.9 and Equations 4.10/ 4.11, respectively. The VF models are selected in our study due to their simple structure, accuracy of prediction and wide range of applicability.

$$\lambda = \left[V_s\lambda_s^s + V_b\lambda_b^s + V_w\lambda_w^s\right]^{1/s} \tag{4.8}$$

$$\lambda = \left[(1-n)\lambda_s^s + (n-\theta)\lambda_b^s + \theta\lambda_w^s\right]^{1/s} \tag{4.9}$$

$$\varepsilon_{r,eff}^{*a} = V_s\varepsilon_{r,g}^{*a} + V_b\varepsilon_{r,b}^{*a} + V_w\varepsilon_{r,w}^{*a} \tag{4.10}$$

$$\varepsilon_{r,eff}^{\prime a} = (1-n)\varepsilon_{r,g}^{\prime a} + (n-\theta)\varepsilon_{r,b}^{\prime a} + \theta\varepsilon_{r,w}^{\prime a} \tag{4.11}$$

where, λ ($\mathrm{W\,m^{-1}\,K^{-1}}$) is the effective thermal conductivity of the oil sand, λ_s, λ_b and λ_w ($\mathrm{W\,m^{-1}\,K^{-1}}$) are the thermal conductivities of the solids, bitumen and water constituent phases of the oil sand, respectively, V_s, V_b and V_w are the volumetric fractions of the solids, bitumen and water constituent phases of the oil sand, respectively, coefficient $s = -0.25$, n is the porosity of the oil sand, θ is the volumetric water content of the oil sand, $\varepsilon_{r,eff}^{*}$ is the relative effective complex permittivity of the oil sand, $\varepsilon_{r,g}^{*}$, $\varepsilon_{r,b}^{*}$ and $\varepsilon_{r,w}^{*}$ are the relative complex permittivities of the solid grains, bitumen and water constituent phases of the oil sand, respectively, structural exponent $a = 1/2$ (CRIM) (Birchak et al., 1974), $\varepsilon_{r,eff}^{\prime}$ is the real part of the relative effective complex permittivity of the oil sand, and $\varepsilon_{r,g}^{\prime}$, $\varepsilon_{r,b}^{\prime}$ and $\varepsilon_{r,w}^{\prime}$ are the real parts of the relative complex permittivities of the solid grains, bitumen and water constituent phases of the oil sand, respectively.

It should be noted that the geometric mean (GM) model, which is typically used to model thermal conductivity of porous media with multiple constituent phases, cannot be used for predicting the thermal conductivity of oil sands with good accuracy, and hence has not been used in the development of the new thermal-dielectric correlation model of oil sands in this study. The GM model gives satisfactory results for water saturated porous media, where the ratio of the thermal conductivities of the solid grains to the saturating fluid (in this case water) $\lambda_s/\lambda_f < 15$ (Côté and Konrad, 2005; Hailemariam et al., 2016), but significantly overestimates the thermal conductivity of dry porous media, where the ratio of the thermal conductivities of the solid grains to the saturating fluid (in this case air) $\lambda_s/\lambda_f > 100$ (Johansen, 1975; Farouki, 1981; Hailemariam et al., 2016), and to a lower extent oil saturated porous media, where the ratio of the thermal conductivities of the solid grains to the saturating fluid (in this case bitumen) $\lambda_s/\lambda_f > 15$. Hence the VF model suggested by Yun and Santamarina (2007), which provides a better accuracy for the prediction of effective thermal conductivity of porous media with a higher λ_s/λ_f ratio is selected.

Equation 4.11 can be rewritten in terms of the volumetric water content θ as:

$$\theta = \frac{\varepsilon'^{a}_{r,eff} - (1-n)\varepsilon'^{a}_{r,g} - n\varepsilon'^{a}_{r,b}}{\varepsilon'^{a}_{r,w} - \varepsilon'^{a}_{r,b}} \tag{4.12}$$

The effective thermal conductivity model (at room temperature of 20°C), which is independent of moisture content, is thus obtained by substituting the value of θ from Equation 4.12 in to Equation 4.9 as:

$$\lambda = \left[(1-n)\lambda_s^s + \left(n - \frac{\varepsilon'^{a}_{r,eff} - (1-n)\varepsilon'^{a}_{r,g} - n\varepsilon'^{a}_{r,b}}{\varepsilon'^{a}_{r,w} - \varepsilon'^{a}_{r,b}}\right)\lambda_b^s + \left(\frac{\varepsilon'^{a}_{r,eff} - (1-n)\varepsilon'^{a}_{r,g} - n\varepsilon'^{a}_{r,b}}{\varepsilon'^{a}_{r,w} - \varepsilon'^{a}_{r,b}}\right)\lambda_w^s\right]^{1/s} \tag{4.13}$$

Furthermore, the thermal conductivity of the solid grains can be calculated based on the volumetric quartz fraction using Equation 2.18 (Johansen, 1975) as $\lambda_s = \lambda_q^{q_f}\lambda_o^{(1-q_f)}$, and the real part of the relative complex permittivity of the solid grains can be calculated based on the specific gravity of the solid grain particles using Equation 3.1 (Dobson et al., 1985) as $\varepsilon'_{r,g} = (1.01 + 0.44G_s)^2 - 0.062$.

The model is valid for the full range of bitumen-water saturation and takes in to account the mineral composition, oil sand structure and the three-phase oil sand form. The model is also sensitive to frequency changes in the complex dielectric permittivity analysis in the form of $\varepsilon'_{r,eff}$, $\varepsilon'_{r,g}$, $\varepsilon'_{r,b}$ and $\varepsilon'_{r,w}$ of Equations 4.12 and 4.13. In this study, the values at 1 GHz frequency only are considered.

For a typical oil sand with specific gravity of solid particles $G_s = 2.67$ (taken from the oil sand used in this study, section 6.2.2), $\varepsilon'_{r,g} = 4.71$ (Equation 3.1), $\varepsilon'_{r,w} = 80$ (at 1 GHz) (Hailemariam et al., 2017), $\varepsilon'_{r,b} = 2.5$ (Rambabu et al., 2011; Oloumi and Rambabu, 2016), structural exponent $a = 1/2$, $\lambda_b = 0.126\,\mathrm{W\,m^{-1}\,K^{-1}}$ (at 20°C) (American Petroleum Institute, 1997), $\lambda_w = 0.594\,\mathrm{W\,m^{-1}\,K^{-1}}$ (at 20°C) (Hailemariam et al., 2017) and coefficient $s = -0.25$, Equations 4.12 and 4.13 can be simplified as:

$$\theta = 0.136\varepsilon'^{0.5}_{r,eff} + 0.08n - 0.295 \tag{4.14}$$

$$\lambda = \left[(1-n)\lambda_s^{-0.25} - 0.073\varepsilon'^{0.5}_{r,eff} + 1.635n + 0.159\right]^{-4} \tag{4.15}$$

The main sources of error (uncertainties) in the use of the new model to predict the thermal conductivity from dielectric measurements are due to: the precision and calibration procedure of the employed electromagnetic device (TDR, VNA, GPR etc.), types of coaxial cables used, inversion algorithms (if any) and high porous medium

grain sizes (as in porous media with high coarse grain fraction) when an open-ended coaxial probe is used.

4.3 Effect of matric suction on the porous media thermo-dielectric parameters

Unsaturated porous media behavior is mainly characterized by the study of the soil-water characteristic curve (SWCC) (Fredlund and Rahardjo, 1993; Fredlund and Xing, 1994). The SWCC for a porous media is defined as the relationship between water content and suction (Williams, 1982). The water content quantifies the amount of water contained within the pores of the porous medium, whereas the suction may be either the matric suction (also called capillary pressure) or the total suction (i.e. matric + osmotic suction).

Due to its importance in unsaturated porous media behavior, numerous researchers have proposed empirical equations to simulate the SWCC (Brooks and Corey, 1964; Campbell, 1974; van Genuchten, 1980; Williams et al., 1983; McKee and Bumb, 1984). Due to the empirical nature of these equations, they can only be used for a particular group of porous media. Fredlund and Xing (1994) proposed a general theoretical equation with the form of an integrated frequency distribution curve for the SWCC of sand, silt and clay soils over the entire suction range using a nonlinear, least-squares computer program to obtain the best-fit parameters of literature data. Due to its simplicity and wide range of application, the Fredlund and Xing model is used in this thesis to establish the dependency of the thermo-dielectric porous media parameters on matric suction.

4.3.1 Variation of thermal conductivity of naturally occurring soils with matric suction

The new model for predicting the effect of matric suction on the thermal conductivity of naturally occurring soils (Equation 4.16) under drying or desorption process is obtained by replacing the volumetric water content term of the modified Johansen (1975) model (Equation 4.1) with its equivalent from the Fredlund and Xing (1994) model as shown by Equation 4.19.

$$\lambda(\psi_m) = (\lambda_{sat} - \lambda_d)\frac{\kappa[\theta(\psi_m)/n]}{1 + (\kappa - 1)[\theta(\psi_m)/n]} + \lambda_d \tag{4.16}$$

$$\lambda_{sat} = \lambda_s^{(1-n)}\lambda_w^n; \lambda_s = \lambda_q^{q_f}\lambda_o^{(1-q_f)} \tag{4.17}$$

$$\lambda_d = \frac{0.135\rho_d + 64.7}{\rho_s - 0.947\rho_d} \tag{4.18}$$

$$\theta(\psi_m) = n\left\{\frac{1}{\ln[\exp + (\psi_m/p_1)^{p_2}]}\right\}^{p_3} \tag{4.19}$$

where, λ ($\mathrm{W\,m^{-1}\,K^{-1}}$) is the matric suction ψ_m dependent effective thermal conductivity, λ_{sat} and λ_d ($\mathrm{W\,m^{-1}\,K^{-1}}$) are the saturated and dry thermal conductivities of the soil, respectively, κ is the soil texture dependent parameter of Côté and Konrad (2005) model, θ, ψ_m (kPa), n and ρ_d ($\mathrm{kg\,m^{-3}}$) are the volumetric water content, matric suction, porosity and bulk dry density, respectively, ρ_s ($\mathrm{kg\,m^{-3}}$) is the density of the solid particles of the soil, λ_s, λ_w, λ_q and λ_o ($\mathrm{W\,m^{-1}\,K^{-1}}$) are thermal conductivities of the solids, water, quartz and minerals other than quartz, respectively, q_f is the volumetric quartz fraction, and p_1, p_2 and p_3 are three soil type dependent parameters of the Fredlund and Xing (1994) model. Parameter p_1 is closely related to the air-entry value (AEV) of the soil, and can be assumed to be equal to the AEV of the soil when the value of parameter p_3 is small (Fredlund and Xing, 1994). Parameters p_2 and p_3 represent the slopes of the main SWCC (desorption curve) and the SWCC at high matric suction range, respectively.

4.3.2 Variation of dielectric permittivity of naturally occurring soils with matric suction

The new model for predicting the effect of matric suction on the complex dielectric permittivity of naturally occurring soils (Equation 4.20) under drying or desorption process is obtained by replacing the volumetric water content term of the volume fraction (VF) model of complex dielectric permittivity (Equation 4.3) (Lichtenecker and Rother, 1931) with its equivalent from the Fredlund and Xing (1994) model as shown by Equation 4.19.

$$\varepsilon_{r,eff}'^{a}(\psi_m) = (1-n)\varepsilon_{r,g}'^{a} + [n - \theta(\psi_m)] + \theta(\psi_m)\varepsilon_{r,w}'^{a} \tag{4.20}$$

where, $\varepsilon'_{r,eff}$ is the matric suction ψ_m dependent real part of the relative effective complex permittivity of the soil, θ and n are the volumetric water content and porosity of the soil, respectively, structural exponent $a = 1/2$ (CRIM) (Birchak et al., 1974),

$\varepsilon'_{r,g} = (1.01 + 0.44G_s)^2 - 0.062$ (Dobson et al., 1985) and $\varepsilon'_{r,w}$ are the real parts of the relative complex permittivities of the solid grains and water constituent phases of the soil, respectively.

4.4 Effect of stress on the porous media thermo-dielectric parameters

The effective stress applied over porous media governs the major heat and electromagnetic wave propagation paths as well as the inter-particle contact condition, by inducing changes in the internal structure or fabric of porous media (Choo et al., 2013; Hailemariam et al., 2015a). Nevertheless, the vital role of stress in the heat flow and EM wave propagation of porous media has not been given adequate attention, as compared to the other commonly studied governing porous media index properties (Kersten, 1949; Penner et al., 1975; Shainberg et al., 1980; Topp et al., 1980; Salomone and Kovacs, 1984; Salomone et al., 1984; Salomone and Marlowe, 1989; Hilhorst, 2000; Fragkogiannis et al., 2010; Logsdon et al., 2010; Wagner et al., 2011a), which are readily incorporated in the empirical and semi-empirical correlations and theoretical mixture models.

Previous studies have shown that stress facilitates heat flow (thermal behavior) in porous media by increasing the inter-particle contact area, but can have opposite effects on the EM wave propagation (dielectric behavior) based on the state of the porous media (Hailemariam et al., 2015a), i.e. an increase in the effective complex dielectric permittivity in dry or unsaturated conditions due to a reduction in porosity and improved inter-particle contact upon the application of stress, and a reduction in the effective complex dielectric permittivity in saturated condition mainly due to the expulsion of pore-water during consolidation (Tehranian et al., 1994; Vargas and McCarthy, 2002; Demirci et al., 2004; Weidenfeld et al., 2004; Abuel-Naga et al., 2008; Abdulagatova et al., 2009; Choo et al., 2013; Lin and Cerato, 2013). Although the studies provide a good insight in to the behavior of porous media under the influence of stress, most of them fail to give a simplified theoretical approach for quantifying the thermal and dielectric parameters in terms of the effective stress imposed on the medium. The experimentally verified theoretical models presented in this study aim to provide a direct correlation between the thermo-dielectric parameters of porous media and the applied effective stress.

4.4.1 Variation of thermal conductivity of naturally occurring soils with stress

The new model for predicting the effect of applied effective stress on the thermal conductivity of naturally occurring soils (Equation 4.21) is obtained by introducing the coefficient of primary compressibility index of soils under drained one-dimensional loading C_c to the parameters of the modified Johansen (1975) model (Equation 4.1), as shown by Equations 4.22 - 4.29.

$$\lambda(\sigma') = [\lambda_{sat}(\sigma') - \lambda_d(\sigma')]\frac{\kappa[\theta(\sigma')/n(\sigma')]}{1 + (\kappa - 1)[\theta(\sigma')/n(\sigma')]} + \lambda_d(\sigma') \tag{4.21}$$

$$\lambda_{sat}(\sigma') = \lambda_s^{[1-n(\sigma')]}\lambda_w^{n(\sigma')}; \lambda_s = \lambda_q^{q_f}\lambda_o^{(1-q_f)} \tag{4.22}$$

$$\lambda_d(\sigma') = \frac{0.135\rho_d(\sigma') + 64.7}{\rho_s - 0.947\rho_d(\sigma')} \tag{4.23}$$

$$\Delta e = C_c[\log(\sigma'_o + \Delta\sigma') - \log\sigma'_o] = C_c \log\left(\frac{\sigma'_o + \Delta\sigma'}{\sigma'_o}\right) \tag{4.24}$$

$$e(\sigma') = e_o - \Delta e = e_o - C_c \log\left(\frac{\sigma'_o + \Delta\sigma'}{\sigma'_o}\right) \tag{4.25}$$

$$n(\sigma') = \frac{e(\sigma')}{1 + e(\sigma')} = \frac{e_o - C_c \log\left(\frac{\sigma'_o+\Delta\sigma'}{\sigma'_o}\right)}{1 + e_o - C_c \log\left(\frac{\sigma'_o+\Delta\sigma'}{\sigma'_o}\right)} = \frac{\frac{n_o}{1-n_o} - C_c \log\left(\frac{\sigma'_o+\Delta\sigma'}{\sigma'_o}\right)}{1 + \frac{n_o}{1-n_o} - C_c \log\left(\frac{\sigma'_o+\Delta\sigma'}{\sigma'_o}\right)} \tag{4.26}$$

$$w_o = \frac{\theta_o}{G_s(1 - n_o)} \tag{4.27}$$

$$\theta(\sigma') = \begin{cases} \frac{w_o G_s n(\sigma')}{e(\sigma')} = w_o G_s[1 - n(\sigma')] = \frac{\theta_o[1-n(\sigma')]}{1-n_o}, & \text{if } n(\sigma') > \frac{w_o G_s}{1+w_o G_s} \\ n(\sigma'), & \text{if } n(\sigma') \leq \frac{w_o G_s}{1+w_o G_s} \end{cases} \tag{4.28}$$

$$\rho_{do} = \left[\frac{G_s}{1 + e_o}\right]1000; \rho_d(\sigma') = \left[\frac{G_s}{1 + e(\sigma')}\right]1000 \tag{4.29}$$

where, λ, λ_{sat} and λ_d ($\mathrm{W\,m^{-1}\,K^{-1}}$) are the stress dependent effective, saturated and dry thermal conductivities of the soil after an increment of an applied effective stress of $\Delta\sigma'$ (kPa), respectively, κ is the soil texture dependent parameter of Côté and Konrad (2005) model, θ, n, e and ρ_d ($\mathrm{kg\,m^{-3}}$) are the stress dependent volumetric water content, porosity, void ratio and bulk dry density, respectively, θ_o, n_o, e_o, w_o and ρ_{do} ($\mathrm{kg\,m^{-3}}$) are the volumetric water content, porosity, void ratio, gravimetric water content and bulk dry density before the application of the effective stress increment $\Delta\sigma'$ or at the initial stress condition of σ'_o ($> 1\,\mathrm{kPa}$), respectively, Δe is the reduction in void ratio of the soil due to the application of the stress increment $\Delta\sigma'$, C_c is the primary compressibility index of the soil, G_s and ρ_s ($\mathrm{kg\,m^{-3}}$) are the specific gravity and density of the solid particles of the soil, respectively, λ_s, λ_w, λ_q and λ_o ($\mathrm{W\,m^{-1}\,K^{-1}}$) are thermal conductivities of the solids, water, quartz and minerals other than quartz, respectively and q_f is the volumetric quartz fraction.

The first case of Equation 4.28 represents dry or unsaturated soil conditions upon drained one-dimensional loading, whereas the second case applies for saturated soils or for unsaturated soils where all the entrapped air has been removed and have just reached saturated conditions upon drained one-dimensional loading. It should be noted that the latter case is associated with the removal of pore-water from the soil (consolidation) and hence the gravimetric water content of the soil will gradually start to decrease.

The compressibility of soils in general and clays in particular is affected by several factors such as mineralogical properties, soil plasticity, texture, pore-water behavior, cementation, loading history, over-consolidation ratio, natural water content etc. On this basis, several researchers have correlated the compressibility characteristics of soils (in the form of the compressibility index C_c) with various soil properties such as liquid limit, natural moisture content, initial in-situ void ratio, dry unit weight, plasticity index, void ratio at liquid limit etc. (Nishida, 1956; Sridharan and Nagaraj, 2000; Gunduz and Arman, 2007; Widodo and Ibrahim, 2012; Hailemariam et al., 2015a), and hence a respresentative compressibility index C_c value for most soil types is readily obtainable from the extensive research and available databases.

4.4.2 Variation of dielectric permittivity of naturally occurring soils with stress

The new model for predicting the effect of applied effective stress on the complex dielectric permittivity of naturally occurring soils (Equation 4.30) is obtained by introducing the coefficient of primary compressibility index of soils under drained one-dimensional loading C_c to the parameters of the volume fraction (VF) model of complex dielectric permittivity (Equation 4.3) (Lichtenecker and Rother, 1931), as shown by Equations 4.24 - 4.28.

$$\varepsilon_{r,eff}'^{a}(\sigma') = [1 - n(\sigma')]\varepsilon_{r,g}'^{a} + [n(\sigma') - \theta(\sigma')] + \theta(\sigma')\varepsilon_{r,w}'^{a} \tag{4.30}$$

where, $\varepsilon'_{r,eff}$ is the stress dependent real part of the relative effective complex permittivity of the soil after an increment of an applied effective stress of $\Delta\sigma'$ (kPa), θ and n are the stress dependent volumetric water content and porosity of the soil, respectively, structural exponent $a = 1/2$ (CRIM) (Birchak et al., 1974), $\varepsilon'_{r,g} = (1.01 + 0.44G_s)^2 - 0.062$ (Dobson et al., 1985) and $\varepsilon'_{r,w}$ are the real parts of the relative complex permittivities of the solid grains and water constituent phases of the soil, respectively.

4.5 Correlation between thermal, dielectric and water-driven settlement behavior of weak porous media

In this section, the tripartite correlation between the thermal conductivity, dielectric permittivity and water-driven settlement potential of weak loessy soils is theoretically studied, and based on the strong correlation between the three parameters, models for predicting the settlement potential of weak soils from thermal or dielectric measurements are suggested.

Weak or loessy or collapsible porous media are those that appear to be stable in their natural state (normally dry condition), but rapidly deform under water saturation (wetting), thus generating large and often unexpected settlements yielding disastrous consequences for structures unwittingly built over them. These porous media deposits usually exist at or dry state as they are mainly found in arid and semi-arid regions of the world. The focus of this study is on dry un-cemented weak soils which may be remolded (i.e. laboratory reconstituted) or found in an undisturbed state in nature. The triggering mechanism for the water-driven settlement in

weak soils is mainly attributed to the weakening or softening of a portion of the fine-grained soil fraction, which exist as a bonding material for the larger-grained particles (Casagrande, 1932), and also due to the loss of strength due to a reduction in the matric suction as a result of wetting (Fredlund and Gan, 1995). The matric potential of a soil is a measure of the bonding forces between water and soil. The degree of saturation and the amount of total suction are primarily used to describe the hydraulic water conditions (soil-water characteristic curve - SWCC). Furthermore, the SWCC is an important tool in the study of the complex physiochemical behavior of most naturally occurring unsaturated soils (Fredlund and Rahardjo, 1993).

Casagrande (1932) has shown that a part of the fine-grained fraction of most weak soils exist as a bonding material for the coarse-grained particles, and that these bonds naturally undergo local compression in the small gaps between adjacent grains resulting in the development of strength of the soil (Figure 4.1). When the loaded soil is exposed to moisture, and a certain critical moisture content is reached, the fine silt or clay bridges that are holding the coarser-grained particles soften, weaken and/or dissolve to some extent. Gradually, the binders reach a stage where they no longer resist deformation forces and the structure collapses (Kafle et al., 2014; Hailemariam et al., 2015b).

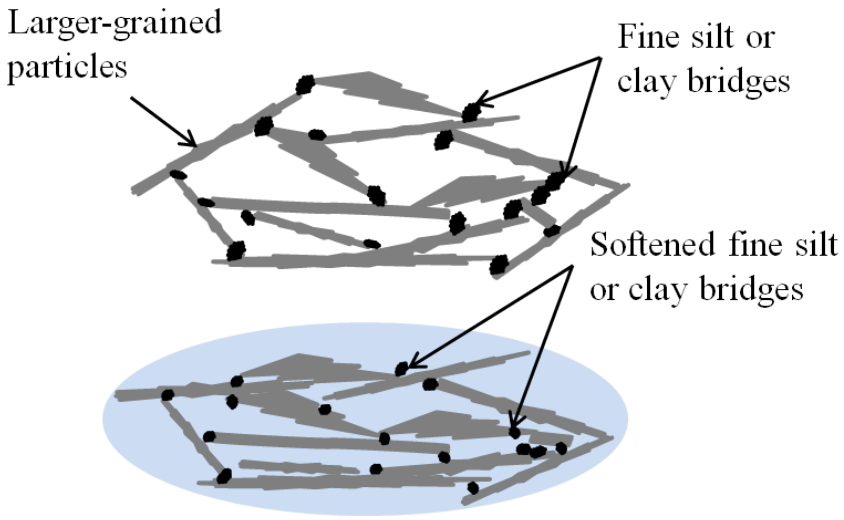

Figure 4.1: Meso-structure of a hydro-collapsible soil in a dry state (top) and after settlement triggered by water inundation (bottom).

The microscopic behavior of un-cemented weak soils is governed by the presence of minerals such as tecosilicates, mica and clay minerals of smectite, kaolinite and chlorite. The shear strength and volume change in terms of the observed macroscopic behavior of the individual clay platelets are predominantly governed by surface physiochemical forces, rather than the gravitational forces (Lin and Cerato, 2013). This is attributed their small texture and the diffuse double layer formed around the clay

platelets. The comprehensive study of the thermal and electromagnetic properties of weak soils can provide a good platform to explain microscopic mechanisms of water-driven settlement and a tool to quantify the settlement during wetting due to physio-chemical forces.

Howayek et al. (2011) and Ayadat and Hanna (2012) conducted a comprehensive review of the existing techniques for the identification of weak soils and the estimation of their associated water-driven settlement upon wetting. As indicated in their studies, majority of the existing settlement prediction models use moisture content as the primary input parameter. However, this technique has major limitations in practical in-situ and laboratory applications, due to the need for soil extraction or the use of moisture measurement techniques which usually disturb the soil structure. And in the case where samples have to be collected from great sub-surface depths, this procedure becomes time consuming and un-economic. As a solution to these aforementioned limitations, new prediction models for the water-driven settlement of weak soils based on thermal or dielectric soil measurements are proposed in this study, and the accuracy of the models is assessed by performing water-driven settlement tests on a collapsible soil. The new models do not require moisture content as an input parameter, and hence provide the opportunity to estimate the water-driven settlement of weak soils with little or no disturbance using soil thermal or dielectric data.

4.5.1 Settlement prediction using thermal conductivity

The water-driven settlement prediction models of weak soils presented in this study are developed by modifying the moisture content dependent model suggested by Minkov et al. (1977), due to its simplicity and accuracy of prediction. The Minkov et al. model (Equation 4.31) predicts the water-driven settlement potential $\delta_{np,3}$ of weak soils at a stress level of $3\,\mathrm{kg\,cm^{-2}}$ ($300\,\mathrm{kPa}$). The particular stress level of $300\,\mathrm{kPa}$ is a representative stress state for weak soils, as the maximum water-driven settlement potential of most weak soils occurs at stress levels between 200 and $400\,\mathrm{kPa}$ (see results and discussion in section 7.2.2.4).

$$\delta_{np,3} = 100K(n - 0.4)(0.3 - w) \tag{4.31}$$

where, $\delta_{np,3} = \Delta h/h_o$ is the water-driven settlement potential of the weak soil (Δh, m, is the change in soil height due to wetting and h_0, m, is the initial height of the soil), n is the soil porosity, w is the gravimetric water content of the soil and K is a soil

texture constant with values of 0.02, 0.03, 0.05, 0.08 and 0.09 for loessy sand, sandy loess, typical loess, clayey loess and loessy clay, respectively. According to the model, in order for a water-driven settlement to occur, the porosity and gravimetric water content of the weak soil should be greater than 0.4 and less than 0.3, respectively. This condition is in agreement with previous findings (Feda, 1966; Jennings and Knight, 1975), and illustrates the fact that weak soils are more susceptible to subsidence when they are in a loose state and with a low moisture content.

The model for obtaining the water-driven settlement of weak soils from thermal conductivity measurement is obtained by eliminating the moisture content term of the Minkov et al. model (Equation 4.31) by its equivalent from the modified Johansen (1975) model (Equation 4.1). The modified Johansen's model can be rewritten in terms of the volumetric water content θ as:

$$\theta = \frac{n(\lambda - \lambda_d)}{\kappa(\lambda_{sat} - \lambda_d) - (\kappa - 1)(\lambda - \lambda_d)} \tag{4.32}$$

Since $w = \theta/[G_s(1-n)]$, Equation 4.32 can be expressed in terms of the gravimetric water content w of the soil as:

$$w = \frac{n(\lambda - \lambda_d)}{\kappa G_s(1-n)(\lambda_{sat} - \lambda_d) - G_s(1-n)(\kappa - 1)(\lambda - \lambda_d)} \tag{4.33}$$

The settlement potential model which is independent of moisture content, is thus obtained by substituting the value of w from Equation 4.33 in to Equation 4.31 as:

$$\delta_{np,3} = 100K(n - 0.4)\left[0.3 - \frac{n(\lambda - \lambda_d)}{\kappa G_s(1-n)(\lambda_{sat} - \lambda_d) - G_s(1-n)(\kappa - 1)(\lambda - \lambda_d)}\right] \tag{4.34}$$

where, $\delta_{np,3}$ is the settlement potential, n is the soil porosity, K is a soil texture constant of the Minkov et al. (1977) model, λ ($\mathrm{W\,m^{-1}\,K^{-1}}$) is the measured thermal conductivity, G_s is the specific gravity of the solid particles, κ is the soil texture dependent parameter of the Côté and Konrad (2005) model. Furthermore, the thermal conductivities of the weak soil in dry and saturated states as well as of the solid particles are obtained as $\lambda_d = (0.135\rho_d + 64.7)/(\rho_s - 0.947\rho_d)$, $\lambda_{sat} = \lambda_s^{(1-n)}\lambda_w^n$ and $\lambda_s = \lambda_q^{q_f}\lambda_o^{(1-q_f)}$ ($\mathrm{W\,m^{-1}\,K^{-1}}$), respectively (Johansen, 1975). ρ_d ($\mathrm{kg\,m^{-3}}$) is the soil bulk dry density and ρ_s ($\mathrm{kg\,m^{-3}}$) is the density of soil solid particles. The model is valid for $n > 0.4$ and the full range of soil saturation, and can also be used to estimate the progress (reduction) of the settlement potential of a weak soil upon wetting (i.e. via an increase in the measured thermal conductivity λ of the weak soil upon wetting in Equation 4.34).

4.5.2 Settlement prediction using dielectric permittivity

The new model for obtaining the water-driven settlement of weak soils from complex dielectric permittivity measurement is obtained by eliminating the moisture content term of the Minkov et al. model (Equation 4.31) by its equivalent from the volume fraction (VF) model of complex dielectric permittivity (Equation 4.4) (Lichtenecker and Rother, 1931). Since $w = \theta/[G_s(1-n)]$, Equation 4.4 can be expressed in terms of the gravimetric water content w of the soil as:

$$w = \frac{\varepsilon_{r,eff}'^{a} - (1-n)\varepsilon_{r,g}'^{a} - n}{G_s(1-n)(\varepsilon_{r,w}'^{a} - 1)} \tag{4.35}$$

The settlement potential model which is independent of moisture content, is thus obtained by substituting the value of w from Equation 4.35 in to Equation 4.31 as:

$$\delta_{np,3} = 100K(n-0.4)\left[0.3 - \frac{\varepsilon_{r,eff}'^{a} - (1-n)\varepsilon_{r,g}'^{a} - n}{G_s(1-n)(\varepsilon_{r,w}'^{a} - 1)}\right] \tag{4.36}$$

where, $\delta_{np,3}$ is the settlement potential, n is the soil porosity, K is a soil texture constant of the Minkov et al. (1977) model, $\varepsilon'_{r,eff}$ is the measured real part of the relative effective complex permittivity of the weak soil, G_s is the specific gravity of the solid particles, structural exponent $a = 1/2$ (CRIM) (Birchak et al., 1974), $\varepsilon'_{r,g} = (1.01 + 0.44G_s)^2 - 0.062$ (Dobson et al., 1985) and $\varepsilon'_{r,w}$ are the real parts of the relative complex permittivities of the solid grains and water constituent phases of the weak soil, respectively. The model is valid for $n > 0.4$ and the full range of soil saturation, and can also be used to estimate the progress (reduction) of the settlement potential of a weak soil upon wetting (i.e. via an increase in the measured $\varepsilon'_{r,eff}$ of the weak soil upon wetting in Equation 4.36). The model takes in to account the mineral composition, soil structure and the three-phase form and is also sensitive to frequency changes in the complex dielectric permittivity analysis in the form of $\varepsilon'_{r,eff}$, $\varepsilon'_{r,g}$ and $\varepsilon'_{r,w}$ of Equations 4.35 and 4.36. In this study, the values at 1 GHz frequency only are considered.

For a typical weak soil with specific gravity of solid particles $G_s = 2.74$ (taken from the collapsible soil used in this study, Chapter 6), $\varepsilon'_{r,g} = 4.847$ (Equation 3.1), $\varepsilon'_{r,w} = 80$ (at 1 GHz) (Hailemariam et al., 2017), structural exponent $a = 1/2$, Equations 4.35 and 4.36 can be simplified as:

$$w = \frac{\varepsilon_{r,eff}'^{0.5} + 1.202n - 2.202}{21.767(1-n)} \tag{4.37}$$

$$\delta_{np,3} = 100K(n-0.4)\left[0.3 - \frac{\varepsilon_{r,eff}'^{0.5} + 1.202n - 2.202}{21.767(1-n)}\right] \tag{4.38}$$

4.6 Effect of temperature on the porous media thermo-dielectric parameters

As discussed in section 3.4, temperature plays a key role in the thermo-dielectric properties of many of the constituent phases of porous media. Hence, the overall or effective thermal and dielectric parameters of porous media are also affected by temperature changes. In this section, semi-theoretical models for the predictions of the effective thermal conductivity and effective dielectric permittivity of porous media with changes in medium temperature are presented.

4.6.1 Variation of thermal conductivity of porous media with temperature

The new model for predicting the effect of temperature on the thermal conductivity of porous media (Equation 4.39) is obtained by using temperature dependent variables in the modified Johansen (1975) model (Equation 4.1).

$$\lambda(T) = [\lambda_{sat}(T) - \lambda_d(T)]\frac{\kappa(\theta/n)}{1+(\kappa-1)(\theta/n)} + \lambda_d(T) \tag{4.39}$$

$$\lambda_{sat}(T) = \lambda_s(T)^{(1-n)}\lambda_w(T)^n \tag{4.40}$$

$$\lambda_d(T) = \begin{cases} \frac{0.135\rho_d(T)+64.7}{\rho_s(T)-0.947\rho_d(T)}, & \text{for uncemented granular media} \\ 0.85\lambda_s(T)^{(1-n)}\lambda_a(T)^n, & \text{for cemented porous media} \end{cases} \tag{4.41}$$

$$\lambda_s(T) = \lambda_{T_o} - qq(1/2)^{(\frac{T_o}{T})}\lambda_{dom}(\frac{T-T_o}{T}) \tag{4.42}$$

$$\lambda_w(T) = \lambda_{w,298.15}\left[-1.48445 + 4.12292\left(\frac{T}{298.15}\right) - 1.63866\left(\frac{T}{298.15}\right)^2\right] \tag{4.43}$$

where, λ ($\mathrm{W\,m^{-1}\,K^{-1}}$) is the temperature T dependent effective thermal conductivity, λ_{sat} and λ_d ($\mathrm{W\,m^{-1}\,K^{-1}}$) are the saturated and dry temperature dependent thermal conductivities of the medium, respectively, κ is the texture dependent parameter of Côté and Konrad (2005) model, θ and n are the volumetric water content and porosity, respectively, ρ_d ($\mathrm{kg\,m^{-3}}$) and ρ_s ($\mathrm{kg\,m^{-3}}$) are the temperature dependent bulk dry density and density of the solid particles, respectively, λ_s, λ_w and λ_a ($\mathrm{W\,m^{-1}\,K^{-1}}$) are the temperature dependent thermal conductivities of the solids, water and air, respectively (although the temperature dependence of conductivity for air can be neglected), λ_{T_o} and λ_{dom} ($\mathrm{W\,m^{-1}\,K^{-1}}$) are thermal conductivities of the solids at reference temperature T_o (°C) and the dominant solid mineral, respectively, and qq is a phonon scattering coefficient with values for different mineral types provided in Hailemariam and Wuttke (2018b). In Equation 4.43, $\lambda_{w,298.15} = 0.6065\,\mathrm{W\,m^{-1}\,K^{-1}}$ and T (K) (Ramires et al., 1995).

4.6.2 Variation of dielectric permittivity of porous media with temperature

The new model for predicting the effect of temperature on the complex dielectric permittivity of porous media (Equation 4.44) is obtained by using temperature dependent variables in the volume fraction (VF) model of complex dielectric permittivity (Equation 4.3) (Lichtenecker and Rother, 1931).

$$\varepsilon'^{a}_{r,eff}(T) = (1-n)\varepsilon'^{a}_{r,g}(T) + (n-\theta) + \theta\varepsilon'^{a}_{r,w}(T) \tag{4.44}$$

where, $\varepsilon'_{r,eff}$ is the temperature T dependent real part of the relative effective complex permittivity of the medium, θ and n are the volumetric water content and porosity, respectively, structural exponent $a = 1/2$ (CRIM) (Birchak et al., 1974), $\varepsilon'_{r,g} = (1.01 + 0.44G_s)^2 - 0.062$ (Dobson et al., 1985) is the dielectric constant of the solids, and along with air can be assumed to be temperature independent, and $\varepsilon'_{r,w}$ (Equation 3.4) is the temperature and frequency dependent real part of the relative complex permittivity of water (Asami, 2002; Zajicek et al., 2006; Wagner and Scheuermann, 2009).

4.7 Extension of the semi-theoretical models

The thermal conductivity of porous media at different hydro-mechanical conditions which do not involve porosity changes at the time of measurement, such as matric

suction (section 4.3) water-driven settlement (section 4.5) and temperature (section 4.6), can be obtained based on dielectric measurements following the appropriate relations given in section 4.2. However, for hydro-mechanical conditions which involve changes in medium porosity such as due to the application of effective stress (section 4.4), the thermal conductivity can be obtained based on dielectric measurements using new relations deduced by following similar procedures to these given in section 4.2 (i.e. the only modification being the inclusion of stress dependent rather than constant porous media parameters such as porosity, dry density etc.).

4.8 Summary of chapter 4

In this chapter, the relationship between the thermal conductivity and complex dielectric permittivity of soils and oil sands was studied. These two parameters generally play a key role in controlling the thermal and dielectric processes of porous media. On this ground, new theoretical models for the prediction of thermal conductivity of porous media (primarily naturally occurring unsaturated soils and bitumen-water saturated oil sands) deposits based on dielectric measurements were presented. Moreover, the variations of the two parameters of porous media with matric suction, applied vertical stress and temperature were studied, and models predicting the water-driven settlement potential of unsaturated weak or loessy porous media based on thermal and dielectric measurements were presented.

Chapter 5

Numerical thermo-dielectric modeling of porous media: LEM

5.1 Introduction

In this chapter, a new LEM based model for providing accurate estimates of the effective thermal conductivity and effective complex dielectric permittivity of bitumen-water saturated oil sands is presented. The new LEM model is also used to obtain the local spatial distributions of the two parameters and to verify their strong correlation, thus complementing the previous theoretical findings of chapter 4.

5.2 LEM approach

5.2.1 Background

The importance and application of the vast field of computational mechanics in solving complex numerical problems of engineering and mathematics continues to grow rapidly with the ever increasing availability of enhanced computational resources. In particular, continuum methods, such as the finite element method (FEM), finite difference method (FDM) and boundary element method (BEM), have been widely in use for solving numerical problems due to their applicability. However, despite their success, continuum methods fail to capture the macroscopic response of heterogeneous materials involving processes on the fine scales, and struggle to deal with material interfaces (where special provisions, such as a highly adaptive mesh is not provided), displacement discontinuities and problems involving very high deformations (due to mesh distortions). Furthermore, the accurate modeling of heat transfer and EM wave propagation in granular madia remains a huge challenge for continuum methods, as

they lack information on the heat and electric conduction paths and porous media fabric.

Particle based and discrete methods, such as the material point method (MPM), particle in cell (PIC), discrete element method (DEM) and lattice approaches provide a promising alternative for solving the aforementioned problems. Discrete methods model the meso-structure with regular arrays of simple shapes, such as spheres, cubes and cylinders with predefined properties. In spite of their low mathematical rigor, discrete models are computationally efficient. One such method, the lattice element method (LEM) approach is the focus of the study in this thesis.

Discrete lattice approaches can be used to solve wide variety of problems in computational mechanics. Lattice models have been found to be very efficient in effectively describing the complex fracture patterns in concrete (Herrmann et al., 1989; Delaplace et al., 1996; Bolander and Saito, 1998). The lattice approach can also be used to model mass transport and its inter-coupling with fracture mechanics, to analyze system mechanical response and mass transport along discrete cracks etc. (Bolander and Berton, 2004; Bolander and Sukumar, 2005; Chatzigeorgiou et al., 2005; Nakamura et al., 2006; Wang et al., 2008; Grassl, 2009). Although discrete methods such as DEM are commonly used to solve heat transfer problems (Vargas and McCarthy, 2001; Feng et al., 2008; Yun and Evans, 2010), the technique of using lattice or a hybrid pipe-network-DEM approaches for modeling heat transfer (Feng et al., 2009; Rizvi et al., 2016; Rizvi et al., 2018; Sattari et al., 2017; Wuttke et al., 2017) and electromagnetic (Hailemariam and Wuttke, 2018a) processes in granular media is relatively new, and needs further investigation. The focus of this thesis is to contribute in this aspect with the target of using the lattice approach in solving thermal and dielectric porous media problems.

Continuum models, such as the FEM, generally employ the discretization of the domain into a finite number of continuum elements (1D, 2D or 3D elements) to solve the fundamental equations, whereas, the lattice approach uses a simple arrangement of discrete line elements (truss or beam elements for mechanical problems, and pipe elements for heat and electric conduction). Once the domain is discretized by a network of lattice elements, a combination of Voronoi diagrams/cells and Delaunay triangulation schemes are utilized to solve the necessary numerical equations.

5.2.2 Node generation

Lattices can be regular or random based on the way the nodal points are generated (Lilliu and van Mier, 2003). The degree of uniformity or randomness of the lattices

hugely affects the degree of anisotropy or the level of disorder introduced at the geometrical level (Moukarzel and Herrmann, 1992; Wang and Cohen, 1996; Lilliu and van Mier, 2003). Three most common types of lattices and their node generation are discussed next.

5.2.2.1 Regular or quasi-uniform lattices

When a medium is discretized in such a way that the nodes are positioned fully uniformly or with little variations in their alignment, then the resulting lattice distribution is a random or quasi-uniform distribution and all discrete lattice elements have more or less the same length (Figure 5.1) (Lilliu and van Mier, 2003).

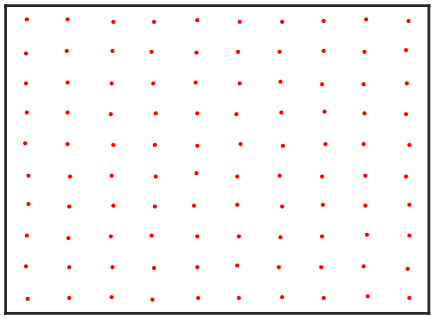

Figure 5.1: Node generation of a quasi-uniform lattice.

Due to the lack of disorder at the geometrical level, regular lattices show anisotropy effects, and hence the regularity appears in the numerical solution of the physical system (Moukarzel and Herrmann, 1992). Isotropy is measured in terms of the probability that a node located at the origin has a neighbor at the point (r, θ) in polar coordinates (Wang and Cohen, 1996).

5.2.2.2 Random lattices

Random lattices are created when the nodes of the medium are generated randomly. The lattices generally have different lengths/geometry and hence posses less anisotropy due to the disorder created at the geometrical level (Moukarzel and Herrmann, 1992; Wang and Cohen, 1996; Lilliu and van Mier, 2003). Random lattices have figured in a large number of applications, which include quantum field theory (Christ et al., 1982), grain mosaics (Weaire and Rivier, 1984) and foams (Moukarzel, 1993).

The two commonly used random lattice node generation techniques are the Poisson random lattice (PRL) and the Vectorizable random lattice (VRL) (Figure 5.2) (Christ et al., 1982; Moukarzel and Herrmann, 1992; Wang and Cohen, 1996).

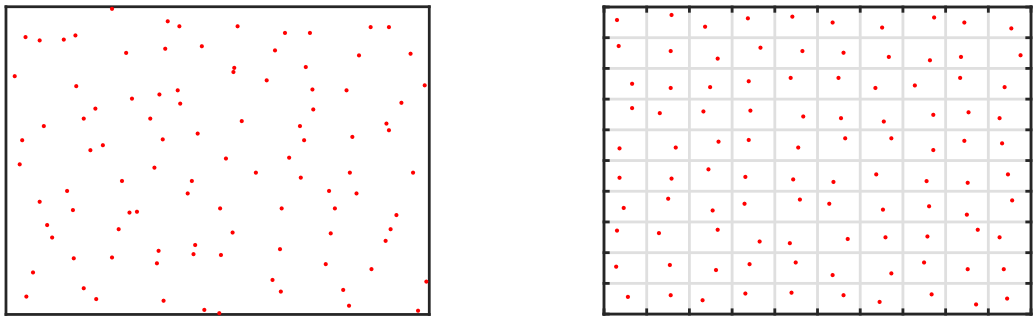

(a) (b)

Figure 5.2: Node generation of a Poisson random lattice (PRL) a) and a Vectorized random lattice (VRL) b).

When the nodes are distributed randomly over the medium, a PRL introduced by Christ et al. (1982) is obtained (since the number of lattice points in a given dimension of the medium is a random variable with a Poisson distribution) (Figure 5.2a). For the PRL, the local properties of the lattice are fully isotropic, and hence anisotropic effects are non-existent.

Moukarzel and Herrmann (1992) introduced the VRL technique, which is obtained by first covering the medium with regular sized meshes and then distributing the nodes randomly and homogeneously inside each mesh, such that each mesh contains only one point (Figure 5.2b). The random lattices are formed by checking each node for a number of possible connectivities (36 in 2D and 178 in 3D). The VRL is vectorizable (i.e. for parallel computation) and has a mild anisotropy. The degree of randomness, and hence the anisotropy can also be controlled with the introduction of a tunable parameter which is called the degree of randomness.

5.2.3 Lattice generation

The dual combination of two techniques, namely Delaunay triangulation and Voronoi discretization, is typically used for the generation of lattice elements in a domain. A Delaunay triangulation for a set of points is a triangulation such that no point lies within the circumcircle of any of the triangles. Voronoi discretization is the geometric dual of Delaunay triangulation, and is formed by creating Voronoi cells as open subsets of nodes that are nearer to a given site than to any other, and with neighboring

cells sharing a face. Each pair of sites whose cells share a face is then connected by a Delaunay line, which is perpendicular to the face, but may not necessarily intersect it (Moukarzel and Herrmann, 1992). Two approaches for the generation of lattice elements using the combination of Delaunay triangulation and Voronoi discretization are shown next.

5.2.3.1 Voronoi scaling

In this approach, the edges of the Delaunay triangles (which connect the generated nodes of the medium) define the lattice elements (Figure 5.3) (Bolander and Berton, 2004). Each node of the triangulation is represented by the Voronoi cell containing it.

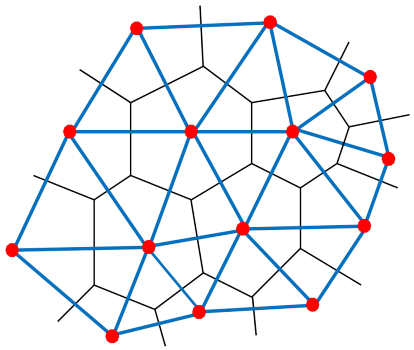

Figure 5.3: Voronoi scaling (Delaunay lattice elements - blue lines, Voronoi cells - black lines and nodes - red points).

5.2.3.2 Delaunay scaling

In this approach, the edges of the Voronoi polygons (which connect the generated nodes of the medium) define the lattice elements (Figure 5.4). Each node of the Voronoi discretization is represented by the Delaunay triangle containing it.

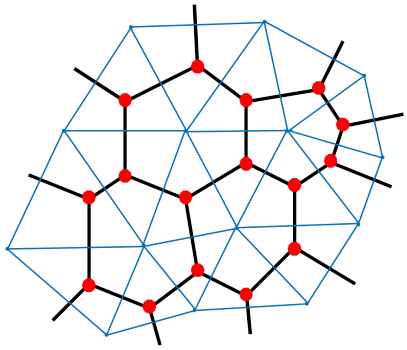

Figure 5.4: Delaunay scaling (Delaunay triangulation - blue lines, Voronoi lattice elements - black lines and nodes - red points).

5.3 Model development

5.3.1 Background

Several researchers have suggested theoretical or numerical based models for estimating the effective thermal conductivity and the effective dielectric permittivity of composites (Farouki, 1981; Usowicz, 1992; Todd and Shi, 2005; Wang and Pan, 2007; Abuel-Naga et al., 2008; Côté and Konrad, 2009; Chen et al., 2014; Ezzat et al., 2014; Dong et al., 2015). Majority of these models were developed by considering the combined nature of the heat or electric conduction via the composite medium (i.e. parallel and series configurations). In spite of the correctness of this approach, some of the models do not include information on the shape or fabric effects of the composites and interaction between them. Hence in this section, a new LEM model, which considers the parallel and series nature of heat or electric flow in porous media, is presented. The new model takes in to account the shape or fabric and interaction between the constituent phases of the porous medium and also introduces randomness at the geometrical level, thus minimizing anisotropic effects.

5.3.2 Model structure

The parallel and series configurations represent the two geometrical extremes that can exist for the transfer of heat or electric current in a composite medium (Farouki, 1981; Todd and Shi, 2005; Chen et al., 2014; Ezzat et al., 2014). For any given porous medium, the actual rate of heat or electric conduction (effective parameters) lies in between the two bounds and can be modeled as a weighted combination of the series and parallel structures. Chen et al. (2014) modeled the effective parameters of unsaturated bentonites by arranging the constituent phases in a combination of series and parallel arrangements with good results. Usowicz (1992) suggested a model for obtaining the effective soil parameters by representing a volumetric unit of soil by a system of regularly arranged spheres, and by calculating the effective resistivity of the arrangement using a combination of parallel and series flows between the layers. However, due to the lack of randomness of this type of particle generation, anisotropic effects are expected to be seen in the results. The new LEM model presented in this study, also uses a similar approach of obtaining the effective parameters numerically from the individual thermal or electrical resistivities of the constituent phases of the porous media, but has also the added benefit of minimizing anisotropic effects by distributing the phases randomly in the domain as a network of lattices.

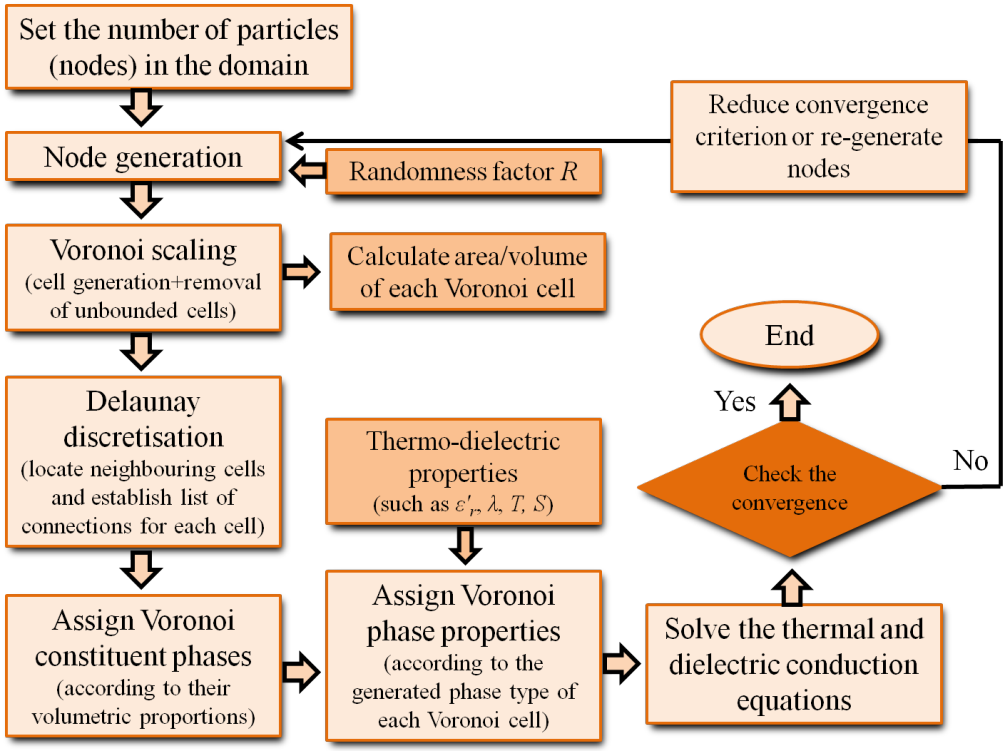

Figure 5.5: Schematic flow chart of the new LEM model for obtaining effective porous media parameters.

Figure 5.5 shows a schematic flow chart of the new LEM model for obtaining the effective thermal conductivity and effective dielectric permittivity of porous media. First, the nodes are generated randomly according to the desired volumetric proportions of solids, pore-water and bitumen present in the oil sand. The Voronoi cells representing the nodes and the associated Delaunay lattice elements are then generated via the Voronoi scaling approach using MATLAB. The corresponding dielectric, thermal and other constituent properties are then assigned to each node before solving the heat or electric resistance equations using an in house MATLAB implementation, and the convergence of the solutions are checked.

5.3.3 Model geometry

Due to its effectiveness, lack of anisotropy and simplicity, the VRL technique (Moukarzel and Herrmann, 1992; Lilliu and van Mier, 2003) is used for generating the nodal elements of the lattice model presented in this thesis.

In the VRL technique of random lattice generation, disorder is introduced at the geometrical level by placing the nodes inside sub-cells of the original regular sized meshes via the tunable parameter (randomness factor R) (Figure 5.6) (Moukarzel and

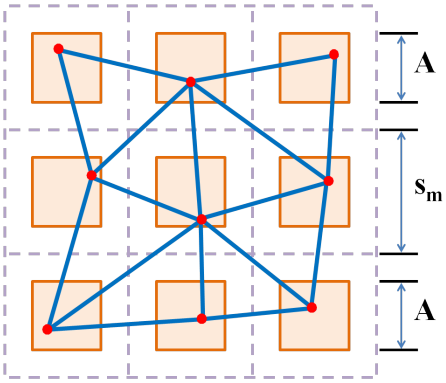

Figure 5.6: Node generation via the VRL technique, after Lilliu and van Mier (2003).

Herrmann, 1992; Lilliu and van Mier, 2003).

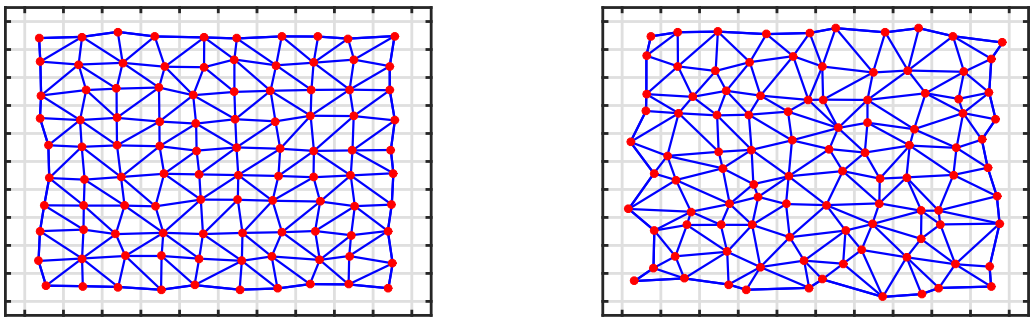

(a) (b)

Figure 5.7: Delaunay lattice elements of 10×10 nodal elements with a randomness factor $R = 0.3$ a) and $R = 0.7$ b), generated with the VRL technique.

Randomness R is defined as the ratio of the size of the sub-cell A (m) to the main cell (generated mesh) s_m (m). Hence, the randomness factor R ($0 \leq R \leq 1$) produces lattice elements with a maximal randomness when $R = 1$ and a regular reference lattice when $R = 0$ (Figure 5.7).

5.3.4 Model resistance equations

The analogous nature of heat flow and electrical circuits has long been recognized. And it is common to model heat flow by analogy to an electrical circuit, where current represents heat flow, voltages represent temperatures, current sources represent heat sources, resistors represent thermal resistances etc. The analogy between heat and electric flows is shown in Table 5.1.

Table 5.1: Analogy between heat and electric flows.

Type	**Heat flow**	**Electric flow**
Quantity	heat Q_T (J)	charge q_E (C)
Potential	temperature T (K)	voltage V_E (V)
Transfer rate	rate of heat transfer Q (W)	current I (A)
Flux density	heat flux $\mathbf{q}$ ($\mathrm{W\,m^{-2}}$)	current density $\mathbf{J}$ ($\mathrm{A\,m^{-2}}$)
Resistance	thermal resistance R_T ($\mathrm{K\,W^{-1}}$)	electrical resistance R_E (Ω)
Resistivity	thermal resistivity[a] $R_\lambda = R_T \frac{A_c}{l}$ ($\mathrm{m\,K\,W^{-1}}$)	electrical resistivity[a] $\rho_E = R_E \frac{A_c}{l}$ ($\Omega\,\mathrm{m}$)
Conductance	thermal conductance $C_T = \frac{1}{R_T}$ ($\mathrm{W\,K^{-1}}$)	electrical conductance $G_E = \frac{1}{R_E}$ (S)
Conductivity	thermal conductivity $\lambda = \frac{1}{R_\lambda}$ ($\mathrm{W\,m^{-1}\,K^{-1}}$)	electrical conductivity $\sigma_E = \frac{1}{\rho_E}$ ($\mathrm{S\,m^{-1}}$)
Linear model	Fourier's law $\mathbf{q} = -\lambda \nabla T$	Ohm's law $\mathbf{J} = \sigma_E\ \mathbf{E}$

[a]: A_c ($\mathrm{m^2}$) and l (m) are the cross sectional area and length of the medium, respectively

For a series electric conduction of the system of two neighboring Voronoi cells shown in Figure 5.8, the same quantity of electric current I (A) flows through the two cells, while the total voltage drop across the two cells $\Delta V_{E,kl}$ (V) is the sum of their individual drops as shown in Equations 5.1 and 5.2. The equivalent electrical resistance of the imaginary Delaunay lattice element $R_{E,kl}$ (Ω) representing the two Voronoi cells is given by Equation 5.3.

$$\Delta V_{E,kl} = \Delta V_{E,k} + \Delta V_{E,l} \tag{5.1}$$

$$I R_{E,kl} = I R_{E,k} + I R_{E,l} \tag{5.2}$$

$$R_{E,kl} = R_{E,k} + R_{E,l} \tag{5.3}$$

where, $\Delta V_{E,k} = V_{E,k,i} - V_{E,k,o}$ and $\Delta V_{E,l} = V_{E,l,i} - V_{E,l,o}$ (V) are the voltage drops across Voronoi cells k and l, respectively, $V_{E,k,i}$ and $V_{E,l,i}$ (V) are the input voltages of Voronoi cells k and l, respectively, $V_{E,k,o}$ and $V_{E,l,o}$ (V) are the output voltages of Voronoi cells k and l, respectively, and $R_{E,k}$ and $R_{E,l}$ (Ω) are the electrical resistances of Voronoi cells k and l, respectively. When electric flows from Voronoi cell k to l, $V_{E,k,o} = V_{E,l,i}$.

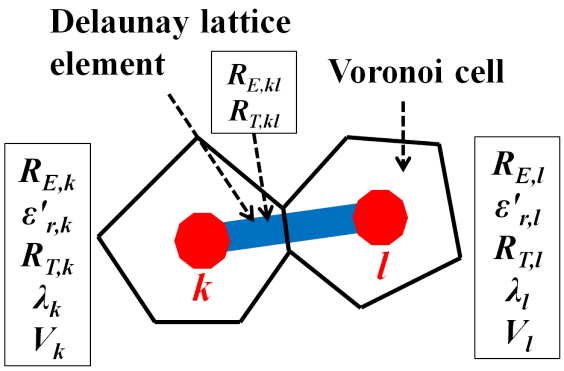

Figure 5.8: Schematic representation of the interaction between two neighboring constituent phases or nodes k and l.

Whereas, for a parallel electric conduction, the voltage drop across the two cells $\Delta V_E = \Delta V_{E,k} = \Delta V_{E,l}$ (V) is the same (i.e. $V_{E,k,i} = V_{E,l,i}$ and $V_{E,k,o} = V_{E,l,o}$), while the total quantity of electric current flow through the two cells I_{kl} (A) is the sum of the individual currents as shown in Equations 5.4 and 5.5. The equivalent electrical resistance of the imaginary Delaunay lattice element $R_{E,kl}$ (Ω) representing the two Voronoi cells is given by Equation 5.6.

$$I_{kl} = I_k + I_l \tag{5.4}$$

$$\frac{\Delta V_E}{R_{E,kl}} = \frac{\Delta V_E}{R_{E,k}} + \frac{\Delta V_E}{R_{E,l}} \tag{5.5}$$

$$\frac{1}{R_{E,kl}} = \frac{1}{R_{E,k}} + \frac{1}{R_{E,l}} \tag{5.6}$$

where, I_k and I_l (A) are the electric current flows through Voronoi cells k and l, respectively.

In terms of heat flow, for a series heat conduction of the system of two neighboring Voronoi cells shown in Figure 5.8, the rate of heat transfer Q (W) through the two cells is the same, while the total temperature drop across the two cells ΔT_{kl} (K) is the sum of their individual drops as shown in Equations 5.7 and 5.8. The equivalent thermal resistance of the imaginary Delaunay lattice element $R_{T,kl}$ ($\mathrm{K\,W^{-1}}$) representing the two Voronoi cells is given by Equation 5.9.

$$\Delta T_{kl} = \Delta T_k + \Delta T_l \tag{5.7}$$

$$QR_{T,kl} = QR_{T,k} + QR_{T,l} \tag{5.8}$$

$$R_{T,kl} = R_{T,k} + R_{T,l} \tag{5.9}$$

where, $\Delta T_k = T_{k,i} - T_{k,o}$ and $\Delta T_l = T_{l,i} - T_{l,o}$ (K) are the temperature drops across Voronoi cells k and l, respectively, $T_{k,i}$ and $T_{l,i}$ (K) are the input temperatures of Voronoi cells k and l, respectively, $T_{k,o}$ and $T_{l,o}$ (K) are the output temperatures of Voronoi cells k and l, respectively, and $R_{T,k}$ and $R_{T,l}$ ($\mathrm{K\,W^{-1}}$) are the thermal resistances of Voronoi cells k and l, respectively. When heat flows from Voronoi cell k to l, $T_{k,o} = T_{l,i}$.

Whereas, for a parallel thermal conduction, the temperature drop across the two cells $\Delta T = \Delta T_k = \Delta T_l$ (K) is the same (i.e. $T_{k,i} = T_{l,i}$ and $T_{k,o} = T_{l,o}$), while the total rate of heat transfer through the two cells Q_{kl} (W) is the sum of the individual rates as shown in Equations 5.10 and 5.11. The equivalent thermal resistance of the imaginary Delaunay lattice element $R_{T,kl}$ ($\mathrm{K\,W^{-1}}$) representing the two Voronoi cells is given by Equation 5.12.

$$Q_{kl} = Q_k + Q_l \tag{5.10}$$

$$\frac{\Delta T}{R_{T,kl}} = \frac{\Delta T}{R_{T,k}} + \frac{\Delta T}{R_{T,l}} \tag{5.11}$$

$$\frac{1}{R_{T,kl}} = \frac{1}{R_{T,k}} + \frac{1}{R_{T,l}} \tag{5.12}$$

where, Q_k and Q_l (W) are the rates of heat flow through Voronoi cells k and l, respectively.

In reality, the actual rates of heat or electric conduction between two constituent phases or nodes of a porous medium is a combination or is in between the parallel and series configurations. Hence, the actual equivalent thermal or electrical resistance of the imaginary Delaunay lattice element representing the two Voronoi cells shown in Figure 5.8 can be expressed analytically using the Power-law (Todd and Shi, 2005; Yun and Santamarina, 2007; Ezzat et al., 2014) as:

$$\left(\frac{1}{R_{E,kl}, R_{T,kl}}\right)^{\beta} = \left(\frac{1}{R_{E,k}, R_{T,k}}\right)^{\beta} + \left(\frac{1}{R_{E,l}, R_{T,l}}\right)^{\beta} \tag{5.13}$$

where, β is an exponent which depends on the shape and rates of electric and thermal conduction of the solid and fluid phases of the medium, and lies in between -1 and 1. When the value of $\beta = -1$, a series flow is obtained and Equation 5.13 turns to Equations 5.3 or 5.9, and when the value of $\beta = 1$, a parallel flow is obtained and Equation 5.13 turns to Equations 5.6 or 5.12 (Farouki, 1981; Todd and Shi, 2005; Chen et al., 2014; Ezzat et al., 2014).

In the LEM model, the effective thermal or electrical resistances of the porous medium are obtained using the generated networks of Delaunay lattices and Voronoi cells. The solution convergence of the iterative procedure for the resistivity equations is checked using MATLAB with the following equation:

$$\epsilon_k = \frac{|(V_{E,k}, T_k)^{(n_i)} - (V_{E,k}, T_k)^{(n_i-1)}|}{(V_{E,k}, T_k)^{(n_i-1)}} \leq \phi_L \tag{5.14}$$

where, $V_{E,k}$ (V) and T_k (K) are the electric potential (voltage) and temperature of the k^{th} constituent phase or node (alternatively electrical $R_{E,k}$, Ω, and thermal $R_{T,k}$, $\mathrm{K\,W^{-1}}$, resistances can be used, respectively), ϵ_k is the convergence error of the k^{th} constituent phase or node, n_i is the step or number of iteration and ϕ_L is the preset error limit. For this study a value of $\phi_L = 0.001$ is chosen.

5.4 Nature of heat and electric conduction in porous media

In spite of the strong analogy between the nature of heat and electric flows in porous media as explained extensively in this section, a certain degree of dissimilarity between the two cases, arising due to the corresponding physical properties of thermal and electric conductivities of the constituent phases is to be expected (Lasance, 2008). In this regard, the dominant form of flow (i.e. parallel or series flow) in the two cases is different, due to differences in the comparative rates of the heat or electric conduction of the individual solid and fluid phases of the medium. When the ratio of the rates of conduction of the solid grains to the saturating fluid is low, parallel flow dominates, while for high ratio of the rates of conduction of the solid grains to the saturating fluid, series flow is dominant (Farouki, 1981). Therefore, for the case of heat flow in a porous media, $\lambda_s > \lambda_f$, and the ratio λ_s/λ_f is high, hence series flow is expected to be dominant. Whereas, for the case of electric flow in a porous media, $\varepsilon^*_{r,g} \ll \varepsilon^*_{r,f}$, and the ratio $\varepsilon^*_{r,g}/\varepsilon^*_{r,f}$ is very low, hence parallel flow is expected to be dominant.

5.5 Summary of chapter 5

A new LEM based model for predicting the effective thermal conductivity and effective dielectric permittivity of bitumen-water saturated oil sands was presented. The new LEM model can also be used to obtain the local spatial distributions of the two parameters and to verify their strong correlation, thus complementing the theoretical findings of the previous chapter.

Chapter 6

Experimental program

6.1 Introduction

This chapter presents the experimental program followed to study the thermal and dielectric behavior of the porous media used in this study. In this regard, the different types of porous media analyzed in this thesis, the thermal and dielectric properties measurement techniques employed and the experimental methodology followed for obtaining the thermo-dielectric parameters are discussed.

6.2 Materials used

A total of three types of un-cemented porous media are used in this thesis for the experimental studies of the thermal and dielectric parameters and their variations with hydro-mechanical changes. A description of the used porous media types is presented next.

6.2.1 Soils

6.2.1.1 Silty clay soils

Three naturally occurring silty clay soils (Figure 6.1), referred to in this thesis as silty clays A to C (SC-A to C, respectively), from Thuringia, Germany, were investigated. The obtained geotechnical, following ASTM D 420 - D 5876 (2011) guidelines, and physiochemical properties of the silty clay soils are provided in Tables 6.1 and 6.2, respectively. The phase content was determined by combined X-ray diffraction and X-ray fluorescence analysis.

(a) (b) (c)

Figure 6.1: Silty clay soils A a), B b) and C c).

Table 6.1: Geotechnical properties of the investigated silty clay soils.

Property	**SC-A**	**SC-B**	**SC-C**
Depth (m)	0.3 - 0.7	0.3 - 0.7	0.3 - 0.7
Gravel, > 2 mm (wt.%)	16.1	14.9	2.8
Sand, 0.063 - 2 mm (wt.%)	8.8	12.2	7.1
Silt, 0.002 - 0.063 mm (wt.%)	58.2	52.5	65.4
Clay, < 0.002 mm (wt.%)	16.8	20.2	24.6
Porosity n (-)	0.443	0.464	0.473
Solids specific gravity G_s (-)	2.673	2.670	2.621
Bulk dry density ρ_d ($\mathrm{kg\,m^{-3}}$)	1489	1431	1381
Liquid limit L_L (%)	34.6	43.1	48.2
Plasticity index P_I (%)	14.81	19.45	23.19
Natural gravimetric water content w_n (-)	0.168	0.191	0.194
Unified soil classification system (USCS)	CL	CL	CL

CL: Clay of low plasticity

Table 6.2: Physiochemical properties of the investigated silty clay soils.

Elemental composition	**SC-A**	**SC-B**	**SC-C**
Silicon dioxide, SiO_2 (%)	65.81	57.31	66.76
Aluminium oxide, Al_2O_3 (%)	9.18	7.56	10.24
Iron (III) oxide, Fe_2O_3 (%)	3.42	2.64	3.59
Calcium oxide, CaO (%)	5.15	13.89	4.23
Magnesium oxide, MgO (%)	1.17	1.54	1.66
Potassium oxide, K_2O (%)	2.55	2.09	2.68
Sodium oxide, Na_2O (%)	0.92	0.85	0.91
Titanium oxide, TiO_2 (%)	0.75	0.62	0.74
Others (%)	11.05	13.50	9.19
Organic content (wt.%)	3.763	4.677	6.410

6.2.1.2 Loess soil

A remolded loess soil (Figure 6.2) taken from near Baku area, Azerbaijan, was investigated. The obtained geotechnical, following ASTM D 420 - D 5876 (2011) guidelines, and physiochemical properties of the loess soil are provided in Table 6.3. The loess soil was prepared under two remolded conditions, namely in its natural condition ($n = 0.453$ and $\rho_d = 1.495\,\mathrm{g\,cm^{-3}}$, labeled here as loess A, L-A) and a lab compacted condition ($n = 0.301$ and $\rho_d = 1.913\,\mathrm{g\,cm^{-3}}$, labeled here as loess B, L-B).

Table 6.3: Geotechnical and physiochemical properties of the investigated loess soil.

Property/mineralogical composition	Value
Depth (m)	2.0 - 2.5
Gravel, > 2 mm (wt.%)	0
Sand, 0.063 - 2 mm (wt.%)	15
Silt, 0.002 - 0.063 mm (wt.%)	51
Clay, < 0.002 mm (wt.%)	34
Porosity n (-)	0.453/0.301
Solids specific gravity G_s (-)	2.735
Bulk dry density ρ_d ($\mathrm{kg\,m^{-3}}$)	1495/1913
Liquid limit L_L (%)	31.3
Plasticity index P_I (%)	14.3
Natural gravimetric water content w_n (-)	0.093
Unified soil classification system (USCS)	CL
Tecosilicates (%)	44
Mica (%)	25
Smectite (%)	7
Chlorite (%)	5
Kaolinite (%)	3
Others (%)	16
Lime content (wt.%)	12.944
Organic content (wt.%)	5.811

CL: Clay of low plasticity

Figure 6.2: A sample of the loess or weak porous medium used in this study.

6.2.2 Oil sand

Several samples of a three-grade (low, medium and high) bitumen-water saturated reconstituted oil sand, prepared by mixing a fixed weight proportion of a silty sand soil, water and bitumen, were investigated. The physical properties of the silty sand soil, bitumen and the reconstituted oil sand are provided in Tables 6.4, 6.5 and 6.6, respectively, and a sample of a high grade reconstituted oil sand specimen is shown in Figure 6.3.

Table 6.4: Geotechnical properties of the silty sand soil used for preparing the oil sand.

Property	**Value**
Gravel, > 2 mm (wt.%)	5.78
Sand, 0.063 - 2 mm (wt.%)	82.41
Silt, 0.002 - 0.063 mm (wt.%)	8.38
Clay, < 0.002 mm (wt.%)	3.42
Solids specific gravity G_s (-)	2.67
Grain diameter at 10% passing D_{10} (mm)	0.05
Grain diameter at 50% passing D_{50} (mm)	0.53
Coefficient of uniformity C_u (-)	13.60
Coefficient of curvature C_c (-)	3.20
Unified soil classification system (USCS)	SP-SM

SP-SM: Poorly graded sand with silt

Table 6.5: Specifications of the used bitumen.

Property	**Value**
Dynamic viscosity at 60°C $\mu_{v,60}$ (mPa s)	1845.7
Flash point (°C)	183
Solubility (wt.%)	99.53

Table 6.6: Physical properties of the bitumen-water saturated reconstituted oil sand.

Property	**Value**
Porosity n (-)	0.27
Solids specific gravity G_s (-)	2.67
Bulk dry density ρ_d ($\mathrm{kg\,m^{-3}}$)	1949
Solids fraction W_s (wt.%)	88
(Bitumen + Water) fraction $W_b + W_w$ (wt.%)	12
Volumetric quartz fraction q_f (-)	0.47

Figure 6.3: A sample of a high grade oil sand used in this study.

6.3 Equipments used

In this section, details of the equipments used for conducting the thermal and dielectric tests on the different porous materials considered in this thesis are presented. A more detailed information on the different types of thermal and dielectric measurement techniques is given in sections 2.2.3 and 2.3.1, respectively. The techniques employed for the determination of the thermal (transient or steady state) and dielectric (TDR or VNA) properties in this thesis were selected based on: their suitability for the particular porous medium type (section 6.2), time of measurement needed, controlling hydro-mechanical test parameters etc.

6.3.1 Thermal measurements

6.3.1.1 Transient measurements

The transient thermal conductivity and specific heat capacity of the investigated materials were measured with a Decagon KD2 Pro thermal needle probe (Figure 6.4a), based on transient line source measurement technique in compliance to ASTM D 5334 - 08 (2008) and IEEE 442 (1981) standards. Thermal needle probes SH-1 (dual needle), with length of 30 mm, diameter 1.3 mm and 6 mm spacing of probe needles (Figure 6.4b), and specimen dimensions of 50 mm diameter and 50 mm height, and

TR-1 (single needle) with length of 100 mm and diameter 2.4 mm (Figure 6.4c), and specimen dimensions of 50 mm diameter and 150 mm height, were used to measure the specific heat capacity and thermal conductivity of the samples at room temperature and atmospheric pressure, respectively, based on Carslaw and Jaeger (1959) and Kluitenberg et al. (1993) line heat source analysis.

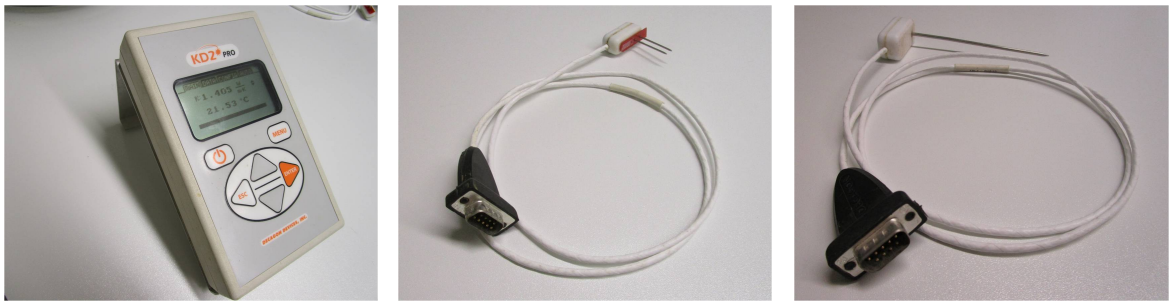

(a) (b) (c)

Figure 6.4: Decagon KD2 Pro thermal device a), SH-1 dual needle probe b) and TR-1 single needle probe c).

The sufficient length to diameter ratios of the probes ensure that conditions for an infinitely long and infinitely thin heating source are met. The measurement error recorded for the samples was kept well below the 0.015% limit. The KD2 Pro includes a linear heat source and a temperature measuring element with a resolution of 0.001°C, and computes the thermal conductivity and thermal diffusivity (using TR-1 probe) of the medium using the following relations:

$$\lambda = \frac{Q_s(\ln t_2 - \ln t_1)}{4\pi(\Delta T_2 - \Delta T_1)} \tag{6.1}$$

$$\Delta T = -\frac{Q_s}{4\pi\lambda}\mathrm{Ei}\left(\frac{-r^2}{4\alpha t}\right) \tag{6.2}$$

where, λ ($\mathrm{W\,m^{-1}\,K^{-1}}$) is the thermal conductivity of the sample, Q_s ($\mathrm{W\,m^{-1}}$) is the constant rate of application of heat, ΔT (K) is the temperature response of the source over time, 'Ei' is the exponent integral (Abramowitz and Stegun, 1972), r (m) is the distance between the heater and the sensor where temperature is measured, t (s) is the amount of time that has passed since the start of heating and α ($\mathrm{m^2\,s^{-1}}$) is the thermal diffusivity of the sample.

For the determination of the specific heat capacity using the dual needle thermal probe SH-1, heat is initially applied to the heating needle for a heating time of t_h (s), and the respective temperature is measured in the monitoring needle, 6 mm distant. The readings are then processed by subtracting the ambient temperature at time 0

(T_0), multiplying by a factor of 4π and then dividing by the heat per unit length Q_s ($\mathrm{W\,m^{-1}}$). The resulting data are fitted with the following equations using a non-linear least squares method.

$$T^* = b_0 t + b_1 \mathrm{Ei}\left(\frac{b_2}{t}\right) \tag{6.3}$$

$$T^* = b_0 t + b_1 \left[\mathrm{Ei}\left(\frac{b_2}{t}\right) - \mathrm{Ei}\left(\frac{b_2}{t - t_h}\right)\right] \tag{6.4}$$

$$T^* = \frac{4\pi(T - T_0)}{Q_s} \tag{6.5}$$

where, b_0, b_1 and b_2 are the constants to be fit and T_0 (K) is the temperature at the start of the measurement (at time 0). Equation 6.3 is valid for the initial t_h seconds, when the heat is applied, while Equation 6.4 applies when the heat is off (cooling period). The thermal conductivity λ ($\mathrm{W\,m^{-1}\,K^{-1}}$), thermal diffusivity α ($\mathrm{m^2\,s^{-1}}$) and specific heat capacity c ($\mathrm{J\,kg^{-1}\,K^{-1}}$) of the specimen are obtained as:

$$\lambda = \frac{1}{b_1} \tag{6.6}$$

$$\alpha = \frac{r_h^2}{4b_2} \tag{6.7}$$

$$c = \frac{\lambda}{\rho\alpha} \tag{6.8}$$

where, ρ ($\mathrm{kg\,m^{-3}}$) is the density of the medium and r_h (m) is the distance between the two needles.

6.3.1.2 Steady state measurements

The simultaneous measurements of thermal conductivity, deformation, vertical stress and other porous media hydro-mechanical conditions were obtained by using recently developed steady state devices. The steady state thermal conductivity measurement devices where developed in two stages, i.e. with and without matric suction provisions, as discussed next.

With no matric suction control

The first version of the steady state device for measuring the thermal conductivity (Stegner et al., 2011; Sass and Stegner, 2012; Hailemariam et al., 2016; Stegner et al., 2017) has no provisions for controlling the matric suction of the specimen, and hence is suitable for use in dry porous media as well as un-saturated/saturated porous media at low temperature ranges. The device is not suitable for measuring the thermal conductivity of porous media with considerable moisture content at high temperature ranges due to moisture migration and evaporation effects.

This first version of the steady state thermal conductivity and diffusivity meter (Figures 6.5 and 6.6) which works on the principle of the divided bar apparatus (Birch and Clark, 1940; Popov et al., 1999; McGuinness et al., 2014) was used for analyzing the steady state thermal conductivity of the investigated materials at low temperature ranges (20 - 30°C). In the divided bar apparatus, the temperature drop across a disc of rock or porous medium is compared with that across a disc of standard material of known thermal conductivity. The method is deemed to be the most accurate method of measuring the thermal conductivity of intact porous materials in the laboratory with an estimated measurement accuracy of 5% and repeatability variance between 2 - 5% (McGuinness et al., 2014).

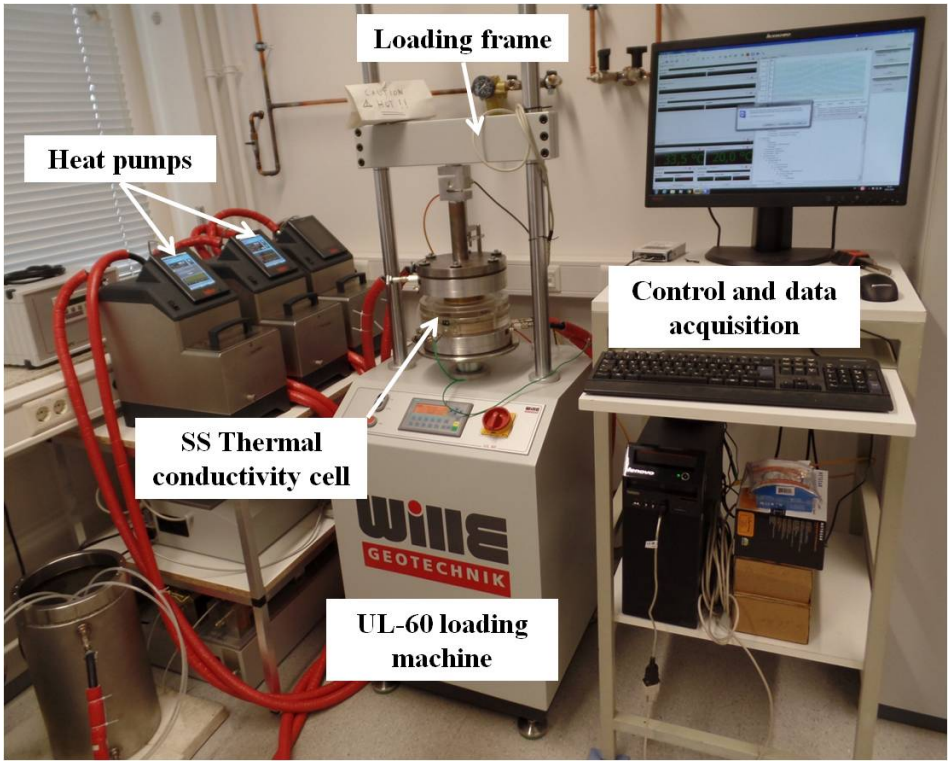

Figure 6.5: First version of the steady state thermal conductivity measurement setup.

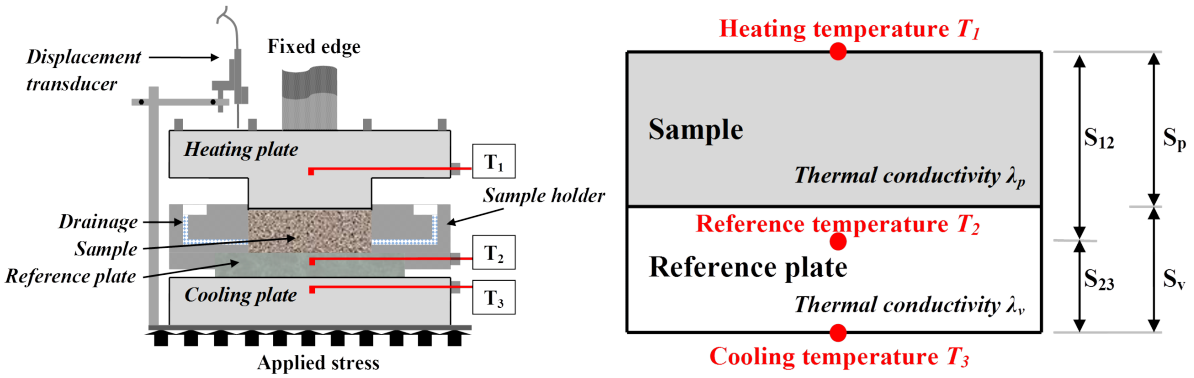

Figure 6.6: Schematic representation a) and dimensional analysis b) of the first version of the steady state thermal conductivity cell.

The steady state thermal conductivity determination apparatus consists of a top heating plate, a bottom cooling plate and a PPS Laticonther thermoplastic reference disc with known thermal conductivity (Figure 6.6a). Upon calibration, the change of the thermal conductivity of the reference disc with temperature for the range considered in the experimental studies presented in this thesis was found to be negligible, and hence its thermal conductivity is considered to be constant. The temperature of the top heating T_1 and bottom cooling T_3 plates is controlled via a circulating fluid (distilled water + glycol), which is pumped using Huber Ministat 125 Pilot ONE heat pumps, and the resulting temperature of the reference plate T_2 is recorded. The specimen (with dimensions of 100 mm diameter and adjustable height of 25 - 35 mm) is sandwiched between the top heating and reference plates and is laterally confined/insulated by a PMMA Plexiglas sample holder with a very low thermal conductivity (Figure 6.6a). The top and bottom heating/cooling plates consist of extremely thin PT 100 temperature sensors with an accuracy of 0.05°C. The system measures sample thermal expansion or contraction with a TRS-0050 linear transducer with a defined electrical range of $50\,\mathrm{mm}$, an independent linearity of $\pm 0.15\%$ and repeatability of $2\,\mu\mathrm{m}$. Vertical stress (with a maximum force limit of 60 kN) can be applied to the specimen via a UL-60 loading machine integrated with the system as shown in Figure 6.5.

As discussed in section 2.2.1, heat energy can be transmitted in a porous medium via a combination of one or more of three main processes, namely: conduction, convection and radiation. The dominant form of heat transfer in the porous materials considered in this thesis is via conduction, as the contributions from the buoyancy driven (natural) convection and radiation are neglected due to the low hydraulic conductivities (Clauser and Huenges, 1995; Hailemariam and Wuttke, 2016) of the materials and the considered lower temperature range (Hofmeister, 1999; Jokinen, 2000;

McKenzie et al., 2005) of this study (i.e. radiative form of heat transfer starts to contribute only at temperatures above 727°C), respectively. It is important to note that the contributions of natural convection can be neglected for most porous media and sedimentary formations; however, fluid driven convection can be important in crystalline rock formations with very high hydraulic conductivities and on a crustal scale (Etheridge et al., 1983; Torgersen, 1990; Clauser, 1992).

The mathematical description of the one dimensional conductive heat transport within the device is given by the Fourier's law and conservation of energy (Cannon, 1984). By Fourier's law, the rate of flow of heat energy per unit area through a surface is proportional to the negative temperature gradient across the surface. The heat flux q ($\mathrm{W\,m^{-2}}$) (generated by the temperature gradient created due to the heating T_1 and cooling T_3 plates) through the specimen can be expressed in terms of the thermal conductivity λ ($\mathrm{W\,m^{-1}\,K^{-1}}$) as:

$$q = -\lambda \nabla T = -\lambda \frac{\Delta T}{\Delta S_i} = -\frac{\Delta T}{\Delta S_i / \lambda} \tag{6.9}$$

where, ΔS_i (m) is the vertical distance between the respective temperature gradient points (with temperature difference of ΔT, K) across the central axis of the device (Figure 6.6b). Under steady state heat transfer conditions, provided that $T_1 > T_2 > T_3$ (ensuring that heat flow occurs from the top plate via the specimen and reference disc to the bottom plate creating a linear temperature gradient over the height of the specimen), Equation 6.9 can be used to deduce Equations 6.10 and 6.11 for the heat flux between temperature sensors T_2 and T_3 and between temperature sensors T_1 and T_3, respectively. λ_v ($\mathrm{W\,m^{-1}\,K^{-1}}$) is the known thermal conductivity of the reference plate.

$$q = -\frac{T_2 - T_3}{S_{23}/\lambda_v} \tag{6.10}$$

$$q = -\frac{T_1 - T_3}{\frac{S_v}{\lambda_v} + \frac{S_p}{\lambda_p}} \tag{6.11}$$

Equating Equations 6.10 and 6.11 and solving for the unknown thermal conductivity of the specimen λ_p yields:

$$\lambda_p = \frac{\lambda_v S_p}{\left[\frac{T_1 - T_3}{T_2 - T_3}\right] S_{23} - S_v} \tag{6.12}$$

The average sample temperature (at the center of the specimen) corresponding to T_1, T_2 and T_3 can thus be obtained as:

$$T_{av} = \frac{1}{2}\left\{T_1 + T_3\left[1 + \frac{S_v(T_2 - T_3)}{T_3 S_{23}}\right]\right\} \tag{6.13}$$

where, T_1, T_2 and T_3 (°C) are the temperatures of the top (heating), reference and bottom (cooling) plates, respectively, T_{av} (°C) is the average specimen temperature, λ_p and λ_v ($\mathrm{W\,m^{-1}\,K^{-1}}$) are the thermal conductivities of the specimen and the reference disc, respectively, and S_p, S_v and S_{23} (m) are the distances as shown in Figure 6.6b.

With matric suction control

Ridley and Wray (1996) classified the porous media suction measuring techniques in to two categories, namely: those that measure the suction directly and those that measure it indirectly. With the direct measurement techniques, the relevant parameter such as the pore-water energy or tensile stress is measured directly. Whereas, the indirect techniques measure parameters such as relative humidity, conductivity or moisture content, which are then related to the suction of the porous medium via calibration relationships. For each case it is necessary to note whether the total (matric + osmotic) suction or matric suction only is being measured. In general, when no contact is made between the measuring equipment and the porous media moisture, the relative humidity of the ambient air within the porous medium is measured and hence it is the total suction. However, if a proper contact is ensured between the measuring device and the porous medium moisture, and the concentration of the dissolved salts in the medium is assumed to be the same everywhere, then the matric suction is being measured. The accuracy of the measurement of matric suction at very low degrees of saturation can however be limited, as it is normally difficult to ensure that a proper and even contact between the measuring device and the moisture of the porous medium is achieved due to the migration of moisture towards the finer pores resulting in a discontinuous medium.

The two commonly used techniques for controlling the suction of a porous medium are the axis translation technique (ATT) and the relative humidity control or vapor equilibrium technique (VET). The ATT can be used to obtain the drying and wetting paths of porous media in the low matric suction range (i.e. $\leq$ 1500 kPa). In the ATT, matric suction is defined as the difference between the pore-air u_a (kPa) and pore-water u_w (kPa) pressures of the porous medium as $\psi_m = u_a - u_w$ (kPa). Hence, measuring a negative matric suction can be avoided by increasing the pore-air u_a pressure

while maintaining the pore-water u_w pressure to a positive reference pressure (Hilf, 1956). The measurement of matric suction using the ATT is only limited by the bubble point (air-entry value, AEV) of the used commercial air-water interfaces such as ceramic discs or cellulose acetate (CA) membranes. However, the use of air-water interfaces with high AEVs is not desirable when lower matric suction values are to be applied, as the hydraulic permeability/pore size of the air-water interfaces with high AEVs is lower than the hydraulic permeability/pore size of the air-water interfaces with low AEVs, resulting in a prolonged matric suction stabilization times and hence longer test durations. For obtaining the drying and wetting paths of porous media at high suction ranges (i.e. > 1500 kPa), the VET is usually employed.

The second version of the steady state device for measuring the thermal conductivity was developed by modifying the first version presented earlier by adding a controlled ambient temperature and humidity (usually kept at around 23°C and 50%, respectively) climate chamber unit containing the thermal conductivity cell (Figure 6.7), and by providing extra provision for controlling the matric suction ψ_m (kPa) of the specimen with the ATT (Figure 6.8) (Richards, 1941; Gardner, 1956; Hilf, 1956; Delage et al., 2008). The climate chamber temperature and humidity control unit provides the same starting (initial) temperature and humidity conditions, and maintains a constant outer boundary condition for all the steady state tests. The provision for controlling the matric suction of the specimen with the ATT enables the determination of the thermal conductivity of the specimen at different levels of moisture content/matric suction.

The axis translation technique is introduced to the system by replacing the original open-system design (from the first version) (Figure 6.6a) with a new closed-system thermal conductivity cell (Figure 6.8a), where controlled pore-air u_a (kPa) and pore-water u_w (kPa) pressures can be applied simultaneously, thus imposing the desired level of matric suction $\psi_m = u_a - u_w$ (kPa) on the specimen. The air pressure u_a is applied via the perforated porous top heating plate (Figures 6.8a and 6.8b). The water potential u_w is controlled by means of liquid phase (water) transfer through a saturated air-water interface CA membrane - which is permeable to dissolved salts (Figure 6.8a). The properties of the used CA membrane are listed in Table 6.7. As the AEV of the CA membrane is 400 kPa, the setup can only be used for matric suction ψ_m measurements lower than 400 kPa. With the addition of the closed-system ATT to control the matric suction of the specimen, the thermal conductivity of the porous materials can be determined accurately at unsaturated as well as fully saturated conditions at high temperature states, which is difficult to achieve with an open-cell apparatus due to moisture migration and evaporation effects when the porous materials are heated.

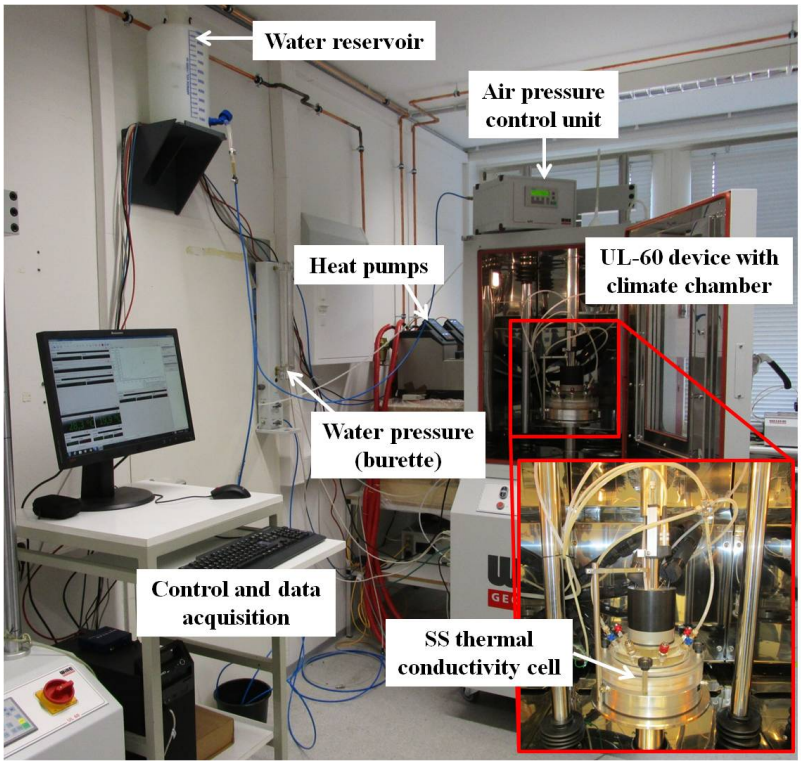

Figure 6.7: Modified (second) version of the steady state thermal conductivity measurement setup.

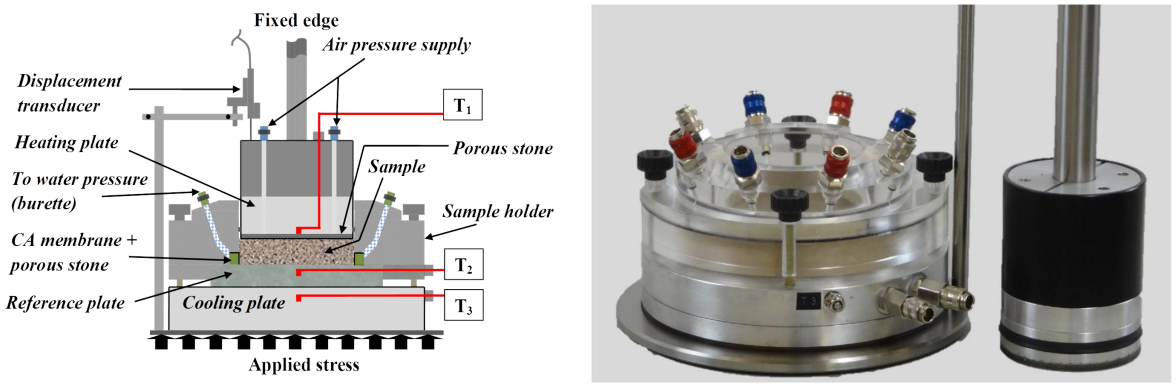

(a) (b)

Figure 6.8: Schematic representation a) and view of the bottom cooling plate, Plexiglas sample holder and top heating plate b) of the modified (second) version of the steady state thermal conductivity cell.

Table 6.7: Properties of the cellulose acetate membrane.

Max. pore size (μm)	Air-entry value, AEV (kPa)	Thermal stability
0.20	400	Up to 180°C

The same formulations (Equations 6.9 - 6.13 and Figure 6.6b) used for obtaining the thermal conductivity and the average temperature of the specimen with the first

version also apply for the modified (second) version of the steady state device. Thermal conductivity measurements obtained using the second version of the steady state device under controlled matric suction conditions and elevated temperatures are presented in Hailemariam and Wuttke (2018b).

6.3.2 Dielectric measurements

For obtaining the complex dielectric permittivity of the porous materials investigated in this thesis, the open-ended coaxial line technique was employed with both the TDR and VNA devices within the stable frequency range of 1 MHz - 10 GHz at room temperature conditions. At frequencies above 10 GHz, the complex dielectric permittivity measurements are highly affected by radiation effects of the probe, hence frequencies above 10 GHz are not considered in this study. The open-ended coaxial line technique provides a non-destructive determination of the dielectric spectra of porous media (Schwing et al., 2010). The technique was originally developed for broadband determination of dielectric properties of biological tissues (Stuchly and Stuchly, 1980; Marsland and Evans, 1987) as well as for microwave dielectric spectroscopy of fluids (Kraszewski et al., 1983; Wei and Sridhar, 1991), for food quality assessment (Kent and Knöchel, 2004; Schimmer et al., 2009), for geotechnical and physical soil behavior analysis (Chen and Or, 2006; Wagner et al., 2014), etc. An extensive review of dielectric spectrometric techniques including the open-ended coaxial technique was provided by Kaatze and Feldman (2006).

The reflection coefficient measured by a HF-EM device as the electromagnetic field around the open-ended coaxial probe opening fringes from the interface to the surrounding specimen can be used to obtain the complex dielectric permittivity of the material (Stuchly and Stuchly, 1980; Stuchly et al., 1982a). The complex impedance Z^* (ω,T) or admittance Y^* (ω,T) at the interface between the flat end of the open-ended probe and the specimen, which depends on the probe geometry and specimen dielectric properties, is related to the complex reflection coefficient Γ^* (ω,T) as:

$$Z^* = \frac{1}{Y^*} = Z_o \frac{1 - \Gamma^*}{1 + \Gamma^*} \tag{6.14}$$

where $Z_o = 50\ \Omega$ is the real characteristic impedance of the probe. However, due to errors from the connections of the coaxial probe, type of probe head and coaxial line used etc, it is difficult to determine the true reflection coefficient Γ^* (ω,T) at the aperture plane, and hence the actual measured complex reflection coefficient S_m^* (ω,T) is different from the true reflection coefficient Γ^* (ω,T) (Stuchly and Stuchly,

1980; Stuchly et al., 1982a). In order to correct these systematic errors, a calibration procedure should be performed prior to the determination of the dielectric spectra (Blackham and Pollard, 1997). Two typically used approaches are: i) a two stage calibration procedure, where during the first stage the true reflection coefficient Γ^* (ω,T) is determined by calibration with three known reflection coefficients S^* (ω,T) and a second stage where the dielectric permittivity is obtained by means of a theoretical or a numerical formulation of the open-ended coaxial line system with an infinite ground plane and with a semi-infinite specimen size (Otto and Chew, 1991; Sheen and Woodhead, 1999; Popovic et al., 2005; Wagner et al., 2014), and ii) a single stage calibration procedure, which is based on a bilinear relationship between measured reflection coefficients S_m^* (ω,T) and relative complex dielectric permittivities ε_r^* (ω,T) of appropriate reference materials (Bao et al., 1994; Kaatze, 2010; Wagner et al., 2014).

In this thesis, a calibration procedure based on approach ii) was employed to avoid instabilities in the determination of the broadband relative effective complex permittivity of the porous media due to assumptions in the theoretical formulation of the inverse problem and the employed numerical implementation of the open-ended coaxial probe.

Prior to the bilinear (permittivity) calibration and the subsequent measurements of complex dielectric permittivity of the porous media, full one port three-term corrections were done mechanically with Open, Short and 50 Ω-Match or Load calibrations at the TDR - coaxial line SMA connector level and at the coaxial line - probe N (m) connector level for the TDR and VNA, respectively, to minimize errors in measurement resulting from the devices. The three-term calibrations were performed following the standard procedure by Rhode & Schwarz N - 50 Ω ZV-Z21. Then after the open-ended coaxial probe (with 2.2 mm diameter and 175 mm length) was connected to the ends of the calibrated coaxial lines and the single stage bilinear calibration procedures were performed by measuring the complex scattering coefficients S_m^* (ω,T) of air (open) - distilled water - short circuits for the TDR and air (open) - distilled water - pure methanol - short circuits for the VNA. The depth of penetration of the EM waves and the distribution of electric field using an open-ended coaxial probe typically reaches more than 14 mm inside the sample (Wagner et al., 2011a; Hailemariam et al., 2017).

The relative complex dielectric permittivity of a material ε_r^* (ω,T) can be obtained from the measured complex reflection factor S_m^* (ω,T) using the bilinear Equation 6.15 with complex calibration parameters c_1, c_2 and c_3 (ω,T) (see appendix B).

$$\varepsilon_r^* = \frac{c_1 S_m^* - c_2}{c_3 - S_m^*} \tag{6.15}$$

6.3.2.1 Time domain reflectometry (TDR)

The TDR measurements in this thesis were carried out with a Sequid STDR-65 device (Figure 6.9), which has a resolution of $10\,\mathrm{ps}$ and a sampling interval of $50\,\mathrm{ns}$.

Figure 6.9: Portable Sequid STDR-65 device.

The TDR acquires step-like time domain curves, which are then pre-processed and transmitted to a laptop computer, which transforms the signals to the frequency domain using the fast Fourier transform (FFT) and carries out the permittivity calculations (Wagner et al., 2011b). The bilinear permittivity calibrations were performed by measuring the complex scattering parameters S^*_m (ω,T) of three reference materials (i.e. air/open, distilled water and a short circuit). Each calibration standard was measured using 10 averages.

For the open-water-short (OWS) calibration, substituting the short parameters ($\Gamma^* = -1$ and $S^*_m = S^*_{m,s}$) into Equations B.6 - B.9, we have:

$$c_3 = S^*_{m,s} \tag{6.16}$$

where, the subscript s represents short. Substituting the open ($\varepsilon^*_r = \varepsilon^*_{r,o} = 1$ and $S^*_m = S^*_{m,o}$) and water ($\varepsilon^*_r = \varepsilon^*_{r,w}$ and $S^*_m = S^*_{m,w}$) parameters into Equation 6.15, we have:

$$S^*_{m,o}c_1 - c_2 - c_3 = -S^*_{m,o} \tag{6.17}$$

$$S^*_{m,w}c_1 - c_2 - \varepsilon^*_{r,w}c_3 = -\varepsilon^*_{r,w}S^*_{m,w} \tag{6.18}$$

where, the subscripts o and w represent open and water, respectively, and $\varepsilon^*_{r,w}$ is the known relative complex dielectric permittivity of water. The procedure for obtaining the relative complex dielectric permittivity of water has been discussed in detail

in section 3.4.1. As the complex dielectric permittivity of water is temperature dependent, the temperature of the distilled water used for the calibration was measured and used to calculate the frequency and temperature dependent complex dielectric permittivity of the water. Solving the set of complex equations (i.e. Equations 6.16 - 6.18) gives c_1, c_2 and c_3. After obtaining these three complex parameters, the unknown relative effective complex permittivity $\varepsilon^*_{r,eff}$ of the porous medium at each frequency point and temperature can be found from the measured effective complex scattering parameter $S^*_m = S^*_{m,eff}$ (ω,T) of the porous medium using Equation 6.15 as:

$$\varepsilon^*_{r,eff} = \frac{c_1 S^*_{m,eff} - c_2}{S^*_{m,s} - S^*_{m,eff}} \tag{6.19}$$

with

$$c_1 = \frac{\varepsilon^*_{r,w}(S^*_{m,s} - S^*_{m,w}) - S^*_{m,s} + S^*_{m,o}}{S^*_{m,w} - S^*_{m,o}} \tag{6.20}$$

$$c_2 = \frac{\varepsilon^*_{r,w} S^*_{m,o}(S^*_{m,s} - S^*_{m,w}) - S^*_{m,w}(S^*_{m,s} - S^*_{m,o})}{S^*_{m,w} - S^*_{m,o}} \tag{6.21}$$

Although the complex scattering matrix only takes into account the connector of the coaxial line to the probe, Bao et al. (1994) showed that other elements, such as the effects of the probe and sample container, can also be eliminated.

6.3.2.2 Vector network analyzer (VNA)

The VNA measurements in this thesis were carried out with a VNA Master MS2027C network analyzer (Figure 6.10).

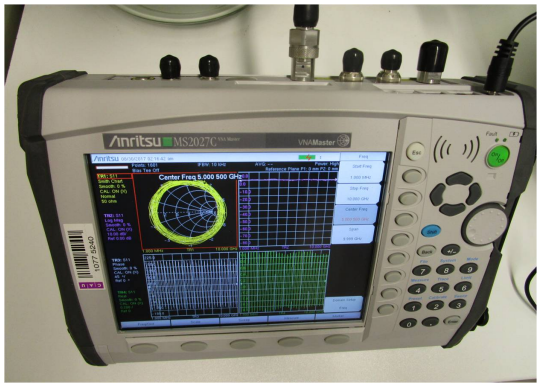

Figure 6.10: VNA Master MS2027C network analyzer.

The bilinear permittivity calibrations were performed by measuring the complex scattering parameters S^*_m (ω,T) of three reference materials (i.e. air/open, distilled water and pure methanol), in order to avoid the limitations of the OWS calibration at high frequency ranges (> 500 MHz) due to inaccuracy of the short calibration. Moreover, the purity of the methanol standard in the open-water-liquid (OWL) calibration procedure at frequencies below 500 MHz was checked by measuring an additional short circuit. For this OWL calibration procedure, Equations 6.16 - 6.18 can be rewritten as:

$$S^*_{m,o}c_1 - c_2 - c_3 = -S^*_{m,o} \tag{6.22}$$

$$S^*_{m,w}c_1 - c_2 - \varepsilon^*_{r,w}c_3 = -\varepsilon^*_{r,w}S^*_{m,w} \tag{6.23}$$

$$S^*_{m,m}c_1 - c_2 - \varepsilon^*_{r,m}c_3 = -\varepsilon^*_{r,m}S^*_{m,m} \tag{6.24}$$

or as:

$$\begin{pmatrix} S^*_{m,o} & -1 & -1 \\ S^*_{m,w} & -1 & -\varepsilon^*_{r,w} \\ S^*_{m,m} & -1 & -\varepsilon^*_{r,m} \end{pmatrix} \begin{pmatrix} c_1 \\ c_2 \\ c_3 \end{pmatrix} = \begin{pmatrix} -S^*_{m,o} \\ -\varepsilon^*_{r,w}S^*_{m,w} \\ -\varepsilon^*_{r,m}S^*_{m,m} \end{pmatrix} \tag{6.25}$$

where, the subscripts o, w and m represent open, water and methanol, respectively, $\varepsilon^*_{r,w}$ and $\varepsilon^*_{r,m}$ are the known relative complex dielectric permittivities of water and methanol, respectively. The procedure for obtaining the relative complex dielectric permittivity of water has been discussed in detail in section 3.4.1. And the relative complex dielectric permittivity of methanol was obtained according to the extensive database provided by Gregory and Clarke (2012). As the complex dielectric permittivities of water and methanol are temperature dependent, the temperatures of the distilled water and pure methanol used for the calibration were measured and used to calculate their frequency and temperature dependent complex dielectric permittivities.

In a compact form, Equation 6.25 can be expressed as:

$$\mathbf{Mc} = \mathbf{e} \tag{6.26}$$

The three complex calibration parameters of the system were solved numerically

using MATLAB as $\mathbf{c} = \mathbf{M}^{-1}\mathbf{e}$. In the case where the system is over-determined due to more than three standard measurements, the inverse of matrix $\mathbf{M}$ has to be rewritten and numerically solved as the least-squares solution $\mathbf{c} = (\mathbf{M}^T\mathbf{M})^{-1}\mathbf{M}^T\mathbf{e}$. After obtaining these three complex parameters, the unknown relative effective complex permittivity $\varepsilon^*_{r,eff}$ of the porous medium at each frequency point and temperature can be found from the measured effective complex scattering parameter $S^*_m = S^*_{m,eff}$ (ω,T) of the porous medium using Equation 6.15 as:

$$\varepsilon^*_{r,eff} = \frac{c_1 S^*_{m,eff} - c_2}{c_3 - S^*_{m,eff}} \tag{6.27}$$

The relative error of the obtained complex dielectric permittivity depends on the accuracy of the HF-EM device, types of coaxial cables and connectors used, employed inversion algorithms etc. The measured complex dielectric permittivity at frequencies below 200 MHz is stable and the resultant relative error is lower than 3% (Wagner et al., 2010; Wagner et al., 2011a). Whereas, for frequencies higher than 200 MHz, the relative error is of the order of 5% due to mismatches between the coaxial line, connectors and probe (Wagner et al., 2011a).

Figures 6.11a and 6.11b show the absolute value and phase shift (displacement) of the complex scattering coefficient of the used calibration standards, respectively. At low frequencies, the scattering coefficients are close and difficult to differentiate. However, at higher frequencies, the differences are distinct.

In Figures 6.11c and 6.11d, the real and imaginary parts of the relative complex dielectric permittivities of the calibration standards are shown. As expected, a good signal-to-noise ratio was recorded for all the measured calibration standards in the considered frequency range. Moreover, as the sensitivity of the open-ended coaxial line probe to determine the complex dielectric permittivity at frequencies lower than 100 MHz was found to be quite low, results below 100 MHz frequency have not been shown. Possible factors affecting the insensitivity of the probe at very low frequencies are the dependence on the dynamic range of the instrument, probe geometry and radiation effects, used averaging factor (if any) as well as the carefulness of the calibration and the measurements. The dielectric spectra of the employed OWL-short calibration standards are in close agreement with the expected theoretical spectra of the reference materials (Figures 6.11c and 6.11d).

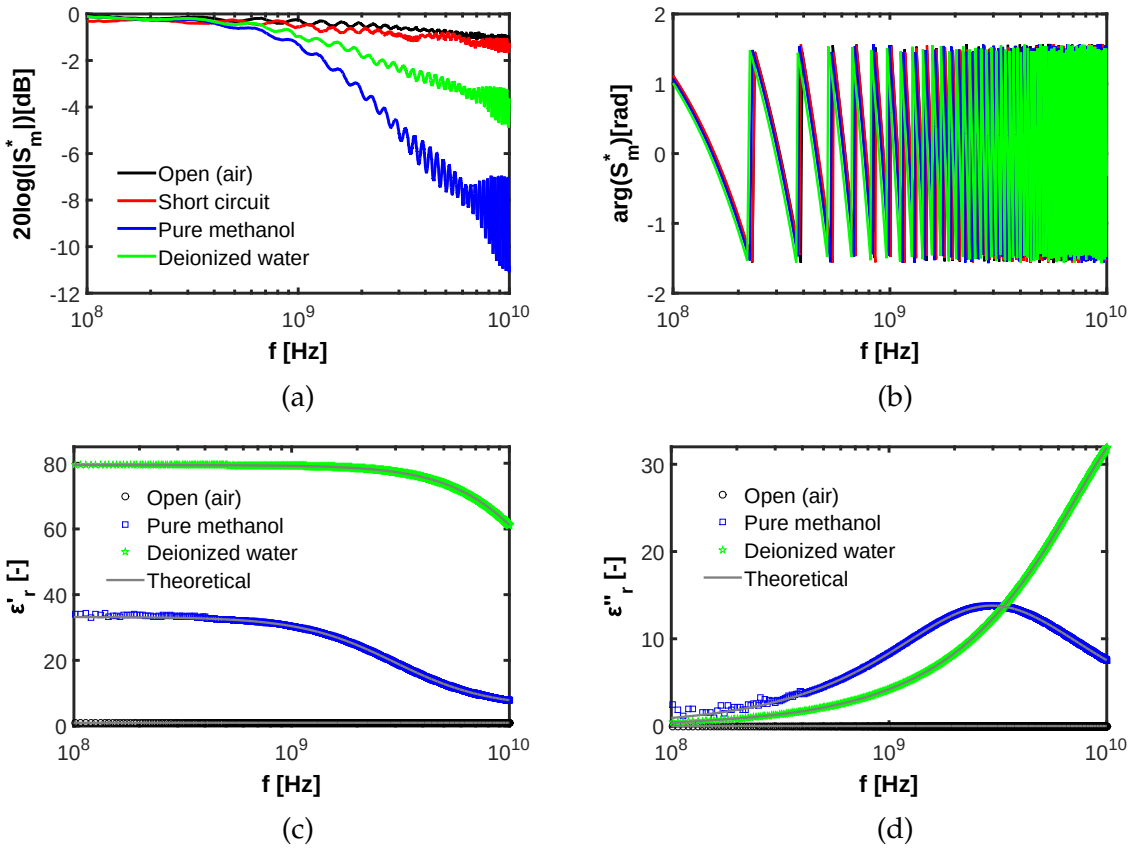

Figure 6.11: Absolute value a) and phase shift b) of the complex scattering parameter S_m^*, real ε_r' c) and imaginary ε_r'' d) parts of the relative complex dielectric permittivities of the OWL-short calibration standards as functions of frequency.

6.3.2.3 Matric suction and effective stress modifications

The simultaneous measurements of complex dielectric permittivity or conductivity, deformation, vertical stress and other porous media hydro-mechanical conditions were obtained using a new approach, by fitting the open-ended coaxial line probe (connected with the HF-EM device i.e. TDR/VNA) horizontally in to one-dimensional controlled loading consolidation cells. As in the thermal conductivity measurements, the devices where developed in two stages, i.e. with and without matric suction provisions, as discussed next.

With no matric suction control

The first version of the newly developed one-dimensional consolidation & EM cell for measuring the complex dielectric permittivity of porous media is shown in Figures 6.12 and 6.13.

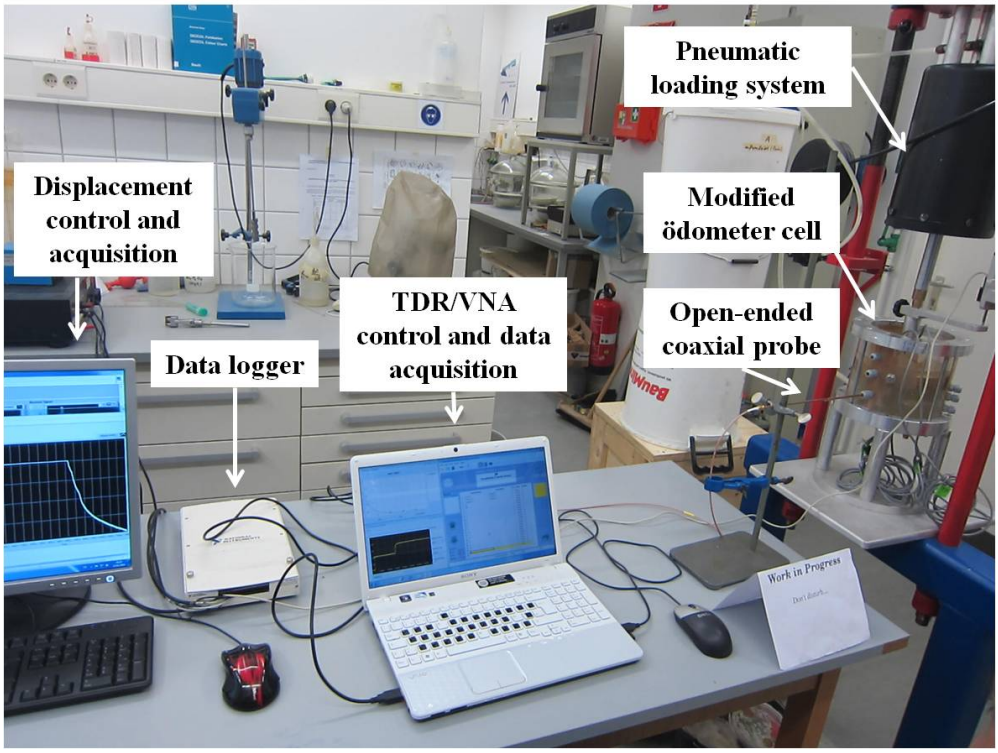

Figure 6.12: First version of the one-dimensional consolidation & EM cell setup.

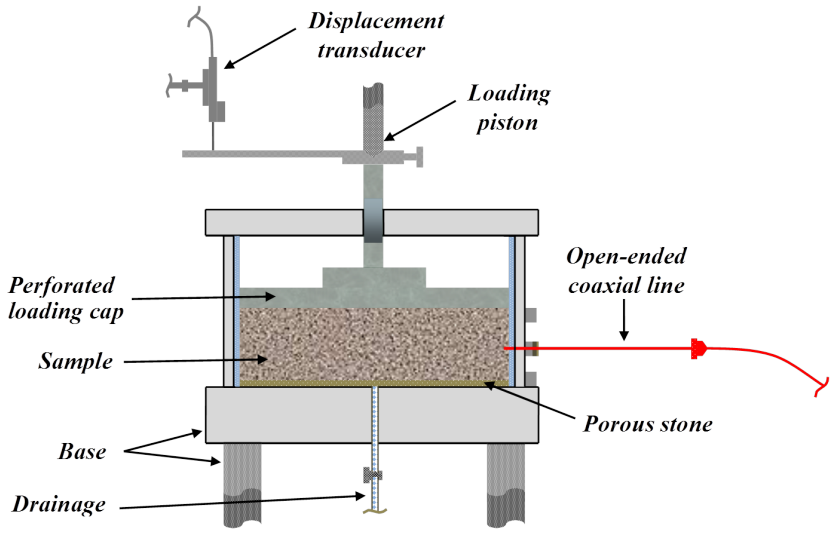

Figure 6.13: Schematic representation of the first version of the one-dimensional consolidation & EM cell setup.

The setup has no provisions for controlling the matric suction of the investigated specimen, and hence is suitable for use in two-phase (dry/saturated) and in unsaturated media with negligible moisture migration upon changes in porous media thermo-hydro-mechanical conditions. The apparatus consists of a cylindrical test box

(with dimensions of 154 mm diameter and adjustable height of 30 - 90 mm) with a perforated top loading cap and a bottom drainage system for specimen saturation, which can be connected to a burette or a water reservoir, and an open-ended coaxial probe, which is inserted horizontally to the cylindrical text box (Figure 6.13). Depending on the specimen height, the position of the open-ended coaxial probe can be adjusted vertically, thus avoiding any boundary interference on the EM measurements. Tests can also be performed with smaller sample sizes by fitting smaller steel consolidation rings (with typical dimensions of 50 or 70 mm diameter and heights between 20 and 50 mm) to the setup. The perforated loading cap allows the application of load on the specimen without hindering the movement of pore-water out of the specimen during consolidation tests. The perforated loading cap can also be used as part of a leaching apparatus when determining the settlement potential of loess porous media, where the water flows from the bottom drainage in to the specimen and is then collected via the perforated loading cap for analysis of electrical conductivity at regular intervals to determine the completion of the water-driven settlement of the porous medium (i.e. when the electrical conductivity measurements show no further decrease or when the change in the specimen deformation is negligible).

The test box has an outer steel frame with an inner lining of Plexiglas. The outer steel frame avoids lateral bending that may occur at higher loads. As the deformation behavior of the porous medium depends considerably on the stiffness and roughness of the walls of the test box, the use of the Plexiglas inner lining helps to limit the amount of shear stress developed between the glass walls and the porous medium specimen, ensuring that actual plane-strain conditions are met. Vertical stress is applied to the specimen via a piston connected to a pneumatic air pressure system which is operated manually (Figure 6.12). Alternatively, the consolidation cell can also be fitted to a UL-25 automatic loading machine for the application of vertical stress. The vertical displacement of the specimen can be measured via a TR-0050/TRS-0050 linear transducer with a defined electrical range of $50\,\mathrm{mm}$, an independent linearity of $\pm 0.15\%$ and repeatability of $2\,\mu\mathrm{m}$, or a TRS-0025 linear transducer with a defined electrical range of $25\,\mathrm{mm}$, an independent linearity of $\pm 0.2\%$ and repeatability of $2\,\mu\mathrm{m}$, and the data is stored in a data logger connected to the system (Figure 6.12).

With matric suction control

The second version of the one-dimensional consolidation & EM cell for measuring the complex dielectric permittivity of porous media (Figures 6.14 and 6.15) was developed by modifying a suction-controlled ödometer cell by inserting an open-ended coaxial probe horizontally to the specimen consolidation ring of the cell. The matric

suction in the ödometer cell is controlled via the axis translation technique (ATT), as explained in section 6.3.1.2. The provision for controlling the matric suction of the specimen with the ATT enables the determination of the complex dielectric permittivity of the specimen at different levels of moisture content/matric suction.

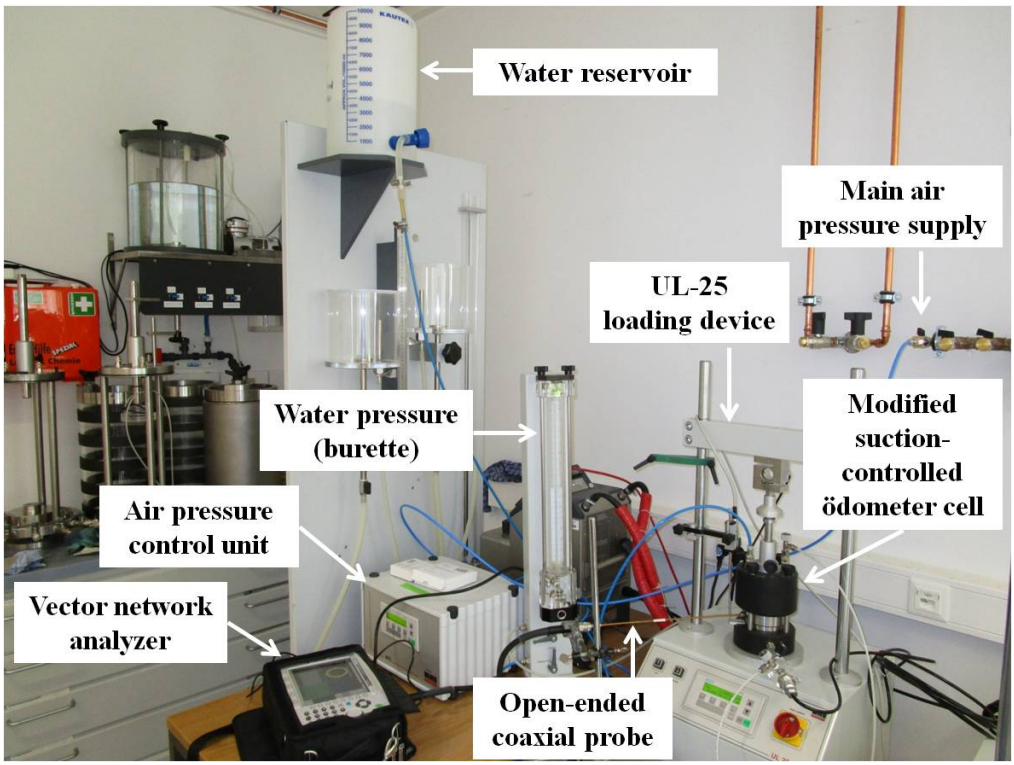

Figure 6.14: Second version of the one-dimensional consolidation & EM cell setup.

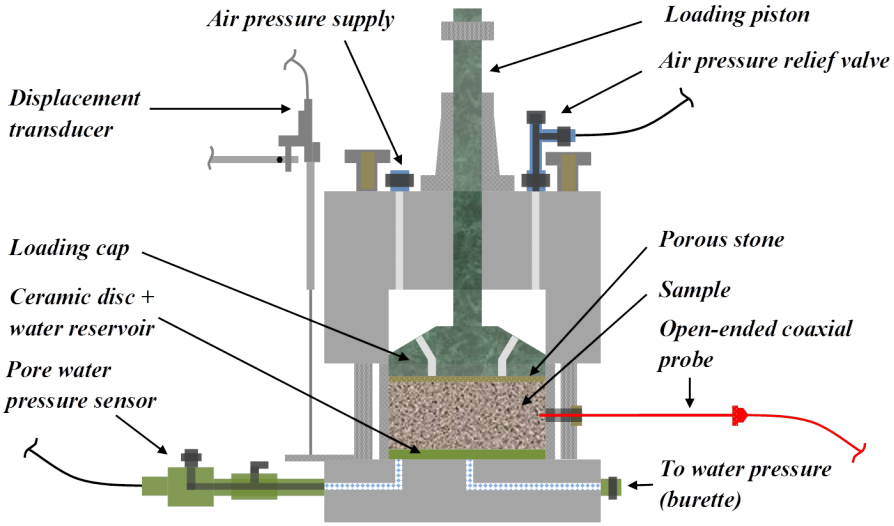

Figure 6.15: Schematic representation of the second version of the one-dimensional consolidation & EM cell setup.

The axis translation technique is introduced to the system by applying controlled pore-air u_a (kPa) and pore-water u_w (kPa) pressures to the system (Figure 6.15), thus imposing the desired level of matric suction $\psi_m = u_a - u_w$ (kPa) on the specimen (with dimensions of 70 mm diameter and adjustable height of 25 - 50 mm). The air pressure u_a is applied via the top porous stone and the water potential u_w is controlled by means of liquid phase (water) transfer through a saturated air-water interface ceramic disc with an air-entry value (AEV) of 400 kPa and a thickness of 5 mm. Vertical stress (with a maximum force limit of 25 kN) can be applied to the specimen via the UL-25 loading machine integrated with the system (Figure 6.14). The vertical displacement of the specimen is measured via a TRS-0025 linear transducer with a defined electrical range of $25\,\mathrm{mm}$, an independent linearity of $\pm 0.2\%$ and repeatability of $2\,\mu\mathrm{m}$. The pore-water pressure in the specimen can be monitored during the test via a pore-water pressure sensor attached to the bottom of the specimen. The applied vertical stress, specimen displacement and the pore-water pressure data are monitored and stored with a PC and a data acquisition unit.

The apparatus can be used to accurately determine the complex dielectric permittivity of porous media with two-phase or at unsaturated states and effective stress conditions. Dielectric measurements performed using the second version of the one-dimensional consolidation & EM cell will be presented in separate publications.

6.4 Experimental procedure

In this section, the experimental procedure followed in performing the thermal and dielectric measurements of the un-cemented porous media (i.e. the silty clay and loess soils as well as the oil sand) studied in this thesis (section 6.2) using the different techniques of measurements (section 6.3) is presented.

6.4.1 Tests on soils

6.4.1.1 Tests on silty clay soils

The tests on the silty clay soils (section 6.2.1.1) were performed for analyzing the behavior and correlation of the thermal and dielectric properties of fine-grained soils under varying moisture content conditions.

Three silty clay soil samples (one from each silty clay soil) were incrementally wetted from air dry up to saturation by adding a controlled amount of distilled water required for each gravimetric water content and were then allowed to equilibrate for 24 hours. From the prepared samples, subsamples were taken for simultaneous measurements of thermal conductivity (using the TR-1 single transient needle probe, section 6.3.1.1) and complex dielectric permittivity (using the VNA device, section 6.3.2.2) for each gravimetric water content.

The dry density/porosity of each soil was kept constant for all gravimetric water contents (see Table 6.1). Care was taken to pack the soils with a homogeneous bulk density (throughout the specimen volume) and to a constant volume, and a total of 108 measurements of thermal conductivity and complex dielectric permittivity were taken. The measurements were repeated at least three times for each subsample for verification.

Moreover, to verify the accuracy of the experimental measurements of transient thermal conductivity of the silty clay soils, steady state measurements of thermal conductivity of the soils were performed at both dry and saturated conditions using the first version of the steady state device (section 6.3.1.2). The samples (with dimensions of 100 mm diameter and heights of around 30 and 34 mm for dry and saturated conditions, respectively) were placed carefully in to the thermal cell making sure that the bulk density was homogeneous throughout the specimen volume. The temperatures of the top heating and bottom cooling plates were set to the desired values, and once steady state conditions were achieved, the recorded temperatures of the reference plate were used to obtain the steady state thermal conductivity of the samples. The measurement data was automatically recorded at an interval of 5 seconds for each test.

6.4.1.2 Tests on loess soil

The loess soil (section 6.2.1.2) investigated in this thesis was used for analyzing the behavior and correlation of the thermal and dielectric properties of weak soils under varying moisture, porosity, matric suction, effective stress and for verifying the new models for estimating the settlement potential of weak porous media using thermal and dielectric measurements. The complex dielectric permittivity measurements on the loess soil were done with the TDR and VNA devices, whereas, the thermal conductivity measurements were obtained using the transient and steady state techniques. As shown by the results in section 7.2.2, the TDR and VNA measurements of complex dielectric permittivity as well as the transient and steady state thermal

conductivity data of the loess soil are in close agreement.

Variations with water content and porosity

The loess soil was prepared under the two remolded conditions, namely in its natural condition, L-A (with a porosity $n = 0.453$ and bulk dry density $\rho_d = 1.495\,\mathrm{g\,cm^{-3}}$) and the lab compacted condition, L-B (with a porosity $n = 0.301$ and bulk dry density $\rho_d = 1.913\,\mathrm{g\,cm^{-3}}$). Two loess soil samples (one from each remolded condition) were incrementally wetted from air dry up to saturation by adding a controlled amount of distilled water required for each gravimetric water content and were then allowed to equilibrate for 48 hours. From the prepared samples, subsamples were taken for measurements of thermal conductivity (using the TR-1 single transient needle probe, section 6.3.1.1) and complex dielectric permittivity (using the TDR device, section 6.3.2.1) for each gravimetric water content. Furthermore, the matric suction ψ_m (kPa) of the subsamples was simultaneously measured using the filter paper method as discussed in the next section, to study the relationship between the drying path matric suction of the SWCC and the thermo-dielectric parameters of the loess soil.

The dry density/porosity of each loess soil sample was kept constant for all gravimetric water contents (see Table 6.3). Care was taken to pack the soils with a homogeneous bulk density (throughout the specimen volume) and to a constant volume, and a total of 36 measurements of thermal conductivity and complex dielectric permittivity were taken. The measurements were repeated at least three times for each subsample for verification.

Variations with matric suction

The drying path matric suction ψ_m for the simultaneous measurements of thermal conductivity and complex dielectric permittivity was performed via the filter paper method. As discussed in the previous section, the correlation between the thermal conductivity (using the TR-1 single transient needle probe, section 6.3.1.1) and complex dielectric permittivity (using the TDR device, section 6.3.2.1) and the simultaneous measurement of the drying path of the SWCC of the loess soil (with porosities n of 0.453 and 0.301) via the filter paper method was performed on the same subsamples used for the water content and porosity studies. The filter paper matric suction measurement procedure was performed following the guidelines of the ASTM D 5298 - 94 (1994) standard. In order to obtain the drying/desorption curve of the soils, initially wet filter papers were used (Note that for obtaining the wetting/adsorption curve, the filter papers must be initially dried before contact with the soil). Care was taken

when measuring the matric suction, because intimate contact between the filter paper and the loess soil subsamples is very significant for the determination of matric suction by the filter paper technique. Once the proper contact between the filter paper and the loess soil subsamples was ensured, the soil suction measurement setup was kept in a temperature controlled environment with fluctuations kept within $\pm 1^{\circ}$C, for at least one week to achieve steady state conditions. The filter paper moisture content measurements were conducted by two persons in order to decrease the time of exposure of the filter papers to the laboratory atmosphere, and thus, the amount of moisture lost/gained during the measurements was kept to a minimum. The moisture content of the filter papers was weighed to the nearest 0.1 mg accuracy, and the matric suction of the subsamples was determined according to the appropriate filter paper calibration curves as given by ASTM D 5298 - 94 (1994).

Variations with effective stress

The correlation between the thermal conductivity (using the first version of the steady state device, section 6.3.1.2) and complex dielectric permittivity (using the TDR device along with the first version of the one-dimensional consolidation & EM cell, section 6.3.2.3) at different effective stress conditions was performed on the loess soil in drained conditions with its natural porosity n of 0.453 and at optimum gravimetric moisture condition w (around 0.18 for maximum dry density from standard Proctor test). The specimens for the thermo-dielectric tests were taken from a loess soil sample which was initially at natural moisture condition $w_n = 0.093$, but was incrementally wetted to achieve optimum gravimetric moisture condition. After allowing the new mix to equilibrate for around 48 hours, sub-samples were taken from each specimen for gravimetric water content check, and an average gravimetric water content w of 0.186 was obtained.

For both the steady state test and one-dimensional consolidation & EM cell setups, the specimens (with dimensions of 100 mm diameter and height of 30 mm for the thermal tests and 154 mm diameter and height of 60 mm for the dielectric tests) were placed carefully in to the consolidation cells making sure that the bulk density was homogeneous throughout the specimen volume. The effective stress was then increased with increments to the values of 1/5, 12, 25, 50, 100, 200 and 400 kPa, which was then followed by unloading to 100, 25 and 1/5 kPa. Load increment (stabilization) times of around 45 and 5 minutes (after which time the deformations due to the load increments were considered insignificant) were alloted for attaining steady state temperature conditions and for the stabilization of stress of the steady state thermal

and complex dielectric permittivity measurements, respectively. The thermal conductivity of the specimen was automatically recorded at an interval of 5 seconds, while the complex dielectric permittivity measurements were taken manually before and after each load increment to observe the changes in the measured values of the complex dielectric permittivity due to each load increment. The specimen deformation data for the dielectric measurements was automatically recorded at an interval of 0.04 seconds.

Variations with water-driven settlement potential

The correlation between the thermal conductivity (using the TR-1 single transient needle probe, section 6.3.1.1) and complex dielectric permittivity (using the VNA device, section 6.3.2.2) at various water-driven settlement potentials was performed on the loess soil in drained conditions with its natural porosity n of 0.453 and at different initial gravimetric moisture conditions by following ASTM D 5333 - 03 (2003) standards.

A total of 36 water-driven settlement potential tests were performed on the loess soil at moisture contents ranging from air dry to saturated conditions. The loess soil specimens were prepared by adding a controlled amount of the desired quantity of distilled water required for each gravimetric water content and were then allowed to equilibrate for 48 hours. Prior to the placement of the samples in the consolidation cell, sub-specimens were taken from the specimens for the simultaneous measurement of thermal conductivity of each specimen at the desired porosity and gravimetric water content using the TR-1 probe. The thermal measurements were repeated at least three times for each sub-specimen for verification. These thermal measurements of each of the equilibrated specimens correspond to the water-driven settlement potential values of each specimen. After placing the specimens in the first version of the one-dimensional consolidation & EM apparatus (section 6.3.2.3) by making sure that the bulk density was homogeneous throughout the specimen volume, the complex dielectric permittivity of each of the equilibrated specimens, which correspond to the water-driven settlement potential values, were then measured and recorded via the VNA device + open-ended coaxial line integrated with the consolidation cell. The dielectric measurements were repeated at least three times for each specimen for verification. Then after, the model standard collapse load of 300 kPa was applied to each specimen and sufficient time was alloted until the changes in specimen deformation due to the applied collapse load was insignificant. Finally, each specimen was inundated via the bottom drainage valve with distilled and de-aired water from an overhead water reservoir to initiate the water-driven settlement process (ASTM D 5333

- 03, 2003; Mansour et al., 2008). The specimen deformation due to the water inundation was automatically recorded every 2 seconds, and the tests were stopped once the settlement due to the addition of water of each specimen was negligible (typically after around 90 - 120 minutes after the addition of water). The total specimen deformation corresponding only to the collapse of the specimens due to water inundation was recorded for verifying the tripartite correlation between thermal conductivity, complex dielectric permittivity and settlement potential of weak soils.

6.4.2 Tests on oil sand

A total of 48 bitumen-water saturated specimens (17 low grade, 17 medium grade and 14 high grade oil sands) of the reconstituted oil sand (section 6.2.2) were prepared for the purpose of analyzing the behavior and correlation of the thermal and dielectric properties of oil sands under varying bitumen-moisture contents. The oil sands were remolded by mixing a fixed weight fraction of a silty sand soil initially with the desired amount of gravimetric distilled water content and then after by adding the required quantity of heated bitumen (up to 80°C) to the resulting mix (water coated solid particles), and were then allowed to equilibrate for 24 hours before the measurements were taken. This technique enables the formation of a thin water film around the solid grains (in addition to the entrapped pore-water), which is typically exhibited by naturally occurring oil sands. The heating of the bitumen was done prior to the mixing process in order to lower its viscosity. The dry density/porosity of all the oil sand specimens was kept constant ($1.949\,\mathrm{g\,cm^{-3}}$), while the grade or bitumen content varied from 6 to 11.64 wt.%.

Care was taken to pack the oil sand specimens with a homogeneous bulk density (throughout the specimen volume) and to a constant volume. The thermal conductivity and specific heat capacity of the oil sand specimens were measured using the SH-1 dual transient needle probe (section 6.3.1.1), and the simultaneous measurements of the complex dielectric permittivity was performed using the VNA device (section 6.3.2.2). The thermal and dielectric measurements were repeated at least three times for each specimen.

6.5 Summary of chapter 6

In this chapter, the experimental program followed to study the thermal and dielectric behavior of the porous media used in this study was discussed in detail. On this basis, the different types of porous media analyzed in this thesis, the thermal and dielectric properties measurement techniques employed and the experimental methodology followed for obtaining the thermal and dielectric parameters were presented.

Chapter 7

Results and discussion I: Validation of semi-analytical models

7.1 Introduction

In this chapter, results of the theoretical and experimental investigations on the behavior and correlation of the thermal and dielectric porous media parameters at different hydro-mechanical conditions are presented. The details of the studied porous media types and the experimental procedures are shown in sections 6.2 and 6.4, respectively.

7.2 Validation of semi-analytical models for soils and other porous media types

7.2.1 Tests on silty clay soils

The results of the electromagnetic measurements on the studied silty clay soils are shown in Figures 7.1 - 7.3. Figure 7.1 shows the variation of the real part $\varepsilon'_{r,eff}$ of the relative effective complex permittivity of the soils at a measurement frequency of 1 GHz with gravimetric water content w. As stated in section 4.2.1, the values of the real part $\varepsilon'_{r,eff}$ of the relative effective complex permittivity at a particular frequency range of around 1 GHz were selected from the spectra, as at this frequency range, information on the free water in the porous medium can be obtained, and the dispersion and absorption processes be compared directly (Blonquist Jr. et al., 2006; Wagner and Scheuermann, 2009; Wagner et al., 2014). Overall, the measured $\varepsilon'_{r,eff}$ of the soils increases with an increase in moisture content, as for the given porosity of each soil, an increase in moisture content indicates the replacement of air with moisture, which has a much higher complex dielectric permittivity than air.

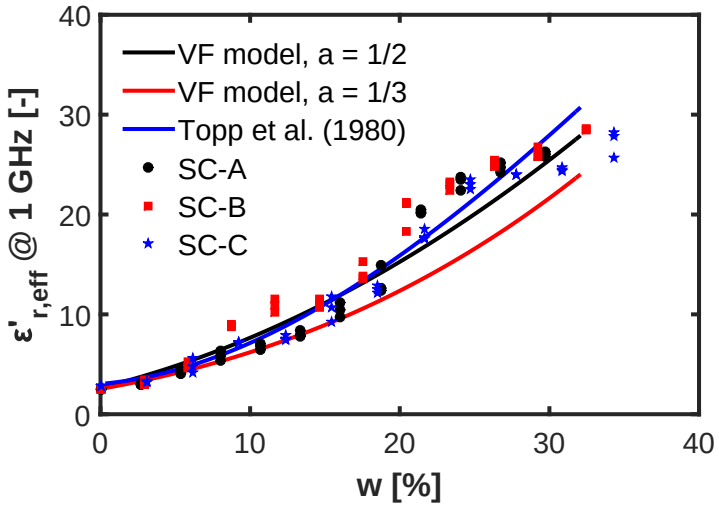

Figure 7.1: Real part $\varepsilon'_{r,eff}$ of the relative effective complex permittivity of the silty clay soils as a function of gravimetric water content w (VF model - Equation 4.3).

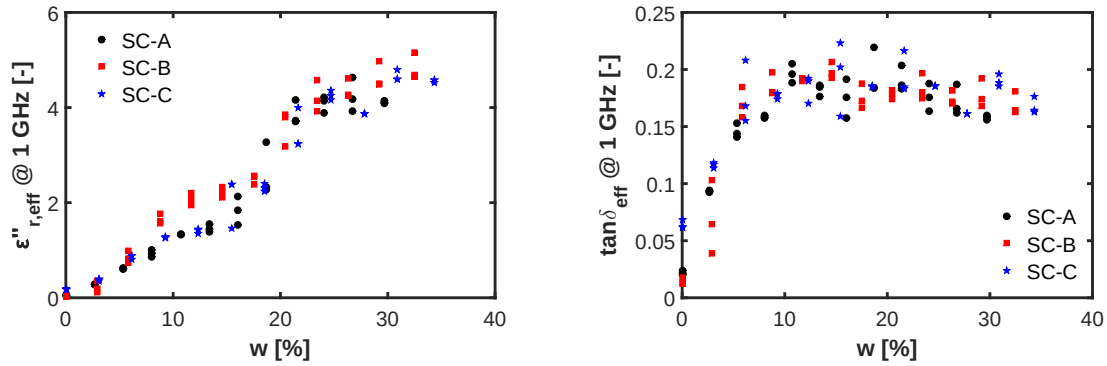

(a) (b)

Figure 7.2: Imaginary part $\varepsilon''_{r,eff}$ of the relative effective complex permittivity a) and effective loss tangent $\tan\delta_{eff}$ b) of the silty clay soils as functions of gravimetric water content w.

Furthermore, in Figure 7.1, the experimental findings are compared to the VF model (Equation 4.3), with structural exponents $a = 1/2$ (CRIM) (Birchak et al., 1974) and $a = 1/3$ (LLLM) (Landau and Lifschitz, 1985; Campbell, 1990), as well as the Topp et al. (1980) model. The predictions from the VF model with exponent $a = 1/2$ and the Topp et al. model match comparatively well with the experimental results as compared to the predictions from the VF model with exponent $a = 1/3$, which considerably underestimates the measured $\varepsilon'_{r,eff}$ at 1 GHz data for the whole range of soil saturation.

The experimental results of the imaginary part $\varepsilon''_{r,eff}$ of the relative effective complex permittivity and the effective loss tangent $\tan\delta_{eff}$ of the three silty clay soils are

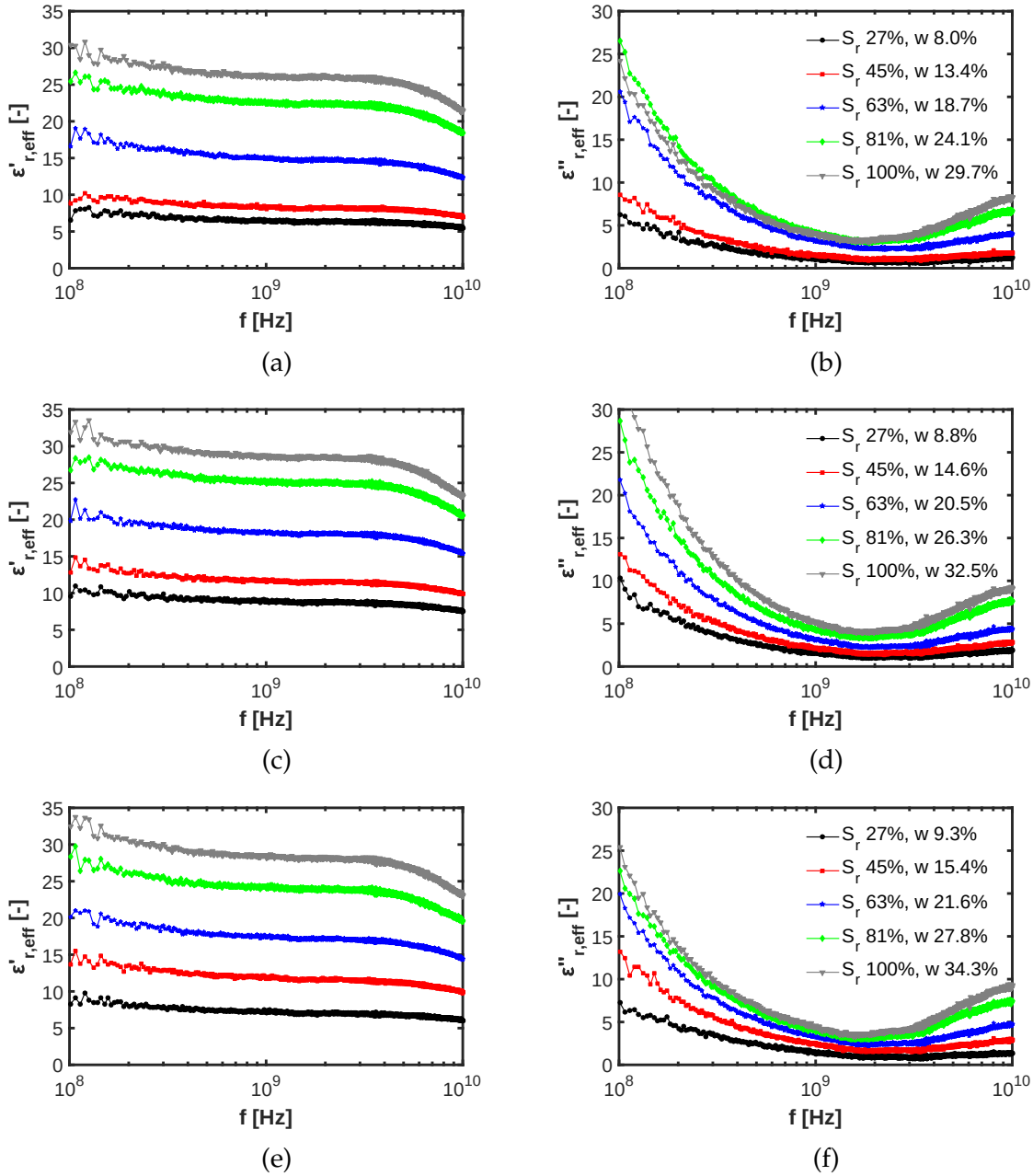

Figure 7.3: Dielectric spectra of the silty clay soils at five gravimetric water contents w: $\varepsilon'_{r,eff}$ a), c) and e), and $\varepsilon''_{r,eff}$ b), d) and f) of SC-A, SC-B and SC-C, respectively (Plotted volumtric water contents θ for: SC-A 11.9, 19.9, 27.9, 35.8 & 44.3%; SC-B 12.5, 20.9, 29.3, 37.6 & 46.4%; and SC-C 12.8, 21.3, 29.8, 38.4 & 47.3%).

shown in Figure 7.2. It is difficult to quantify the imaginary part $\varepsilon''_{r,eff}$ of the relative effective complex permittivity or the effective loss tangent $\tan\delta_{eff}$ of porous media with empirical or theoretical equations, due to the presence of dissolved/aqueous salts in the medium, and hence, only experimental results are shown. Overall, the measured $\varepsilon''_{r,eff}$ and $\tan\delta_{eff}$ of the soils increase with an increase in moisture content. This is to be expected, as for the given porosity of each soil, an increase in moisture

content indicates the replacement of air with moisture, which also increases the degree of solubility of the solutes contained within the solid particles in to the pore water solution, thus increasing the salinity of the pore-water solution of the soils, which results in an increased imaginary part of the complex dielectric permittivity or electrical conductivity of the medium.

In Figure 7.3, the measured dielectric spectra of the relative effective complex permittivity $\varepsilon^*_{r,eff}$ of the silty clay soils at five gravimetric water contents w is presented. In principle, the open-ended coaxial probe and the calibration procedure used in the study enable an accurate determination of the frequency dependence of the complex dielectric permittivity. However, as expected, the accuracy of the measurements below the frequency of 100 MHz and above 10 GHz is substantially low due to probe geometry and radiation effects (Figure 7.3). Generally, all three silty clay soils exhibit a very high degree of variation of complex dielectric permittivity (mainly the imaginary part) with frequency especially at lower frequency ranges, the phenomenon of which is called *dielectric dispersion* or *relaxation*, due to the presence of a high proportion of clay minerals with readily dissoluble salts (16.8 wt.% for SC-A, 20.2 wt.% for SC-B and 24.6 wt.% for SC-C, Table 6.1) (Wagner and Scheuermann, 2009). The magnitude of dielectric dispersion in the frequency range of 0.1 MHz - 1 GHz is defined as the difference in magnitude at high and low frequencies at which the relative effective complex permittivity curve levels off. This value has been shown to be highly influenced by the mineralogical and mineral solution interface characteristics of the porous medium (Arulanandan, 2003).

In summary, the dielectric spectra of all the soils show a typical frequency dependence (with the dielectric dispersion increasing with an increase in soil moisture content, Figure 7.3) with: a) a stronger frequency dependence of the complex dielectric permittivity at low frequency ranges due to the presence of clay minerals; b) a strong decrease in the imaginary part as compared to the real part with increasing frequency below around 1 GHz for all soils, mainly due to electrical induced losses and c) an increase in the imaginary part above around 1 GHz mainly due to main water relaxation contribution (Wagner et al., 2007b; Wagner and Scheuermann, 2009).

Figure 7.4 shows the results of effective thermal conductivity λ measurements of the silty clay soils as a function of gravimetric water content w. The experimental findings of λ are further compared to the modified Johansen model (Equation 4.1), the original Johansen's model (Johansen, 1975) and the Lu et al. (2007) model. The quartz fraction q_f used for calculating the thermal conductivity of the soil solids λ_s in all the models is obtained based on the coarse grain fraction of each silty clay soil (Peters-Lidard et al., 1998; Lu et al., 2007). All three models match the experimental

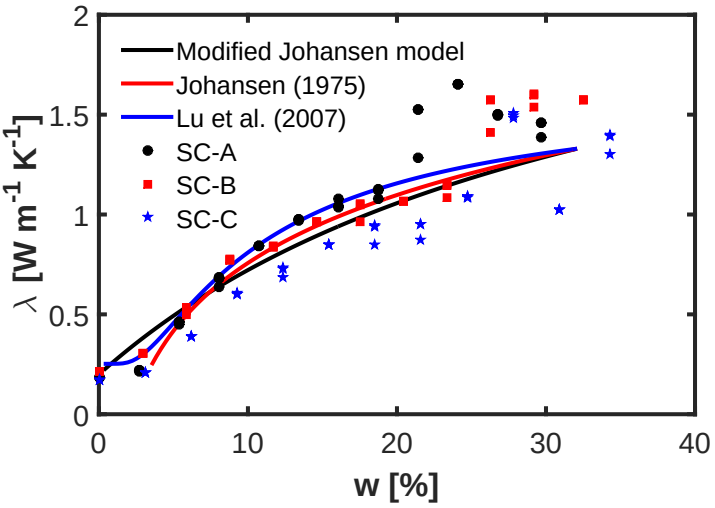

Figure 7.4: Effective thermal conductivity λ of the silty clay soils as a function of gravimetric water content w (Modified Johansen model - Equation 4.1).

measurements of λ with good accuracy below 20% gravimetric water content, but with slight underestimation for gravimetric water contents above 20%. The prediction results of the original Johansen model at low moisture contents are neglected due to its inapplicability for degrees of saturation lower than 20% (see section 2.2.5).

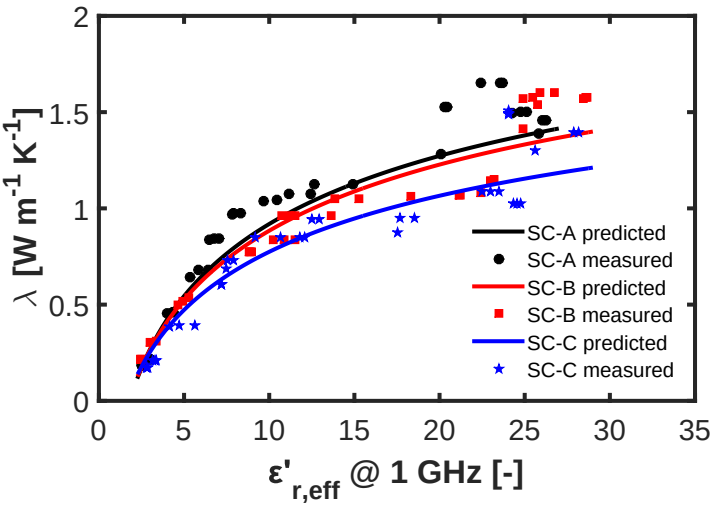

Figure 7.5: Variation of effective thermal conductivity λ with the real part $\varepsilon'_{r,eff}$ of the relative effective complex permittivity of the silty clay soils (New model prediction - Equation 4.7).

Generally, the effective thermal conductivity λ of the silty clay soils increases with an increase in moisture content in three stages. At low gravimetric water content w of up to 3%, the moisture first coats the soil grains. The voids between the soil grains are not rapidly filled, and hence, a gradual increase in λ is exhibited. With further

increase in w of up to 20%, water bridges start to form between the soil particles filling air voids, and λ starts to increase rapidly due to improved contact and increase in heat conduction path between the grains (Sepaskhah and Boersma, 1979). Then after, the increase in λ mainly depends on the replacement of air by water only, and as a result, λ increases at a slower rate.

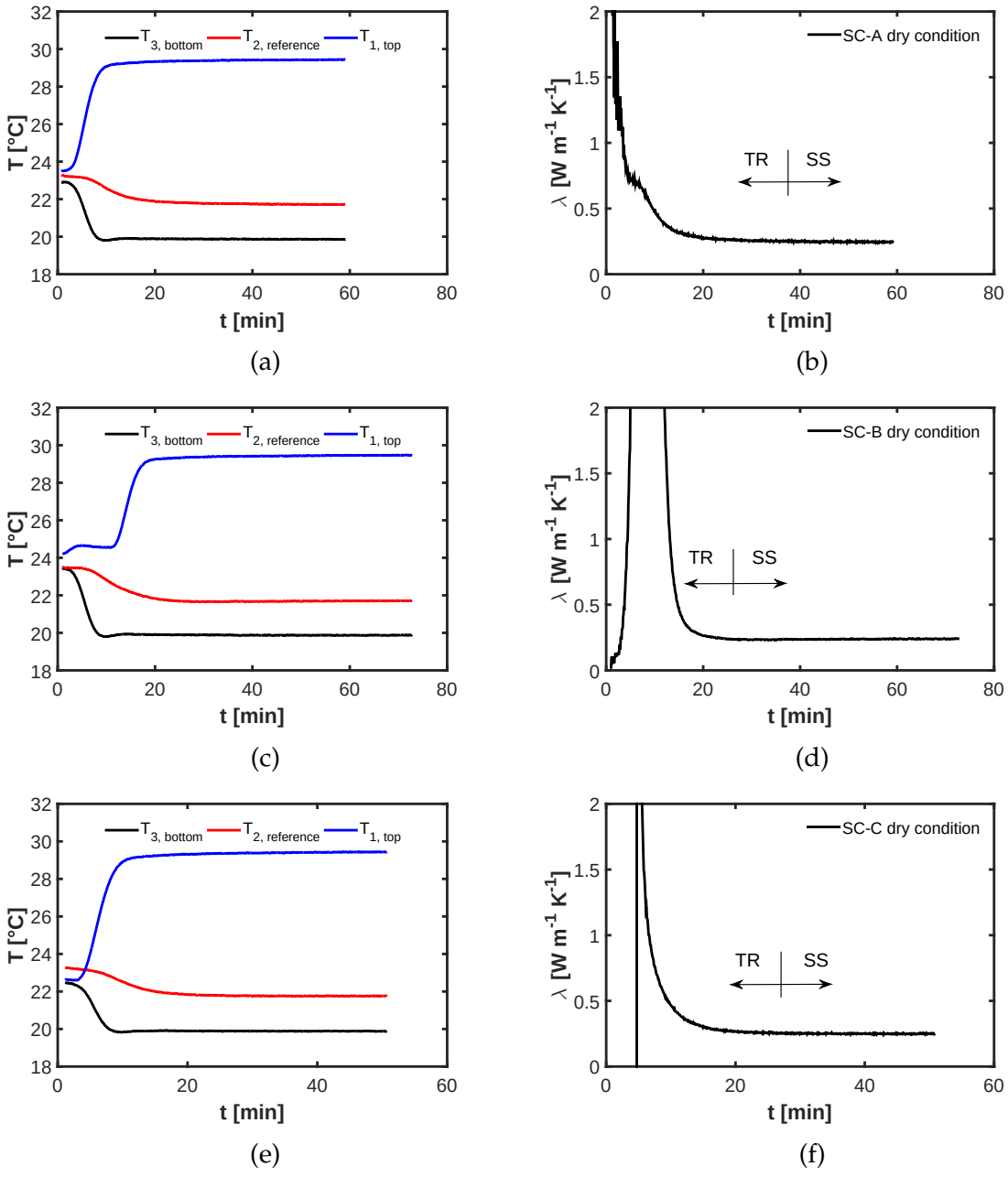

Figure 7.6: Temperature T and effective thermal conductivity λ of the silty clay soils in dry condition as functions of time t.

The comparison of the new model for predicting the thermal conductivity of naturally occurring un-saturated soils from complex dielectric permittivity (Equation 4.7) and experimental data is shown in Figure 7.5. The prediction of the new model

matches well to the experimental findings with a slight underestimation at higher moisture contents (higher $\varepsilon'_{r,eff}$ at 1 GHz). The average errors of prediction of the new model for the three silty clay soils used in this study are: 10.33% for SC-A, 10.44% for SC-B and 14.48% for SC-C (with an overall average of 11.75%).

The results of the steady state thermal conductivity tests which were performed on the silty clay soils (at dry and saturated states) to verify the transient tests are shown in Figures 7.6 and 7.7.

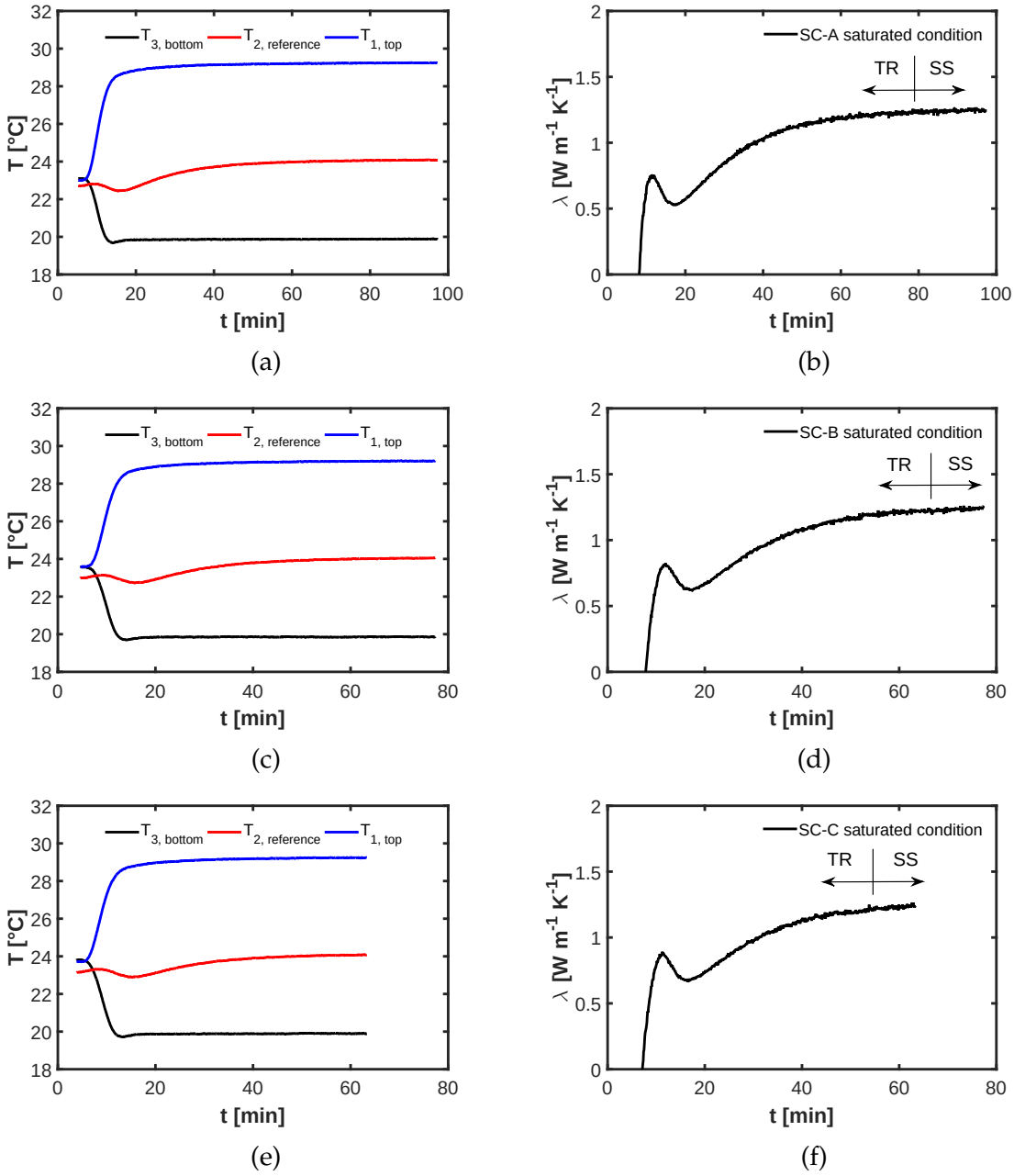

Figure 7.7: Temperature T and effective thermal conductivity λ of the silty clay soils in saturated condition as functions of time t.

The plots show the recorded temperatures of the three plates (i.e. top T_1, reference

T_2 and bottom T_3) of the steady state device (section 6.3.1.2) with the progress of time. A temperature stabilization time of a minimum of around 50 to 60 minutes was alloted for each test to achieve steady state conditions. Using the values of the measured temperatures of the three plates, the effective thermal conductivity λ of the samples is obtained using Equation 6.12.

The measured temperature of the reference disc T_2 and hence the measured effective thermal conductivity λ of the three silty clay soils increase with an increase in moisture content (saturation condition), thus indicating an improvement of the heat conduction path with the addition of moisture. When comparing the transient and steady state measurements for each soil type and saturation condition: the effective transient λ of the three soils ranges from 0.173 to 0.215 $\mathrm{W\,m^{-1}\,K^{-1}}$ in dry condition, and from 1.303 to 1.574 $\mathrm{W\,m^{-1}\,K^{-1}}$ in saturated condition, whereas, the effective steady state λ of the soils ranges from 0.239 to 0.247 $\mathrm{W\,m^{-1}\,K^{-1}}$ in dry condition, and from 1.241 to 1.253 $\mathrm{W\,m^{-1}\,K^{-1}}$ in saturated condition. The measured effective transient λ of the soils show higher dispersion as compared to the steady state measurements. Overall, the transient technique provided lower effective thermal conductivity in dry condition, but higher values in saturated condition, as compared to the steady state technique.

7.2.2 Tests on loess soil and other porous media types

In this section, results of the thermal and dielectric measurements on the loess soil at different medium conditions such as water content, porosity, matric suction, effective stress and settlement potential are presented. Moreover, the prediction models for analyzing the variations of the thermal and dielectric parameters with medium temperature are verified by comparison with data from the literature.

7.2.2.1 Variations with water content and porosity

The results of the electromagnetic measurements on the investigated loess soil are shown in Figures 7.8 - 7.10. Figure 7.8 shows the variation of the real part $\varepsilon'_{r,eff}$ of the relative effective complex permittivity of the two remolded conditions of the loess soil (L-A with $n = 0.453$ and L-B with $n = 0.301$) at a measurement frequency of 1 GHz with gravimetric water content w. The measured $\varepsilon'_{r,eff}$ of the loess soil increases with an increase in moisture content, as for the given porosity of the soil, an increase in moisture content indicates the replacement of air with moisture, which has a much higher complex dielectric permittivity than air.

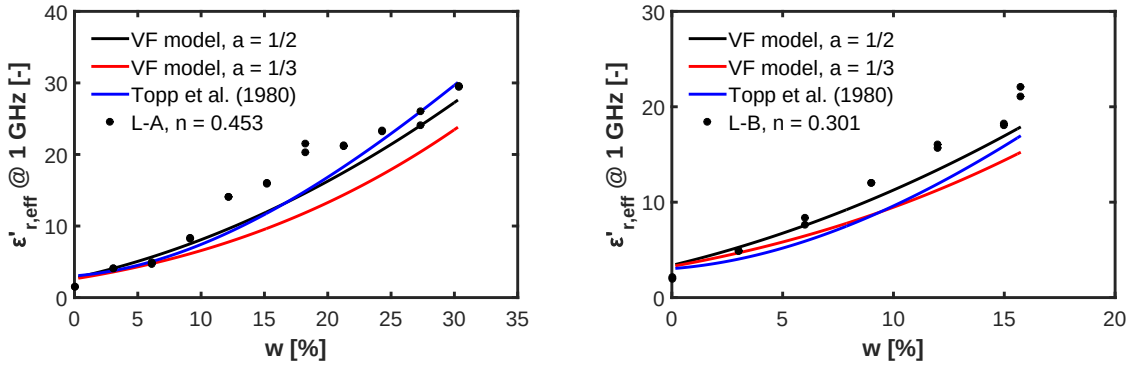

(a) (b)

Figure 7.8: Real part $\varepsilon'_{r,eff}$ of the relative effective complex permittivity of L-A a) and L-B b) as a function of gravimetric water content w (VF model - Equation 4.3).

The measured $\varepsilon'_{r,eff}$ of the loess soil at loose/natural saturated condition (L-A), $\varepsilon'_{r,eff}$ at 1 GHz $= 29.42$, is much higher as compared to that at lab compacted condition (L-B), $\varepsilon'_{r,eff}$ at 1 GHz $= 21.12$ (Figure 7.8). This is primarily due to the fact that the loess soil at loose saturated condition (with a comparatively higher porosity), has a relatively higher fraction of liquid phase/pore-water (which corresponds to a lower fraction of solid grains) as compared to the loess at compacted condition, resulting in a much better conducting pathway for dielectric permittivity or electrical conductivity (i.e. moisture content has a much higher complex dielectric permittivity than the soil grains) (Hilhorst, 2000; Ewing and Hunt, 2006).

Moreover, in Figure 7.8, the experimental findings are compared to the VF model (Equation 4.3), with structural exponents $a = 1/2$ (CRIM) (Birchak et al., 1974) and $a = 1/3$ (LLLM) (Landau and Lifschitz, 1985; Campbell, 1990), as well as the Topp et al. (1980) model. Although all the models tend to underestimate the measured $\varepsilon'_{r,eff}$ data, the VF model with exponent $a = 1/2$ and the Topp et al. model match comparatively well with the experimental results as compared to the VF model with exponent $a = 1/3$, which tends to significantly underestimate the measured $\varepsilon'_{r,eff}$ at 1 GHz data for the whole range of the loess soil saturation.

The experimental results of the imaginary part $\varepsilon''_{r,eff}$ of the relative effective complex permittivity and the effective loss tangent $\tan\delta_{eff}$ of the loess soil are shown in Figure 7.9. Generally, the measured $\varepsilon''_{r,eff}$ and $\tan\delta_{eff}$ of the loess soil increase with an increase in moisture content. This is to be expected, as for the given porosity of the soil, an increase in moisture content indicates the replacement of air with moisture, which also increases the degree of solubility of the solutes contained within the solid particles in to the pore water solution.

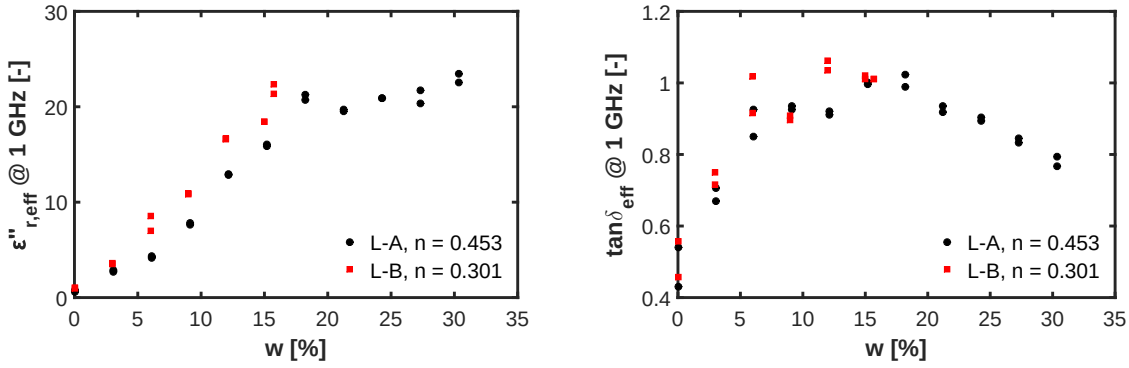

(a) (b)

Figure 7.9: Imaginary part $\varepsilon''_{r,eff}$ of the relative effective complex permittivity a) and effective loss tangent $\tan\delta_{eff}$ b) of the loess samples as functions of gravimetric water content w.

However, unlike the measurements of $\varepsilon'_{r,eff}$, the difference between the measured $\varepsilon''_{r,eff}$ of the loess soil at loose saturated condition (L-A), $\varepsilon''_{r,eff}$ at 1 GHz $= 22.57$, and that at lab compacted condition (L-B), $\varepsilon''_{r,eff}$ at 1 GHz $= 21.34$ is comparatively very small (Figure 7.9). The $\varepsilon''_{r,eff}$ is mainly affected by the presence of dissolved solutes in the pore-water solution and the corresponding Ohmic and polarization losses (Hasted, 1973; Ewing and Hunt, 2006) when the soil is subjected to an electric field, which are both not significantly influenced by changes in soil compaction/porosity.

Furthermore, in Figure 7.9, for L-A, it can be seen that upon wetting and the resulting increase in the amount and salinity of the entrapped pore-water due to the dissolution of solutes, the measured $\varepsilon''_{r,eff}$ of the soil increases significantly until gravimetric water content w of around 18.2%. After this point, the increase in $\varepsilon''_{r,eff}$ with the addition of moisture is insignificant, as most of the hydrophilic solutes/fine-grained clay and/or silt bridges, which hold and bind the relatively coarser grained particles in the soil structure, present in the soil are already dissolved in the pore-water solution. With the application of vertical stress to the soil upon wetting, however, a higher degree of breaking of these fine-grained bridges can be attained, resulting in much higher values of $\varepsilon''_{r,eff}$ or $\tan\delta_{eff}$ as shown in the discussions of the water-driven collapse behavior of the loess soil in Hailemariam et al. (2015b). As expected, the measured $\tan\delta_{eff}$ of L-A after w of around 18.2% decreases significantly, as the rate of increase of $\varepsilon''_{r,eff}$ is much lower than that of the $\varepsilon'_{r,eff}$ above this moisture content (Figures 7.8 and 7.9).

In Figure 7.10, the measured spectra of the relative effective complex permittivity $\varepsilon^*_{r,eff}$ of the loess soil at the two porosities and different gravimetric water contents w is presented. At frequencies above 4 GHz, a low accuracy of signal measurements were recorded for all the samples, possibly due to a limitation in the dynamic range

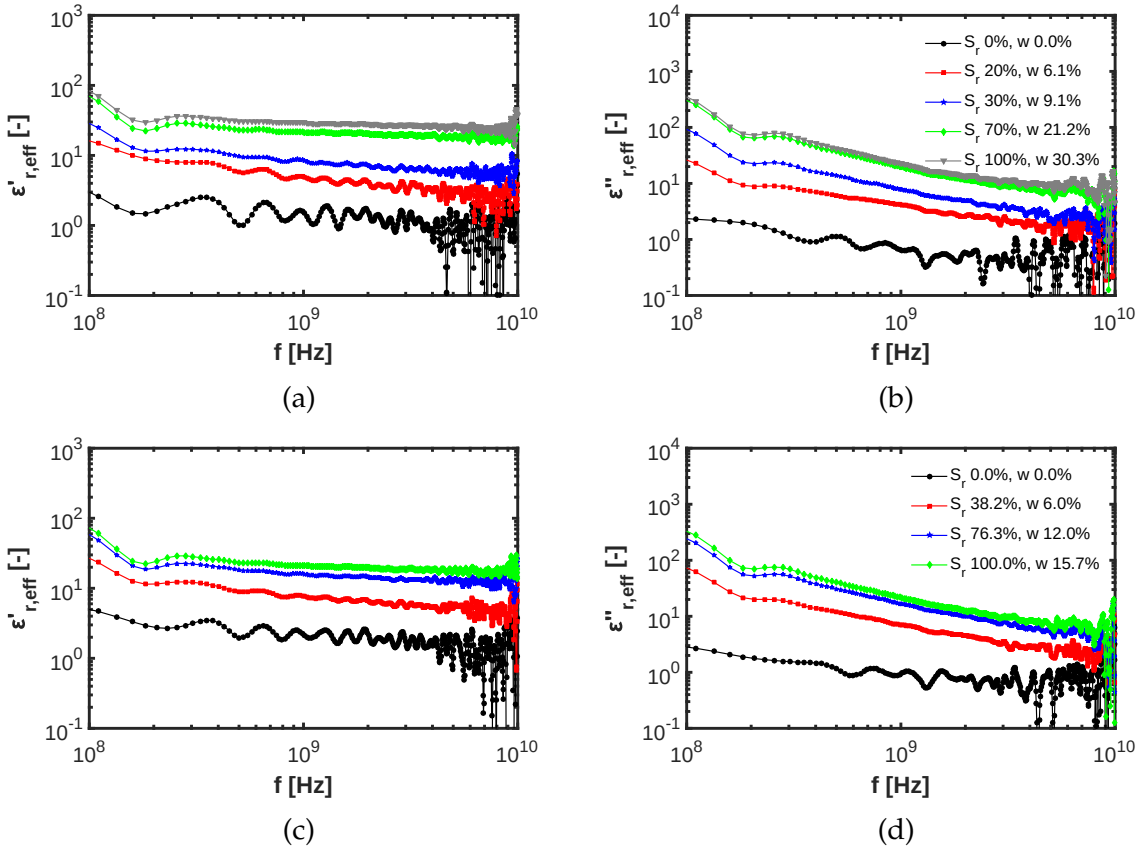

Figure 7.10: Dielectric spectra of the loess samples at different gravimetric water contents w: $\varepsilon'_{r,eff}$ a) and c), and $\varepsilon''_{r,eff}$ b) and d) of L-A and L-B, respectively.

of the employed TDR instrument and radiation effects. Generally, the loess soil exhibits a very high degree of dielectric dispersion or relaxation, due to the presence of a high proportion of clay minerals with readily dissoluble salts (34.0 wt.%, Table 6.3) (Arulanandan, 2003; Wagner and Scheuermann, 2009). When comparing the results of the electromagnetic tests on the loess soil at loose natural condition with those from the silty clay soils (section 7.2.1), the loess soil exhibits a higher complex dielectric permittivity (especially the imaginary component), polarization and dielectric dispersion (Figures 7.1 - 7.3 and 7.8 - 7.10) due to its much higher clay content with soluble salts.

In summary, the dielectric spectra of the loess soil shows a typical frequency dependence (with the dielectric dispersion increasing with an increase in soil moisture content, Figure 7.10) with: a) a stronger frequency dependence of the complex dielectric permittivity at low frequency ranges due to the presence of clay minerals; b) a strong decrease in the imaginary part as compared to the real part with increasing frequency below around 4 GHz (measurement accuracy above 4 GHz is quite low) for all soils, mainly due to electrical induced losses and c) an absence of the main water relaxation contribution (Wagner et al., 2007b; Wagner and Scheuermann, 2009),

confirmed by a lack of an increase in the imaginary part above around 1 GHz.

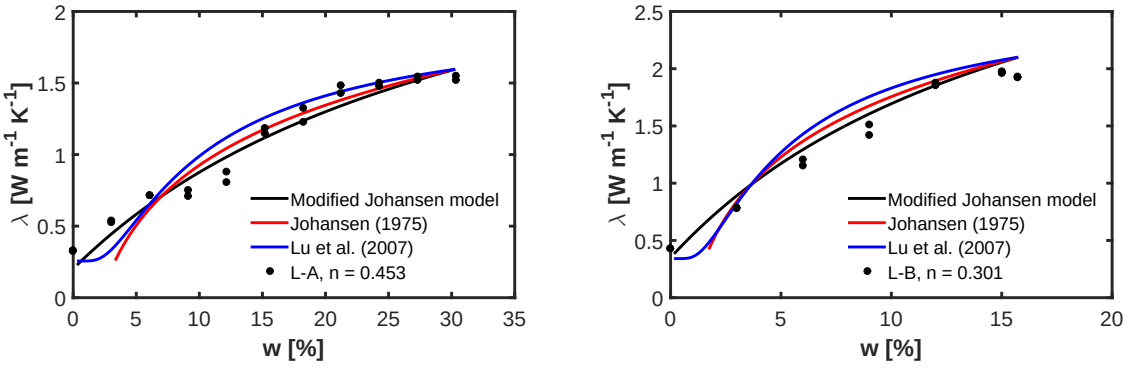

(a) (b)

Figure 7.11: Effective thermal conductivity λ of L-A a) and L-B b) as a function of gravimetric water content w (Modified Johansen model - Equation 4.1).

Figure 7.11 shows the results of effective thermal conductivity λ measurements of the loess soil at the two remolded conditions as a function of gravimetric water content w. The measured effective λ of the loess soil at loose/natural saturated condition (L-A), $\lambda = 1.521\,\mathrm{W\,m^{-1}\,K^{-1}}$, is much lower as compared to that at lab compacted condition (L-B), $\lambda = 1.934\,\mathrm{W\,m^{-1}\,K^{-1}}$. This is primarily due to the fact that the loess soil at loose saturated condition (with a comparatively higher porosity), has a relatively lower fraction of solid grains (which corresponds to a higher fraction of liquid phase/pore-water) as compared to the loess at compacted condition, resulting in a much poorer conducting pathway for heat conduction (i.e. mineral grains have a much higher thermal conductivity than moisture) (Hailemariam et al., 2017; Hailemariam and Wuttke, 2018b). Moreover, a reduction in soil porosity (or an increase in dry density) generally causes an increase in the inter-particle contact area and the number of solid particles packed per unit volume. As a result, the number and quality of contact points between the grains increases, resulting in an enhanced heat flow path, and consequently the effective thermal conductivity of the medium increases (Salomone and Kovacs, 1984; Salomone et al., 1984; Salomone and Marlowe, 1989; Hailemariam et al., 2015a).

The experimental findings of λ are further compared to the modified Johansen model (Equation 4.1), the original Johansen's model (Johansen, 1975) and the Lu et al. (2007) model. All three models match the experimental measurements of λ with good accuracy, except at gravimetric water content w levels below around 7% for L-A and around 3% for L-B, where only the modified Johansen model provides a good accuracy (Figure 7.11). The prediction results of the original Johansen model at low

moisture contents are neglected due to its inapplicability for degrees of saturation lower than 20% (see section 2.2.5).

Generally, the effective thermal conductivity λ of the loess soil increases with an increase in moisture content in two stages. At gravimetric water content w of up to around 21% for L-A and around 12% for L-B, water bridges start to form between the soil particles filling air voids, and λ starts to increase rapidly due to improved contact and increase in heat conduction path between the grains (Sepaskhah and Boersma, 1979). Then after, the increase in λ mainly depends on the replacement of air by water only, and as a result, λ increases at a slower rate.

When comparing the results of the thermal measurements on the loess soil at loose natural condition with those from the silty clay soils (section 7.2.1), the loess soil (with max. λ at saturated condition) exhibits a similar thermal conductivity as the silty clay soils (with max. λ at saturated conditions) (Figures 7.4 and 7.11a). The similarities in the thermal behaviors of the loess soil and the silty clay soils at natural conditions is attributed to the similarities in their geotechnical properties (Tables 6.1 and 6.3).

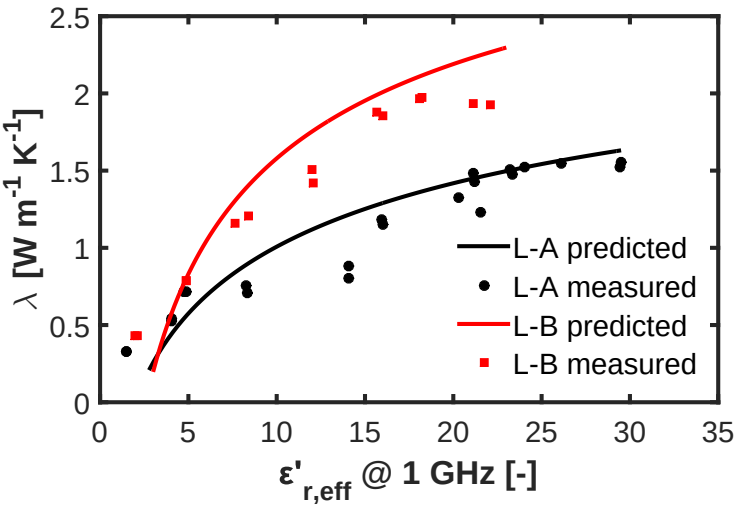

Figure 7.12: Variation of effective thermal conductivity λ with the real part $\varepsilon'_{r,eff}$ of the relative effective complex permittivity of the loess samples (New model prediction - Equation 4.5).

The comparison of the new model for predicting the thermal conductivity of naturally occurring un-saturated soils from complex dielectric permittivity (Equation 4.5) and experimental data of the loess soil is shown in Figure 7.12. The prediction of the new model generally matches well to the experimental findings, with a slight overestimation of thermal conductivity of L-B at higher moisture contents (higher $\varepsilon'_{r,eff}$ at 1 GHz). As expected, both the model prediction and experimental data exhibit a higher thermal conductivity of L-B than L-A for a given value of $\varepsilon'_{r,eff}$ at 1 GHz (equivalent

soil moisture content), due to the lower porosity (higher dry density) of L-B as compared to L-A, as discussed earlier. The average errors of prediction of the new model for the loess soil prepared in the two remolded conditions in this study are: 14.18% for L-A and 11.07% for L-B (with an overall average of 12.63%).

7.2.2.2 Variations with matric suction

In this section, results of the drying path matric suction ψ_m of the SWCC and the simultaneous measurements of thermal conductivity and complex dielectric permittivity performed via the filter paper method are presented. As discussed in section 6.4.1.2, the correlation between the thermal conductivity and complex dielectric permittivity and the simultaneous measurement of the drying path of the SWCC of the loess soil (with porosities n of 0.453 and 0.301) via the filter paper method was performed on the same subsamples used for the water content and porosity studies. Hence, in this section, results such as the dielectric spectra of the samples, which have already been presented in the previous section, are not shown.

Figure 7.13 shows the drying path SWCCs of the two remolded conditions of the loess soil. The experimental findings are also compared to the prediction of the Fredlund and Xing (1994) model (Equation 4.19) with satisfactory results. Values of the soil type dependent parameters of the Fredlund and Xing model of $p_1 = 237.5$, $p_2 = 2.1$ and $p_3 = 1.3$ for L-A, and $p_1 = 547.2$, $p_2 = 1.2$ and $p_3 = 1.3$ for L-B are used, providing the best fit of the experimental data. The air entry values (AEVs) of the loess soil at the two remolded conditions are estimated from the extensions of the tangent lines in the saturated and transition zones of the SWCCs (Vanapalli et al., 1996; Hong et al., 2016) as around: 107 kPa for L-A and 175 kPa for L-B.

The results of the electromagnetic measurements and matric suction on the investigated loess soil are shown in Figures 7.14 and 7.15. Figure 7.14 shows the variation of the real part $\varepsilon'_{r,eff}$ of the relative effective complex permittivity of the two remolded conditions of the loess soil at a measurement frequency of 1 GHz with matric suction ψ_m. Upon drying, the measured $\varepsilon'_{r,eff}$ of the loess soil decreases with an increase in matric suction (or a decrease in moisture content), as for the given porosity of the soil, an increase in matric suction indicates the replacement of moisture with air, which has a much lower complex dielectric permittivity than water (Hilhorst, 2000; Ewing and Hunt, 2006). Furthermore, when the matric suction of the loess soil at the two remolded conditions is increased beyond the AEV and then further towards more drier states upon desorption process, the measured $\varepsilon'_{r,eff}$ of the loess soil at loose/natural

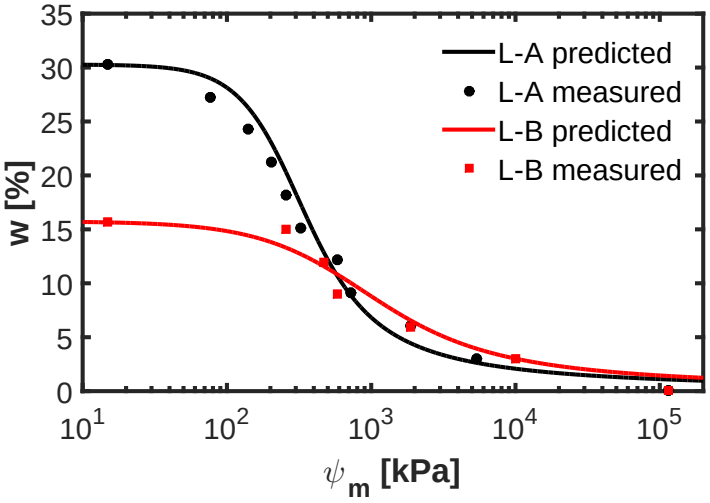

Figure 7.13: Gravimetric water content w of the loess soil at the two remolded conditions as a function of matric suction ψ_m, drying path (Model prediction - Equation 4.19).

condition (L-A) falls more sharply as compared to that of the loess soil at lab compacted condition (L-B), due to its higher porosity and hence the requirement of low suction potential to drive moisture out of its pores (which is also verified by the lower AEV of L-A as compared to L-B).

The experimental findings are further compared to the prediction of the new model (Equation 4.20). Although the new model tends to underestimate the measured $\varepsilon'_{r,eff}$ data at low matric suction levels (near saturation), satisfactory results are obtained for the wider range of matric suction of both remolded conditions (Figure 7.14).

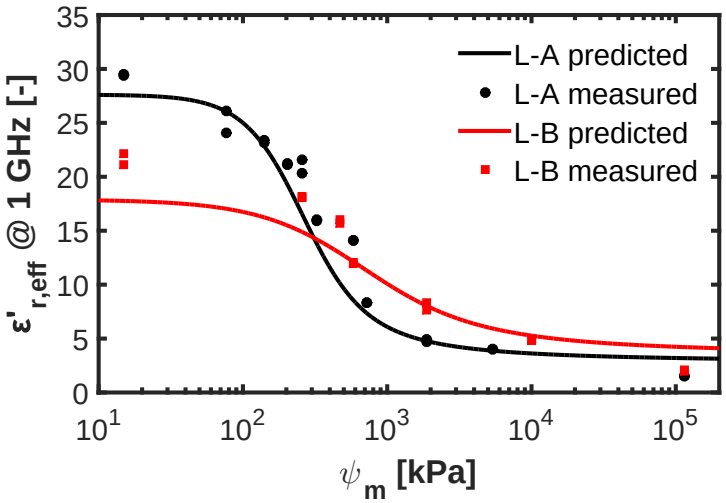

Figure 7.14: Real part $\varepsilon'_{r,eff}$ of the relative effective complex permittivity of the loess soil at the two remolded conditions as a function of matric suction ψ_m (New model prediction - Equation 4.20).

The experimental results of the imaginary part $\varepsilon''_{r,eff}$ of the relative effective complex permittivity and the effective loss tangent $\tan\delta_{eff}$ of the loess soil are shown in Figure 7.15. Generally, the measured $\varepsilon''_{r,eff}$ and $\tan\delta_{eff}$ of the loess soil decrease with an increase in matric suction. This is to be expected, as for the given porosity of the soil, an increase in matric suction indicates the removal of moisture content from the soil along with the high amounts of dissolved solutes from the pore water solution, resulting in a decrease in the degree of polarization of the soil.

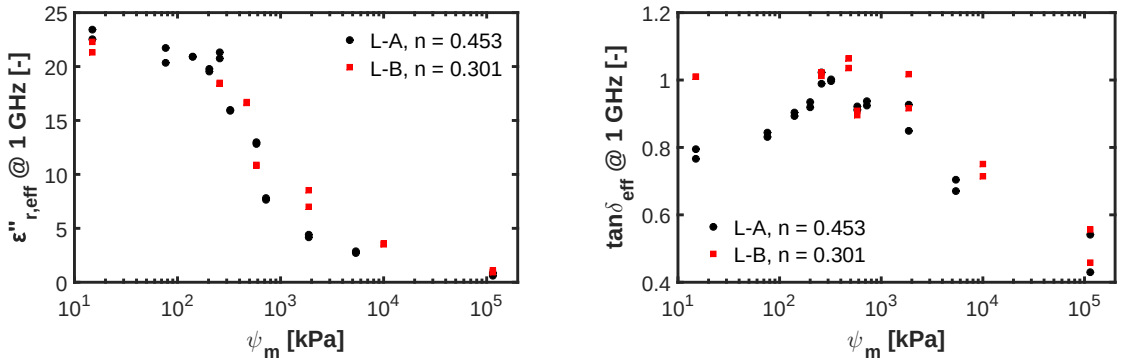

(a) (b)

Figure 7.15: Imaginary part $\varepsilon''_{r,eff}$ of the relative effective complex permittivity a) and effective loss tangent $\tan\delta_{eff}$ b) of the loess soil at the two remolded conditions as a function of matric suction ψ_m.

However, unlike the measurements of $\varepsilon'_{r,eff}$, the difference between the measured $\varepsilon''_{r,eff}$ of the loess soil at loose saturated condition (L-A) and that at lab compacted condition (L-B) at low matric suction levels (near saturation) is comparatively very small (Figure 7.15a). The $\varepsilon''_{r,eff}$ is mainly affected by the presence of dissolved solutes in the pore-water solution and the corresponding Ohmic and polarization losses (Hasted, 1973; Ewing and Hunt, 2006) when the soil is subjected to an electric field, which are both not significantly influenced by changes in soil compaction/porosity.

Upon further increase in matric suction beyond the AEVs of the two remolded conditions, the rate of drop of the measured $\varepsilon''_{r,eff}$ or the rate of decrease of the degree of polarization of the loess soil at the two remolded conditions is also similar. Although, for a given matric suction increment, a higher volumetric water content is expelled from the pores of L-A (due to its higher pore-size/porosity) as compared to L-B, the overall drop in rate of polarization of the two remolded conditions is similar because the pore-water expelled from L-B has a comparatively higher concentration of dissolved solutes as compared to that of L-A (i.e. compaction or change in soil porosity does not alter the total amount of dissolved solutes in a soil mass).

Figure 7.16 shows the results of effective thermal conductivity λ measurements of the loess soil at the two remolded conditions as a function of matric suction ψ_m.

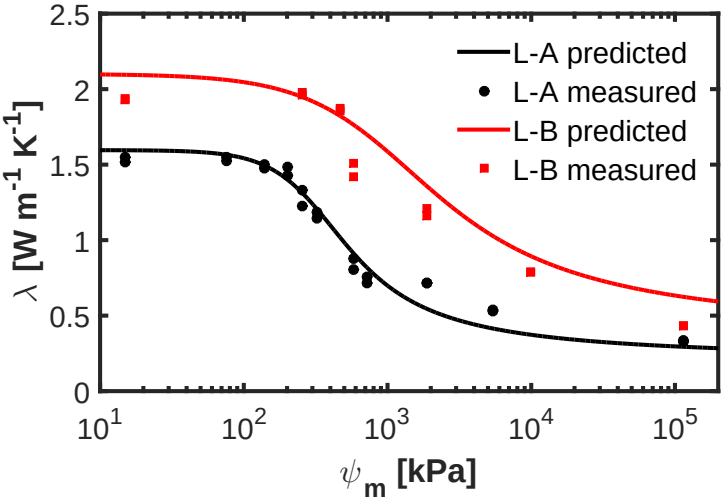

Figure 7.16: Effective thermal conductivity λ of the loess soil at the two remolded conditions as a function of matric suction ψ_m (New model prediction - Equation 4.16).

When the matric suction of the loess soil at the two remolded conditions is increased beyond the AEV and then further towards drier states upon desorption process, the measured λ of the loess soil decreases, as for the given porosity of the soil, an increase in matric suction indicates the replacement of moisture with air, which has a much lower thermal conductivity than water. Generally, for any given matric suction level, the measured λ of the loess soil at loose/natural saturated condition (L-A) is much lower than that of the lab compacted condition (L-B). This is primarily due to the fact that, L-A (with a comparatively higher porosity), has a relatively lower fraction of solid grains (which corresponds to a higher fraction of liquid phase) as compared to L-B, resulting in a much poorer conducting pathway for heat conduction (i.e. mineral grains have a much higher thermal conductivity than moisture/air) (Hailemariam et al., 2017; Hailemariam and Wuttke, 2018b). Moreover, a reduction in soil porosity (or an increase in dry density) generally causes an increase in the inter-particle contact area and the number of solid particles packed per unit volume. As a result, the number and quality of contact points between the grains increases, resulting in an enhanced heat flow path, and consequently the effective thermal conductivity of the medium increases (Salomone and Kovacs, 1984; Salomone et al., 1984; Salomone and Marlowe, 1989; Hailemariam et al., 2015a). The experimental findings of λ are further compared to the the prediction of the new model (Equation 4.16) with good accuracy (Figure 7.16).

7.2.2.3 Variations with effective stress

In Figures 7.17 - 7.20, results of the study of the variation of dielectric measurements of L-A at optimum gravimetric moisture conditions with applied effective stress are shown. Figure 7.17 shows the plots of the relative effective complex permittivity $\varepsilon^*_{r,eff}$ at a measurement frequency of 1 GHz and the corresponding vertical strain $\Delta h/h_o$ data of the loess soil specimen upon the application of effective stress σ'.

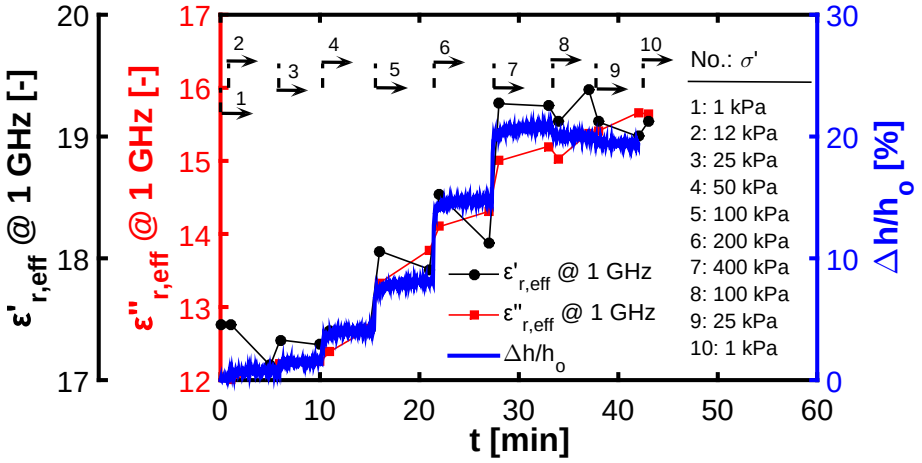

Figure 7.17: Relative effective complex permittivity $\varepsilon^*_{r,eff}$ and vertical strain $\Delta h/h_o$ of L-A as functions of time t.

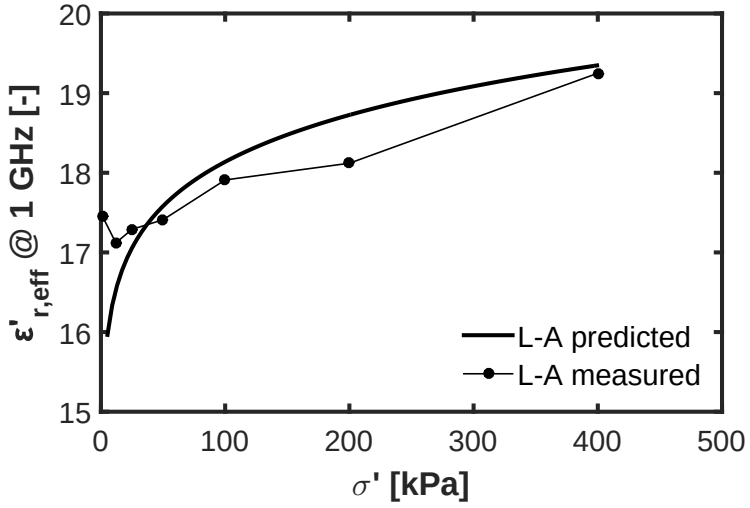

Figure 7.18: Real part $\varepsilon'_{r,eff}$ of the relative effective complex permittivity of L-A as a function of effective stress σ' (Model prediction: modified VF model - Equation 4.30).

Overall, both the real $\varepsilon'_{r,eff}$ and imaginary $\varepsilon''_{r,eff}$ parts of the relative effective complex permittivity as well as the effective loss tangent $\tan\delta_{eff}$ (Figures 7.18 and 7.19)

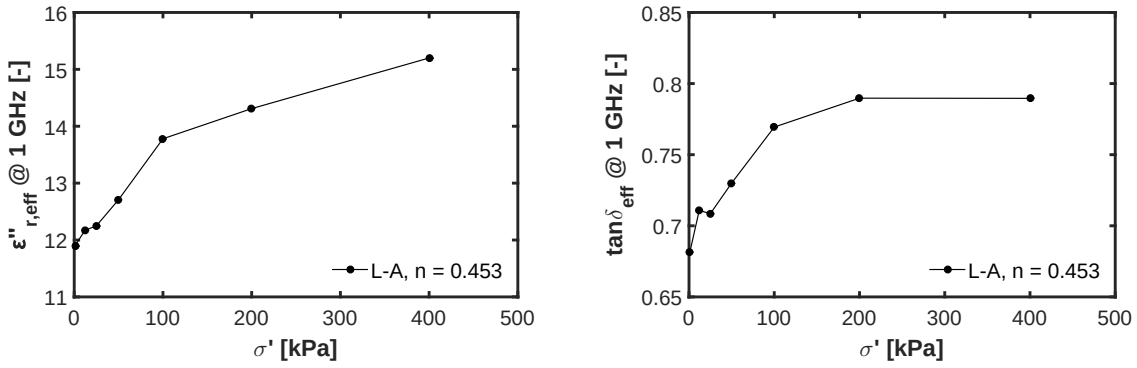

(a) (b)

Figure 7.19: Imaginary part $\varepsilon''_{r,eff}$ of the relative effective complex permittivity a) and effective loss tangent $\tan\delta_{eff}$ b) of L-A as functions of effective stress σ'.

of L-A increase upon the application of stress until the maximum applied load of 400 kPa is reached (the sudden changes are particularly evident during the onset of stress change, Figure 7.17). Moreover, a higher rate of increase is generally observed at the beginning (lower effective stress) as compared to higher stress levels following the load-deformation pattern of the loading tests.

Application of stress on a porous medium alters the inter-particle contact condition, by inducing changes in the internal structure or fabric of porous media (Choo et al., 2013; Hailemariam et al., 2015a), and generally causes an increase in the dielectric constant (due to a reduction in porosity, i.e. removal of entrapped air or an increase in the soil volumetric water content) and loss tangent or degree of polarization (due to improved inter-particle contact, i.e. an increase in the degree and quality of contacts between the pore-water solutes) in dry or unsaturated conditions. Whereas in fully saturated soil conditions, in spite of the reduction in soil porosity and improved inter-granular contact upon compaction with the application of stress, a reduction in the effective complex dielectric permittivity of the soil is expected, mainly due to the expulsion of pore-water during consolidation, as the loss contribution due to the expulsion of pore-water outweighs the gain from the reduction in porosity and improved contact (Hailemariam et al., 2015a).

In contrast and as expected, insignificant changes in the measured complex dielectric permittivity of the soil are recorded, due to the low deformation recovery (elasticity) of the loess soil upon unloading, resulting in negligible changes in the soil structure.

The experimental values of $\varepsilon'_{r,eff}$ of L-A in Figure 7.18 are additionally compared to the prediction of the modified VF model (Equation 4.30). A value of coefficient

of compressibility index C_c (taken in this study as the primary compressibility index for normally consolidated soils and the average compressibility index for the considered effective stress range for overconsolidated soils) of 0.11 is used to model the soil dielectric-stress behavior. The value is obtained as the average/representative value for stiff clays (Widodo and Ibrahim, 2012). Although, the new model prediction slightly underestimates the measured $\varepsilon'_{r,eff}$ data at low effective stress levels, a good overall match is obtained for the studied effective stress range.

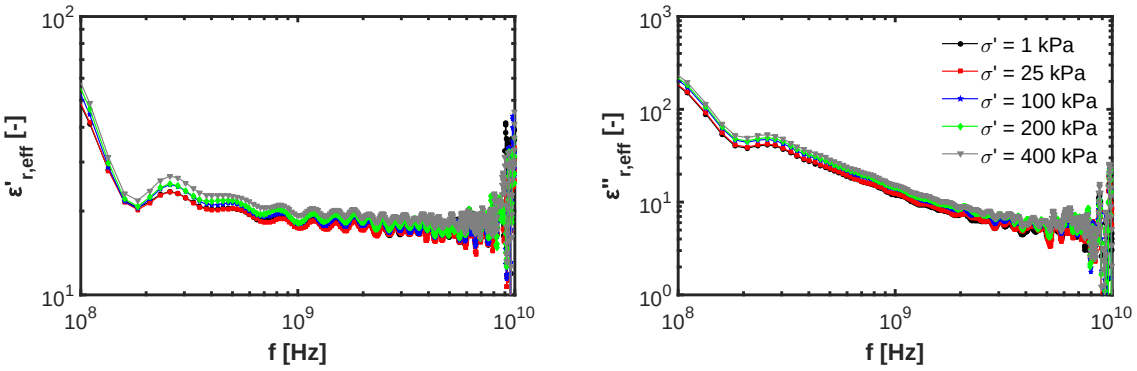

(a) (b)

Figure 7.20: Dielectric spectra of L-A at five effective stress σ' levels: $\varepsilon'_{r,eff}$ a) and $\varepsilon''_{r,eff}$ b).

Figure 7.20 presents the measured dielectric spectra of the relative effective complex permittivity $\varepsilon^*_{r,eff}$ of L-A at five effective stresses σ'. At frequencies above 4 GHz, a low accuracy of signal measurements was recorded for all the stress levels, possibly due to a limitation in the dynamic range of the employed TDR instrument and radiation effects. Generally, the loess soil exhibits a very high degree of dielectric dispersion or relaxation at the considered effective stress levels, due to the presence of a high proportion of clay minerals with readily dissoluble salts (34.0 wt.%, Table 6.3) (Arulanandan, 2003; Wagner and Scheuermann, 2009).

In summary, the dielectric spectra of the loess soil at the considered stress levels show a typical frequency dependence (with the dielectric dispersion increasing very mildly with an increase in the applied effective stress, Figure 7.20) with: a) a stronger frequency dependence of the complex dielectric permittivity at low frequency ranges due to the presence of clay minerals; b) a strong decrease in the imaginary part as compared to the real part with increasing frequency below around 4 GHz (measurement accuracy above 4 GHz is quite low) for all stress levels, mainly due to electrical induced losses and c) an absence of the main water relaxation contribution (Wagner et al., 2007b; Wagner and Scheuermann, 2009), confirmed by a lack of an increase in the imaginary part above around 1 GHz.

In Figures 7.21 and 7.22, the results of the study of the variation of effective thermal conductivity λ with applied effective stress σ' of L-A are shown. In Figure 7.21, plots of the recorded temperatures of the three plates (i.e. top T_1, reference T_2 and bottom T_3) of the steady state device (section 6.3.1.2) and the corresponding vertical strain $\Delta h/h_o$ of the L-A specimen upon the application of effective stress σ' are shown. Upon the application of a nominal effective stress level of $\sigma' = 5$ kPa, a temperature stabilization time of around 2.8 hours was required to achieve steady state conditions before proceeding with the application of higher effective stress levels. Using the values of the measured temperatures of the three plates, the measured λ of L-A at each effective stress level is obtained using Equation 6.12 as shown in Figure 7.22.

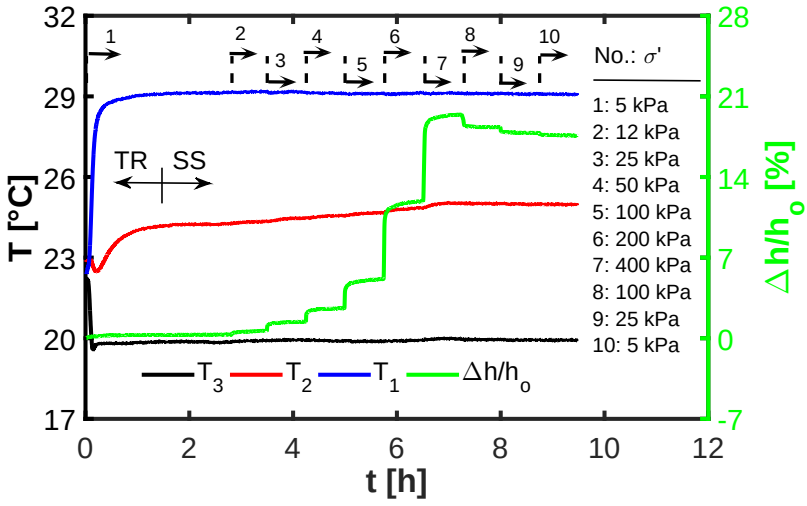

Figure 7.21: Temperature T and vertical strain $\Delta h/h_o$ for the steady state thermal conduction test of L-A as functions of time t.

The measured temperature of the reference disc T_2 and hence the measured effective thermal conductivity λ of L-A increase upon the application of stress, with a high rate of increase at the beginning (lower effective stress) and gradually slowing down at higher effective stress values following the load-deformation pattern of the loading tests (Figure 7.22).

As stated earlier, application of stress on a porous medium alters the inter-particle contact condition, by inducing changes in the internal structure or fabric of porous media (Choo et al., 2013; Hailemariam et al., 2015a), and generally causes an increase in the effective thermal conductivity of the medium mainly due to an increase in the inter-particle contact area and reduction of medium porosity. The reduction of medium porosity with the application of effective stress results in an increase of the medium's dry density, and the number of solid particles packed per unit volume increases improving the number and quality of contact points between the grains. As a

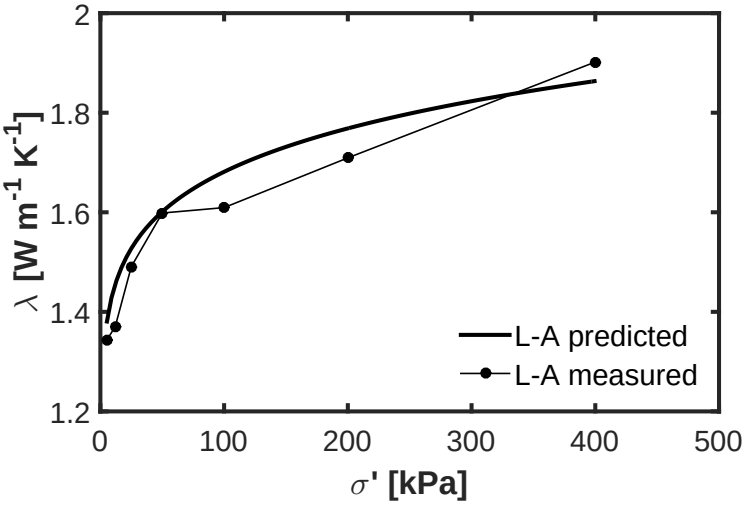

Figure 7.22: Effective thermal conductivity λ of L-A as a function of effective stress σ' (Model prediction: modified Johansen model - Equation 4.21).

result, the heat flow path, and consequently the effective thermal conductivity of the medium increases (Salomone and Marlowe, 1989; Hailemariam et al., 2015a).

Unlike the dielectric soil behavior (where a reduction in the effective complex dielectric permittivity is expected upon the application of effective stress at saturated conditions), the thermal behavior of the loess soil is expected to show a similar trend for both unsaturated and saturated states, where the effective thermal conductivity increases with the application of effective stress. The changes in soil thermal conductivity are highly influenced by changes in porosity as compared to moisture content upon the application of stress, and hence, at saturated state, the gain in soil thermal conductivity due to reduction of porosity or increase in inter-particle contact area outweighs the losses due to the removal of pore-water from the soil mass during consolidation (Hailemariam et al., 2015a).

The experimental values of the effective λ of L-A as a function of σ' in Figure 7.22 are additionally compared to the prediction of the modified Johansen model (Equation 4.21). The same coefficient of compressibility index C_c (with a value of 0.11 for stiff clays (Widodo and Ibrahim, 2012)) used previously for the dielectric-stress behavior is also used here to model the soil thermal-stress behavior. Overall, a good match between the predictions from the new model and the experimental data is achieved for the considered effective stress range.

When comparing the time/effective stress vs deformation/strain plots of the two consolidation cells/sample sizes, i.e. the steady state thermal conductivity cell/samples (with dimensions of 100 mm diameter and height of 30 mm, giving diameter to height

d/h ratio of 3.33) and the consolidation & EM cell/samples (with dimensions of 154 mm diameter and height of 60 mm, giving diameter to height d/h ratio of 2.57), used in the thermo-dielectric and effective stress studies, respectively, similar outcomes are obtained with regards to the degree of compressibility or average compressibility index of the loess soil for the considered effective stress range (Figures 7.17 and 7.21). These results are in agreement with previous findings (Rosine and Sabbagh, 2015; Rosine, 2015), where the d/h ratios of consolidation cells/sample sizes has no or negligible effect on the degree or index of compressibility C_c of soils at effective stresses above around 100 kPa, but with profound influence on the rate or coefficient of consolidation C_v.

Generally, for consolidation tests, lateral pressure acting on the walls of consolidation cells produce a frictional resistance to the compression of the soil specimen in the cell. Taylor (1942) studied the influence of side friction on consolidation test results and concluded that the frictional resistance varies from 12 - 22% and 10 - 15% of the applied pressure for remoulded and undisturbed soils, respectively, and, the higher the sample thickness, the higher the lateral surface area of the soil in contact with the walls of the consolidation cell and the higher the side friction or resistance to deformation (Rosine and Sabbagh, 2015).

7.2.2.4 Variations with water-driven settlement potential

In this section, the tripartite correlation between the simultaneously measured thermal conductivity, complex dielectric permittivity and the settlement potential of the loess soil at loose natural condition (L-A) is presented.

The quantity of water-driven settlement of loess soils is highly influenced by the magnitude of the applied collapse load (Kafle et al., 2014; Al-Janabi, 2015). This is verified by the results of single ödometer tests shown in Figure 7.23. The settlement potential at any given load level is determined by performing single ödometer consolidation tests by wetting the soil, which is initially at natural gravimetric water content condition, at the desired level of effective stress or collapse load. Generally, the water-driven settlement potential of loess soils increases with effective stress (Figure 7.23). The rate of increase of the settlement potential is comparatively much higher at low effective stress levels and decreases to a minimum at stresses between 200 - 400 kPa, thereby achieving more than 95% of the overall settlement potential of the loess soil once a stress level of around 300 kPa is reached (Figure 7.23b).

The settlement potential requires a combination of water saturation to dissolve the existing fine-grained bonds and sufficient stress to break the bonds between the

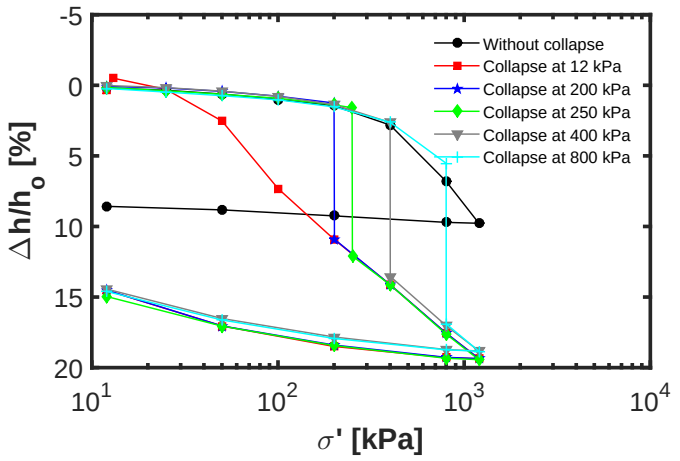

(a)

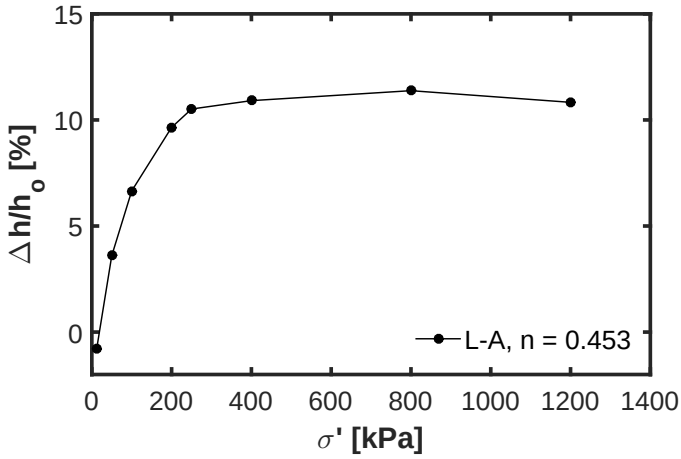

(b)

Figure 7.23: Single ödometer collapse tests ($\Delta h/h_o$ vs σ') of specimens of L-A inundated with water at different effective stress levels σ' a) and variation of the settelement potential $\Delta h/h_o$ with effective stress σ' b).

particles. Hence, for low effective stress levels, such as of the order of 50 kPa, the stresses are too small to cause significant breaks in the bonds and not large enough to cause a maximal compaction, which happens at stress levels higher than 200 kPa. And when the effective stress or collapse load is too small, a swelling/heaving rather than settlement is observed, as shown by a negative settlement potential of $\Delta h/h_o = -0.805\%$ for effective stress of $\sigma' = 12$ kPa (Figure 7.23b). Considering these findings, it is reasonable to select a design or collapse load of 300 kPa for assessing the water-driven settlement of weak soils, and for the development of prediction models, as shown is section 4.5.

Furthermore, based on the recorded value of settlement potential of $\Delta h/h_o = 9.650\%$ for effective stress of $\sigma' = 200$ kPa, the loess soil used in this study can be categorized as a weak soil with a severe potential for collapse based on the criteria

suggested by Jennings and Knight (1975).

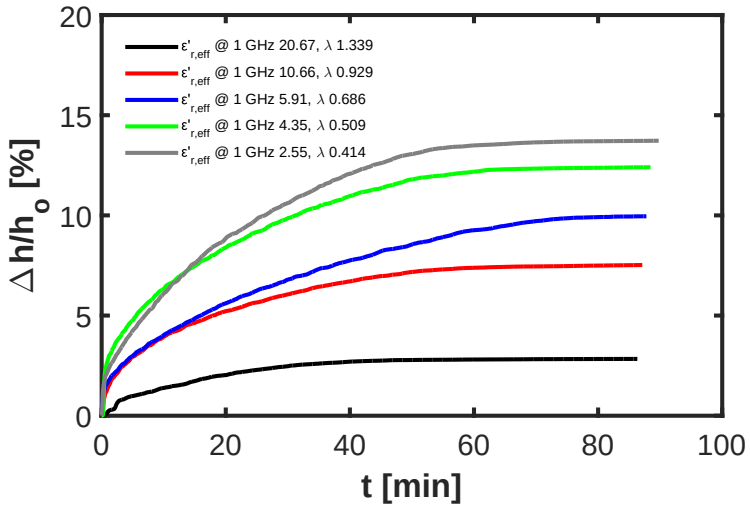

Figure 7.24: Variation of the settlement potential $\Delta h/h_o$ of L-A at different initial gravimetric moisture conditions (i.e. different $\varepsilon'_{r,eff}$ and λ), stressed at a stress level of 300 kPa, with time t, after the initiation of water-driven settlement process.

Figure 7.24 shows the plots of the progression of settlement potential $\Delta h/h_o$ of L-A, which was initially stressed at 300 kPa, after the addition of water to initiate water-driven settlement. As expected, the L-A specimens with a higher initial measured $\varepsilon'_{r,eff}$ and λ (corresponding to a higher soil volumetric water content before inundation by water), show a lower settlement potential and vice versa. This condition is in agreement with previous findings, which state that weak soils are more susceptible to subsidence when they are in a loose state and with a low moisture content (Feda, 1966; Jennings and Knight, 1975; Minkov et al., 1977).

Figures 7.25 - 7.27 show the results of the correlation between the electromagnetic measurements and the settlement potential of L-A. Figure 7.25 shows the variation of the settlement potential $\Delta h/h_o$ of L-A with the real part $\varepsilon'_{r,eff}$ of the relative effective complex permittivity at a measurement frequency of 1 GHz. An increase in the measured $\varepsilon'_{r,eff}$ of L-A (which corresponds to an increase in the initial moisture content of the soil (Hilhorst, 2000; Ewing and Hunt, 2006)) correlates to a decrease in the measured $\Delta h/h_o$ of the soil, verifying previous proposals (Feda, 1966; Jennings and Knight, 1975; Minkov et al., 1977). The experimental findings are further compared to the prediction of the new model (Equation 4.38) with good results (Figure 7.25).

Figure 7.26 presents the experimental results of the correlation between the settlement potential $\Delta h/h_o$ of L-A and the imaginary part $\varepsilon''_{r,eff}$ of the relative effective complex permittivity as well as the effective loss tangent $\tan\delta_{eff}$. Generally, the measured $\Delta h/h_o$ of the loess soil decreases with an increase in the measured $\varepsilon''_{r,eff}$ or

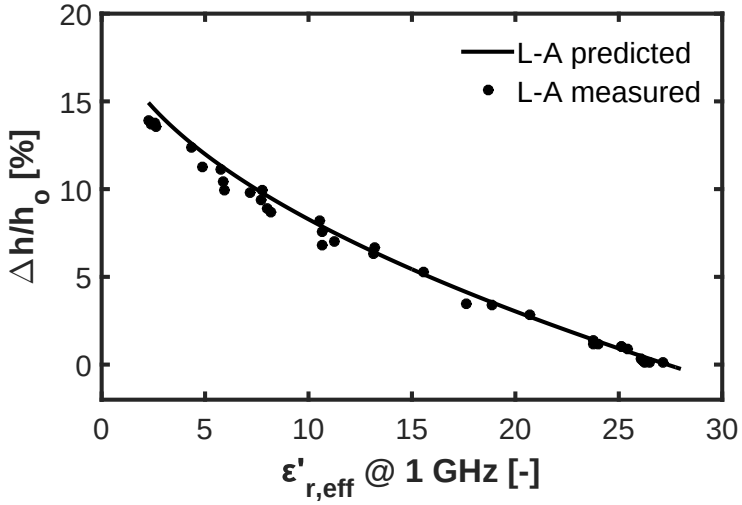

Figure 7.25: Settlement potential $\Delta h/h_o$ of L-A as a function of the real part $\varepsilon'_{r,eff}$ of the relative effective complex permittivity (New model prediction - Equation 4.38).

$\tan\delta_{eff}$ (which corresponds to an increase in soil moisture content, which is then accompanied by an increase in the pore-water salinity due to the dissolution of solutes (Kafle et al., 2014; Hailemariam et al., 2015b)) verifying previous findings (Feda, 1966; Jennings and Knight, 1975; Minkov et al., 1977).

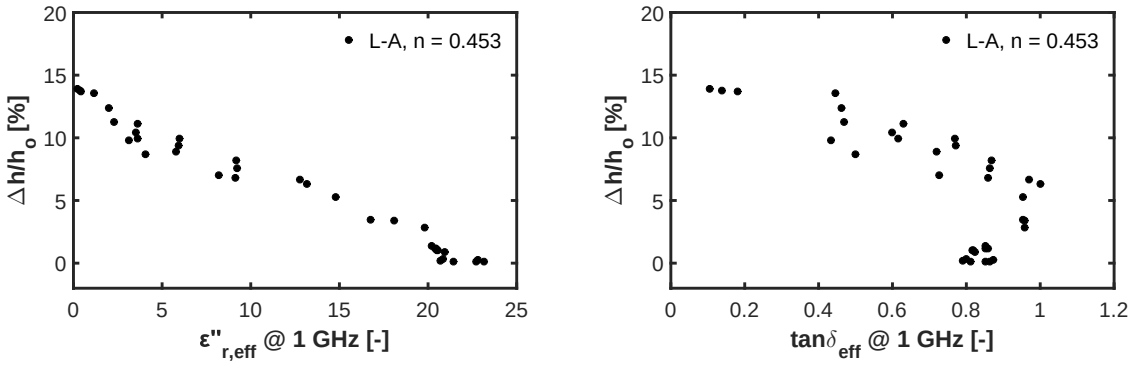

(a) (b)

Figure 7.26: Settlement potential $\Delta h/h_o$ of L-A as a function of the imaginary part $\varepsilon''_{r,eff}$ of the relative effective complex permittivity a) and effective loss tangent $\tan\delta_{eff}$ b).

In Figure 7.27, the measured dielectric spectra of the relative effective complex permittivity $\varepsilon^*_{r,eff}$ of L-A at five different initial conditions (i.e. corresponding to five w, λ or $\Delta h/h_o$ levels) is shown. Generally, the loess soil exhibits a very high degree of dielectric dispersion or relaxation at the considered conditions, due to the presence of a high proportion of clay minerals with readily dissoluble salts (34.0 wt.%, Table 6.3) (Arulanandan, 2003; Wagner and Scheuermann, 2009).

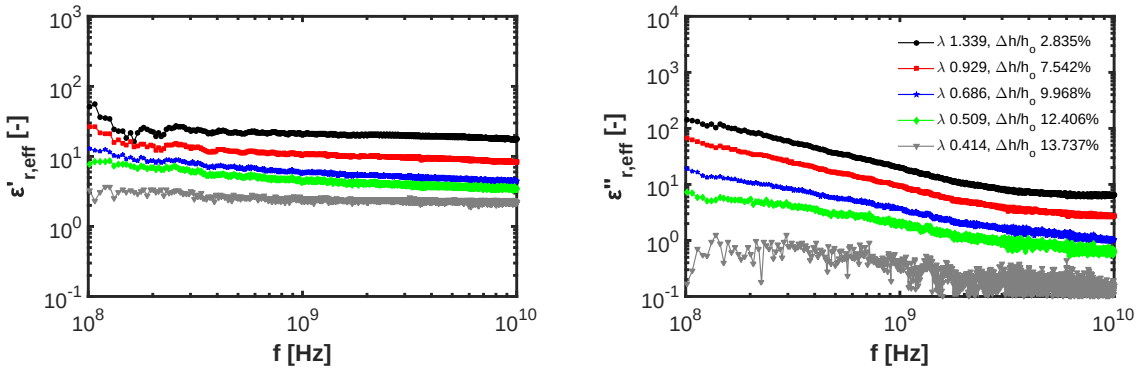

(a) (b)

Figure 7.27: Dielectric spectra of L-A at five different initial conditions (i.e. different λ and $\Delta h/h_o$): $\varepsilon'_{r,eff}$ a) and $\varepsilon''_{r,eff}$ b).

In summary, the dielectric spectra of L-A at the given conditions show a typical frequency dependence (with the dielectric dispersion increasing with a decrease in the measured $\Delta h/h_o$, which corresponds to an increase in soil initial moisture content, Figure 7.27) with: a) a stronger frequency dependence of the complex dielectric permittivity at low frequency ranges due to the presence of clay minerals; b) a strong decrease in the imaginary part as compared to the real part with increasing frequency below around 4 GHz frequency, mainly due to electrical induced losses and c) an absence of the main water relaxation contribution (Wagner et al., 2007b; Wagner and Scheuermann, 2009), confirmed by a lack of an increase in the imaginary part above around 1 GHz.

The results of the study of the variation of the settlement potential $\Delta h/h_o$ of L-A with the effective thermal conductivity λ is shown in Figure 7.28. An increase in the measured λ of L-A (which corresponds to an increase in the initial moisture content of the soil (Hailemariam et al., 2017; Hailemariam and Wuttke, 2018b)) correlates to a decrease in the measured $\Delta h/h_o$ of the soil, verifying previous findings (Feda, 1966; Jennings and Knight, 1975; Minkov et al., 1977). The experimental findings are also compared to the prediction of the new model (Equation 4.34) with good results (Figure 7.28).

The comparison of the new model for predicting the thermal conductivity of naturally occurring un-saturated soils from complex dielectric permittivity (Equation 4.5) and experimental data of the loess soil at different settlement potential values is shown in Figure 7.29. The prediction of the new model matches well to the experimental findings with an average error of prediction of 7.92%.

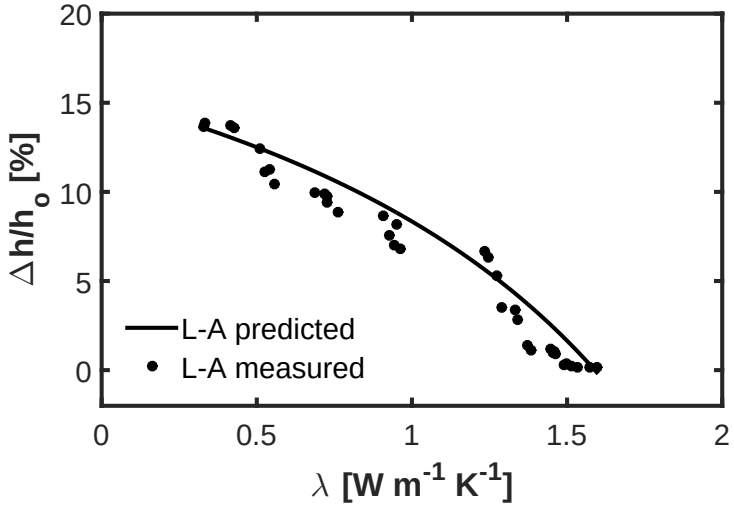

Figure 7.28: Settlement potential $\Delta h/h_o$ of L-A as a function of the effective thermal conductivity λ (New model prediction - Equation 4.34).

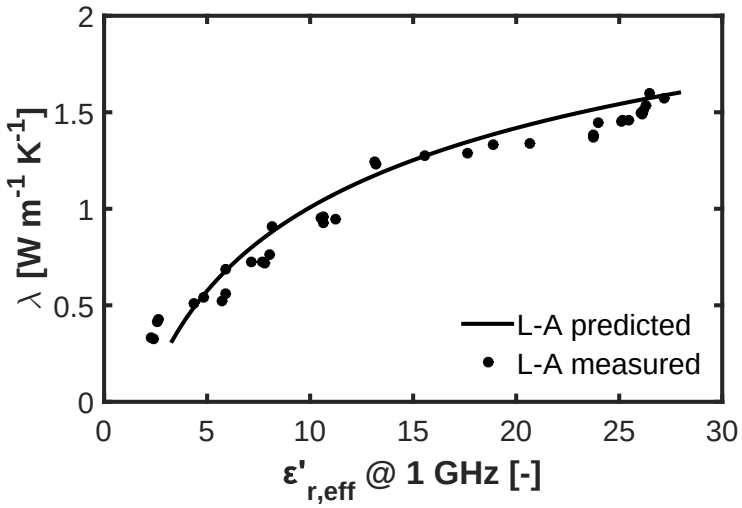

Figure 7.29: Variation of effective thermal conductivity λ with the real part $\varepsilon'_{r,eff}$ of the relative effective complex permittivity of L-A for different settlement potential conditions (New model prediction - Equation 4.5).

7.2.2.5 Variations with temperature

In this section results of the variations of the effective thermal conductivity and effective dielectric permittivity with medium temperature are presented. For verifying the predictions of the new semi-theoretical dielectric and thermal models, experimental dielectric data of soil from Skierucha (2011) and thermal data of porous limestone samples from Aurangzeb et al. (2007) are used.

Variations of effective dielectric permittivity with temperature

Figure 7.30 shows the comparison of the prediction of the new semi-theoretical model (Equation 4.44) and experimental data from Skierucha (2011) of the variation of the bulk or effective dielectric permittivity of soil no. 621 with temperature at five volumetric water contents. Overall the new model provides a satisfactory match, with a slight overestimation, of the experimental observations for the considered temperature range. Generally, the effective dielectric permittivity or the real apparent relative permittivity $\varepsilon_{r,a}$ of the soil decreases with an increase in medium temperature, especially at higher volumetric water contents, mainly due to the reduction of the dielectric permittivity of the pore-water at low frequencies with an increase in temperature.

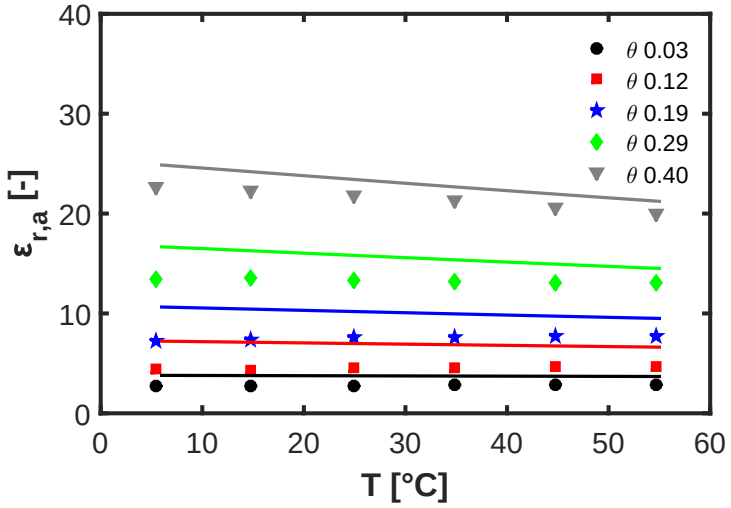

Figure 7.30: Effective dielectric permittivity $\varepsilon_{r,a}$ of soil no. 621 from Skierucha (2011) as a function of temperature T (Solid lines: new model predictions - Equation 4.44 and data points: experiment).

Variations of effective thermal conductivity with temperature

In Figure 7.31, verification of the prediction of Equation 4.42 with experimental data from literature of the variation of the thermal conductivities of various rock forming minerals with temperature is shown. Values of the phonon scattering coefficient qq for different mineral types is provided in Hailemariam and Wuttke (2018b).

Figure 7.32 shows the comparison of the prediction of the new semi-theoretical model (Equation 4.39) and experimental data from Aurangzeb et al. (2007) of the variation of the effective thermal conductivities of four porous limestone samples (designated as LS-1 to 4) with temperature. Overall the new model provides a good match for the experimental observations for the considered temperature range. Generally,

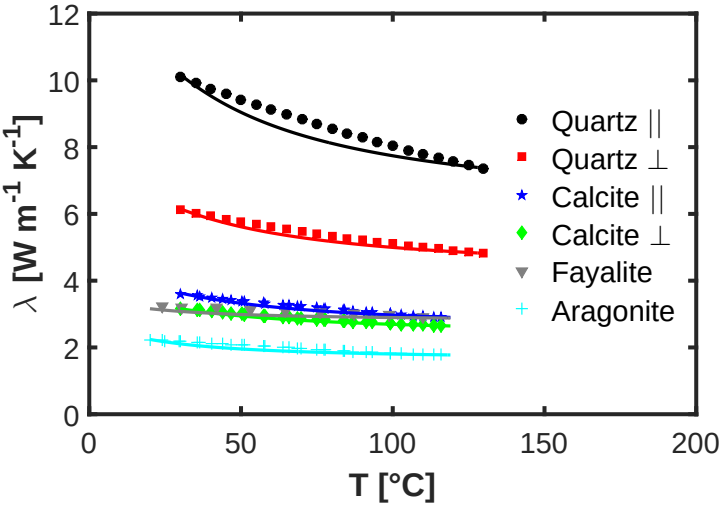

Figure 7.31: Thermal conductivities λ of various rock forming minerals as a function of temperature T (Solid lines: new model predictions - Equation 4.42 and data points: experiment (literature); Data for quartz mineral - Powell et al. (1966) and Irani and Cokar (2016), calcite, olivine-fayalite and aragonite minerals - Robertson (1988)).

the effective thermal conductivity λ of the limestone samples decreases with an increase in medium temperature, mainly due to the reduction of the thermal conductivity of the solid phase due to phonon scattering (McKenzie et al., 2005; Hailemariam and Wuttke, 2018b).

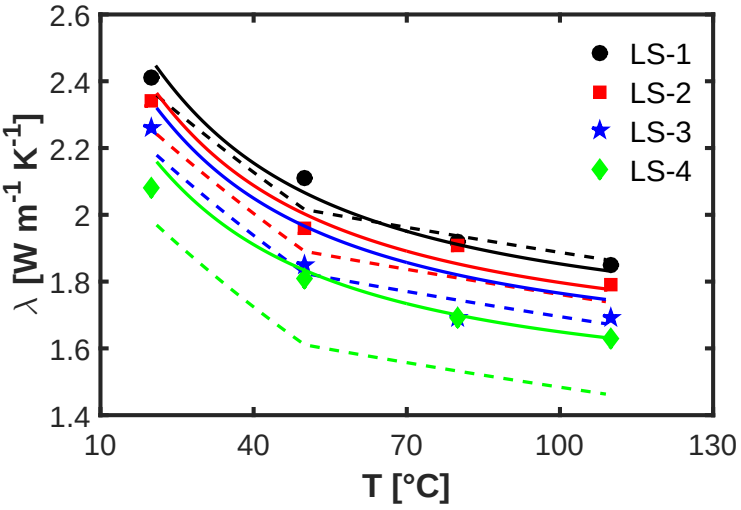

Figure 7.32: Effective thermal conductivity λ of four limestone samples from Aurangzeb et al. (2007) as a function of temperature T (Solid lines: new model predictions - Equation 4.39, dashed lines: Aurangzeb et al. (2007) model predictions and data points: experiment).

7.3 Application of analytical models for oil sands

The results of the electromagnetic measurements on the studied reconstituted oil sand are shown in Figures 7.33 - 7.35.

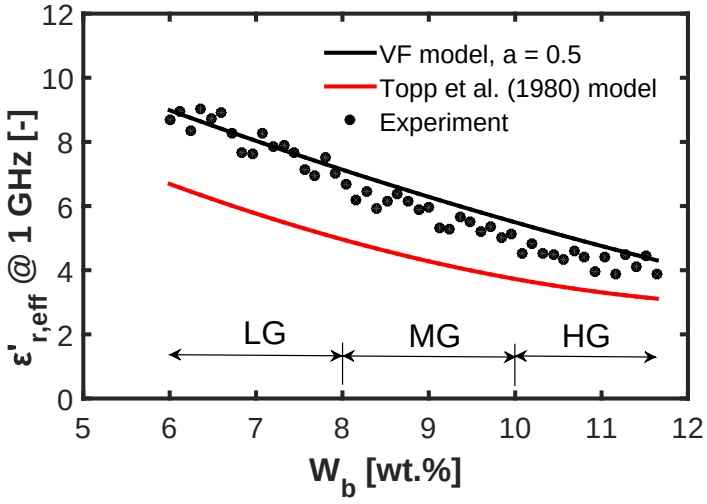

Figure 7.33: Real part $\varepsilon'_{r,eff}$ of the relative effective complex permittivity of the bitumen-water saturated reconstituted oil sand as a function of bitumen weight fraction W_b (VF model - Equation 4.11).

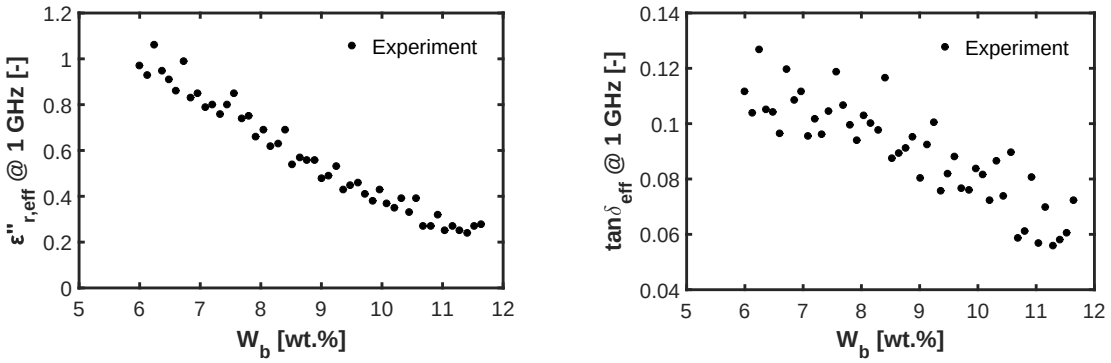

(a) (b)

Figure 7.34: Imaginary part $\varepsilon''_{r,eff}$ of the relative effective complex permittivity a) and effective loss tangent $\tan\delta_{eff}$ b) of the bitumen-water saturated reconstituted oil sand as functions of bitumen weight fraction W_b.

In Figure 7.33, result of the variation of the real part $\varepsilon'_{r,eff}$ of the relative effective complex permittivity of the reconstituted oil sand at a measurement frequency of 1 GHz with bitumen content is presented. The experimental findings are further compared to the VF model (Equation 4.11), with structural exponent $a = 1/2$ (CRIM) (Birchak et al., 1974), and the Topp et al. (1980) model. The prediction from the VF

model generally matches well with the experimental results for the considered range of bitumen-water saturation (Figure 7.33). However, the Topp et al. model significantly underestimates the measured $\varepsilon'_{r,eff}$, as it does not account for the dielectric properties of the bituminous part of oil sands.

The experimental results of the imaginary part $\varepsilon''_{r,eff}$ of the relative effective complex permittivity and the effective loss tangent $\tan\delta_{eff}$ of the bitumen-water saturated reconstituted oil sand are shown in Figure 7.34. Generally, the relative effective complex permittivity $\varepsilon^*_{r,eff}$ and the effective loss tangent $\tan\delta_{eff}$ of the oil sand decreases with an increase in the grade or bitumen content (Figures 7.33 and 7.34). This is to be expected, as for the given porosity of the oil sand, the low grade oil sands have a higher volumetric fraction of water (or a lower bitumen fraction) as compared to the high grade oil sands, and water has a much higher complex dielectric permittivity and polarization than bitumen (Buchner et al., 1999; Kaatze, 2007a; Rambabu et al., 2011; Oloumi and Rambabu, 2016).

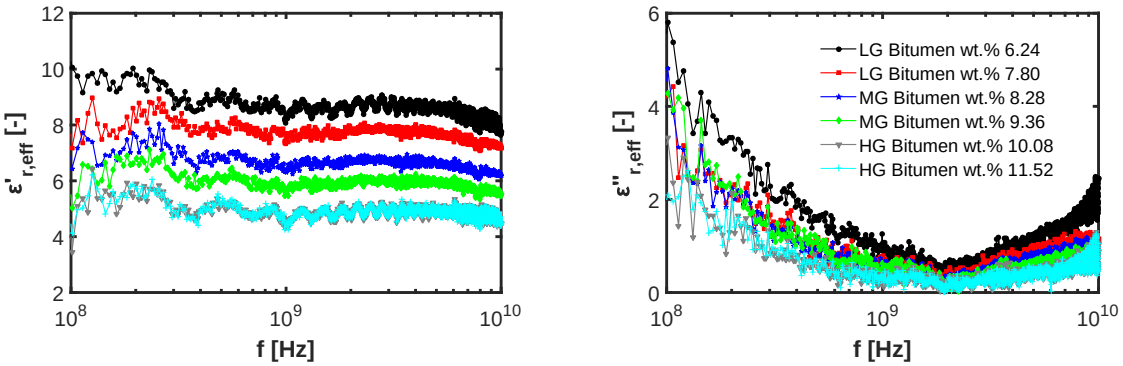

(a) (b)

Figure 7.35: Dielectric spectra of the oil sand: $\varepsilon'_{r,eff}$ a) and $\varepsilon''_{r,eff}$ b) at six bitumen weight fractions W_b.

In Figure 7.35, the measured dielectric spectra of the relative effective complex permittivity $\varepsilon^*_{r,eff}$ of the oil sand at six bitumen weight fractions W_b is presented. Generally, the reconstituted oil sand exhibits a high degree of variation of complex dielectric permittivity (mainly the imaginary part) with frequency especially at lower frequency ranges, due to the presence of clay minerals with readily dissoluble salts (3.42 wt.%, Table 6.4) (Wagner and Scheuermann, 2009).

When comparing the results of the electromagnetic tests on the oil sand with the silty clay soils (section 7.2.1) and the loess soil (section 7.2.2), the oil sand exhibits a much lower complex dielectric permittivity, polarization and dielectric dispersion (Figures 7.1 - 7.3, 7.8 - 7.10 and 7.33 - 7.35) due to its much lower moisture and clay (with soluble salts) contents.

In summary, the dielectric spectra shows a typical frequency dependence for the reconstituted oil sand (with the dielectric dispersion decreasing with an increase in the bitumen fraction or grade of the oil sand, Figure 7.35) with: a) a stronger frequency dependence of the complex dielectric permittivity at low frequency ranges due to the presence of clay minerals; b) a strong decrease in the imaginary part as compared to the real part with increasing frequency below around 2 GHz for all grades of the oil sand, mainly due to electrical induced losses and c) an increase in the imaginary part above around 2 GHz mainly due to main water relaxation contribution (Wagner et al., 2007b; Wagner and Scheuermann, 2009).

Figure 7.36 presents the results of effective thermal conductivity λ and effective specific heat capacity c measurements of the bitumen-water saturated reconstituted oil sand as a function of bitumen weight fraction W_b.

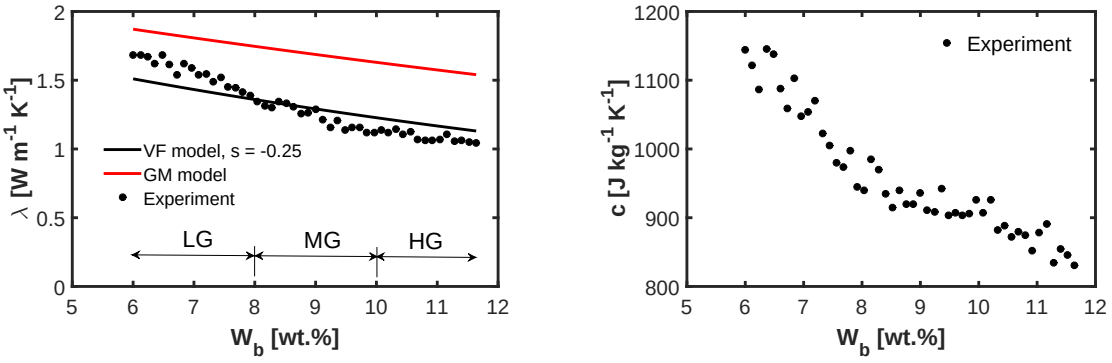

(a) (b)

Figure 7.36: Effective thermal conductivity λ a) and effective specific heat capacity c b) of the bitumen-water saturated reconstituted oil sand as functions of bitumen weight fraction W_b (VF model - Equation 4.9).

The experimental findings of thermal conductivity λ are further compared to the VF model (Equation 4.9), with coefficient $s = -0.25$ (Yun and Santamarina, 2007), and the geometric mean (GM) model (McGaw, 1969; Farouki, 1981). The VF model provides a good match to the experimental findings for the considered grades of the oil sand (Figure 7.36a). However, although the GM model includes information on all the three constituent phases of the oil sand (i.e. solids, pore-bitumen and pore-water), it generally overestimates the measured effective thermal conductivity (Figure 7.36a). As discussed in section 4.2.2, the GM model gives satisfactory results for water saturated porous media, where the ratio of the thermal conductivities of the solid grains to the saturating fluid (in this case water) $\lambda_s/\lambda_f < 15$ (Côté and Konrad, 2005; Hailemariam et al., 2016), but overestimates the thermal conductivity of oil saturated porous media, where the ratio of the thermal conductivities of the solid grains to the saturating fluid (in this case bitumen) $\lambda_s/\lambda_f > 15$.

Generally, the effective thermal conductivity λ and the effective specific heat c of the bitumen-water saturated oil sand decrease with an increase in the grade or bitumen content (Figures 7.36a and 7.36b). This is to be expected, as for the given porosity of the oil sand, the low grade oil sands have a higher volumetric fraction of water (or a lower bitumen fraction) as compared to the high grade oil sands, and water has a much higher heat conduction and storage ability than bitumen (Smith-Magowan et al., 1982; Ramires et al., 1995; American Petroleum Institute, 1997; Hirono and Hamada, 2010; Irani and Cokar, 2016).

When comparing the results of the thermal measurements on the oil sand with the silty clay soils (section 7.2.1) and the loess soil (section 7.2.2), the oil sand (with max. λ at lowest bitumen grade) exhibits a slightly higher thermal conductivity than the silty clay soils (with max. λ at saturated conditions) and the loess soil at loose natural condition (with max. λ at saturated conditions) (Figures 7.4, 7.11a and 7.36a). Although the oil sand has a lower gravimetric water content fraction than the soils at saturated conditions (which should result in a lower λ), its observed higher thermal conductivity is attributed to its comparatively higher fraction of coarse grains/quartz mineral (Hailemariam et al., 2017), lower clay fraction (Abu-Hamdeh and Reeder, 2000) and lower organic content (Gupta et al., 1977) (Tables 6.1, 6.3 and 6.4).

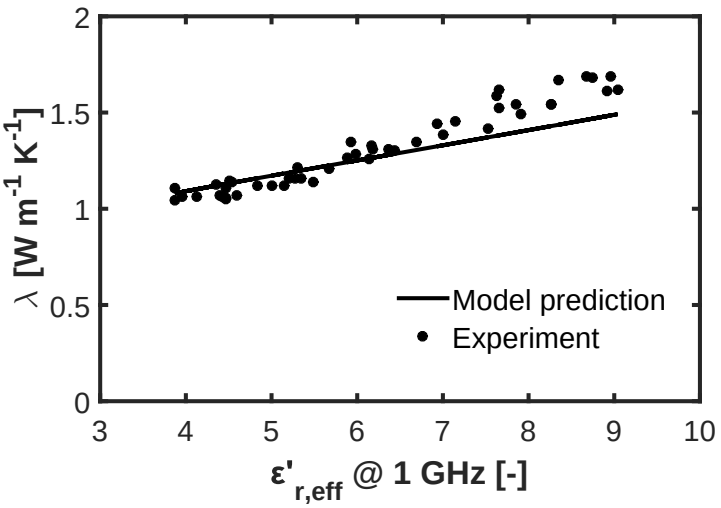

Figure 7.37: Variation of effective thermal conductivity λ with the real part $\varepsilon'_{r,eff}$ of the relative effective complex permittivity of the bitumen-water saturated reconstituted oil sand (New model - Equation 4.15).

The comparison of the new model for predicting the thermal conductivity of bitumen-water saturated oil sands from complex dielectric permittivity (Equation 4.15) and experimental data is shown in Figure 7.37. The prediction of the new model matches

well to the experimental findings with a slight underestimation at higher water contents (higher $\varepsilon'_{r,eff}$ at 1 GHz). The average error of prediction of the new model for the reconstituted oil sand used in this study is 5.51%.

7.4 Comparison between the results of the different thermo-dielectric equipments used

In this section, the accuracy of the different equipments used in this thesis to obtain the thermal and dielectric measurements is assessed.

Table 7.1 shows the results of the real part $\varepsilon'_{r,eff}$ of the relative effective complex permittivity measurements obtained with the TDR (section 6.3.2.1) and VNA (section 6.3.2.2) devices. The results from the two devices generally match well with an average difference of 7.99% for the two sets of data presented here.

Table 7.1: Comparison of the real part $\varepsilon'_{r,eff}$ of the relative effective complex permittivity measurements obtained with the TDR and VNA devices.

Soil name and state	**TDR**	**VNA**	**Difference (%)**
L-A, natural moisture condition	8.29	7.7	7.66
L-A, saturated condition	29.42	27.16	8.32

Table 7.2 shows the results of the effective thermal conductivity λ measurements obtained with the transient, TR, (section 6.3.1.1) and steady state, SS, (section 6.3.1.2) devices. The results from the two devices generally match well with an average difference of 9.64% for the two sets of data presented here.

Table 7.2: Comparison of the effective thermal conductivity λ measurements obtained with the transient (TR) and steady state (SS) devices.

Soil name and state	**TR**	**SS**	**Difference (%)**
L-A, optimum moisture condition	1.229	1.342	8.42
SC-A, saturated condition	1.389	1.253	10.85

7.5 Summary of the prediction results of the new thermo-dielectric models

In this section, a summary of the comparison between experimental data and the new effective thermal conductivity prediction models (using porous media dielectric permittivity data) (Equations 4.13 and 4.5) is presented. The thermo-dielectric results of the silty clay and loess soils as well as the oil sand which were separately presented in sections 7.2 and 7.3 are combined and plotted in Figure 7.38. The prediction of the new model matches well to the experimental findings with an overall average error of prediction of 9.45%.

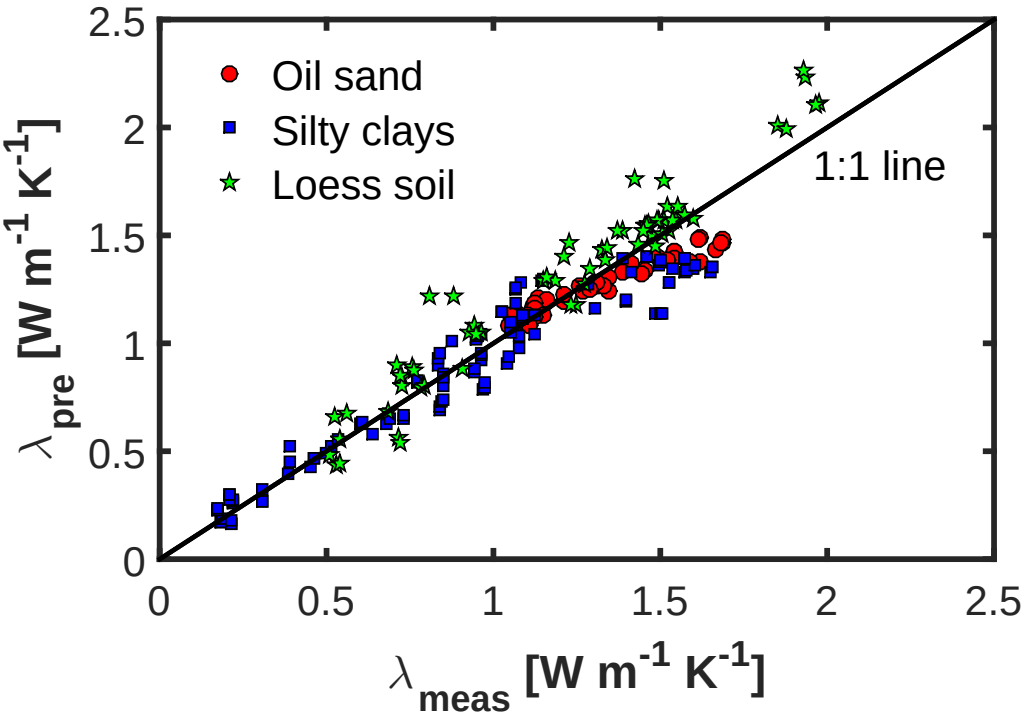

Figure 7.38: Comparison of the predicted effective thermal conductivity λ_{pre} (using porous media dielectric permittivity data) and measured effective thermal conductivity λ_{meas} of the silty clay and loess soils as well as the oil sand used in this study (New models prediction - Equations 4.5 and 4.13).

7.6 Summary of chapter 7

Results of the theoretical and experimental investigations on the behavior and correlation of the thermal and dielectric porous media parameters at different porous media hydro-mechanical conditions were presented. Generally, a strong correlation between the effective thermal conductivity and effective dielectric permittivity of the investigated porous media was obtained, thus enabling the prediction of one parameter from the other, as shown by the good accuracy and matching of the semi-theoretical models with the experimental data.

Chapter 8

Results and discussion II: Validation of numerical models

8.1 Introduction

In this chapter, results of the numerical LEM modeling (see chapter 5) of the behavior and correlation of the thermal and dielectric parameters of bitumen-water saturated oil sands are presented. The newly developed LEM model is first verified by comparison with analytical and FEM solutions, and then validated with the experimental study of effective thermal conductivity and effective dielectric permittivity of the oil sand presented in section 7.3. In this regard, the model prediction results for the variations of the thermal and dielectric parameters with bitumen/water content, frequency, randomness factor, salinity and temperature are discussed.

8.2 Verification of LEM model with analytical and FEM results

To verify the LEM results with analytical and FEM outputs under steady state conditions, a homogeneous domain (of dimensions 1×1 m) with the thermal (thermal conductivity λ as input function) and electrical (electrical conductivity σ_E as input function) boundary and initial conditions specified in Figure 8.1 is used.

Figure 8.2 shows the generated nodes or Voronoi cells and the associated Delaunay lattice elements for the domains shown in Figure 8.1. The nodal points of the LEM domains are generated using the VRL technique (Moukarzel and Herrmann, 1992; Lilliu and van Mier, 2003) with $R = 0.5$ and 15×15 (225) elements.

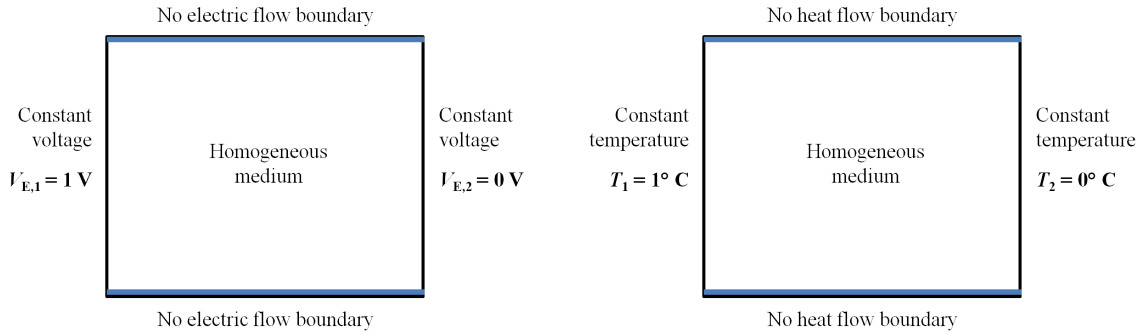

Figure 8.1: Schematics of the boundary and initial conditions of the domain for: electric flow a) and thermal flow b).

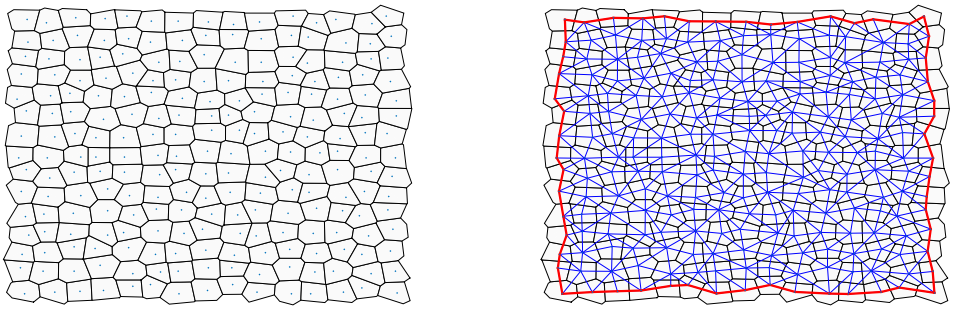

Figure 8.2: The generated nodes a) and Voronoi scaling b) of the representative domain.

In Figures 8.3 and 8.4, comparison of results of FEM and LEM for the spatial distributions of electric potential (voltage) V_E (V) and temperature T (°C) in the representative domain, respectively, are presented. As the medium taken is homogeneous for verification purposes, a good match between the two numerical approaches is obtained. In general, for homogeneously distributed constituent phases of a porous medium, the predictions of LEM match those of FEM when the degree of randomness of the lattices R is very low. However, for such regular lattices or elements, anisotropic effects are high due to the lack of disorder in the geometry. Furthermore, naturally occurring porous media formations exhibit a high degree of geometrical disorder as well as variations in the spatial arrangement of constituent phases, thus making the use of the LEM technique with a higher randomness factor R a more preferable approach. In addition, the electric potential and temperature profiles across the representative domain obtained with LEM are compared with analytical solutions with satisfactory accuracy (Figure 8.5).

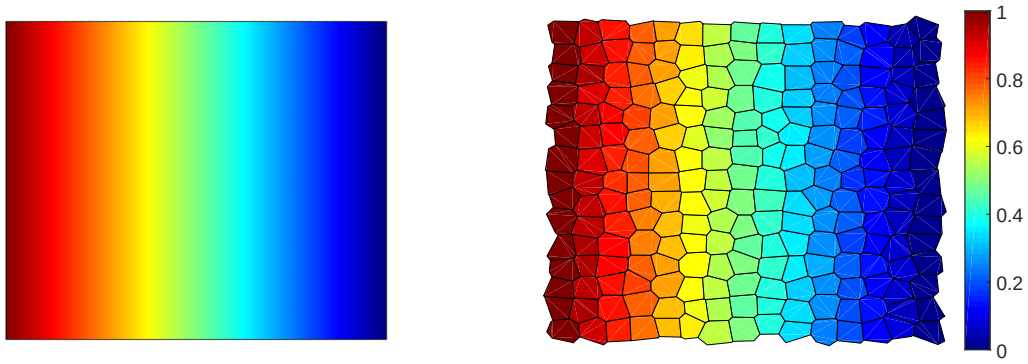

(a) (b)

Figure 8.3: Electric potential V_E (V) distribution in the domain with: FEM a) and LEM b).

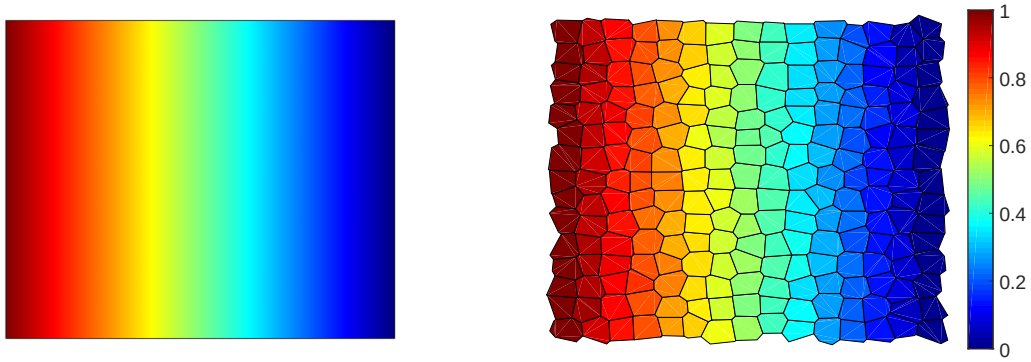

(a) (b)

Figure 8.4: Temperature T (°C) distribution in the domain with: FEM a) and LEM b).

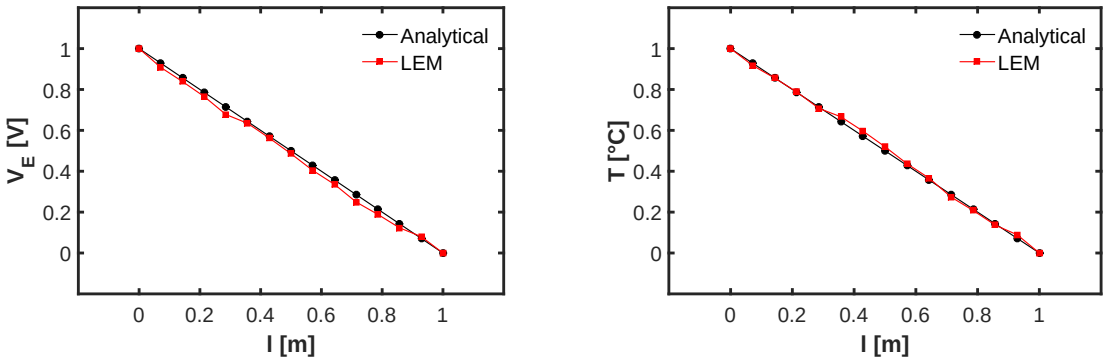

(a) (b)

Figure 8.5: Comparison between analytical and LEM solutions for: electric potential V_E profile a) and temperature T profile b).

8.3 Variations with bitumen/water content

8.3.1 Variations of the effective parameters of the domain with grade of oil sand

LEM domains with varying bitumen/water contents of the oil sand studied in this thesis are generated to obtain the variation of the effective parameters with bitumen content or grade of oil sand. LEM domains of three bitumen contents of the oil sand are shown in Figure 8.6. The nodal points of the LEM domains are generated using the VRL technique (Figures 8.6a, 8.6d and 8.6g) (Moukarzel and Herrmann, 1992; Lilliu and van Mier, 2003) with $R = 0.5$ and 25 $\times$ 25 (625) elements. The representative domain has dimensions of 5 $\times$ 5 cm. Better accuracy of results is obtained when a higher number of nodes is used, however, this requires a higher computational effort and CPU time. With the use of the randomness factor R in the VRL technique, disorder is introduced (increasing with the value of R) at the geometric level and hence anisotropic effects are reduced. The nodes (and consequently the Voronoi cells) are then assigned the properties of the respective constituent phases of the porous medium randomly according to their volumetric proportions as shown in Figures 8.6b, 8.6e and 8.6h (i.e. a single node/Voronoi cell may represent a single constituent phase, e.g. a solid particle, or an assembly of phases e.g. several solid particles). Other methods of assigning the constituent phases include the particle packaging method (i.e. a set of nodes/Voronoi cells together form a single constituent phase with no fixed pattern) and via image processing (i.e. a set of nodes/Voronoi cells together form a single constituent phase based on data collected from image processing). The Delaunay lattice elements and the associated Voronoi cells representing the nodes generated via the Voronoi scaling approach using MATLAB are shown in Figures 8.6c, 8.6f and 8.6i.

The convergence plots for solving the effective parameters of the three generated domains are shown in Figure 8.7. A typical CPU run time for obtaining the effective parameters of a domain with the given number of nodes is around $640\,\mathrm{s}$.

In Figure 8.8, LEM model prediction results are compared with the experimental data of the variation of the real part $\varepsilon'_{r,eff}$ of the relative effective complex permittivity (hereafter simply called effective dielectric permittivity) at a measurement frequency of 1 GHz with bitumen content or grade of oil sand. As stated in earlier chapters, the values of the effective dielectric permittivity at a particular frequency range of around 1 GHz were selected from the spectra, as at this frequency range, information on the free water in the porous medium can be obtained, and the dispersion and absorption

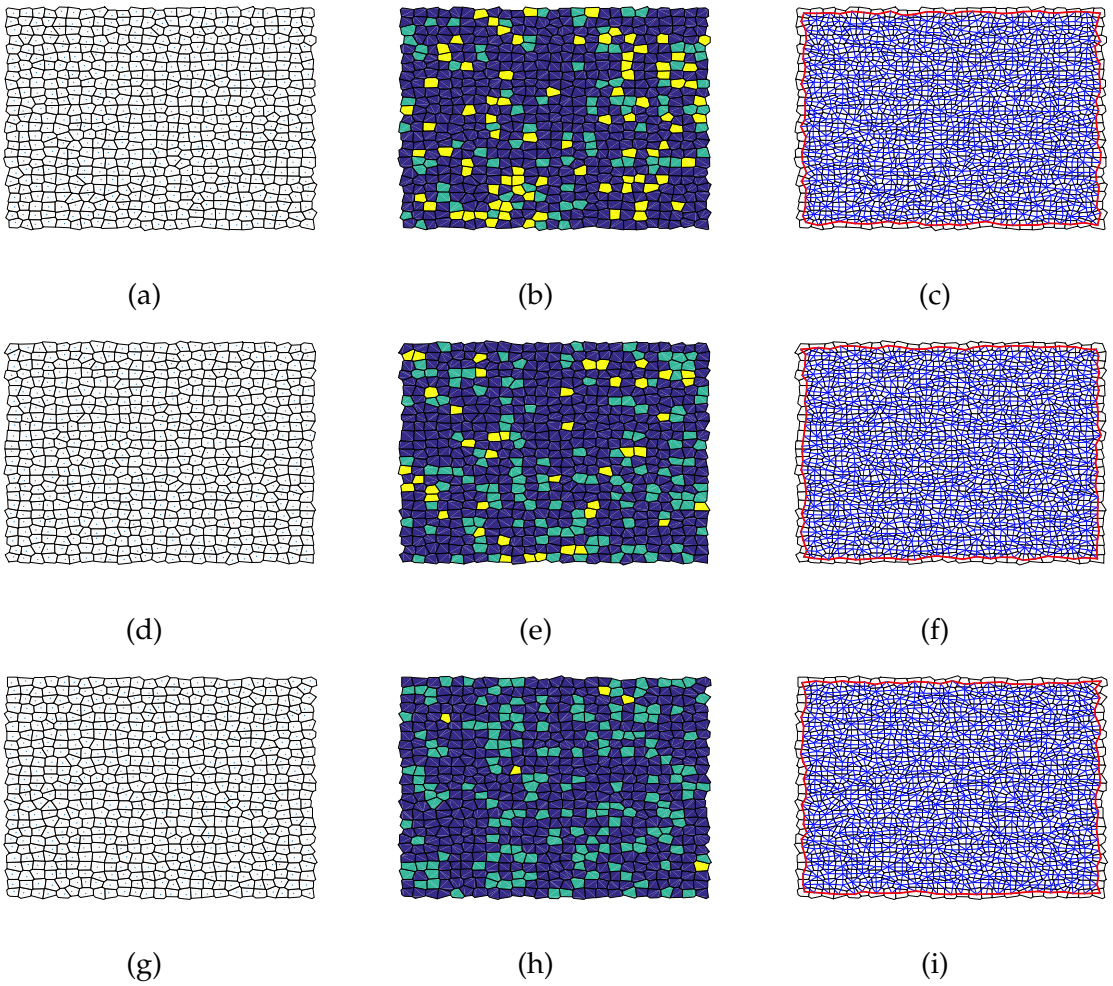

Figure 8.6: The generated nodes, distribution of the three constituent phases and Voronoi scaling of the oil sand domains with: $W_b = 6.00$ wt.% a, b, c), $W_b = 8.88$ wt.% d, e, f), and $W_b = 11.64$ wt.% g, h, i), respectively (solids - dark blue cells, bitumen - dark green cells and pore-water - yellow cells) (Delaunay lattice elements - blue lines and Voronoi cells - black lines).

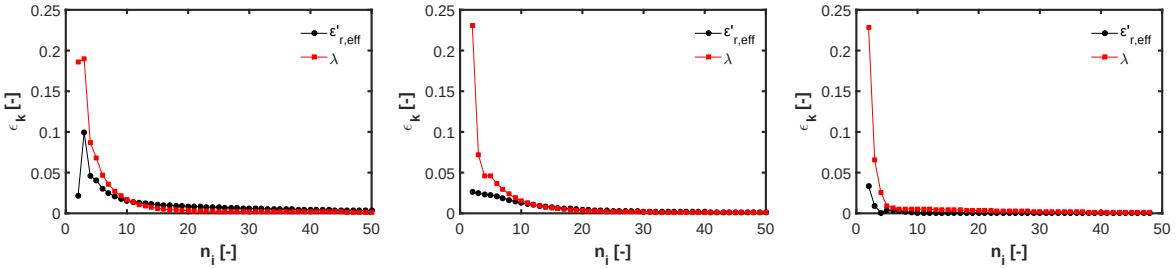

Figure 8.7: Convergence plots for the domains with $W_b = 6.00$ wt.% a), $W_b = 8.88$ wt.% b) and $W_b = 11.64$ wt.% c).

processes be compared directly (Blonquist Jr. et al., 2006; Wagner and Scheuermann, 2009; Wagner et al., 2014).

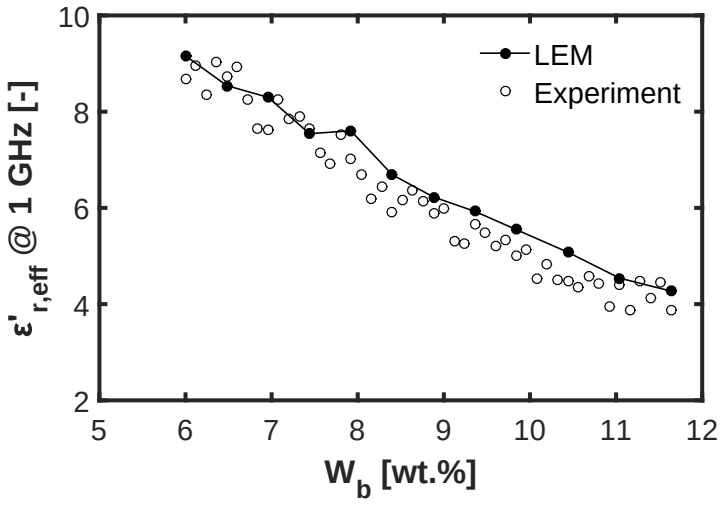

Figure 8.8: Comparison of numerical and experimental results of the variation of the effective dielectric permittivity $\varepsilon'_{r,eff}$ of the bitumen-water saturated reconstituted oil sand with bitumen weight fraction W_b.

The prediction of the LEM model matches well with the experimental results for the considered range of bitumen-water saturation. The effective dielectric permittivity $\varepsilon'_{r,eff}$ of the bitumen-water saturated reconstituted oil sand decreases with an increase in the grade or bitumen content, as for the given porosity of the oil sand, the low grade oil sands have a higher volumetric fraction of water (or a lower bitumen fraction) as compared to the high grade oil sands, and water has a much higher dielectric permittivity than bitumen (Buchner et al., 1999; Kaatze, 2007a; Rambabu et al., 2011; Oloumi and Rambabu, 2016).

Figure 8.9 shows the comparison between LEM model prediction results and the experimental data of the variation of effective thermal conductivity λ with bitumen content or grade of oil sand. The prediction of the LEM model matches well with the experimental results for the considered range of bitumen-water saturation. Overall, the effective thermal conductivity λ of the bitumen-water saturated oil sand decreases with an increase in the grade or bitumen content, as for the given porosity of the oil sand, the low grade oil sands have a higher volumetric fraction of water (or a lower bitumen fraction) as compared to the high grade oil sands, and water has a much higher heat conduction ability than bitumen (Ramires et al., 1995; American Petroleum Institute, 1997).

Figure 8.10 shows the comparison between LEM model prediction results and the

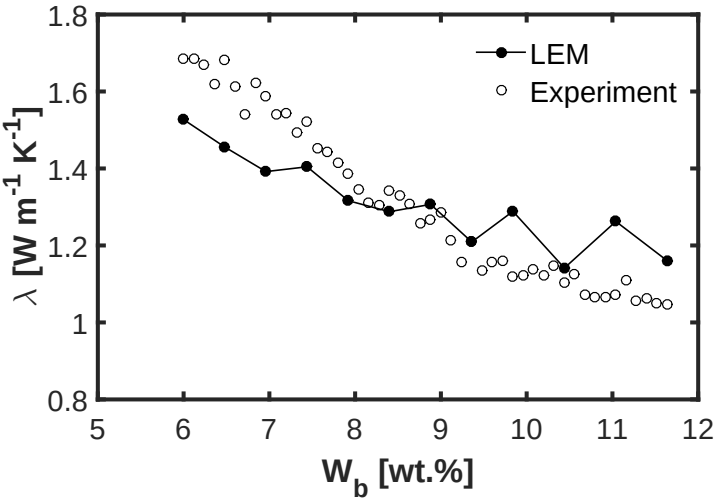

Figure 8.9: Comparison of numerical and experimental results of the variation of the effective thermal conductivity λ of the bitumen-water saturated reconstituted oil sand with bitumen weight fraction W_b.

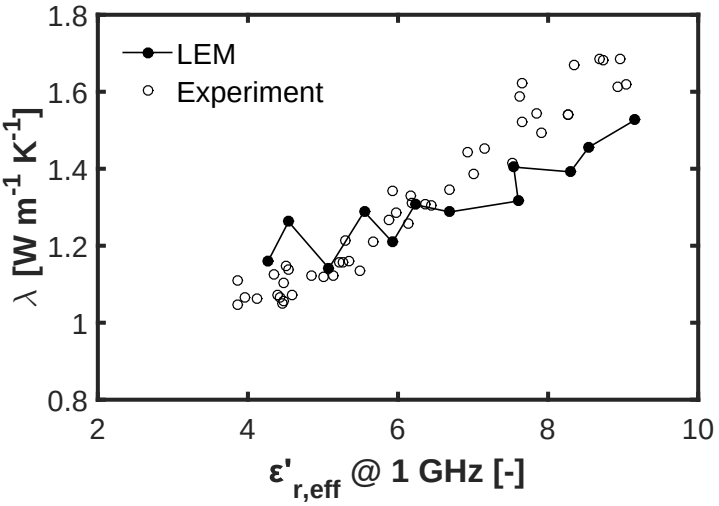

Figure 8.10: Comparison of numerical and experimental results of the variation of the effective thermal conductivity λ of the bitumen-water saturated reconstituted oil sand with effective dielectric permittivity $\varepsilon'_{r,eff}$.

experimental data of the variation of the effective thermal conductivity of bitumen-water saturated oil sands with effective dielectric permittivity. The prediction of the numerical model matches well to the experimental findings with an average error of prediction of 8.55%. Although the prediction of the numerical model for estimating the effective parameters of the oil sand is not as accurate as that of the theoretical model (5.51%, section 7.3), the results are satisfactory considering the wide range of applicability of the numerical model as well as its ability to estimate spatial parameter distributions.

8.3.2 Spatial variations of the effective parameters of the domain with grade of oil sand

Figure 8.11 shows the spatial variations of the effective dielectric permittivity $\varepsilon'_{r,eff}$ and effective thermal conductivity λ of the three LEM domains of the oil sand grades shown in Figure 8.6. When plotted in terms of nodal wave velocity or effective electrical conductivity, the predictions of the spatial distributions of the LEM model provide a numerical alternative to obtaining the effective parameters with experimental or field measurement techniques such as electrical resistivity tomography (ERT) or electrical resistivity imaging (ERI).

As discussed earlier, both the effective dielectric permittivity and effective thermal conductivity decrease with an increase in the bitumen content or grade of the oil sand. Moreover, as the water phase of the oil sand has the highest magnitude of dielectric constant as compared to the solid and bituminous phases, the best electric conduction paths of the domains are concentrated along the pore-water nodes (Figures 8.11a, 8.11c and 8.11e) (Buchner et al., 1999; Kaatze, 2007a; Rambabu et al., 2011; Oloumi and Rambabu, 2016; Hailemariam et al., 2017). In contrast, as the solid phases of the oil sand have the highest magnitude of thermal conductivity as compared to the pore-water and bituminous phases, the best heat conduction paths of the domains are concentrated along the solid nodes (Figures 8.11b, 8.11d and 8.11f) (Ramires et al., 1995; American Petroleum Institute, 1997; Hailemariam et al., 2017).

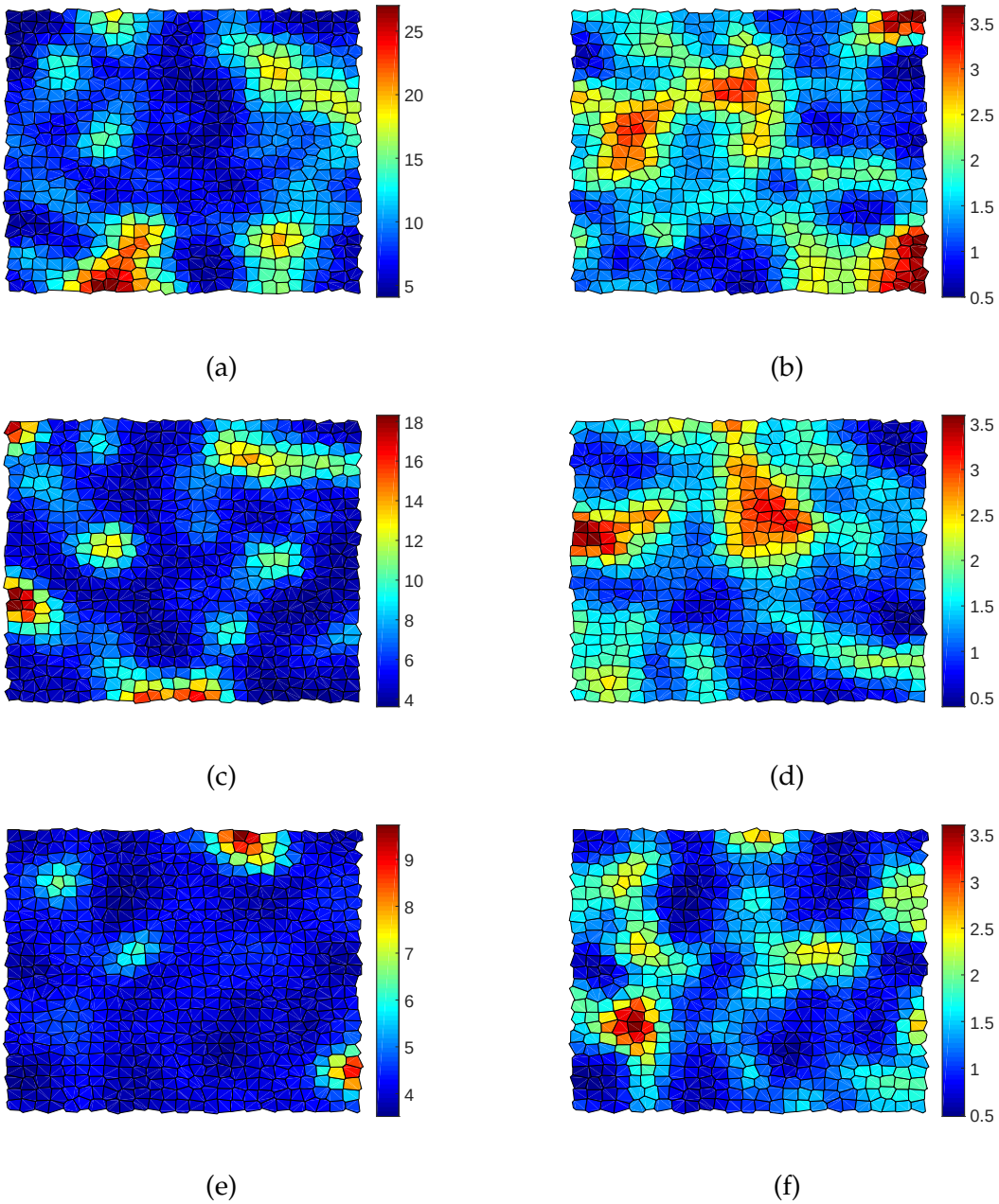

Figure 8.11: Spatial distributions of the effective dielectric permittivity $\varepsilon'_{r,eff}$ (-) and effective thermal conductivity λ (W m^{-1} K^{-1}) of the oil sand domains with: $W_b = 6.00$ wt.% a, b), $W_b = 8.88$ wt.% c, d), and $W_b = 11.64$ wt.% e, f), respectively.

8.4 Variations with frequency

8.4.1 Variation of the effective dielectric permittivity of the domain with frequency

In Figure 8.12, comparison between LEM model prediction results and the experimental data of the dielectric spectra of the effective dielectric permittivity $\varepsilon'_{r,eff}$ of the oil sand at three bitumen weight fractions W_b is shown. As discussed in earlier chapters, the accuracy of the experimental measurements below the frequency of 100 MHz and above 10 GHz is substantially low due to probe geometry and radiation effects. The prediction of the LEM model matches well with the experimental results for the three grades of oil sand shown at the considered frequency range, including the static and high frequency limits of permittivity, as well as the magnitude of the dielectric dispersion. Moreover, both the LEM and experimental dielectric spectra show a typical frequency dependence for the reconstituted oil sand, with the dielectric dispersion decreasing with an increase in the bitumen fraction or grade of the oil sand.

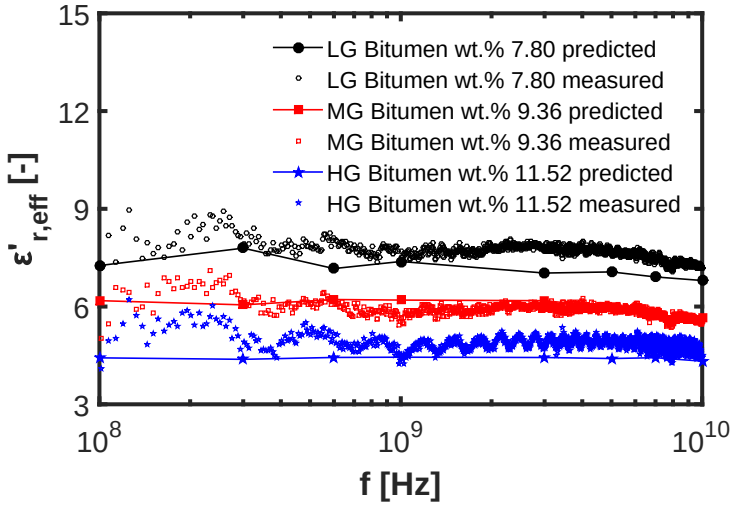

Figure 8.12: Comparison of numerical and experimental results of the dielectric spectra of the effective dielectric permittivity $\varepsilon'_{r,eff}$ of the oil sand at three bitumen weight fractions W_b.

8.4.2 Spatial variation of the effective dielectric permittivity of the domain with frequency

Figure 8.13 shows the spatial variations of the effective dielectric permittivity $\varepsilon'_{r,eff}$ with frequency f of the LEM domain of the oil sand with bitumen grade $W_b = 6.00$ wt.% shown in Figures 8.6a, 8.6b and 8.6c.

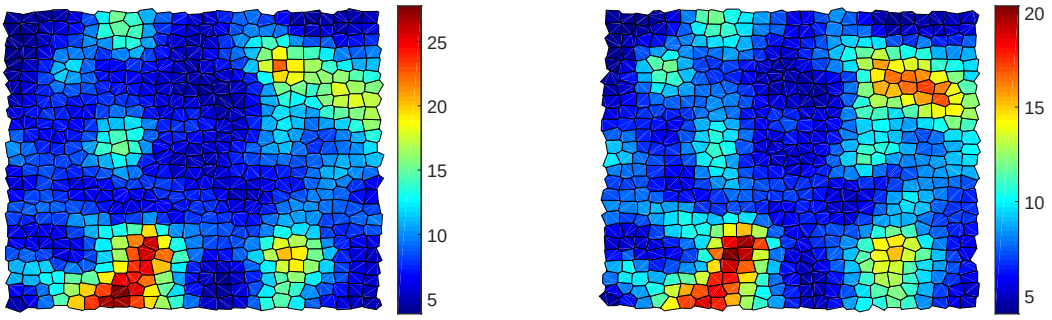

(a) (b)

Figure 8.13: Spatial distributions of the effective dielectric permittivity $\varepsilon'_{r,eff}$ (-) of the oil sand domain with $W_b = 6.00$ wt.% at frequencies: $f = 0.1$ GHz a) and $f = 10$ GHz b).

The effective dielectric permittivity of the domain decreases with an increase in frequency (Figure 8.13) above around 3 GHz, especially around the location or concentrations of the pore-water phases of the oil sand domain. This is mainly attributed to the reduction of the dielectric permittivity of water above around 3 GHz frequencies (Buchner et al., 1999; Kaatze, 2007a).

8.5 Variations with randomness factor

Figure 8.14 shows the spatial variations of the effective dielectric permittivity $\varepsilon'_{r,eff}$ and the effective thermal conductivity λ with randomness factor R of the LEM domain of the oil sand with bitumen grade $W_b = 6.00$ wt.% shown in Figures 8.6a, 8.6b and 8.6c.

A higher randomness factor R results in a more complex array of nodes, thus requiring a higher computation effort for generating the Voronoi discretizations and Delaunay triangulations as compared to a regular domain (with a lower R). However, lattices with a higher R possess different lengths or geometry and hence have minimum anisotropic effects at the geometrical level (Moukarzel and Herrmann, 1992; Wang and Cohen, 1996; Lilliu and van Mier, 2003). For this reason they are more preferable.

Generally, when the constituent phases of an LEM domain of a porous medium are uniformly generated, and when a low value of R with a small degree of disorder is used to obtain a regular lattice, the numerical results of the LEM will approach values predicted by continuum models such as FEM. However, it should be noted that although these domain generation techniques minimize computational effort and

enhance parallel computation, they do not represent typical structures exhibited by naturally occurring porous media formations, and may provide inaccurate estimates of the desired parameters.

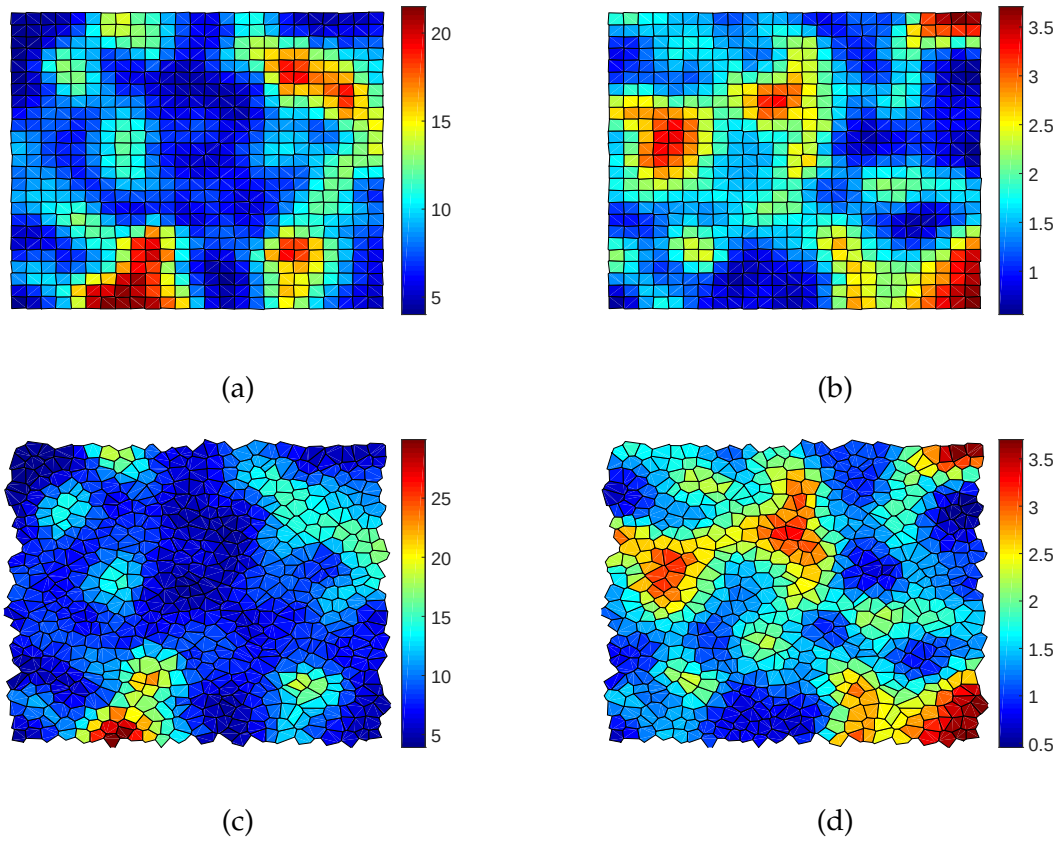

Figure 8.14: Spatial distributions of the effective dielectric permittivity $\varepsilon'_{r,eff}$ (-) and effective thermal conductivity λ (W m^{-1} K^{-1}) of the oil sand domain with $W_b = 6.00$ wt.% and randomness factors: $R = 0.1$ a, b), and $R = 0.9$ c, d), respectively.

8.6 Variations with pore-water salinity

Figure 8.15 shows the spatial variations of the effective dielectric permittivity $\varepsilon'_{r,eff}$ and the effective thermal conductivity λ with pore-water salinity S of the LEM domain of the oil sand with bitumen grade $W_b = 6.00$ wt.% shown in Figures 8.6a, 8.6b and 8.6c.

The effective dielectric permittivity of the domain decreases with an increase in the pore-water salinity (Figure 8.15), especially around the location or concentrations of the pore-water phases of the oil sand domain. This is mainly attributed to the reduction of free water in high salinity electrolytes. In contrast, the changes in the values

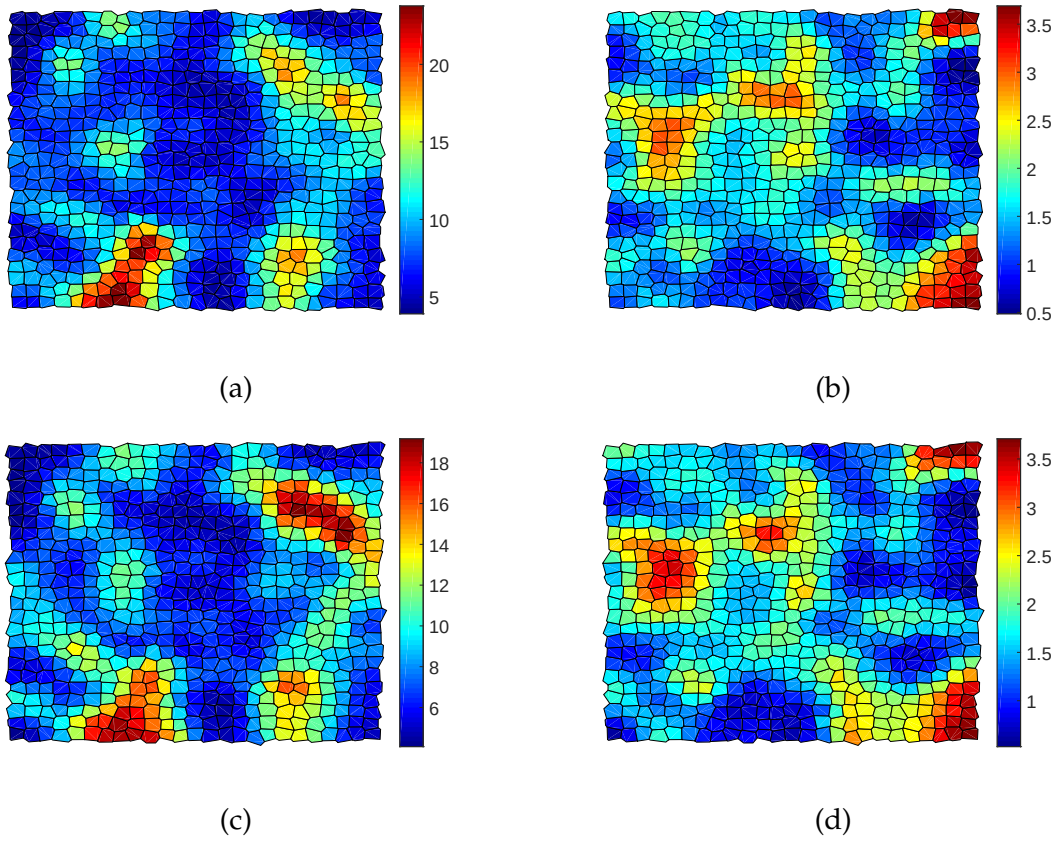

Figure 8.15: Spatial distributions of the effective dielectric permittivity $\varepsilon'_{r,eff}$ (-) and effective thermal conductivity λ (W m^{-1} K^{-1}) of the oil sand domain with $W_b = 6.00$ wt.% and pore-water salinities: $S = 5$ psu a, b), and $S = 35$ psu c, d), respectively.

of the effective thermal conductivity of the domain with an increase in the pore-water salinity are negligible, due to the comparatively small changes of the thermal conductivity of water with an increase in its salinity (Jamieson and Tudhope, 1970).

8.7 Variations with temperature

Figure 8.16 shows the spatial variations of the effective dielectric permittivity $\varepsilon'_{r,eff}$ and the effective thermal conductivity λ with medium temperature T of the LEM domain of the oil sand with bitumen grade $W_b = 6.00$ wt.% shown in Figures 8.6a, 8.6b and 8.6c.

The effective dielectric permittivity of the domain decreases considerably with an increase in the temperature of the domain (Figure 8.16), especially around the location or concentrations of the pore-water phases of the oil sand domain. This is mainly attributed to the reduction of the dielectric permittivity of water with an increase in

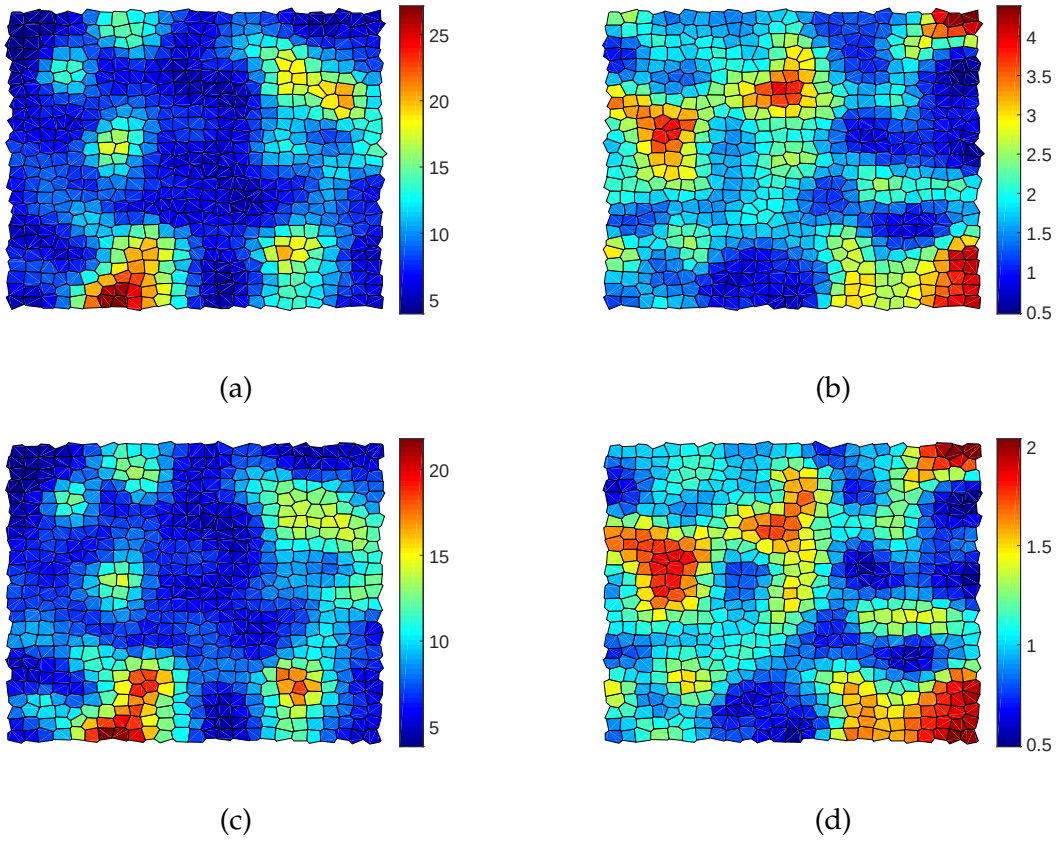

Figure 8.16: Spatial distributions of the effective dielectric permittivity $\varepsilon'_{r,eff}$ (-) and effective thermal conductivity λ (W m^{-1} K^{-1}) of the oil sand domain with $W_b = 6.00$ wt.% at temperatures: $T = 10$°C a, b), and $T = 70$°C c, d), respectively.

temperature, due to a reduction in its relaxation time with an increase in temperature (Kaatze, 2007b; Wagner et al., 2014). The relaxation time of water is directly related to the average number of hydrogen bonds (Buchner et al., 1999). Similarly, the values of the effective thermal conductivity of the domain decrease at a high magnitude with an increase in the temperature of the domain, especially around the location or concentrations of the solid phases or skeleton of the oil sand domain. This is mainly attributed to the reduction of the thermal conductivity of the quartz dominated minerals of the solid phase with an increase in temperature (Irani and Cokar, 2016; Hailemariam and Wuttke, 2018b). For both parameters, pore-water evaporation processes, which may occur at temperatures above 70°C, have not been considered in this study.

8.8 Summary of chapter 8

Results of the numerical LEM modeling of the behavior and correlation of the thermal and dielectric properties of bitumen-water saturated oil sands were presented in this chapter. The newly developed LEM model was first verified by comparison with analytical and FEM solutions, and then validated with the experimental study of effective thermal conductivity and effective dielectric permittivity of the oil sand studied in this thesis. Furthermore, the LEM model prediction results for the variations of the thermal and dielectric parameters with bitumen/water content, frequency, randomness factor, salinity and temperature were analyzed with satisfactory results.

Chapter 9

Conclusions and outlook

9.1 Conclusions

Assessing the heat transfer and electromagnetic (EM) porous media behavior is vital in understanding and solving wide variety of problems in the fields of engineering, geology, hydrology, agriculture, food processing, biological tissues, etc. In this regard, the variation and correlation of the key thermal and dielectric parameters, such as the effective thermal conductivity, effective specific heat capacity and effective complex dielectric permittivity with different porous media hydro-mechanical conditions, such as water content, porosity, matric suction, effective stress etc. was analyzed theoretically and experimentally. The extensive experimental investigation included, full behavior characterization of selected porous media (silty clay and loess soils as well as an oil sand), detailed planning for the adopted experimental procedure as well as the use of various equipments to obtain the desired thermal (using transient and steady state techniques) and dielectric (using high frequency electromagnetic time domain reflectometry and vector network analyzer) parameters.

The theoretical and experimental formulations were focused on the two most influential thermo-dielectric parameters (i.e. effective thermal conductivity and effective complex dielectric permittivity or electrical conductivity) of porous media, and their variations with controlling hydro-mechanical conditions (such as water content, porosity, matric suction, effective stress, temperature and settlement potential in the case of weak media). The outcome showed a strong correlation between the two parameters considering the wide variety of materials and hydro-mechanical conditions that were considered, complementing our previous investigations, which were done on a smaller scale. Quantitatively, the new semi-theoretical models for predicting the effective thermal conductivity of porous media based on measured dielectric data, provided an accurate ability to estimate the effective thermal conductivity of

porous media for a wide variety of hydro-mechanical conditions with an average error of prediction of 9.45%. The new models enable the estimation and assessment of the spatial variation of porous media thermal conduction of large scale deposits, such as naturally occurring unsaturated soil deposits and oil sand reservoirs, using dielectric data obtained from effective and applicable spatial large scale sub-surface exploration techniques such as ground penetrating radar (GPR), reducing the need to extract samples for the determination of moisture and bitumen contents, and saving time and costs of investigation.

Moreover, the findings of the theoretical and experimental studies were further corroborated with the development of a new numerical lattice element method (LEM) based model, which can accurately predict the magnitudes of the effective thermal conductivity and effective complex dielectric permittivity as well as their local spatial distributions in porous media domains. Unlike most continuum models, such as the finite element method (FEM), which fail to account for material heterogeneity and porous media fabric, LEM replicates the micro- and meso-scale EM and heat transfer behavior and captures the actual electric and heat conduction paths of the constituent phases of naturally occurring porous media formations which are highly heterogeneous in nature. The newly developed LEM model was verified by comparison with analytical and FEM solutions for a homogeneous medium with good accuracy. Furthermore, the numerical model prediction results for the variations of the two parameters with bitumen/water content, frequency, salinity, temperature etc. were discussed and validated against the experimental findings with satisfactory results.

The semi-theoretical and numerical models presented in this thesis are only valid for the types of porous media or geomaterials discussed in this research. The applicability of the proposed models to other types of porous media should be checked in future studies.

9.2 Scope of future work

In this research, the correlation between the key thermo-dielectric parameters was studied theoretically, numerically and experimentally under different hydro mechanical conditions with satisfactory results. Possible areas of future work on the improvement and extension of the present work are discussed next.

- Extension and validation of the existing thermo-dielectric parameter prediction theoretical models for coarse-grain textured porous media, such as sands.

- Extension and validation of the existing thermo-dielectric parameter prediction models for long-term consolidation and creep porous media behavior.
- Theoretical and experimental study of the correlation between the effective thermal conductivity and effective complex dielectric permittivity of unsaturated oil sands.
- Extension and validation of the LEM model for unsaturated porous media conditions.
- Validation of the theoretical and numerical parameter prediction models with experimental data for saline porous media deposits.
- Addition of the coupling of mechanical part (mainly due to over-burder porous media pressure) to the existing thermo-dielectric numerical model frame work, in order to accurately simulate the thermo-dielectric behavior of porous media deposits located at a considerable depth.
- Extension of the 2D LEM model to three dimensions to account for the actual anisotropic behavior of natural porous media deposits.

Appendix A

Complex dielectric permittivity of seawater

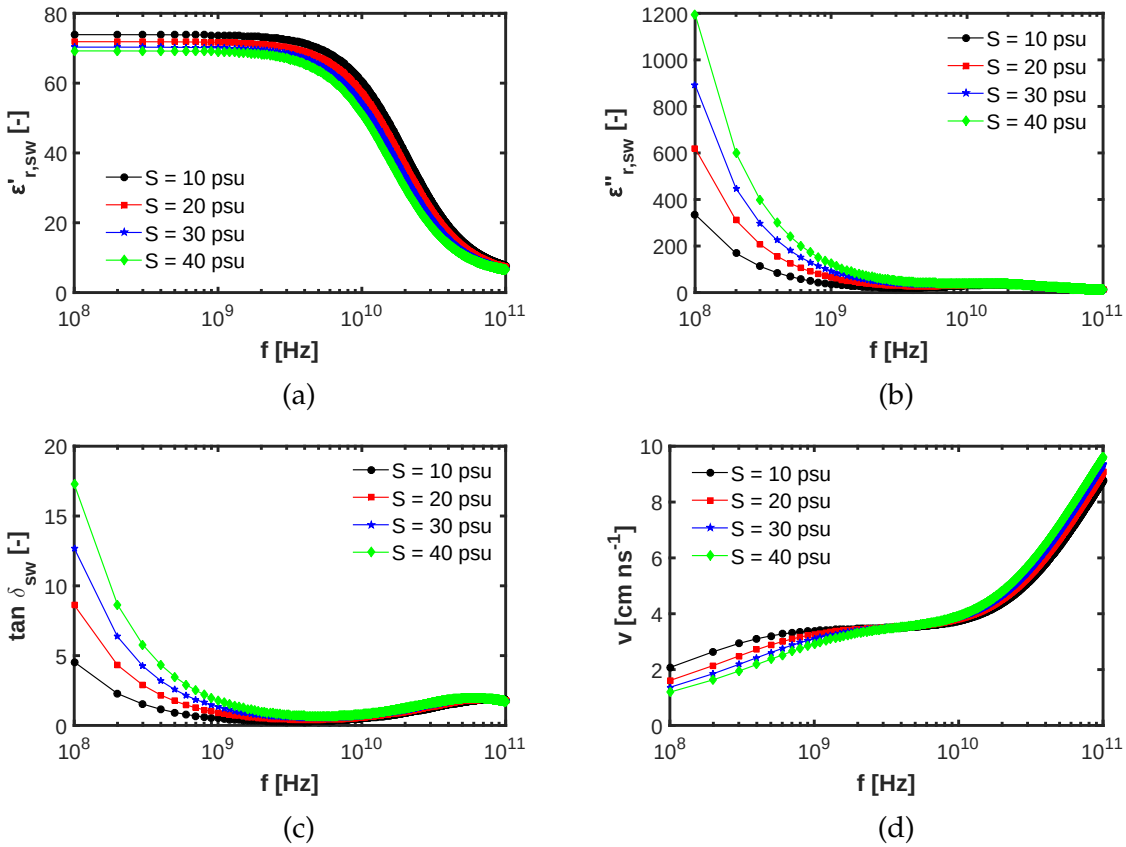

Figure A.1: Dielectric spectrum of seawater at temperature $T = 30°C$ under the effect of a relaxation process according to the modified Debye model of Blanch and Aguasca (2004) (Equation 3.9) with the real $\varepsilon'_{r,sw}$ a) and imaginary $\varepsilon''_{r,sw}$ b) parts of the relative complex dielectric permittivity, loss tangent $\tan\delta_{sw}$ c) and propagation velocity v d) of seawater at salinities $S = 10$, 20, 30 and 40 psu.

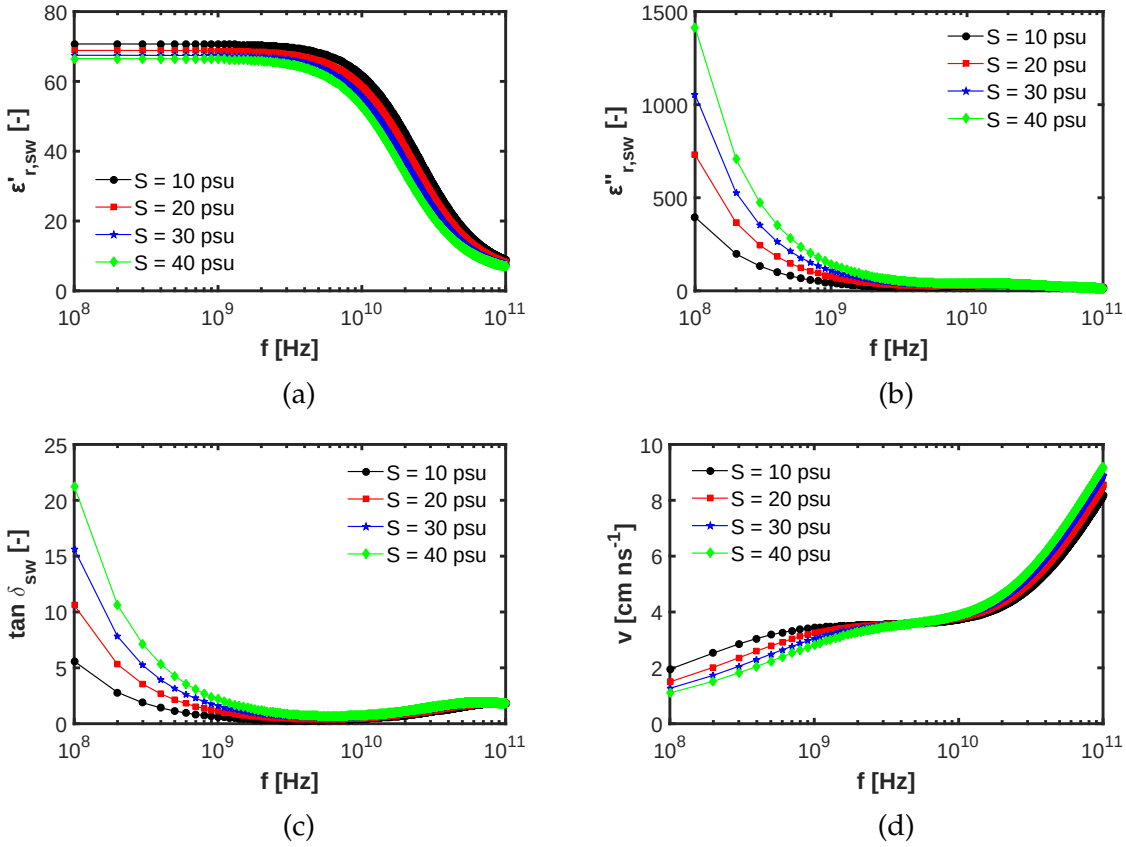

Figure A.2: Dielectric spectrum of seawater at temperature $T = 40°\text{C}$ under the effect of a relaxation process according to the modified Debye model of Blanch and Aguasca (2004) (Equation 3.9) with the real $\varepsilon'_{r,sw}$ a) and imaginary $\varepsilon''_{r,sw}$ b) parts of the relative complex dielectric permittivity, loss tangent $\tan\delta_{sw}$ c) and propagation velocity v d) of seawater at salinities $S = 10$, 20, 30 and 40 psu.

Appendix B

Bilinear calibration of complex dielectric permittivity

Following Bao et al. (1994) and Wagner et al. (2014), the bilinear relationship between the relative complex permittivity ε_r^* (ω,T) and the measured reflection or scattering factor S_m^* (ω,T) of a specimen is derived here. In general, for a two-port network (Figure B.1), we have:

$$\begin{pmatrix} b_1 \\ b_2 \end{pmatrix} = \begin{pmatrix} S_{11}^* & S_{12}^* \\ S_{21}^* & S_{22}^* \end{pmatrix} \begin{pmatrix} a_1 \\ a_2 \end{pmatrix} \tag{B.1}$$

where, S_{kl}^* with k, l = 1, 2 are the elements of the scattering matrix, a_k and b_k with k = 1, 2 are the incident and reflected waves, respectively and k = 1 and 2 represent the port connected to the HF-EM device and the port in contact with the investigated specimen, respectively (Figure B.1a).

Given that the actual measured reflection coefficient of the material $S_m^* = b_1/a_1$ and $\Gamma^* = a_2/b_2$ (Bao et al., 1994; Wagner et al., 2007a; Wagner et al., 2014), Equations B.2 and B.3 can be obtained from Equation B.1 as follows:

$$S_m^* = S_{11}^* + S_{12}^* \frac{a_2}{a_1} \tag{B.2}$$

$$\frac{1}{\Gamma^*} = S_{21}^* \frac{a_1}{a_2} + S_{22}^* \tag{B.3}$$

Solving for a_1/a_2 from Equation B.2 and substituting the obtained value in Equation B.3 and rearranging the terms we get:

$$\Gamma^* = \frac{S_m^* - S_{11}^*}{S_{22}^* S_m^* - (S_{11}^* S_{22}^* - S_{12}^* S_{21}^*)} \tag{B.4}$$

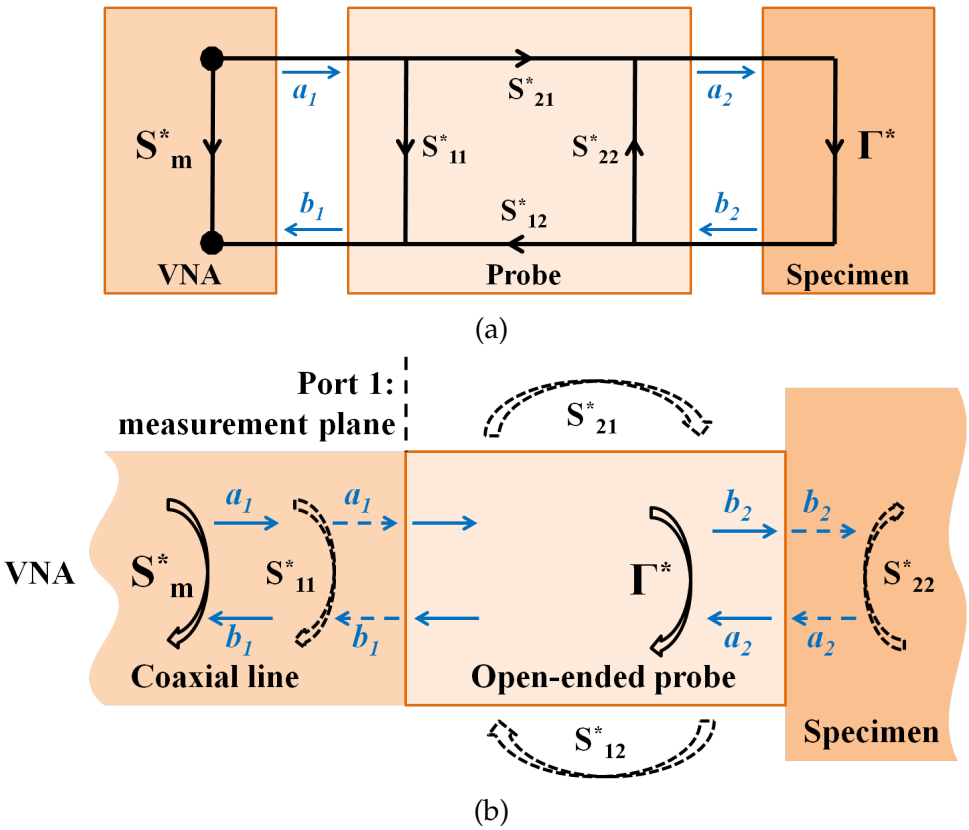

Figure B.1: Appropriate representation of a two port signal flow graph a) and a schematic representation of the measurement planes of an open-ended coaxial line system b), after Wagner et al. (2014).

In a first order approximation, the interface between the probe aperture and specimen can be modeled as two parallel capacitors (Athey et al., 1982; Stuchly et al., 1982b; Bao et al., 1994; Kaatze, 2007b; Wagner et al., 2014), which gives the following impedance:

$$Z^* = \frac{1}{j\omega(C_f + \varepsilon_r^* C_o)} \tag{B.5}$$

where, C_f is a capacitance determined by fringing-field effects inside the probe, C_o is a capacitance which depends on effects of the fringing-fields outside the probe that couples to the sample, $j = \sqrt{-1}$ is the imaginary unit, $\omega = 2\pi f$ is the angular frequency and ε_r^* is the relative complex dielectric permittivity of the specimen. The bilinear relationship between the measured scattering coefficient S_m^* and the relative complex permittivity ε_r^* (Equation B.6) is obtained by using Equation 6.14 with Equations B.4 and B.5 as (Marsland and Evans, 1987; Bao et al., 1994; Wagner et al., 2014):

$$S_m^* = \frac{c_2 + c_3\varepsilon_r^*}{c_1 + \varepsilon_r^*} \tag{B.6}$$

where, c_1, c_2 and c_3 are given by:

$$c_1 = \frac{1 - S_{22}^*}{j\omega Z_o C_o (1 + S_{22}^*)} + \frac{C_f}{C_o} \tag{B.7}$$

$$c_2 = \frac{S_{11}^* - S_{11}^* S_{22}^* + S_{12}^* S_{21}^*}{j\omega Z_o C_o (1 + S_{22}^*)} + \frac{C_f (S_{11}^* + S_{11}^* S_{22}^* - S_{12}^* S_{21}^*)}{C_o (1 + S_{22}^*)} \tag{B.8}$$

$$c_3 = \frac{S_{11}^* + S_{11}^* S_{22}^* - S_{12}^* S_{21}^*}{1 + S_{22}^*} \tag{B.9}$$

Bibliography

Abdulagatova, Z., I. M. Abdulagatov, and V. N. Emirov (2009). "Effect of temperature and pressure on the thermal conductivity of sandstone". In: *International Journal of Rock Mechanics & Mining Sciences* 46.6, pp. 1055–1071.

Abramowitz, M. and I. A. Stegun (1972). *Handbook of mathematical functions*. Dover Publications, New York, USA.

Abu-Hamdeh, N. H. and R. C. Reeder (2000). "Soil thermal conductivity: Effects of density, moisture, salt concentration, and organic matter". In: *Soil Science Society of America Journal* 64.4, pp. 1285–1290.

Abuel-Naga, H. M., D. T. Bergado, and A. Bouazza (2008). "Thermal conductivity evolution of saturated clay under consolidation process". In: *International Journal of Geomechanics* 8.2, pp. 114–122.

Al-Janabi, A. (2015). "Hydro-mechanical analysis of unsaturated collapsible soils and their stabilization". PhD thesis. Faculty of Mathematics and Natural Sciences, Kiel University, Kiel, Germany.

Alboudwarej, H., J. Felix, S. Taylor, R. Badry, C. Bremner, and B. Brough et al. (2006). *Highlighting heavy oil*. Oilfield Review, Schlumberger, Houston, Texas, USA.

Alessandro, F. (2007). "An apparatus for the routine measurement of thermal conductivity of materials for building application based on a transient hot-wire method". In: *Applied Thermal Engineering* 27.14-15, pp. 2495–2504.

Ali, S. M. Farouq (2003). "Heavy-oil evermore mobile". In: *Journal of Petroleum Science and Engineering* 37, pp. 5–9.

Alrtimi, A. A. (2008). "Experimental investigation of thermal conductivity of soils and borehole grouting materials". PhD thesis. School of Civil Engineering and Geosciences, Newcastle University, UK.

American Petroleum Institute (1997). *Technical data book: Petroleum refining*. 6th Ed. Refining Department, American Petroleum Institute, Washington DC, USA.

Archie, G. E. (1942). "The electrical resistivity log as an aid in determining some reservoir characteristics". In: *Transaction of the Society of Petroleum Engineers of the American Institute of Mining, Metallurgical and Petroleum Engineers* 146.01, pp. 54–62.

Arulanandan, K. (2003). *Soil structure: In situ properties and behavior*. Department of Civil and Environmental Engineering, University of California, Davis, California, USA.

Asami, K. (2002). "Characterization of heterogeneous systems by dielectric spectroscopy". In: *Progress in Polymer Science* 27.8, pp. 1617–1659.

ASTM D 420 - D 5876 (2011). *Soil and rock (I)*. ASTM International, West Conshohocken, Pennsylvania, USA.

ASTM D 445 - 97 (1997). *Standard test method for kinematic viscosity of transparent and opaque liquids (the calculation of dynamic viscosity)*. ASTM International, West Conshohocken, Pennsylvania, USA.

ASTM D 5298 - 94 (1994). *Standard test method for measurement of soil potential (suction) using filter paper*. ASTM International, West Conshohocken, Pennsylvania, USA.

ASTM D 5333 - 03 (2003). *Standard test method for measurement of collapse potential of soils*. ASTM International, West Conshohocken, Pennsylvania, USA.

ASTM D 5334 - 08 (2008). *Standard test method for determination of thermal conductivity of soil and soft rock by thermal needle probe procedure*. ASTM International, West Conshohocken, Pennsylvania, USA.

Athey, T. W., M. A. Stuchly, and S. S. Stuchly (1982). "Measurement of radio frequency permittivity of bilological tissues with an open-ended coaxial line: Part I". In: *IEEE Transactions on Microwave Theory and Techniques* 30.1, pp. 82–86.

Aurangzeb, L. A. Khan, and A. Maqsood (2007). "Prediction of effective thermal conductivity of porous consolidated media as a function of temperature: a test case of limestones". In: *Journal of Physics D: Applied Physics* 40.16, pp. 4953–4958.

Ayadat, T. and A. M. Hanna (2012). "Assessment of soil collapse prediction methods". In: *IJE Transactions B: Applications* 25.1, pp. 19–26.

Banerjee, D. K. (2012). *Oil sands, heavy oil and bitumen: From recovery to refinery*. Penn Well Corporation, Tulsa, Oklahoma, USA.

Bao, J.-Z., C. C. Davis, and M. L. Swicord (1994). "Microwave dielectric measurements of erythrocyte suspensions". In: *Biophysical Journal* 66.6, pp. 2173–2180.

Behari, J. (2005). *Microwave dielectric behaviour of wet soils*. Springer International Publishing AG, Cham, Switzerland.

Birch, F. and H. Clark (1940). "The thermal conductivity of rocks and its dependence upon temperature and composition". In: *American Journal of Science* 238.8, pp. 529–558.

Birchak, J., C. Gardner, J. Hipp, and J. Victor (1974). "High dielectric constant microwave probes for sensing soil moisture". In: *Proceedings of the IEEE* 62.1, pp. 93–98.

Blackham, D. V. and R. D. Pollard (1997). "An improved technique for permittivity measurements using a coaxial probe". In: *IEEE Transactions on Instrumentation and Measurement* 46.5, pp. 1093–1099.

Blanch, S. and A. Aguasca (2004). "Seawater dielectric permittivity model from measurements at L Band". In: *Geoscience and Remote Sensing Symposium IGARSS*. Anchorage, Alaska, USA: IEEE, pp. 1362–1365.

Bland, W. F. and R. L. Davidson (1967). *Petroleum processing handbook*. McGraw-Hill, New York, USA.

Blonquist Jr., J. M., S. B. Jones, I. Lebron, and D. A. Robinson (2006). "Microstructural and phase configurational effects determining water content: Dielectric relationships of aggregated porous media". In: *Water Resources Research* 42, W05424.

Bolander, J. E. and S. Berton (2004). "Simulation of shrinkage induced cracking in cement composite overlays". In: *Cement and Concrete Composites* 26.7, pp. 861–871.

Bolander, J. E. and S. Saito (1998). "Fracture analysis using spring networks with random geometry". In: *Engineering Fracture Mechanics* 61, pp. 569–591.

Bolander, J. E. and N. Sukumar (2005). "Irregular lattice model for quasistatic crack propagation". In: *Physical Review B* 71.094106, pp. 1–12.

Briggs, J. P., V. R. Puttagunta, and N. B. Khiamel (1984). "The viscosity of heavy oil and bitumen which contain subsaturation concentrations of carbon dioxide". In: *WRI-DOE Tar Sand Symposium*. Vail, Colorado, USA.

Brooks, R. H. and A. T. Corey (1964). *Hydraulic properties of porous media*. Hydrology Papers No. 3, Colorado State University, Fort Collins, Colorado, USA.

Brouyère, S. (2001). "Etude et Modélisation du Transport et du Piégeage des Solutés en Milieu Souterrain Variablement Saturé". PhD thesis. University of Liege, Liege, Belgium.

Buchner, R., J. Barthel, and J. Stauber (1999). "The dielectric relaxation of water between 0°C and 35°C". In: *Chemical Physics Letters* 306, pp. 57–63.

Bunger, J. W., K. P. Thomas, and S. M. Dorrence (1979). "Compound types and properties of Utah and Athabasca tar sand bitumens". In: *Fuel* 58, pp. 183–195.

Camp, F. W. (1976). *The tar sands of Alberta*. Cameron Engineers, Denver, Colorado, USA.

Campbell, G. S. (1974). "A simple method for determining unsaturated conductivity from moisture retention data". In: *Soil Science* 117.6, pp. 311–314.

Campbell, J. E. (1990). "Dielectric properties and influence of conductivity in soils at one to fifty megahertz". In: *Soil Science Society of America Journal* 54.2, pp. 332–341.

Canadian Energy Research Institute (2008). *Green bitumen: The role of nuclear, gasification and CCS in Alberta's oil sands*. Calgary, Alberta, Canada.

Canadian Energy Research Institute (2011). *Emission abatement potential for the alberta oil sands industry and carbon capture and storage (CCS) applicability to coal-fired electricity generation and oil sands*. Calgary, Alberta, Canada.

Cannon, J. R. (1984). "The one-dimensional heat equation". In: *Encyclopedia of Mathematics and its Applications*. Ed. by G.-C. Rota. Vol. 23. Cambridge University Press, Cambridge, UK.

Carslaw, H. S. and J. C. Jaeger (1959). *Conduction of heat in solids*. 2nd Ed. Oxford, London, UK.

Casagrande, A. (1932). "The structure of clay and its importance in foundation engineering". In: *Journal of Boston Society of Civil Engineers* 19, pp. 168–209.

Cerutti, A., M. Bandinelli, M. Bientinesi, L. Petarca, M. De Simoni, and M. Manotti et al. (2013). "A new technique for heavy oil recovery based on electromagnetic heating: System design and numerical modeling". In: *Chemical Engineering Transactions* 32, pp. 1255–1260.

Cervanan, M. R., F. E. Vermeulen, and F. S. Chute (1981). "Thermal conductivity and specific heat of oil sand samples". In: *Canadian Journal of Earth Sciences* 18.5, pp. 926–931.

Chatzigeorgiou, G., V. Picandet, A. Khelidj, and G. Pijaudier-Cabot (2005). "Coupling between progressive damage and permeability of concrete: Analysis with a discrete model". In: *International Journal for Numerical and Analytical Methods in Geomechanics* 29.10, pp. 1005–1018.

Chen, F., N. Taylor, N. Kringos, and B. Birgisson (2015). "A study on dielectric response of bitumen in the low-frequency range". In: *Road Materials and Pavement Design* 16, pp. 153–169.

Chen, Y. and D. Or (2006). "Effects of Maxwell-Wagner polarization on soil complex dielectric permittivity under variable temperature and electrical conductivity". In: *Water Resources Research* 42.6, W06424.

Chen, Y., S. Zhou, R. Hu, and C. Zhou (2014). "Estimating effective thermal conductivity of unsaturated bentonites with consideration of coupled thermo-hydro-mechanical effects". In: *International Journal of Heat and Mass Transfer* 72, pp. 656–667.

Choo, J., Y. J. Kim, J. H. Lee, T. S. Yun, J. Lee, and Y. S. Kim (2013). "Stress-induced evolution of anisotropic thermal conductivity of dry granular materials". In: *Acta Geotechnica* 8.1, pp. 91–106.

Christ, N. H., R. Friedberg, and T. D. Lee (1982). "Random lattice field theory: General formulation". In: *Nuclear Physics B* 202.1, pp. 89–125.

Clauser, C. (1992). "Permeability of crystalline rocks". In: *Eos Transactions American Geophysical Union* 73.21, pp. 233–238.

Clauser, C. and E. Huenges (1995). *Thermal conductivity of rocks and minerals*. Rock Physics and Phase Relations: A Handbook of Physical Constants. American Geophysical Union, pp. 105–126.

Cole, K. S. and R. H. Cole (1941). "Dispersion and absorption in dielectrics I: Alternating current characteristics". In: *The Journal of Chemical Physics* 9.4–41, pp. 341–351.

Côté, J. and J. M. Konrad (2005). "A generalized thermal conductivity model for soils and construction materials". In: *Canadian Geotechnical Journal* 42, pp. 443–458.

Côté, J. and J. M. Konrad (2009). "Assessment of structure effects on the thermal conductivity of two-phase porous geomaterials". In: *International Journal of Heat and Mass Transfer* 52, pp. 796–804.

Czarnecki, J., B. Radoev, L. L. Schramm, and R. Slavchev (2005). "On the nature of Athabasca Oil Sands". In: *Advances in Colloid and Interface Science* 114, pp. 53–60.

De Vries, D. A. (1963). "Thermal properties of soil". In: *Physics of Plant Environment*. Ed. by V. W. Wijk. Amsterdam, The Netherlands: North Holland Publishing Company, pp. 210–235.

Debye, P. (1929). *Polar molecules*. Chemical Catalog Co. Inc., New York, USA.

Debye, P. (1934). "Part I. Dielectric constant. Energy absorption in dielectrics with polar molecules". In: *Transactions of the Faraday Society* 30, pp. 679–684.

Delage, P., E. Romero, and A. Tarantino (2008). "Recent developments in the techniques of controlling and measuring suction in unsaturated soils". In: *Proceedings of the 1st European Conference on Unsaturated Soils*. Durham, UK: Taylor & Francis Group, Balkema CRC Press, pp. 33–52.

Delaplace, A., G. Pijaudier-Cabot, and S. Roux (1996). "Progressive damage in discrete models and consequences on continuum modelling". In: *Journal of the Mechanics and Physics of Solids* 44.1, pp. 99–136.

Demirci, A., K. Görgülü, and Y. S. Durutürk (2004). "Thermal conductivity of rocks and its variation with uniaxial and triaxial stress". In: *International Journal of Rock Mechanics & Mining Sciences* 41.7, pp. 1133–1138.

Dinčov, D. D., K. A. Parrott, and K. A. Pericleous (2004). "A new computational approach to microwave heating of two-phase porous materials". In: *International Journal of Numerical Methods for Heat & Fluid Flow* 14.6, pp. 783–802.

Dobson, M. C., F. T. Ulaby, M. T. Hallikainen, and M. A. El-Rayes (1985). "Microwave dielectric behaviour of wet soil - Part II: Dielectric mixing models". In: *IEEE Transactions on Geoscience and Remote Sensing* GE 23.1, pp. 35–46.

Dong, Y., J. S. McCartney, and N. Lu (2015). "Critical review of thermal conductivity models for unsaturated soils". In: *Geotechnical and Geological Engineering* 32.2, pp. 207–221.

Doughty, C., A. Nir, C. F. Tsang, and G. S. Bodvarsson (1983). "Heat storage in unsaturated soils: Initial theoretical analysis of storage design and operation method". In: *Proceedings of the International Conference on Subsurface Heat Storage in Theory and Practice*. Stockholm, Sweden.

Ellison, W., A. Balana, G. Delbos, K. Lamkaouchi, L. Eymard, and C. Guillou et al. (1998). "New permittivity measurements of seawater". In: *Radio Science* 33.3, pp. 639–648.

Ellison, W. J. (2007). "Permittivity of pure water, at standard atmospheric pressur, over the frequency range 0-25 thz and the temperature range 0 - 100°C". In: *Journal of Physical and Chemical Reference Data* 36.1, pp. 1–18.

Eritrean Ministry of Energy and Mines (2006). *Eritrea hydrocarbon potential and exploration opportunities*. Asmara, Eritrea.

Etheridge, M. A., V. J. Wall, and R. H. Vernon (1983). "The role of the fluid phase during regional metamorphism and deformation". In: *Journal of Metamorphic Geology* 1.3, pp. 205–226.

Evett, S. R., R. C. Schwartz, J. A. Tolk, and T. A. Howell (2009). "Soil profile water content determination: Spatiotemporal variability of electromagnetic and neutron probe sensors in access tubes". In: *Vadose Zone Journal* 8.4, pp. 926–941.

Ewing, R. P. and A. G. Hunt (2006). "Dependence of the electrical conductivity on saturation in real porous media". In: *Vadose Zone Journal* 5.2, pp. 731–741.

Ezzat, M., N. A. Sabiha, and M. Izzularab (2014). "Accurate model for computing dielectric constant of nanocomposites". In: *Applied Nanoscience* 4.3, pp. 331–338.

Farouki, O. T. (1981). *Thermal properties of soils*. CRREL Monograph 81-1, US Army Corps of Engineers, Cold Regions Research and Engineering Laboratory, Hanover, New Hampshire, United States.

Feda, J. (1966). "Structural stability of subsident loess soils from Praha-Dejvice". In: *Engineering Geology*. Vol. 1. 3. Elsevier, Amsterdam, The Netherlands, pp. 201–219.

Feng, Y. T., K. Han, C. F. Li, and D. R. J. Owen (2008). "Discrete thermal element modelling of heat conduction in particle systems: Basic formulations". In: *Journal of Computational Physics* 227, pp. 5072–5089.

Feng, Y. T., K. Han, and D. R. J. Owen (2009). "Discrete thermal element modelling of heat conduction in particle systems: Pipe-network model and transient analysis". In: *Powder Technology* 193, pp. 248–256.

Fragkogiannis, G., G. Apostolopoulos, and S. Stamataki (2010). "Correlation of thermal conductivity and electrical resistivity of soil - for near surface geothermal applications". In: *Proceedings of the 72nd EAGE Conference & Exhibition incorporating SPE EUROPEC 2010*. Barcelona, Spain, pp. 3989–3993.

Fredlund, D. G. (1979). "Second Canadian Geotechnincal Colloquium: Appropriate concepts and technology for unsaturated soils". In: *Canadian Geotechnical Journal* 16.1, pp. 121–139.

Fredlund, D. G. and J. K. M. Gan (1995). "The collapse mechanism of a soil subjected to one-dimensional loading and wetting". In: *Genesis and Properties of Collapsible Soils*. Ed. by E. Derbyshire et al. Vol. 468. NATO ASI Series C: Mathematical and Physical Sciences. Kluwer Academic Publishers, Dordrecht, The Netherlands, pp. 173–205.

Fredlund, D. G. and N. R. Morgenstern (1977). "Stress state variables for unsaturated soils". In: *Journal of the Geotechnical Engineering Division* 103.5, pp. 447–466.

Fredlund, D. G. and H. Rahardjo (1993). *Soil mechanics for unsaturated soils*. John Wiley & Sons, Inc., New York, USA.

Fredlund, D. G. and A. Xing (1994). "Equations for the soil-water characteristic curve". In: *Canadian Geotechnical Journal* 31.4, pp. 521–532.

Gardner, W. R. (1956). "Calculation of capillary conductivity from pressure plate outflow data". In: *Soil Science Society of America Proceedings* 20, pp. 317–320.

Gavriliev, R. I. (2004). "Thermal properties of soils and surface covers". In: *Thermal Analysis, Construction, and Monitoring Methods for Frozen Ground*. Ed. by D. C. Esch. American Society of Civil Engineers, Reston, Virginia, USA, pp. 277–294.

Giambastiani, B. M. S., N. Colombanii, and M. Mastrocicco (2013). "Limitation of using heat as a groundwater tracer to define aquifer properties: Experiment in a large tank model". In: *Environmental Earth Science* 70, pp. 719–728.

Gong, Y., Q. Cao, and Z. Sun (2003). "The effects of soil bulk density, clay content and temperature on soil water content measurement using time-domain reflectometry". In: *Hydrological Processes* 17, pp. 3601–3614.

Gori, F. and S. Corasaniti (2004). "Theoretical prediction of the thermal conductivity and temperature variation inside Mars soil analogues". In: *Planetary and Space Science* 52, pp. 91–99.

Grassl, P. (2009). "A lattice approach to model flow in cracked concrete". In: *Cement and Concrete Composites* 31.7, pp. 454–460.

Gregory, A. P. and R. N. Clarke (2012). *Tables of the complex permittivity of dielectric reference liquids at frequencies up to 5 GHz*. Tech. Rep. NPL-Report-MAT-23. National Physical Laboratory, Teddington, UK.

Gunduz, Z. and H. Arman (2007). "Possible relationships between compression and recompression indices of a low-plasticity clayey soil". In: *The Arabian Journal for Science and Engineering* 32.2B, pp. 179–190.

Gupta, S. C., R. H. Dowdy, and W. E. Larson (1977). "Hydraulic and thermal properties of a sandy soil as influenced by incorporation of sewage sludge". In: *Soil Science Society of America Journal* 41.3, pp. 601–605.

Hailemariam, H. and F. Wuttke (2016). "Hydrothermal modelling and analysis of sensible heat storages for small-scale dwellings considering natural convection". In: *Energy Procedia* 97, pp. 462–469.

Hailemariam, H. and F. Wuttke (2018a). "Modelling EM heating of porous media with lattice element method". In: *Energy Geotechnics*. Ed. by A. Ferrari and L. Laloui. Springer Series in Geomechanics and Geoengineering. Springer International Publishing AG, Cham, Switzerland, pp. 315–322.

Hailemariam, H. and F. Wuttke (2018b). "Temperature dependency of the thermal conductivity of porous heat storage media". In: *Heat and Mass Transfer* 54.4, pp. 1031–1051.

Hailemariam, H., D. Shrestha, K. Sembdner, F. Wuttke, and N. Wagner (2015a). "Effect of hydro-mechanical changes on the relationship between thermal conductivity and dielectric permittivity of soils". In: *Proceedings of the 2nd EAGE Workshop on Geomechanics and Energy: The Ground as Energy Source and Storage*. Ed. by L. Laloui and B. François. Celle, Germany: European Association of Geoscientists and Engineers EAGE, pp. 110–114.

Hailemariam, H., A. Al-Janabi, F. Wuttke, and N. Wagner (2015b). "Wave based monitoring of water-driven deterioration process of unsaturated, stressed collapsible soils". In: *Proceedings of the International Symposium Non-Destructive Testing in Civil Engineering (NDT-CE)*. Berlin, Germany: BAM, TU Berlin, pp. 1–4.

Hailemariam, H., D. Shrestha, and F. Wuttke (2016). "Steady state vs transient thermal conductivity of soils". In: *Proceedings of the 1st International Conference on Energy Geotechnics ICEGT 2016*. Ed. by F. Wuttke, S. Bauer, and M. Sánchez. Kiel, Germany: Taylor & Francis Group, Balkema CRC Press, pp. 389–396.

Hailemariam, H., D. Shrestha, F. Wuttke, and N. Wagner (2017). "Thermal and dielectric behaviour of fine-grained soils". In: *Environmental Geotechnics* 4.2, pp. 79–93.

Hart, G. K. and W. I. Whiddon (1984). "Ground source heat pump planning workshop". In: *Summary of Proceedings, Palo Alto: Electric Power Research Institute*. EPRI Report RP 2033-12.

Hashin, Z. and S. Shtrikman (1962). "A variational approach to the theory of the effective magnetic permeability of multiphase materials". In: *Journal of Applied Physics* 33.10, pp. 3125–3131.

Hasted, J. B. (1973). *Aqueous dielectrics*. Chapman and Hall, London, UK.

Heimovaara, T. J., J. A. Huisman, J. A. Vrugt, and W. Bouten (2004). "Obtaining the spatial distribution of water content along a TDR probe using the SCEM-UA Bayesian inverse modeling scheme". In: *Vadose Zone Journal* 3, pp. 1128–1145.

Hermans, T., F. Nguyen, T. Robert, and A. Revil (2014). "Geophysical methods for monitoring temperature changes in shallow low enthalpy geothermal systems". In: *Energies* 7.8, pp. 5083–5118.

Hermans, T., S. Wildemeersch, P. Jamin, P. Orban, S. Brouyère, A. Dassargues, and F. Nguyen (2015). "Quantitative temperature monitoring of a heat tracing experiment using cross-borehole ERT". In: *Geothermics* 53, pp. 14–26.

Herrmann, H. J., A. Hansen, and S. Roux (1989). "Fracture of disordered, elastic lattices in two dimensions". In: *Physical Review B* 39.1, pp. 637–648.

Hilf, J. W. (1956). "An investigation of pore-water pressure in compacted cohesive soils". PhD thesis. Technical Memorandum No. 654, United States Bureau of Reclamation/University of Colorado, Boulder, Colorado, USA.

Hilhorst, M. A. (2000). "A pore water conductivity sensor". In: *Soil Science Society of America Journal* 64.6, pp. 1922–1925.

Hilhorst, M. A., C. Dirksen, F. W. H. Kampers, and R. A. Feddes (2001). "Dielectric relaxation of bound water versus soil matric pressure". In: *Soil Science Society of America Journal* 65.2, pp. 311–314.

Hirono, T. and Y. Hamada (2010). "Specific heat capacity and thermal diffusivity and their temperature dependencies in a rock sample from adjacent to the Taiwan Chelungpu fault". In: *Journal of Geophysical Research* 115.B05313.

Hofmeister, A. (1999). "Mantle values of thermal conductivity geotherm from phonon lifetimes". In: *Science* 283, pp. 1699–1709.

Hong, W.-T., Y.-S. Jung, S. Kang, and J.-S. Lee (2016). "Estimation of soil-water characteristics curves in multiple-cycles using membrane and TDR system". In: *Materials* 9.12, p. 1019.

Howayek, A. E., P. T. Huang, R. Bisnett, and M. C. Santagata (2011). *Identification and behavior of collapsible soils*. Tech. Rep. FHWA/IN/JTRP-2011/12. Indiana Department of Transportation and Purdue University, West Lafayette, Indiana, USA.

Huisman, J. A., S. S. Hubbard, J. D. Redman, and A. P. Annan (2003). "Measuring soil water content with ground penetrating radar: A review". In: *Vadose Zone Journal* 2.4, pp. 476–491.

IEEE 442 (1981). *IEEE guide for soil thermal resistivity measurements*. Institute of Electrical and Electronics Engineers, New York, USA.

Irani, M. and M. Cokar (2016). "Discussion on the effects of temperature on thermal properties in the steam-assisted-gravity-drainage (SAGD) process. Part 1: Thermal conductivity". In: *Society of Petroleum Engineers Journal* 21.02, pp. 334–352.

Ishida, T., T. Makino, and C. Wang (2000). "Dielectric-relaxation spectroscopy of kaolinite, montorillonite, allophane, and imogolite under moist conditions". In: *Clays and Clay Minerals* 48.1, pp. 75–84.

Ishida, T., M. Kawase, K. Yagi, J. Yamakawa, and K. Fukada (2003). "Effects of the counterion on dielectric spectroscopy of a montmorillonite suspension over the frequency range 10e5 - 10e10 Hz". In: *Journal of Colloid and Interface Science* 268.1, pp. 121–126.

Jamieson, D. T. and J. S. Tudhope (1970). "Physical properties of sea water solutions: Thermal conductivity". In: *Desalination* 8.3, pp. 393–401.

Jamieson, D. T., J. S. Tudhope, R. Morris, and G. Cartwright (1969). "Physical properties of sea water solutions: Heat Capacity". In: *Desalination* 7.1, pp. 23–30.

Japan Society of Mechanical Engineers (1983). *JSME data book: Thermophysical properties of fluids*. The Japan Society of Mechanical Engineers, Tokyo, Japan.

Jardani, A., A. Revil, and J. P. Dupont (2013). "Stochastic joint inversion of hydrogeophysical data for salt tracer test monitoring and hydraulic conductivity imaging". In: *Advances in Water Resources* 52, pp. 62–77.

Jennings, J. E. and K. Knight (1975). "A guide to construction on or with materials exhibiting additional settlement due to collapse of grain structure". In: *Proceedings of the 6th Regional Conference for Africa on Soil Mechanics and Foundation Engineering*. Vol. 1. Durban, South Africa, pp. 99–105.

Johansen, O. (1975). "Thermal conductivity of soils". PhD thesis. CRREL draft translation 637, 1977, Norwegian University of Science and Technology, Trondheim, Norway.

Jokinen, J. (2000). *Uncertainity analysis and inversion of geothermal conductive models using random simulation methods*. Oulu Universiy, Oulu, Finland.

Jol, H. M. (2009). *Ground penetrating radar: Theory and applications*. Elsevier, Amsterdam, The Netherlands.

Jonscher, A. K. (1977). "The universal dielectric response". In: *Nature* 267.5613, pp. 673–679.

Kaatze, U. (2000). "Hydrogen network fluctuations and the microwave dielectric properties of liquid water". In: *Subsurface Sensing Technologies and Applications* 1.4, pp. 377–391.

Kaatze, U. (2007a). "Non-conducting and conducting reference liquids for the calibration of dielectric measurement systems". In: *Proceedings of the 7th International Conference of ISEMA 2007 on Electromagnetic Wave Interaction with Water and Moist Substances*. Ed. by S. Okamura. Hamamatsu, Japan, pp. 3–10.

Kaatze, U. (2007b). "Reference liquids for the calibration of dielectric sensors and measurement instruments". In: *Measurement Science and Technology* 18.4, pp. 967–976.

Kaatze, U. (2010). "Techniques for measuring the microwave dielectric properties of materials". In: *Metrologia* 47.2, S91–S113.

Kaatze, U. and Y. Feldman (2006). "Broadband dielectric spectrometry of liquids and biosystems". In: *Measurement Science and Technology* 17.2, R17–R35.

Kafle, B., H. Hailemariam, and F. Wuttke (2014). "Theoretical and experimental modeling of settlement of rigid footing over collapsible soil". In: *Proceedings of the International Symposium on Geomechanics from Micro to Macro*. Ed. by K. Soga et al. Cambridge, UK: Taylor & Francis Group, CRC Press, UK, pp. 1617–1622.

Karim, G. A. and A. Hanafi (1981). "The thermal conductivity of oil-sands". In: *The Canadian Journal of Chemical Engineering* 59.4, pp. 461–464.

Kelleners, T. J., D. A. Robinson, P. J. Shouse, J. E. Ayars, and T. H. Skaggs (2005). "Frequency dependence of the complex permittivity and its impact on dielectric sensor calibration in soils". In: *Soil Science Society of America Journal* 69, pp. 67–76.

Kent, M. and R. Knöchel (2004). *A new method for the objective measurement of the quality of seafood*. Project SEQUID Final Report. Christian-Albrechts-Universität, Kiel, Germany.

Kersten, M. S. (1949). *Thermal properties of soils*. Bulletin 28, Engineering Experiment Station, University of Minnesota, Minneapolis, USA.

Klein, L. A. and C. T. Swift (1977). "An improved model for the dielectric constant of sea water at microwave frequencies". In: *IEEE Journal of Oceanic Engineering* 2.1, pp. 104–111.

Kluitenberg, G. J., J. M. Ham, and K. L. Bristow (1993). "Error analysis of the heat pulse method for measuring soil volumetric heat capacity". In: *Soil Science Society of America Journal* 57, pp. 1444–1451.

Kopyt, P. and M. Celuch-Marcysiak (2006). "One-dimensional fully analytical model of the microwave heating effect". In: *2006 International Conference on Microwaves, Radar & Wireless Communications*. Krakow, Poland, pp. 581–584.

Kraszewski, A., M. A. Stuchly, and S. S. Stuchly (1983). "ANA calibration method for measurements of dielectric properties". In: *IEEE Transactions on Instrumentation and Measurement* 32.2, pp. 385–387.

Landau, L. L. and E. M. Lifschitz (1985). "Elektrodynamik der Kontinua". In: *Lehrbuch der Theoretischen Physik*. Vol. 8. 5th Ed. Akademie-Verlag, Berlin, Germany.

Lasance, C. J. M. (2008). "Ten years of boundary-condition-independent compact thermal modeling of electronic parts: A review". In: *Heat Transfer Engineering* 29.2, pp. 149–168.

Lauer, K., N. Wagner, and P. Felix-Henningsen (2012). "A new technique for measuring broadband dielectric spectra of undisturbed soil samples". In: *European Journal of Soil Science* 63.2, pp. 224–238.

Lichtenecker, K. and K. Rother (1931). "Die Herleitung des logarithmischen Mischungsgesetzesaus allgemeinen Prinzipien der stationären Strömung". In: *Physikalische Zeitschrift* 32, pp. 255–260.

Lilliu, G. and J. G. M. van Mier (2003). "3D lattice type fracture model for concrete". In: *Engineering Fracture Mechanics* 70, pp. 927–941.

Lin, B. and A. B. Cerato (2013). "Electromagnetic properties of natural expansive soils under one-dimensional deformation". In: *Acta Geotechnica* 8.4, pp. 381–393.

Liu, X., G. Zhao, and Y. Jin (2006). "Coupled reservoir/wormholes model for cold heavy oil production wells". In: *Journal of Petroleum Science and Engineering* 50, pp. 258–268.

Logsdon, S. D., T. R. Green, J. V. Bonta, M. S. Seyfried, and S. R. Evett (2010). "Comparison of electrical and thermal conductivities for soils from five states". In: *Soil Science* 175.12, pp. 573–578.

Low, J. E., F. A. Loveridge, and W. Powrie (2013). "Measuring soil thermal properties for use in energy foundation design". In: *Proceedings of the 18th International Conference on Soil Mechanics and Geotechnical Engineering*. Paris, France.

Lowry, C. S., D. Fratta, and M. P. Anderson (2009). "Ground penetrating radar and spring formation in a groundwater dominated peat wetland". In: *Journal of Hydrology* 373, pp. 68–79.

Lu, S., T. Ren, Y. Gong, and R. Horton (2007). "An improved model for predicting soil thermal conductivity from water content at room temperature". In: *Soil Science Society of America Journal* 71.1, pp. 8–14.

Ma, L., D.-L. Paul, N. Pothecary, C. Railton, J. Bows, and L. Barratt et al. (1995). "Experimental validation of a combined electromagnetic and thermal FDTD model of a microwave heating process". In: *IEEE Transactions on microwave theory and techniques* 43.11, pp. 2565–2572.

Mains, G. J., J. W. Larson, and L. G. Hepler (1984). "General thermodynamic analysis of the contributions of temperature-dependent chemical equilibria to heat capacities of ideal gases and ideal associated solutions". In: *The Journal of Physical Chemistry* 88.6, pp. 1257–1261.

Malicki, M., R. Plagge, M. Renger, and R. Walczak (1992). "Application of time domain reflectometry (TDR) soil moisture miniprobe for the determination of unsaturated soil water characteristics from undisturbed soil cores". In: *Irrigation Science* 13.2, pp. 65–72.

Mansour, Z. M., Z. Chik, and M. R. Taha (2008). "On the procedures of soil collapse potential evaluation". In: *Journal of Applied Sciences* 8.23, pp. 4434–4439.

Marsland, T. P. and S. Evans (1987). "Dielectric measurements with an open-ended coaxial probe". In: *IEE Proceedings* 134.4, pp. 341–349.

Masliyah, J., J. Czarnecki, and Z. Xu (2010). *Handbook on theory and practice of bitumen recovery from Athabasca oil sands: Theoretical basis*. Vol. 1. Kingsley Publishing Services, Alberta, Canada.

Maxwell Garnett, J. C. (1904). "Colours in metal glasses and in metallic films". In: *Philosophical Transactions of the Royal Society of London*. Vol. 203. Series A, Containing Papers of a Mathematical or Physical Character, pp. 385–420.

McGaw, R. (1969). "Heat conduction in saturated granular materials". In: *Effects of Temperature and Heat on Engineering Behavior of Soils - International Conference*. Washington DC, USA: Special Rep. No. 103, Highway Research Board, pp. 114–131.

McGuinness, T., P. Hemmingway, and M. Long (2014). "Design and development of a low-cost divided bar apparatus". In: *Geotechnical Testing Journal* 37.2, pp. 230–241.

McKee, C. R. and A. C. Bumb (1984). "The importance of unsaturated flow parameters in designing a monitoring system for hazardous wastes and environmental emergencies". In: *Proceedings of Hazardous Materials Control Research Institute National Conference*. Houston, Texas, USA, pp. 50–58.

McKenzie, D., J. Jackson, and K. Priestley (2005). "Thermal structure of oceanic and continental lithosphere". In: *Earth and Planetary Science Letters* 233, pp. 337–349.

Meissner, T. and F. J. Wentz (2004). "The complex dielectric constant of pure and sea water from microwave satellite observations". In: *IEEE Transactions on Geoscience and Remote Sensing* 42.9, pp. 1836–1849.

Miadonye, A., B. Singh, and V. R. Puttagunta (1994). "Modelling the viscosity-temperature relationship of Alberta bitumen". In: *Fuel Science and Technology International* 12.2, pp. 447–450.

Minet, J., S. Lambot, G. Delaide, J. A. Huisman, H. Vereecken, and M. Vanclooster (2010). "A generalized frequency domain reflectometry modeling technique for soil electrical properties determination". In: *Vadose Zone Journal* 9, pp. 1063–1072.

Minkov, M., D. Evstatiev, Al. Alexiev, and P. Donchev (1977). "Deformation properties of Bulgarian loess soils". In: *Proceedings of the 9th International Conference on Soil Mechanics and Foundation Engineering SMFE*. Vol. 1. Tokyo, Japan, pp. 215–218.

Mironov, V., M. Dobson, V. Komarov, S. Komarov, and V. Kleshchenko (2004). "Generalized refractive mixing dielectric model for moist soils". In: *IEEE Transaction on Geoscience and Remote Sensing* 42.4, pp. 773–785.

Mitchell, J. K. and T. C. Kao (1978). "Measurement of soil thermal resistivity". In: *Journal of the Geotechnical Engineering Division* 104, pp. 1307–1320.

Momose, T., I. Sakaguchi, and T. Kasubuchi (2008). "Development of an apparatus for measuring one-dimensional steady-state heat flux of soil under reduced air pressure". In: *European Journal of Soil Science* 59.5, pp. 982–989.

Moore, R. G., C. J. Laureshen, J. D. M. Belgrave, M. G. Ursenbach, and S. A. Mehta (1995). "In situ combustion in Canadian heavy oil reservoirs". In: *Fuel* 74, pp. 1169–1175.

Mottaghy, D., H. D. Vosteen, and R. Schellschmidt (2008). "Temperature dependence of the relationship of thermal diffusivity versus thermal conductivity for crystalline rocks". In: *International Journal of Earth Sciences* 97.2, pp. 435–442.

Moukarzel, C. (1993). "Voronoi foams". In: *Physica A* 199, pp. 19–30.

Moukarzel, C. and H. J. Herrmann (1992). "A vectorizable random lattice". In: *Journal of Statistical Physics* 68.5/6, pp. 911–923.

Mukhametshina, A. and E. Martynova (2013). "Electromagnetic heating of heavy oil and bitumen: A review of experimental studies and field applications". In: *Journal of Petroleum Engineering*, pp. 1–7.

Mutyala, S., C. Fairbridge, J. R. J. Paré, J. M. R. Bélanger, S. Ng, and R. Hawkins (2010). "Microwave applications to oil sands and petroleum: A review". In: *Fuel Processing Technology* 91, pp. 127–135.

Nakamura, H., W. Srisoros, R. Yashiro, and M. Kunieda (2006). "Time-dependent structural analysis considering mass transfer to evaluate deterioration process of RC structures". In: *Journal of Advanced Concrete Technology* 4, pp. 147–158.

Nishida, Y. (1956). "A brief note on compression index of soil". In: *Journal of the Soil Mechanics and Foundations Division, ASCE* 82.3, pp. 1–14.

Olhoeft, G. R. (1981). "Electrical properties of rocks". In: *Physical Properties of Rocks and Minerals*. Ed. by Y. S. Touloukain and C. Y. Ho. McGraw-Hill, New York, USA, pp. 257–330.

Oloumi, D. and K. Rambabu (2016). "Microwave heating of heavy oil reservoirs: A critical analysis". In: *Microwave and optical technology letters* 58.4, pp. 809–813.

OPEC (2011). *Annual statistical bulletin: 2010/2011 Edition*. Vienna, Austria.

Or, D. and J. M. Wraith (1999). "Temperature effects on soil bulk dielectric permittivity measured by time domain reflectometry: A physical model". In: *Water Resources Research* 35, pp. 371–383.

Otto, G. and W. Chew (1991). "Improved calibration of a large open-ended coaxial probe for dielectric measurements". In: *IEEE Transactions on Instrumentation and Measurement* 40.4, pp. 742–746.

Pan, Y. and L. Xiao (2011). "Status of waste treatment methods in heavy oil cold production". In: *Energy Procedia*.

Penner, E., G. H. Johnston, and L. E. Goodrich (1975). "Thermal conductivity laboratory studies of some MacKenzie Highway soils". In: *Canadian Geotechnical Journal* 12.3, pp. 271–288.

Peters-Lidard, C. D., E. Blackburn, X. Liang, and E. F. Wood (1998). "The effect of soil thermal conductivity parameterization on surface energy fluxes and temperature". In: *Journal of the Atmospheric Sciences* 55.7, pp. 1209–1224.

Poling, B. E., J. M. Prausnitz, and J. P. O'Connell (2001). *Properties of gases and liquids*. 5th Ed. McGraw-Hill, New York, USA.

Popov, Y., D. F. C. Pribnow, J. H. Sass, C. F. Williams, and H. Burkhard (1999). "Characterization of rock thermal conductivity by high-resolution optical scanning". In: *Geothermics* 28.2, pp. 253–276.

Popovic, D., L. McCartney, C. Beasley, M. Lazebnik, M. Okoniewski, and S. Hagness et al. (2005). "Precision open-ended coaxial probes for in vivo and ex vivo dielectric spectroscopy of biological tissues at microwave frequencies". In: *IEEE Transactions on Microwave Theory and Techniques* 53.5, pp. 1713–1721.

Porch, A., D. Slocombe, J. Beutler, P. Edwards, A. Aldawsari, and T. Xiao et al. (2012). "Microwave treatment in oil refining". In: *Applied Petrochemical Research* 2, pp. 37–44.

Powell, R. W., C. Y. Ho, and P. E. Liley (1966). *Thermal conductivity of selected materials*. Category 5 - Thermodynamic and Transport Properties. Tech. Rep. NSRDS-NBS 8. National Bureau of Standards, Washington DC, USA.

Puttagunta, V. R., B. Singh, and A. Miadonye (1993). "Correlation of bitumen viscosity with temperature and pressure". In: *The Canadian Journal of Chemical Engineering* 71, pp. 1255–1260.

Rambabu, K., N. Semagina, and C. Lauge (2011). *Microwave and ultra-sound-assisted intensification of extraction and upgrading: Critical literature review and perspectives*. Tech. Rep. Center for Oil Sands Innovation, University of Alberta, Edmonton, Alberta, Canada.

Ramires, M. L. V., C. A. Nieto de Castro, Y. Nagasaka, A. Nagashima, M. J. Assael, and W. A. Wakeham (1995). "Standard reference data for the thermal conductivity of water". In: *Journal of Physical and Chemical Reference Data* 24, pp. 1377–1381.

Richards, L. A. (1941). "A pressure membrane extraction apparatus for soil suction". In: *Soil Science* 51.5, pp. 377–386.

Ridley, A. M. and W. K. Wray (1996). "Suction measurement: A review of current theory and practices". In: *Proceedings of the 1st International Conference on Unsaturated Soils, UNSAT '95*. Ed. by E. E. Alonso and P. Delage. Vol. 3. Paris, France: A. A. Balkema, Rotterdam, The Netherlands, pp. 1293–1322.

Rizvi, Z. H., A. S. Sattari, and F. Wuttke (2016). "Numerical analysis of heat conduction in granular geo-material using lattice element method". In: *Proceedings of the 1st International Conference on Energy Geotechnics ICEGT 2016*. Ed. by F. Wuttke, S.

Bauer, and M. Sánchez. Kiel, Germany: Taylor & Francis Group, Balkema CRC Press, pp. 367–371.

Rizvi, Z. H., D. Shrestha, A. S. Sattari, and F. Wuttke (2018). "Numerical modelling of effective thermal conductivity for modified geomaterial using lattice element method". In: *Heat and Mass Transfer* 54.2, pp. 483–499.

Robertson, E. C. (1988). *Thermal properties of rocks*. Tech. Rep. 88-441. United States Department of the Interior Geological Survey, Reston, Virginia, USA.

Robinson, D. A. (2004). "Calculation of the dielectric properties of temperate and tropical soil minerals from ion polarizabilities using Clausius-Mosotti equation". In: *Soil Science Society of America Journal* 68.5, pp. 1780–1785.

Robinson, D. A. and S. P. Friedman (2003). "A method for measuring the solid particle permittivity or electrical conductivity of rocks, sediments, and granular materials". In: *Journal of Geophysical Research* 108.B2.

Robinson, D. A., S. B. Jones, J. M. Or, D. Wraith, and S. P. Friedman (2003). "A review of advances in dielectric and electrical conductivity measurement in soils using time domain reflectometry". In: *Vadose Zone Journal* 2, pp. 444–475.

Robinson, D. A., C. S. Campbell, J. W. Hopmans, B. K. Hornbuckle, S. B. Jones, and R. Knight et al. (2009a). "Soil profile water content determination: Spatiotemporal variability of electromagnetic and neutron probe sensors in access tubes". In: *Vadose Zone Journal* 8.4, pp. 926–941.

Robinson, J., E. Binner, A. Saeid, M. Al-Harahsheh, and S. Kingman (2014). "Microwave processing of oil sands and contribution of clay minerals". In: *Fuel* 135, pp. 153–161.

Robinson, J. P., S. W. Kingman, C. E. Snape, R. Barranco, H. Shang, and M. S. A. Bradley et al. (2009b). "Remediation of oil-contaminated drill cuttings using continuous microwave heating". In: *Chemical Engineering Journal* 152, pp. 458–463.

Robinson, J. P., S. W. Kingman, C. E. Snape, S. M. Bradshaw, M. S. A. Bradley, and H. Shang et al. (2010). "Scale-up and design of a continuous microwave treatment system for the processing of oil-contaminated drill cuttings". In: *Chemical Engineering Research and Design* 88, pp. 146–154.

Rosen, M. A. and F. C. Hooper (1989). "A model for assessing the effects of berms on the heat loss from partially buried heat storage tanks". In: *Proceedings of the 9th International Heat Transfer Conference*. Jerusalem, Israel.

Rosine, T. N. (2015). "The impact of sample scale on the compressibility parameters of saturated fine-grained soils". PhD thesis. School of Computing, Science and Engineering, University of Salford, Salford, UK.

Rosine, T. N. and T. T. Sabbagh (2015). "The impact of the diameter to height ratio on the compressibility parameters of saturated fine-grained soils". In: *International Journal of Research in Engineering and Technology* 04.06, pp. 8–19.

Rowe, R., J. Shang, and Y. Xie (2001). "Complex permittivity measurement system for detecting soil contamination". In: *Canadian Geotechnical Journal* 38.3, pp. 498–506.

Saarenketo, T. (1998). "Electrical properties of water in clay and silty soils". In: *Journal of Applied Geophysics* 40.1-3, pp. 73–88.

Salomone, L. A. and W. D. Kovacs (1984). "Thermal resistivity of soils". In: *Journal of Geotechnical Engineering* 110.3, pp. 375–389.

Salomone, L. A. and J. I. Marlowe (1989). *Soil and rock classification according to thermal conductivity: Design of ground-coupled heat pump systems*. Tech. Rep. EPRI-CU-6482. Electric Power Research Institute, Palo Alto, California, USA.

Salomone, L. A., W. D. Kovacs, and T. Kusuda (1984). "Thermal performance of fine-grained soils". In: *Journal of Geotechnical Engineering* 110.3, pp. 359–374.

Santamarina, J. C., K. A. Klein, and M. A. Fam (2001). *Soils and waves: Particulate materials behavior, characterization and process monitoring*. John Wiley & Sons, Inc., New York, USA.

Sass, I. and J. Stegner (2012). "Coupled measurements of thermophysical and hydraulical properties of unsaturated and unconsolidated rocks". In: *Proceedings of the 37th Workshop on Geothermal Reservoir Engineering*. Stanford University, Stanford, California, USA.

Sattari, A. S., Z. H. Rizvi, H. B. Motra, and F. Wuttke (2017). "Meso-scale modeling of heat transport in a heterogeneous cemented geomaterial by lattice element method". In: *Granular Matter* 19.4, p. 66.

Schimmer, O., R. Osen, K. Schönfeld, and B. Hemmy (2009). "Detection of added water in seafood using a dielectric time domain reflectometer". In: *Proceedings of the 8th International Conference on Electromagnetic Wave Interaction with Water and Moist Substances, ISEMA*. Ed. by P. Vainikainen and T. Laitinen. Espoo, Finland, pp. 350–357.

Schwartz, R. C., S. R. Evett, M. G. Pelletier, and J. M. Bell (2009). "Complex permittivity model for time domain reflectometry soil water content sensing: I. Theory". In: *Soil Science Society of America Journal* 73.3, pp. 886–897.

Schwing, M., A. Scheuermann, and N. Wagner (2010). "Experimental investigation of dielectric parameters of soils during shrinkage". In: *Proceedings of the 1st European Conference on Moisture Measurement, Aquametry*. Ed. by K. Kupfer. MFPA Weimar, Weimar, Germany, pp. 511–519.

Scott, D. and A. C. Seto (1986). "Thermal property measurements on oil sands". In: *Journal of Canadian Petroleum Technology* 25.06, pp. 70–77.

Scott, J. D. (1989). "Heat transfer". In: *Technical Handbook on oil sands, bitumens and heavy oils*. Ed. by L. G. Hepler and C. Hsi. AOSTRA Technical Publication Series 6. Alberta Oil Sands Technology and Research Authority, Edmonton, Alberta, Canada, pp. 281–308.

Seki, N., K. C. Cheng, and S. Fukusako (1981). "Measurements on thermal conductivity and thermal diffusivity of Alberta oil sands". In: *Proceedings of the 17th International Conference on Thermal Conductivity*. Gaithersburg, Maryland, USA: Plenum Press, pp. 635–642.

Sengers, J. V. and J. T. R. Watson (1986). "Improved international formulations for the viscosity and thermal conductivity of water substance". In: *Journal of Physical and Chemical Reference Data* 15.4, pp. 1291–1314.

Sepaskhah, A. R. and L. Boersma (1979). "Thermal conductivity of soils as a function of temperature and water content". In: *Soil Science Society of America Journal* 43.3, pp. 439–444.

Seyer, F. A. and C. W. Gyte (1989). "Viscosity". In: *AOSTRA Technical Handbook Publication on Oil Sands, Bitumens and Heavy Oils*. Ed. by L. G. Hepler and C. His. Alberta Oil Sands Technology and Research Authority, Edmonton, Alberta, Canada, pp. 153–184.

Shah, A., R. Fishwick, J. Wood, G. Leeke, S. Rigby, and M. Greaves (2010). "A review of novel techniques for heavy oil and bitumen extraction and upgrading". In: *Energy & Environmental Science* 3, pp. 700–714.

Shainberg, I., J. D. Rhoades, and R. J. Prather (1980). "Effect of exchangeable sodium percentage, cation exchange capacity, and soil solution concentration on soil electrical conductivity". In: *Soil Science Society of America Journal* 44.3, pp. 469–473.

Sharqawy, M. H., J. H. Lienhard V, and S. M. Zubair (2010). "Thermophysical properties of seawater: A review of existing correlations and data". In: *Desalination and Water Treatment* 16.1-3, pp. 354–380.

Sheen, N. and I. Woodhead (1999). "An open-ended coaxial probe for broadband permittivity measurement of agricultural products". In: *Journal of Agricultural Engineering Research* 74.2, pp. 193–202.

Shen, L. C., W. C. Savre, J. M. Price, and K. Athavale (1985). "Dielectric properties of reservoir rocks at ultra-high frequencies". In: *Geophysics* 50, pp. 629–704.

Shön, J. (2015). *Physical properties of rocks: Fundamentals and principles of petrophysics*. Vol. 65. 2nd Ed. Elsevier, Amsterdam, The Netherlands.

Singh, B., A. Miadonye, S. S. Huang, R. Srivastava, and V. R. Puttagunta (1994). "Estimating temperature and pressure effects on viscosity of Saskatchewan heavy oils". In: *Fuel Science and Technology International* 12.5, pp. 693–704.

Skauge, A., N. Fuller, H.-K. Yan, R. Cassis, N. S. Srinivasan, and L. G. Hepler (1983). "Specific heat capacities of minerals from oil sands and heavy oil deposits". In: *Thermochimica Acta* 68.2–3, pp. 291–296.

Skierucha, W. (2011). "Time domain reflectometry: Temperature-dependent measurements of soil dielectric permittivity". In: *Electromagnetic Waves*. Ed. by V. Zhurbenko. InTech, Rijeka, Croatia, pp. 369–386.

Smith-Magowan, D., A. Skauge, and L. G. Hepler (1982). "Specific heats of Athabasca oil sands and components". In: *Journal of Canadian Petroleum Technology* 21.3, pp. 28–32.

Smits, K. M., T. Sakaki, S. E. Howington, J. F. Peters, and T. H. Illangasekare (2013). "Temperature dependence of thermal properties of sands over a wide range of temperatures (30-70°C)". In: *Vadose Zone Journal* 12.1.

Somerton, W. H., J. A. Keese, and S. L. Chu (1974). "Thermal behavior of unconsolidated oil-sands". In: *Society of Petroleum Engineers Journal* 14.5, pp. 513–521.

Speight, J. G. (2007). *The chemistry and technology of petroleum*. Chemical Industries, 4th Ed. Taylor & Francis Group, CRC Press, UK.

Sridharan, A. and H. B. Nagaraj (2000). "Compressibility behaviour of remoulded, fine-grained soils and correlation with index properties". In: *Canadian Geotechnical Journal* 37.3, pp. 712–722.

Stegner, J., D. Nguyen, R. Seehaus, and I. Sass (2011). "Development of a thermal conductivity and diffusivity meter for unconsolidated rocks". In: *Proceedings of the 18. Tagung für Ingeniergeologie*. Berlin, Germany.

Stegner, J., C. Drefke, H. Hailemariam, H. Anbergen, F. Wuttke, and I. Sass (2017). "Messtechnik für den Erdkabeltrassenbau - Ermittlung der Wärmeleitfähigkeit von Bettungsmaterialien". In: *Bauphysik* 39.1, pp. 41–48.

Strausz, O. P. and E. M. Lown (1978). *Oil sand and oil shale chemistry*. Verlag Chemie International Inc., New York, USA.

Strausz, O. P. and E. M. Lown (2003). *The chemistry of Alberta oil sands, bitumen and heavy oils*. Alberta Energy Research Institute, Calgary, Alberta, Canada.

Stuchly, M. A. and S. S. Stuchly (1980). "Coaxial line reflection methods for measuring dielectric properties of biological substances at radio and microwave frequencies - A review". In: *IEEE Transactions on Instrumentation and Measurement* 29.3, pp. 176–183.

Stuchly, M. A., M. M. Brady, S. S. Stuchly, and G. Gajda (1982a). "Equivalent circuit of an open-ended coaxial line in a lossy dielectric". In: *IEEE Transactions on Instrumentation and Measurement* 31.2, pp. 116–119.

Stuchly, M. A., T. W. Athey, G. M. Samaras, and G. E. Taylor (1982b). "Measurement of radio frequency permittivity of bilological tissues with an open-ended coaxial

line: Part II - Experimental results". In: *IEEE Transactions on Microwave Theory and Techniques* 30.1, pp. 87–92.

Sun, Z. J. and G. D. Young (2001). "Saline clayey soil moisture measurement using time-domain reflectometry". In: *Proceedings of the TDR 2001 Symposium*. Evanston, Illinois, USA.

Takahashi, K., J. Igel, H. Preetz, and S. Kuroda (2012). "Basics and application of ground penetrating radar as a tool for monitoring irrigation process". In: *Problems, Perspectives and Challenges of Agricultural Water Management*. Ed. by M. Kumar. In-Tech, Rijeka, Croatia, pp. 155–180.

Takamura, K. (1982). "Microscopic structure of Athabasca Oil Sand". In: *The Canadian Journal of Chemical Engineering* 60.4, pp. 538–545.

Tarnawski, V., F. Gori, B. Wagner, and G. Buchan (2000). "Modelling approaches to predicting thermal conductivity of soil at high temperature". In: *International Journal of Energy Research* 24, pp. 403–423.

Taylor, D. W. (1942). *Research on consolidation of clays*. Ser. 82. Department of Civil and Sanitary Engineering, Massachusetts Institute of Technology, Cambridge, Massachusetts, USA.

Tehranian, F., M. A. Abdou, and M. S. Tillack (1994). "Effect of external pressure on particle bed effective thermal conductivity". In: *Journal of Nuclear Materials* 212-215.Part B, pp. 885–890.

Todd, M. G. and F. G. Shi (2005). "Complex permittivity of composite systems: A comprehensive interphase approach". In: *IEEE Transactions on Dielectrics and Electrical Insulation* 12.3, pp. 601–611.

Topp, G. C., J. L Davis, and A. P. Annan (1980). "Electromagnetic determination of soil water content measurements in coaxial transmission lines". In: *Water Resources Research* 16.3, pp. 574–582.

Torgersen, T. (1990). "Crustal-scale fluid transport: Magnitude and mechanisms". In: *Eos Transactions American Geophysical Union* 71.1, pp. 1–13.

Ulaby, F. T. (2007). *Fundamentals of applied electromagnetics*. 5th Ed. Pearson Prentice Hall, New Jersey, USA.

Upreti, S., A. Lohi, R. Kapadia, and R. El-Haj (2007). "Vapor extraction of heavy oil and bitumen: A review". In: *Energy Fuels* 21, pp. 1562–1574.

Usowicz, B. (1992). "Statistical-physical model of thermal conductivity in soil". In: *Polish Journal of Soil Science* XXV/1, pp. 25–34.

van Genuchten, M. T. (1980). "A closed-form equation for predicting the hydraulic conductivity of unsaturated soils". In: *Soil Science Society of America Journal* 44.5, pp. 892–898.

Van Rooyen, M. and H. F. Winterkorn (1959). "Structural and textural influences on thermal conductivity of soils". In: *Highway Research Board Proceedings*. Vol. 38, pp. 576–621.

Vanapalli, S. K., D. G. Fredlund, D. E. Pufahl, and A. W. Clifton (1996). "Model for the prediction of shear strength with respect to soil suction". In: *Canadian Geotechnical Journal* 33, pp. 379–392.

Vandenbohede, A., T. Hermans, F. Nguyen, and L. Lebbe (2011). "Shallow heat injection and storage experiment: Heat transport simulation and sensitivity analysis". In: *Journal of Hydrology* 409, pp. 262–272.

Vargas, W. L. and J. J. McCarthy (2001). "Heat conduction in granular materials". In: *AIChE Journal* 47.5, pp. 1052–1059.

Vargas, W. L. and J. J. McCarthy (2002). "Stress effects on the conductivity of particulate beds". In: *Chemical Engineering Science* 57.15, pp. 3119–3131.

Von Hippel, A. R. (1954). *Dielectrics and waves*. John Wiley & Sons, Inc., New York, USA.

Wagner, N. and A. Scheuermann (2009). "On the relationship between matric potential and dielectric properties of organic free soils: A sensitivity study". In: *Canadian Geotechnical Journal* 46.10, pp. 1202–1215.

Wagner, N., K. Kupfer, and E. Trinks (2007a). "A broadband dielectric spectroscopy study of the relaxation behaviour of subsoil". In: *Proceedings of the 7th International Conference of ISEMA 2007 on Electromagnetic Wave Interaction with Water and Moist Substances*. Ed. by S. Okamura. Hamamatsu, Japan, pp. 31–38.

Wagner, N., E. Trinks, and K. Kupfer (2007b). "Determination of the spatial TDR-sensor characteristics in strong dispersive subsoil using 3D-FEM frequency domain simulations in combination with microwave dielectric spectroscopy". In: *Measurement Science and Technology* 18, pp. 1137–1146.

Wagner, N., B. Müller, K. Kupfer, F. Bonitz, M. Schwing, and A. Scheuermann (2010). "Broadband electromagnetic characterization of two-port rod based transmission lines for dielectric spectroscopy of soil". In: *Proceedings of the 1st European Conference on Moisture Measurement, Aquametry*. Ed. by K. Kupfer. MFPA Weimar, Weimar, Germany, pp. 228–237.

Wagner, N., K. Emmerich, F. Bonitz, and K. Kupfer (2011a). "Experimental investigations on the frequency- and temperature-dependent dielectric material properties of soil". In: *IEEE Transactions on Geoscience and Remote Sensing* 49.7, pp. 2518–2530.

Wagner, N., T. Sokoll, and O. Schimmer (2011b). "Robust low cost open-ended coaxial probe for dielectric spectroscopy in laboratory and in-situ applications". In: *Proceedings of the 6th CMM Conference Innovative Feuchtemessung in Forschung und Praxis*. Karlsruhe, Germany.

Wagner, N., T. Bore, J. C. Robinet, D. Coelho, F. Taillade, and S. Delepine-Lesoille (2013). "Dielectric relaxation behavior of callovo-oxfordian clay rock: A hydraulic-mechanical-electromagnetic coupling approach". In: *Journal of Geophysical Research: Solid Earth* 118.9, pp. 4729–4744.

Wagner, N., M. Schwing, and A. Scheuermann (2014). "Numerical 3D FEM and experimental analysis of the open-ended coaxial line technique for microwave dielectric spectroscopy on soil". In: *IEEE Transaction on Geoscience and Remote Sensing* 52.2, pp. 880–893.

Wallace, D., J. Starr, K. P. Thomas, and S. M. Dorrence (1988). *Characterization of oil sand resources*. Alberta Oil Sands Technology and Research Authority, Edmonton, Alberta, Canada.

Wang, F. and E. G. D. Cohen (1996). "Diffusion on random lattices". In: *Journal of Statistical Physics* 84.1/2, pp. 233–261.

Wang, L., M. Soda, and T. Ueda (2008). "Simulation of chloride diffusivity for cracked concrete based on RBSM and truss network model". In: *Journal of Advanced Concrete Technology* 6.1, pp. 143–155.

Wang, M. and N. Pan (2007). "Numerical analysis of effective dielectric constant of multiphase microporous media". In: *Journal of Applied Physics* 101, p. 114102.

Weaire, D. and N. Rivier (1984). "Soap, cells and statistics-random patterns in two dimensions". In: *Contemporary Physics* 25.1, pp. 59–99.

Wei, Y.-Z. and S. Sridhar (1991). "Radiation-corrected open-ended coax line technique for dielectric measurements of liquids up to 20 GHz". In: *IEEE Transactions on Microwave Theory and Techniques* 39.3, pp. 526–531.

Weidenfeld, G., Y. Weiss, and H. Kalman (2004). "A theoretical model for effective thermal conductivity (ETC) of particulate beds under compression". In: *Granular Matter* 6.2, pp. 121–129.

Widodo, S. and A. Ibrahim (2012). "Estimation of primary compression index (Cc) using physical properties of Pontianak soft clay". In: *International Journal of Engineering Research and Applications (IJERA)* 2.5, pp. 2232–2236.

Williams, J., R. E. Prebble, W. T. Williams, and C. T. Hignett (1983). "The influence of texture, structure and clay mineralogy on the soil moisture characteristic". In: *Australian Journal of Soil Research* 21.1, pp. 15–32.

Williams, P. J. (1982). *The surface of the earth: An introduction to geotechnical science*. Addison-Wesley Longman Ltd, New York, USA.

Wraith, J. M. and D. Or (1999). "Temperature effects on soil bulk dielectric permittivity measured by time domain reflectometry: Experimental evidence and hypothesis development". In: *Water Resources Research* 35.2, pp. 361–369.

Wuttke, F., A. S. Sattari, Z. H. Rizvi, and H. B. Motra (2017). "Advanced meso-scale modelling to study the effective thermo-mechanical parameter in solid geomaterial". In: *Advances in Laboratory Testing and Modelling of Soils and Shales (ATMSS)*. Ed. by A. Ferrari and L. Laloui. Springer Series in Geomechanics and Geoengineering. Springer International Publishing AG, Cham, Switzerland, pp. 85–95.

Yun, T. S. and T. M. Evans (2010). "Three-dimensional random network model for thermal conductivity in particulate materials". In: *Computers and Geotechnics* 37, pp. 991–998.

Yun, T. S. and J. C. Santamarina (2007). "Fundamental study of thermal conduction in dry soils". In: *Granular Matter* 10.3, pp. 197–207.

Zajicek, R., J. Vrba, and K. Novotny (2006). "Evaluation of a reflection method on an open-ended coaxial line and its use in dielectric measurements". In: *Acta Polytechnica* 5, pp. 50–54.

Zakri, T., J. P. Laurent, and M. Vauclin (1998). "Theoretical evidence for 'Lichtenecker's mixture formulae' based on the effective medium theory". In: *Journal of Physics D* 31.13, pp. 1589–1594.

Zhou, Y., R. H. Lang, C. Drego, C. Utku, and D. Le Vine (2012). "Improved measurements of seawater dielectric constant at L-Band". In: *Microwave Radiometry and Remote Sensing of the Environment MicroRad*. Rome, Italy: IEEE.